Multicomponent templating approaches to solid form control in the continuous crystallisation environment

Agnew, Lauren

Award date:
2017

Awarding institution:
University of Bath

CMAC
FUTURE MANUFACTURING
RESEARCH HUB

UNIVERSITY OF
BATH

Multicomponent templating approaches to solid form control in the continuous crystallisation environment

Lauren Rebecca Agnew

A thesis submitted for the degree of Doctor of Philosophy

University of Bath

Department of Chemistry

Supervisor: Professor Chick Wilson

September 2017

Abstract

The work presented in this thesis looks at using multi-component crystallisation techniques to impart solid form control to pharmaceutically relevant systems. In this thesis solid form encompasses both different polymorphic forms of the same material as well as the chemical and physical stability of a non-polymorphic single component compound. The work emerges as part as the EPSRC Future Manufacturing Hub in Continuous Manufacturing and Advanced Crystallisation (CMAC); an academic-industrial collaboration set up to aid the adoption of continuous manufacturing processes into an industrial setting.

Chapters 3-5 explore the use of incorporating a second molecular component into the crystallisation process, termed a template in this work, in order to direct the formation of metastable polymorphic forms. Chapter 3 investigates this templating effect on the formation of the metastable form (II) of paracetamol (PCM) in a small scale batch crystallisation environment; PCM-II displays enhanced compressibility and solubility in comparison to the stable PCM-I. A number of structurally similar and size-matched template molecules are investigated for their templating effects, with the most success observed with the structurally similar metacetamol (MCM). Possible mechanistic insights into the action of the template molecules are also investigated. In Chapter 4, the conditions for the templated production of PCM-II with MCM at the 100 ml scale are optimised through use of a Design of Experiments analysis. Identification of optimal conditions for the production of PCM-II are then used in further batch scale-up experiments at the 800 ml scale, monitored with process analytical technologies.

Chapter 4 also describes initial transfer to continuous crystallisation platforms, investigating production in a periodic mixed suspension mixed product removal (PMSMPR) crystalliser, with Chapter 5 describing flow crystallisation experiments in the continuous oscillatory baffled crystalliser (COBC) and the kinetically regulated automated input crystalliser (KRAIC). The use of the COBC resulted in the successful continuous crystallisation of PCM-II; however elimination of an impurity proved problematic. The use of the PMSMPR platform resulted in the first ever successful continuous crystallisation of phase pure samples of PCM-II.

Chapter 6 describes obtaining solid form control of reactive pharmaceuticals through incorporation inside benign host molecules. Investigations focussed on two hosting systems whereby the APIs thiamphenicol and α-lipoic acid were hosted within γ- and β- cyclodextrin, respectively. Full NMR analysis to elucidate host-guest stoichiometry was performed, with the transfer to cooling crystallisation environments targeted, with preliminary investigations carried out.

Acknowledgments

First and foremost; I would like to thank Chick, not just for the opportunity to do a PhD, but for the overwhelming support and guidance throughout my time in the group. For all our random conversations, for running the Bath Half with me, for providing Hobbes in times of need and for always being there for advice, I never would have survived these four years without you.

To all the doctors and nurses that have kept me standing-up throughout my PhD; Mr Luker, Mr Walker, Dr Bligh, the lovely Sister Kathie Marshall and all those at East Cheshire NHS who looked after me in Macclesfield, it certainly hasn't been an easy ride but we found a way.

To all those in CMAC: thanks to my DTC for making my first year such fun and to those at Strathclyde, especially Thomas McGlone and Maria Bruiglia, for the help on my visits to SIPBS and TIC. Not forgetting EasyJet for getting me 'North of the Border' 15 times and counting.

To all the Wilson group past and present who have made the past four years so enjoyable, thank you for your support and friendship. Louise my singing buddy, Dr Dyanne my morning buddy, Kate for being the person I can moan to, Ruth for always making me laugh with our endless inappropriate conversations, Anneke my travel buddy and roommate on our countless trips away, Alex for the hugs, Lucy for the smiles, Charlotte for putting up with me in my project, PiBa our resident engineer and my two lovely project students Sarah and Lois for your hard work during your projects. And to Karen – thank you for all your help over the years and keeping me amused with the comments on my thesis.

To all the industrial mentors who have helped me throughout my project; Amy Robertson, Helen Wheatcroft, Stefan Taylor and Michal Sowa thank you for all your ideas throughout my PhD. To the lovely Right Particle team (Amy Robertson, Helen Wheatcroft, Rachel Sullivan, Anna Jawor-Baczynska, Andy Robbins, Keddon Powell, Gareth Ensor and David Wilson) at AstraZeneca for providing an invaluable and enjoyable industrial placement within your team and for giving me a job upon completion of this PhD.

To all those in Bath for their help and support. John Lowe and Catherine Lyall; thank you both for your patience and guidance with all things NMR related. And to Gan, thank you for always being a friendly face to chat to – still my personal tutor 8 years later! Not forgetting the 1S porters (Ray, Dave and Pete) for all the morning cups of tea.

Finally, Mum, Dad, El, all my friends and bears, thank you for your support in the best and worst of times over the past four years.

Table of Contents

Abstract 2

Acknowledgments 3

List of Figures 8

List of Tables 14

List of abbreviations 16

1 Introduction – Crystallisation of molecular products 19

1.1 Context of research 19

1.2 Supersaturation 19

1.3 Nucleation 20

1.3.1 Thermodynamics of nucleation 23

1.3.2 Kinetics of nucleation 24

1.3.3 Heterogeneous nucleation 24

1.3.4 Secondary nucleation 25

1.4 Crystal Growth 25

1.4.1 Crystal faces 25

1.4.2 Birth and spread model 27

1.4.3 Burton Cabrera Frank (BCF) model 27

1.4.4 Rough interface model 28

1.5 Crystal morphology 29

1.6 Crystallisation methods 30

1.6.1 Cooling crystallisation 30

1.6.2 Evaporative crystallisation 31

1.6.3 Antisolvent crystallisation 32

1.6.4 Reactive crystallisation 33

1.6.5 Seeded crystallisation 33

1.6.6 Monitoring the crystallisation process 34

1.7 Continuous crystallisation 35

1.8 Polymorphism 38

1.8.1 Thermodynamics of polymorphism 39

1.8.2 Solution mediated phase transitions 41

1.8.3 Solid state polymorphic transformations 44

1.9 Multicomponent crystallisation 44

1.9.1 Crystal engineering 45
1.9.2 Hydrates 51
1.9.3 Additives within crystallisation 51
1.10 Aims of research 53
2 Experimental methods 54
2.1 Solubility Measurements 54
2.2 Cooling crystallisations 55
2.3 Single crystal X-ray diffraction (SCXRD) 56
2.3.1 The crystalline state 56
2.3.2 X-ray diffraction 58
2.3.3 Experimental 61
2.4 Powder X-ray diffraction (PXRD) 62
2.4.1 Theory 62
2.4.2 Experimental 63
2.5 Differential Scanning Calorimetry (DSC) 63
2.5.1 Theory 63
2.5.2 Experimental 64
2.6 Thermogravimetric analysis (TGA) 65
2.6.1 Theory 65
2.6.2 Experimental 65
2.7 Raman Spectroscopy 65
2.7.1 Theory 65
2.7.2 Experimental 66
2.8 Process analytical technologies (PAT) 66
2.8.1 Focussed Beam Reflectance Measurement (FBRM) 66
2.8.2 Raman probe 67
2.9 SEM 67
2.9.1 Theory 67
2.9.2 Experimental 68
2.10 NMR 68
2.10.1 Theory 68
2.10.2 Experimental 68
3 Small-scale batch crystallisation of paracetamol form II 70
3.1 Introduction and Aims 70

3.2 Materials and methods 75
3.2.1 Solubility measurements 75
3.2.2 Cooling crystallisations 76
3.2.3 Seeding experiments 76
3.2.4 Characterisation techniques 77
3.3 Crystallisation with benzoic acid derivatives 78
3.3.1 Seeding experiments 81
3.4 Crystallisation with metacetamol 82
3.4.1 Metacetamol hydrate (MCM.H_2O) 87
3.4.2 SEM 89
3.5 Crystallisation with other structurally related compounds 90
3.6 Mechanistic information 97
3.6.1 Stability of samples 102
3.7 Conclusions 104
4 Scaled batch crystallisation of PCM-II and transfer to a MSMPR crystalliser 107
4.1 Design of Experiments (DoE) at the 100 ml scale 107
4.1.1 Initial investigations into scaling potential in an RBF 107
4.1.2 Introduction to DoE 109
4.1.3 Materials and methods 110
4.1.4 Results and discussion 115
4.1.5 Conclusions 123
4.2 Scaled crystallisation in the OptiMax 124
4.2.1 Introduction and aims 124
4.2.2 Experimental 124
4.2.3 Raman spectra for the polymorphs of paracetamol 126
4.2.4 Results and discussion 127
4.2.5 Conclusions 131
4.3 Continuous crystallisation in a MSMPR 131
4.3.1 Introduction and aims 131
4.3.2 Experimental 132
4.3.3 Results and discussion 136
4.3.4 Conclusions 144
4.4 Chapter Conclusions 144
5 Continuous flow crystallisation of PCM-II 147

5.1 Continuous crystallisation in the COBC....147
5.1.1 Introduction and Aims....147
5.1.2 Experimental....150
5.1.3 Results and Discussion....154
5.1.4 Conclusions....172
5.2 Continuous crystallisation in the KRAIC....174
5.2.1 Introduction and Aims....174
5.2.2 Experimental....178
5.2.3 Results and discussion....180
5.2.4 Conclusions....186
5.3 Chapter conclusions....187
6 Hosting of reactive pharmaceuticals....189
6.1 Introduction and Aims....189
6.2 Experimental....191
6.2.1 Evaporative crystallisations....191
6.2.2 Cooling crystallisations....192
6.2.3 NMR analysis....192
6.2.4 Single crystal X-ray diffraction....196
6.3 Results and discussion....196
6.3.1 The molecular complex of thiamphenicol and γ-cyclodextrin....196
6.3.2 The molecular complex of α-lipoic acid and β-cyclodextrin....208
6.4 Conclusions....214
7 Conclusions and Future Work....216
7.1 Conclusions....216
7.2 Future work....220
7.2.1 Templating for polymorph control....220
7.2.2 Hosting....223
8 References....224
9 Appendices....236
9.1 A3 (Chapter 3)....236
9.2 List of Publications....238
9.3 List of oral conference presentations....238

List of Figures

Figure 1.1: A typical solubility diagram showing the variation in concentration with temperature
Figure 1.2: Nucleation classification (adapted from Beckmann[1])
Figure 1.3: The two commonly accepted nucleation pathways: classical nucleation theory (top) and two-step nucleation (bottom)[3]
Figure 1.4: A free energy diagram for the formation of a cluster (a) at low supersaturation, (b) at high supersaturation
Figure 1.5: The classification of crystal faces according to Hartmann and Perdock[12]
Figure 1.6: The free energy barriers to overcome during the crystal growth process, from solution (right) to crystal (left)
Figure 1.7: Schematic of the birth and spread model[15]
Figure 1.8: The development of spiral growth, originating from a spiral dislocation[13]
Figure 1.9: Spiral growth in L-arginine trifluoroacetate crystals, visualised using AFM
Figure 1.10: Filtration of block-like crystals (left) and plate-like crystals (right)
Figure 1.11: A typical solubility diagram showing the variation of concentration with temperature during a cooling crystallisation experiment
Figure 1.12: A typical solubility diagram showing the variation in temperature during an evaporative crystallisation - the blue arrow shows evaporation and the red arrow shows concentration
Figure 1.13: The variation in solubility of the solute with increasing antisolvent concentration in a typical antisolvent crystallisation
Figure 1.14: A typical solubility curve showing the change in concentration with temperature during a seeded cooling crystallisation (left) and a typical seeded crystallisation temperature profile (right)
Figure 1.15: A typical COBC set-up[65]
Figure 1.16: The molecular structure of ROY
Figure 1.17: The energy landscape of stable and metastable polymorphs
Figure 1.18: Concentration-temperature diagrams for a monotropic and an enantiotropic system
Figure 1.19: Gibbs free energy changes with temperature for monotropically (left) and enantiotropically (right) related polymorphs
Figure 1.20: Phase diagram
Figure 1.21: The four observed trends in solution mediated phase transitions (black – supersaturation, red – metastable polymorph, blue – stable polymorph)
Figure 1.22: Full interaction maps for sulfathiazole form I (left) and form V (right); the greyed out molecules are formed through hydrogen bonding interactions. Generated from CSD references SUTHAZ01 and SUTHAZ05, respectively.
Figure 1.23: The different types of electrostatic interactions between two aromatic systems
Figure 1.24: Attraction through face to face packing when one of the systems contains an electron withdrawing group
Figure 1.25: (a) a supramolecular homosynthon in the form of a carboxylic acid dimer, (b) a supramolecular heterosynthon in the form of an amide-carboxylic acid dimer
Figure 1.26: A co-crystal of theophylline and paracetamol (CSD REF: KIGLUI) and a salt of 4-aminopyridine and 5-acetylamino salicylic acid (CSD REF:CELXOI), with proton transfer from the carboxylic acid to the pyridine nitrogen
Figure 2.1: The Technobis Crystal 16
Figure 2.2: A temperature *vs* transmissivity *vs* time plot for a vial in a Crystal 16 experiment

Figure 2.3: The Polar Bear Plus with interchangeable inserts (right)
Figure 2.4: The unit cell showing the length and angle parameters
Figure 2.5: The four types of unit cell. Each lattice point is represented by a filled circle
Figure 2.6: The Bragg construct used to show the diffraction of X-rays from sets of parallel lattice planes with a d spacing = d_{hkl}
Figure 2.7: The Rigaku Oxford Diffraction Supernova set-up with key features labelled
Figure 2.8: The cone of diffraction produced from a polycrystalline sample
Figure 2.9: The experimental set-up of the D8 Advance diffractometer, with key features labelled
Figure 2.10: Thermal events in a DSC trace showing (a) a glass transition (change in baseline level), (b) a desolvation/phase transition (endothermic), (c) a re-crystallisation (exothermic) and (d) a melt (endothermic)
Figure 2.11: A typical TGA trace, showing mass loss from a decomposition event
Figure 2.12: The measurement of chord length distribution through FBRM (a) a focussed laser beam scanning in a circular path, (b) the measurement of suspended particles in the circular path, (c) the resulting chord length distribution
Figure 3.1: The molecular structure of paracetamol
Figure 3.2: The crystal structures of PCM-I (left) and PCM-II (right), showing the clear difference in their packing arrangements
Figure 3.3: PXRD patterns for PCM-I and PCM-II
Figure 3.4: DSC trace of PCM, with the transition between 130 and 140 °C highlighted. This subtle transition is best observed using a slow temperature scan rate
Figure 3.5: BFDH calculated morphology of PCM-I (left) and PCM-II (right)
Figure 3.6: Solubility diagram showing the increased aqueous solubility of PCM-II over PCM-I, determined by turbidity measurements in the Technobis Crystal 16
Figure 3.7: The molecular structures of the template molecules employed in this work
Figure 3.8: The stepped cooling profile employed in cooling crystallisation experiments
Figure 3.9: The seeding profile employed
Figure 3.10: Solubility curves for 4-BrBA, 4-ClBA, 4-FBA and both polymorphs of PCM in a 60:40 H_2O:IPA solvent system
Figure 3.11: Solubility curves of metacetamol in (a) 60:40 H_2O:IPA and (b) EtOH
Figure 3.12: PXRD analysis confirming the presence of predominately PCM-II, with circled peaks showing the presence of small quantities of MCM.H_2O. The y-axis displays intensity in arbitrary units.
Figure 3.13: PXRD analysis showing the presence of small quantities of MCM from linear cooling experiments (circled in red). The y-axis displays relative intensity in arbitrary units.
Figure 3.14: Refinement parameters and a molecule of paracetamol showing small thermal ellipsoids
Figure 3.15: PXRD analysis of PCM/MCM evaporative crystallisations showing the formation of a physical mixture of PCM-I and MCM. The y-axis displays relative intensity in arbitrary units.
Figure 3.16: PXRD patterns showing the formation of some PCM-II (peaks in red boxes) within MCM samples. The y-axis displays relative intensity in arbitrary units.
Figure 3.17: DSC trace of a PCM-II sample with trace amounts of MCM.H_2O present
Figure 3.19: VT-PXRD for a PCM-II containing small amounts of MCM.H_2O. The y-axis displays relative intensity in arbitrary units.

Figure 3.18: VT-PXRD of a sample of pure PCM-II showing the transition from PCM-II to PCM-I between 121 °C and 146 °C. The y-axis shows relative intensity in arbitrary units.
Figure 3.20: SEM images showing the morphology of samples produced in the presence of (a) 4-FBA and (b) MCM (both from a 60:40 H_2O:IPA solvent system)
Figure 3.21: SEM images showing the morphology of samples produced for samples of (a) pure PCM-II and (b) PCM-II with small quantities of MCM.H_2O
Figure 3.22: Solubility curves for OCM in (a) 60:40 H_2O:IPA, (b) EtOH and (c) IPA solvent systems
Figure 3.23: PXRD analysis showing a mixture of PCM-II and PCM-I being formed with 2 % and 3 % OCM (the peaks boxed in red are those that correspond to PCM-I). The y-axis displays relative intensity in arbitrary units.
Figure 3.24: PXRD analysis confirming the production of a mixture or PCM-II and PCM-I with 2.4 % OCM, but the production of pure PCM-II with 2.8 % OCM. The y-axis displays relative intensity in arbitrary units.
Figure 3.25: Production of PCM-II in the presence of 3A4MA as a template, with peaks from this template boxed in red. The y-axis displays relative intensity in arbitrary units.
Figure 3.26: DSC trace of a sample of PCM with some 3A4MA present
Figure 3.27: VT-PXRD patterns of a sample of PCM-II with small quantities of 3A4MA present. The y-axis displays relative intensity in arbitrary units.
Figure 3.28: PXRD patterns of the filtered solid at the end of slurrying experiments in the presence of varying percentages of MCM. The y-axis displays relative intensity in arbitrary units.
Figure 3.29: The (002) plane in PCM-II showing the carbonyl group lying on this plane
Figure 3.30: N-H···O interactions forming the next layer of molecules in PCM-II
Figure 3.31: Crystal packing similarity of PCM-II (grey) and MCM (green) - hydrogen atoms have been removed for clarity
Figure 3.32: PXRD patterns showing a sample stability of 24 months. The y-axis displays relative intensity in arbitrary units
Figure 3.33: PXRD patterns over a one month period with a 1 % PCM-I seed loading, showing the appearance of PCM-I peaks after 4 weeks. The y-axis displays intensity in arbitrary units.
Figure 4.1: A visual representation of the COST approach (black dots) and the DoE approach (red dots)
Figure 4.2: Polar Bear Crystalliser with overhead motor and shaft to provide overhead stirring to the system
Figure 4.3: PXRD analysis on all 35 DoE experiments, y-axis shows intensity in arbitrary units
Figure 4.4: DSC analysis on the 35 DoE experiments, y axis showing heat flow in mW
Figure 4.5: Summary of fit plot for the both the polymorphic form and yield response
Figure 4.6: Variable Importance plot (VIP) highlighting the importance of factors and their interactions
Figure 4.7: Summary of fit plots after removal of factors with an importance of <0.8
Figure 4.8: Coefficient plots for both the responses, quantifying the effect of each of the factors on each of the responses
Figure 4.9: PXRD patterns showing the DoE samples after a period of 15 months; the y axis shows relative intensity in arbitrary units
Figure 4.10: The Mettler Toledo EasyMax
Figure 4.11: Mettler Toledo OptiMax with inline process monitoring using a Raman PhAT probe and FBRM probe

Figure 4.12: Offline reference spectra for PCM-I, PCM-II and MCM; the y axis shows intensity in arbitrary units
Figure 4.13: Trend output from 800 ml crystallisations in the OptiMax showing the temperature profile employed (blue), total FBRM counts (green), PCM-I Raman at 1236 cm^{-1} (orange) and PCM-II Raman at 1624 cm^{-1} (pink)
Figure 4.14: Raman spectra collected throughout the course of the crystallisation from the inline PhAT probe (0 mins - suspension, 20 mins - after dissolution of all solid, 300 mins - suspension of final product at end of crystallisation). The y-axis shows intensity in arbitrary units
Figure 4.15: PXRD patterns confirming the presence of PCM-II in the OptiMax experiment, with small quantities of MCM.H_2O present; the y-axis shows intensity in arbitrary units
Figure 4.16: Schematic of the MSMPR set-up used
Figure 4.17: The MSMPR set-up at AstraZeneca Macclesfield used in this work with key features labelled
Figure 4.18: Settling of solid in vacuum transfer lines
Figure 4.21: SEM images for the samples from experiment AZ1 (RT2 was not analysed due to the small amount of solid available).
Figure 4.20: DSC analysis on the samples taken from experiment AZ1; the y axis shows heat flow in mW.
Figure 4.19: PXRD analysis of RT2 and RT3 of experiment AZ1 showing the production of predominately PCM-II with some PCM-I present (peaks corresponding to PCM-I boxed in red). The y-axis shows intensity in arbitrary units.
Figure 4.23: PXRD patterns showing the production of PCM-II in Experiment AZ3. The y-axis shows intensity in arbitrary units.
Figure 4.22: Encrustation on the walls of MSMPR 2 in experiments AZ2 and AZ3.
Figure 4.24: DSC traces for experiment AZ3, showing the absence of any MCM.H_2O. The y-axis shows heat flow in mW.
Figure 4.25: SEM analysis of samples from each of the MSMPR vessels in Experiment AZ3
Figure 4.26: Blockage of the inline filtration unit in experiment AZ4
Figure 4.27: PXRD patterns of the solids produced in experiment AZ4; the y-axis shows intensity in arbitrary units
Figure 4.29: SEM analysis of samples from each of the MSMPR vessels in Experiment AZ4
Figure 4.28: DSC traces for experiment AZ4, indicating the absence of any MCM.H_2O. The y-axis shows heat flow in mW
Figure 4.31: 12 month stability PXRD patterns for samples produced from AZ1 with peaks corresponding to PCM-I boxed in red; the y-axis displays intensity in arbitrary units
Figure 4.30: 12 month stability PXRD patterns for samples produced in experiments AZ2, AZ3 and AZ4; the y-axis displays relative intensity in arbitrary units
Figure 5.2: The generation of eddies within the baffles in a COBC [211]
Figure 5.1: The compact 4-straight COBC set-up at the University of Bath (left) with the baffle geometry highlighted (right)
Figure 5.3: Plug and laminar flow through a pipe
Figure 5.4: Encrustation on the baffle walls in Experiment COBC 1
Figure 5.6: PXRD analysis of the samples for experiment COBC 3; the y-axis shows relative intensity in arbitrary units
Figure 5.5: Crystallisation in the exit piece in experiment COBC 3

Figure 5.7: PXRD patterns from experiment COBC 4, showing the production of PCM-II with some peaks from MCM.H_2O present (boxed in red). The y-axis displays relative intensity in arbitrary units
Figure 5.8: Crystallisation in the exit piece in Experiment COBC 5
Figure 5.9: PXRD patterns for Experiment COBC 5 showing the production of predominately PCM-II, with some peaks (boxed in red) from MCM.H_2O. The y-axis displays relative intensity in arbitrary units
Figure 5.10: Temperature profile used for Experiment COBC 6
Figure 5.11: PXRD patterns for Experiment COBC 6 showing the production of PCM-II with some MCM.H_2O present (boxed in red). The y-axis displays relative intensity in arbitrary units.
Figure 5.12: Temperature profile used in Experiment COBC 7
Figure 5.13: PXRD patterns showing the production of PCM-II with some MCM.H_2O (peaks boxed in red) in Experiment COBC 7. The y-axis displays intensity in arbitrary units
Figure 5.14: Temperature profile employed in Experiments COBC 8 and COBC 9
Figure 5.15: PXRD analysis showing the production of PCM-II in Experiment COBC 8; the y-axis displays relative intensity in arbitrary units
Figure 5.16: DSC analysis showing the presence of some MCM·H2O in all three residence times in Experiment COBC 8 (exothermic up)
Figure 5.17: High solid loadings in Experiment COBC 9
Figure 5.18: PXRD patterns confirming the production of PCM-II with trace MCM.H_2O (boxed in red) in Experiment COBC 9. The y-axis displays relative intensity in arbitrary units
Figure 5.19: PXRD analysis of each of the six samples taken during the course of Experiment COBC 10; the y-axis displays relative intensity in arbitrary units
Figure 5.20: DSC analysis for samples 3-6 in Experiment COBC 10 (exothermic up)
Figure 5.21: PXRD analysis for the solid produced in Experiment COBC 11 confirming the production of PCM-II with some peaks from MCM.H_2O (boxed in red). The y-axis displays relative intensity in arbitrary units
Figure 5.22: The temperature profile employed for the 12-straight COBC experiments (COBC 12 and COBC 13)
Figure 5.23: PXRD analysis for the samples taken during experiment COBC 12; the y-axis displays relative intensity in arbitrary units
Figure 5.24: DSC analysis on the samples taken from Experiment COBC 12
Figure 5.26: DSC analysis of the samples taken in Experiment COBC 13
Figure 5.25: PXRD analysis of the samples taken in Experiment COBC 13; the y-axis displays relative intensity in arbitrary units
Figure 5.28: Recirculating motion within slugs which provide mixing to the system
Figure 5.27: Schematic representing the differences between air and liquid segmentation
Figure 5.29: The KRAIC segmented flow crystalliser as set-up at the University of Bath
Figure 5.30: The mixer piece in the heated water bath
Figure 5.31: The cold tube attached to the KRAIC to allow cooling below ambient temperatures
Figure 5.32: Novel end piece to allow separation of carrier fluid from solution flow
Figure 5.33: The cross mixer piece alignment used in KRAIC 1
Figure 5.34: The K-mixer piece alignment used in KRAIC 3A and 3B
Figure 5.35: Crystallisation in the cold tube in Experiment KRAIC 2A
Figure 5.36: High solid loadings in the three coils in Experiment KRAIC 2B (images taken at 12 mins for coil 1 and 38 mins for coils 2 and 3)

Figure 5.37: PXRD patterns for Experiment KRAIC 2A and KRAIC 2B; the y-axis displays relative intensity in arbitrary units
Figure 5.38: The Y-mixer piece utilised in Experiments KRAIC 4 and KRAIC 5
Figure 5.39: PXRD patterns showing the production of PCM-II in Experiment KRAIC 3; the y-axis displays relative intensity in arbitrary units
Figure 5.40: PXRD analysis for Experiment KRAIC 4 – those peaks corresponding to PCM-I in RT2 are boxed in red. The y-axis displays relative intensity in arbitrary units.
Figure 6.1: Structural diagrams of the three native cyclodextrins
Figure 6.2: Schematic representation of a cyclodextrin molecule, illustrating the hydrophobic core and hydrophilic exterior
Figure 6.3: The chemical structures of thiamphenicol and α-lipoic acid, with the bonds that are the source of molecular instability highlighted
Figure 6.4: Illustration of the method of continuous variation, used to generate data for the Job's plot approach to determine host-guest stoichiometry
Figure 6.5: COSY NMR spectrum for γ-CD
Figure 6.6: A single glucose unit showing the proton labelling scheme
Figure 6.7: The packing in the molecular inclusion complex of thiamphenicol and γ-CD as viewed along the crystallographic *c* axis (hydrogen atoms were unable to be assigned)
Figure 6.8: Staggered arrangement of γ–CD molecules in native γ-CD as viewed down the crystallographic *c* axis (for clarity all hydrogen atoms have been removed)
Figure 6.9: ^{1}H NMR spectra of each of the two starting materials and the inclusion complex
Figure 6.10: Horizontal expansion of the region between 3.4 and 3.9 ppm to allow resolution of peaks
Figure 6.11: Job plot for the inclusion complex of thiamphenicol and γ-CD
Figure 6.12: DOSY NMR spectra of the thiamphenicol: γ-CD inclusion complex
Figure 6.13: SSNMR of the inclusion complex before being placed in humid conditions
Figure 6.14: SSNMR spectrum of the complex after being subjected to stressed (humidity) conditions (the peak broadening compared with that in Figure 6.13 indicates the sample has turned amorphous)
Figure 6.15: DSC analysis of thiamphenicol, γ-CD and the molecular inclusion complex of thiamphenicol and γ-CD (exothermic up)
Figure 6.16: TGA analysis of γ-CD
Figure 6.17: PXRD analysis confirming the formation of the molecular inclusion complex of γ-CD and thiamphenicol
Figure 6.18: PXRD pattern of the crystallisation product using a 1:3 THM: γ-CD ratio, showing excess γ-CD boxed in red
Figure 6.19: PXRD pattern showing the production of the molecular inclusion complex at the 5 ml scale
Figure 6.20: The crystal structure of the inclusion complex of ALA and β-CD, as viewed down the crystallographic *c* axis
Figure 6.21: Job plots for the inclusion complex of ALA and β-CD
Figure 6.22: PXRD analysis from initial cooling crystallisation experiments showing comparison to the PXRD pattern predicted from single crystal data for the inclusion complex; although peaks from the complex are present the pattern displays amorphous characteristics

Figure 6.23: PXRD analysis showing the presence of complex in those vials containing higher percentages of water and β-CD in those vials containing higher percentages of MeOH
Figure 6.24: PXRD pattern confirming production of the molecular inclusion complex of ALA and β-CD at the 12 ml scale
Figure 6.25: PXRD patterns for Experiment Set 3, showing the production of the molecular inclusion complex
Figure 6.26: PXRD patterns for Experiment Set 4, showing the formation of the molecular inclusion complex
Figure 6.27: PXRD patterns showing the production of the inclusion complex at both the 6 ml and 12 ml scale
Figure 7.1: The CMAC Hub developed workflow for a continuous cooling crystallisation process

List of Tables

Table 1.1: The advantages and disadvantages of continuous manufacturing of crystalline fine chemical products
Table 1.2: Hydrogen bond properties (adapted from[121])
Table 2.1: The restraints on the seven crystal systems that result in the 14 Bravais lattices [159]
Table 3.1: Experimental parameters for the VT-PXRD study or PCM-II with metacetamol hydrate present
Table 3.2: Experimental parameters for the VT-PXRD of PCM-II
Table 3.3**:** Cooling crystallisation conditions that have produced PCM-II with benzoic acid derivatives
Table 3.4: Experimental parameters investigated for seeding experiments. For templated experiments within the Table, 4-FBA was used
Table 3.5: Crystallisation conditions for the reproducible production of PCM-II using MCM as a template molecule
Table 3.6: Experiments performed with 3A4MA at the 50 ml scale. A concentration of PCM of 300 mg/g was used throughout
Table 3.7: The effect of varying percentages of MCM on the solubility of PCM, at two different concentrations
Table 4.1: Experimental information for RBF crystallisations with magnetic bottom stirring
Table 4.2: Overhead stirring crystallisations of PCM/MCM
Table 4.3: Design of Experiments experimental parameters
Table 4.4: Characteristic Raman bands differentiating PCM-I and PCM-II (adapted from Szelagiewicz et al.[200])
Table 4.5: Each of the spectral regions where differences between PCM-I and PCM-II are visible, showing the shape of the patterns from final product (green) to match PCM-II (orange) and not PCM-I (blue) in all regions
Table 4.6: Operating parameters and start-up calculations for experiments operated with a 45 minute residence time
Table 4.7: Operating paramaters and start-up calculations for experiments operated with a 30 minute residence time
Table 4.8: Experimental Conditions and Output from MSMPR experiments
Table 5.1: Chemical shift information for the NMR spectra of PCM and MCM

Table 5.2: Experimental parameters for the COBC experiments
Table 5.3: Solid yields for experiment COBC 4
Table 5.4: Crystallisation yields from Experiment COBC 5
Table 5.5: Solid yields in Experiment COBC 6
Table 5.6: Crystallisation yields for Experiment COBC 7
Table 5.7: Solid yields in Experiment COBC 8
Table 5.8: Solid yields for Experiment COBC 11
Table 5.9: Percentages of MCM·H_2O in PCM-II samples from quantitative NMR analysis
Table 5.10: Quantitative NMR analysis on samples from COBC 13
Table 5.11: Continuous crystallisation experiments in the KRAIC
Table 5.12: Yields from experiment KRAIC 5
Table 6.1: Proton shifts in thiamphenicol upon inclusion into γ-CD
Table 6.2: Proton shifts γ-CD upon inclusion of thiamphenicol into the cavity
Table 6.3: Proton shifts in ALA upon inclusion into β-CD
Table 6.4: Proton shifts β-CD upon inclusion of ALA into the cavity
Table 6.5: Experimental information for cooling crystallisations of ALA and β-CD (throughout all experiments a concentration of ALA of 6.7 mg/ml and β-CD 36.7 mg/ml and a stirring rate of 400 rpm was used)

List of abbreviations

3A4MA ……	3-amino-4-methoxyacetanilide
4-ABA …….	4-acetamidobenzoic acid
4-BrBA……..	4-bromobenzoic acid
4-ClBA……..	4-chlorobenzoic acid
4-FBA……	4-fluorobenzoic acid
AFM……..	Atomic Force Microscopy
ALA……	α-lipoic acid
API……	Active Pharmaceutical Ingredient
ATR-FTIR…….	Attenuated Total Reflectance Fourier Transform Infrared
BCF……..	Burton Cabrera Frank
BCS……..	Biopharmaceutical Classification System
BFDH……..	Bravais-Friedel-Donnay-Harker
CCD…….	Charge coupled device
CCDC…….	Cambridge Crystallographic Data Centre
CD……	Cyclodextrin
CMAC……..	Continuous Manufacturing and Advanced Crystallisation
CNT……	Classical Nucleation Theory
COBC……	Continuous Oscillatory Baffled Crystalliser
COSY…….	Correlation Spectroscopy
CPMAS……	Cross-polarisation Magic Angle Spinning
CSD……	Cambridge Structural Database
DSC……..	Differential Scanning Calorimetry
DoE……..	Design of Experiments
DOSY……..	Diffusion-ordered Spectroscopy
ED…….	External Diameter
EPSRC……	Engineering and Physical Sciences Research Council
EtOH……..	Ethanol
FEP…….	Fluorinated Ethylene Propylene

FBRM…….	Focussed Beam Reflectance Measurement
FIM…….	Full Interaction Map
HOMO……..	Highest Occupied Molecular Orbital
HPLC……..	High Performance Liquid Chromatography
HSM……	Hot-Stage Microscopy
ID……..	Internal Diameter
IPA……	Isopropanol (2-propanol)
IR……	Infra-red
KRAIC…….	Kinetically Regulated Automated Input Crystalliser
LUMO…….	Lowest Unoccupied Molecular Orbital
MCM……..	Metacetamol
MCM·H_2O……	Metacetamol hydrate
MP……	Methyl paraben
MSMPR…….	Mixed Suspension Mixed Product Removal
MSZ/MSZW……	Metastable Zone/ Metastable Zone Width
NMR……	Nuclear Magnetic Resonance
NSAID……	Non-Steroidal Anti-Inflammatory Drug
OBR…….	Oscillatory Baffled Reactor
OCM……..	Orthocetamol
OFR……	Oscillatory Flow Reactor
OVAT……	One Variable at a Time
PAA……	Polyacrylic acid
PACN……	p-acetanisidide
PAT……	Process Analytical Technology
PCM…….	Paracetamol
PMSMPR…….	Periodic Mixed Suspension Mixed Product Removal
PSD……..	Position Sensitive Detector
PXRD…….	Powder X-ray Diffraction
PVA…….	Polyvinylalcohol
PVM…….	Particle Visualisation Measurement

RBF……..	Round- bottomed flask
RF……..	Radio Frequency
RH…….	Relative Humidity
RT…….	Residence Time
SCXRD……..	Single Crystal X-ray Diffraction
SEM…….	Scanning Electron Microscopy
SMPT…….	Solution Mediated Phase Transformation
SSNMR…….	Solid-state NMR
TGA……	Thermogravimetric Analysis
THM……..	Thiamphenicol
VIP…….	Variable Importance Plot
VT-PXRD……	Variable Temperature Powder X-ray Diffraction

1 Introduction – Crystallisation of molecular products

1.1 Context of research

With over 80 % of marketed pharmaceuticals delivered in a crystalline form, crystallisation is a key step in the manufacture and production of pharmaceuticals and fine chemicals. The ability to control the solid form of active ingredients, in terms of their polymorphic form, crystal size and shape or crystal size distribution is of paramount importance in the crystallisation process and much research has been directed towards it in recent years. The transfer of these systems from small scale discovery environments into large scale batch crystallisation settings is critical for adoption into an industrial setting. The work presented here emerges from the EPSRC Future Manufacturing Hub in Continuous Manufacturing and Advanced Crystallisation (CMAC); an academic-industrial collaboration between seven UK universities and a number of industrial partners set up to aid the adoption of continuous manufacturing processes into an industrial setting, paving the way for more efficient processes for the manufacture of fine chemicals and pharmaceuticals with greater control over particle attributes.

1.2 Supersaturation

Supersaturation is considered to be the thermodynamic driving force of crystallisation; the method of crystallisation will determine how this supersaturation is generated (outlined in section 1.6). A solution is considered supersaturated when it contains more dissolved solute than is dictated by the solubility curve at a given temperature and pressure (i.e. the equilibrium solubility); for this reason it is sometimes referred to as supersolubility. Relative supersaturation (σ) is dimensionless and can be described as the difference between the chemical potential of a molecule in its supersaturated state (μ_{ss}) and its equilibrium state (μ_{eq}), as outlined in Equation 1.1.

$$\boldsymbol{\sigma = \frac{\mu_{ss} - \mu_{eq}}{kT}} \qquad \textbf{Equation 1.1}$$

Supersaturation is more commonly expressed in terms of concentrations (c, solution concentration and c^*, equilibrium concentration), introducing a supersaturation ratio (S), which quantifies the extent to which a solution of a certain concentration exceeds the equilibrium solubility, outlined in Equation 1.2 and Equation 1.3.

$$\boldsymbol{S = \frac{c}{c^*}} \qquad \textbf{Equation 1.2}$$

$$\sigma = \frac{c - c^*}{c^*} = S - 1 \qquad \textbf{Equation 1.3}$$

In order to design any crystallisation process, knowledge of the solubility of the system is crucial. Figure 1.1 shows a typical concentration-temperature solubility diagram, with three main regions highlighted. The solid black line represents the equilibrium solubility curve and the dotted line represents the metastable limit under a given set of conditions; the region between these is known as the metastable zone width (MSZW).

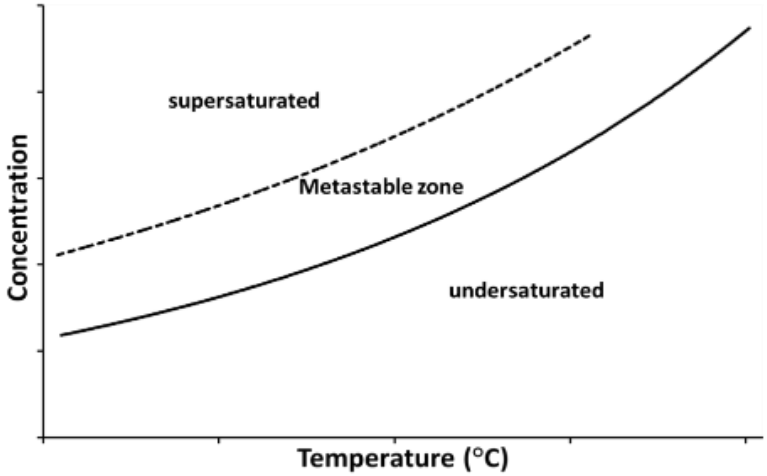

Figure 1.1: A typical solubility diagram showing the variation in concentration with temperature

When the composition of the solution lies below the equilibrium solubility line, the solution is undersaturated and in this region any remaining crystals will dissolve. Utilising the undersaturated region aids experiments such as temperature cycling to allow dissolution of fine particles and using the supersaturation generated by this for growth of larger particles. The region between the solubility line and the metastable limit is termed the metastable zone width. Within this region any existing crystals will grow and secondary nucleation can occur, however primary nucleation is not possible. Knowledge of the metastable zone width is needed to aid the design of seeded crystallisations. However, factors such as cooling rate, scale of crystallisation and presence of impurities can alter the metastable zone limit significantly, and so this should not be considered a definite, fixed quantity. Above the metastable limit is the supersaturated region which is dominated largely by uncontrolled, spontaneous primary nucleation.

1.3 Nucleation

Nucleation is a step that refers to the assembly of molecules within a supersaturated solution to form a new solid phase. It is a key step in determining the outcome of a crystallisation process, dictating properties such as crystal size distribution and polymorphic form. Nucleation can be

broadly categorised as either primary or secondary and the former as either homogeneous or heterogeneous (detailed in Figure 1.2[1]).

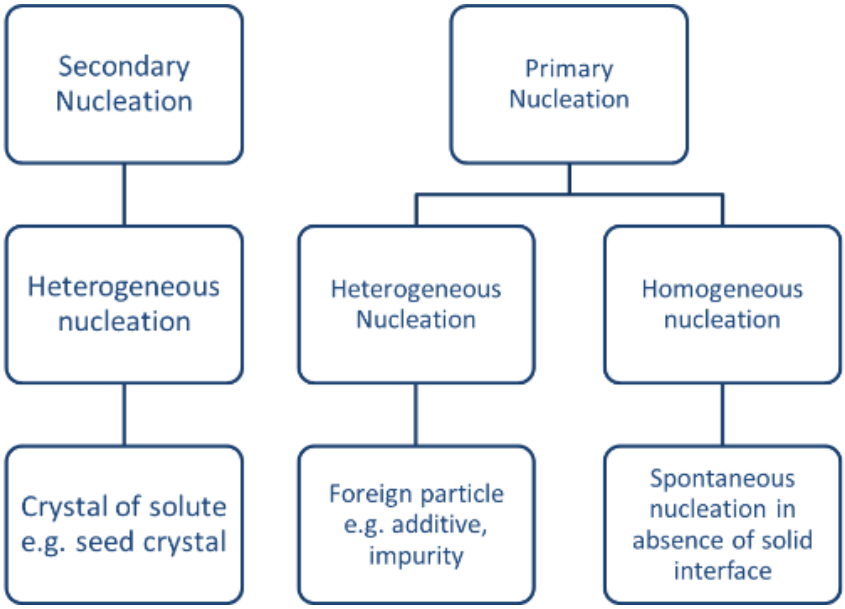

Figure 1.2: Nucleation classification (adapted from Beckmann[1])

Homogeneous nucleation is spontaneous and does not require external stimuli; supersaturation, as outlined above, drives this process. Secondary nucleation, which is by its nature heterogeneous, requires a surface on which to nucleate, which can be an additive, an impurity or a seed crystal of the desired product. The presence of this additional surface, on which to nucleate, lowers the value of free energy of the assembling system, hence allowing nucleation at lower values of supersaturation than those required for spontaneous homogeneous nucleation.[2]

There are two nucleation pathways that are currently accepted within the crystallisation community: classical nucleation theory (CNT) and two-step nucleation. The differences between these are highlighted schematically in Figure 1.3.

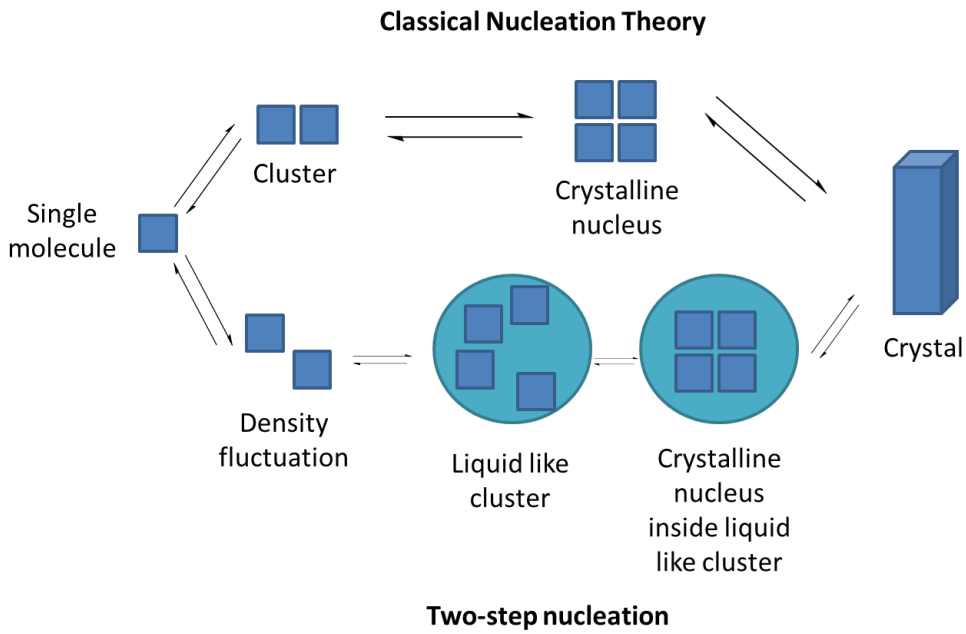

Figure 1.3: The two commonly accepted nucleation pathways: classical nucleation theory (top) and two-step nucleation (bottom)[3]

Classical Nucleation Theory (CNT) was originally postulated by Volmer[4] in the early 1900's. In CNT, it is proposed that there are density and order fluctuations within a supersaturated solution. These various fluctuations result in the formation of clusters, with the packing within each of these clusters representing each of the polymorphic forms of the material being crystallised. The nucleation rate (J), defined as the number of crystalline particles that form per unit of volume and time, is expressed by Equation 1.4.

$$\boldsymbol{J = Aexp[-\frac{B}{(lnS)^2}]} \quad \textbf{Equation 1.4}$$

Where $B/\ln^2 S = W/kT$ and is described as the energy barrier to nucleation.

It is clear that the nucleation rate displays an inverse relationship to the supersaturation ratio of the solution: increasing the supersaturation ratio by even a fraction, results in large decreases in the nucleation rate.

Two- step nucleation was originally proposed by Vekilov[5] and is a mechanism commonly seen in the crystallisation of proteins; the molecules come together in a disordered liquid phase before establishing order within that liquid phase and then forming a crystal. The main distinction between this theory and CNT is the appearance of crystalline order over time compared to immediate establishment of crystalline order in clusters in CNT.

1.3.1 Thermodynamics of nucleation

The thermodynamics of nucleation consider the total free energy required to form a cluster of a critical size; it is the sum of the free energies associated with the formation of a surface (with an r^2 dependence and is positive and hence unfavourable) and with the bulk volume effect (with an r^3 dependence and is negative and so is favourable). The combination of these two free energies produces a curve like that shown in Figure 1.4, with the surface energy dominating initially until r_c is reached and the volume free energy dominating after, resulting in the favourable negative ΔG.

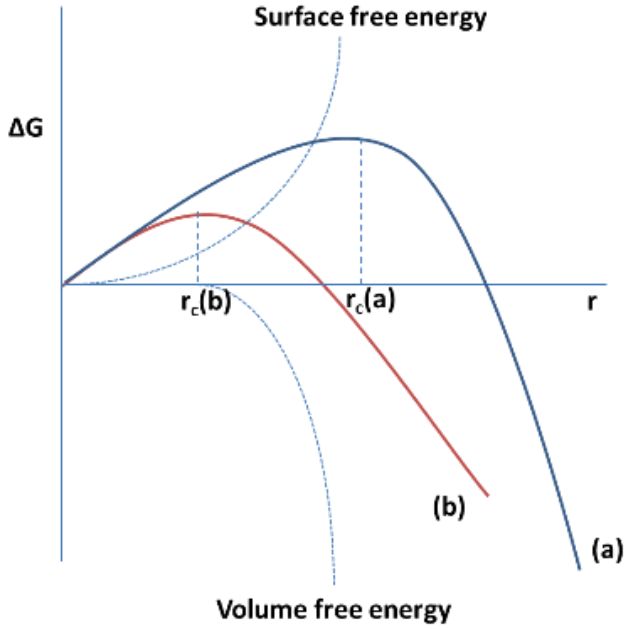

Figure 1.4: A free energy diagram for the formation of a cluster (a) at low supersaturation, (b) at high supersaturation

The negative volume free energy effect is associated with the decrease in free energy observed when a molecule within a supersaturated solution is transferred from the solution to the solid state; this change is favourable as the solid state is more stable under these conditions. The positive surface free energy effect is associated with the formation of new crystal surfaces and contains an interfacial tension term characteristic of each crystal surface formed. At small cluster sizes, the energy associated with the formation of a new surface dominates, whilst at larger cluster sizes the bulk free energy dominates; this gives the characteristic curve shape shown in Figure 1.4. As such, there is a critical cluster size (r_c) where the gain in bulk free energy and reduction in interfacial free energy from formation of a new surface balances. After this point, the growth of clusters is thermodynamically favourable, with total free energy amounting to a negative value. The value for r_c can be calculated using Equation 1.5.

$$r_c = \frac{2\omega\gamma}{kTln(S)} \quad \textbf{Equation 1.5}$$

Where ω = molecular volume, γ = surface energy, k = Boltzmann constant and T = temperature.

Figure 1.4 shows the dependence of r_c on supersaturation, with Equation 1.5 quantifying this dependence. Simply, as supersaturation increases the barrier associated with the formation of a cluster of critical size, r_c, decreases. The size of this free energy barrier is characterised by the constant B in Equation 1.4, and will vary depending on whether the nucleation is homogeneous or heterogeneous.

1.3.2 Kinetics of nucleation

Whilst the B term in Equation 1.4 is accounted for through thermodynamic considerations, the A term describes the kinetics of the nucleation process. Considering the Szilard-Farkas model [6], which considers nucleation as a series of attachments and detachments to form clusters, the pre-exponential factor A can be described by Equation 1.6.

$$\boldsymbol{A = zf^{*}C_{0}} \quad \textbf{Equation 1.6}$$

Where z is the supersaturation dependent Zeldovich factor, f* is the attachment frequency of building units to a nucleus and C_0 is the concentration of nucleation sites. Monte Carlo type computer simulations model this nucleation process well and so can be helpful in simulating nucleation rates.

As an example, lysozyme in a solution of aqueous sodium chloride solution has a value of A of the order of magnitude of 10^8; this fast nucleation rate is often exploited in demonstrations as the crystals grow visibly within seconds. In comparison, paracetamol in water has an A value of the order of magnitude of 10^3.

1.3.3 Heterogeneous nucleation

As mentioned above (section 1.2), the presence of a surface on which to nucleate lowers the free energy barrier to nucleation. The degree to which the barrier is lowered is dependent on the structural similarity of the impurity to the crystallising substance.[7] The use of additives and their effects on nucleation rates has been examined for a range of materials including ice[8], potassium dihydrogen phosphate[9] and polyhydroxybutyrate.[7] Heterogeneous nucleation has been utilised to access often elusive polymorphic forms such as paracetamol form II[10] and isonicotinamide. [11]

1.3.4 Secondary nucleation

Heterogeneous nucleation that occurs due to the presence of a seed particle of the crystallising substance is known as secondary nucleation. This nucleation tends to occur at much lower supersaturations than homogeneous or heterogeneous nucleation induced by a foreign body. Seed crystals are added within the metastable zone width to ensure no spontaneous nucleation (more details in section 1.5.3); as such, tight control over particle size distributions and polymorphic form output are achievable.

Methods of generating these secondary nuclei in the reaction vessel are varied: they can be added deliberately to the crystallisation process either dry or in suspension, they can come from encrustation on vessel walls or they can be a result of particle breakage due to shear from an impellor, often observed with brittle needle crystals.

1.4 Crystal Growth

Once formation of initial nuclei has occurred, supersaturation within the reaction mixture is depleted to aid the growth of these nuclei into larger crystals. There are a number of mechanisms that have been proposed for crystal growth, some of which are outlined in this section.

1.4.1 Crystal faces

Nuclei in a supersaturated solution can be considered to be in equilibrium; growth units are constantly arriving at the surface and if they have the correct interactions to bind they will stay and if not they will leave. When the flux to the surface is higher than those leaving, crystal growth occurs. Hartmann and Perdock[12] introduced a classification system in order to define how growth units can be classified depending on how many interactions they make with the crystal face: a surface in which three bonds are possible is a kinked face, a surface in which two bonds are possible is a stepped face and a flat face is a surface with which only one bond is possible (Figure 1.5).

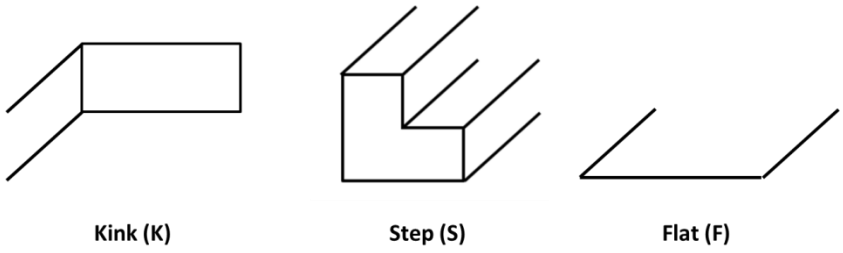

Figure 1.5: The classification of crystal faces according to Hartmann and Perdock[12]

Assuming the crystal growth rate from a certain face is proportional to the number of attachments and hence the binding energy of that surface, it can be concluded that kink faces are the fastest growing faces and flat faces are the slowest growing faces. As such, the morphology of the crystal will be defined by the slowest growing, flat, F faces. Therefore, the basis of crystal growth theory is in the mechanisms through which these F faces grow.

Differences in concentrations between bulk supersaturated solutions and the growth surface, and the corresponding diffusion effects of these concentration gradients, to allow transport of growth units to the surface, also affect crystal growth and should be considered. Berthoud and Valeton[13] proposed a two-step mechanism for the mass transport of growth units to a surface: diffusion from bulk to solid surface followed by a first order reaction whereby growth units arrange and incorporate themselves into the crystal lattice. Mathematically, the overall crystal growth rate coefficient (k_G) can be expressed in terms of the diffusion coefficient (k_D) and the integration of the growth units coefficient (k_r), as in Equation 1.7.

$$\frac{1}{k_G} = \frac{1}{k_D} + \frac{1}{k_r} \quad \textbf{Equation 1.7}$$

There are energy barriers that must be overcome within the diffusion process to allow crystal growth to occur and these are shown in Figure 1.6. When in solution, the growth units are solvated and so must be partially desolvated to allow diffusion (ΔG_{desolv}). Next, the growth unit must diffuse from the bulk solution to the surface, to a position where it is able to adsorb (ΔG_D). Finally, the growth unit must be incorporated itself into the crystal lattice at the crystal surface (ΔG_r).

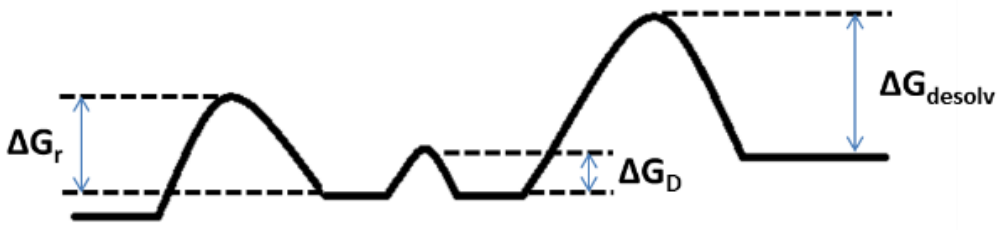

Figure 1.6: The free energy barriers to overcome during the crystal growth process, from solution (right) to crystal (left)

1.4.2 Birth and spread model

In discussion of the thermodynamics of nucleation, it was shown that clusters must reach a critical size before further growth can occur (section 1.2.1). The combination of this nucleation theory with growth in two dimensions on a flat surface leads to the birth and spread model[14] and is illustrated in Figure 1.7. [15]

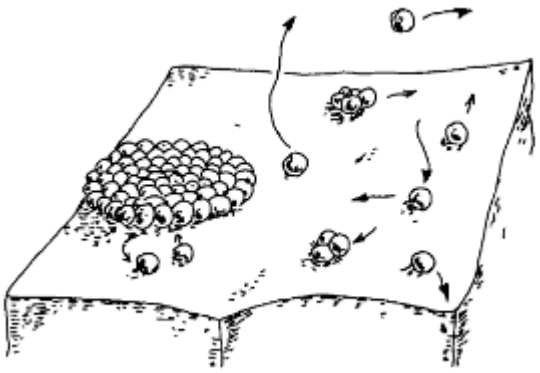

Figure 1.7: Schematic of the birth and spread model[15]

As this model incorporates nucleation kinetics, it has a high dependency on the supersaturation of the system, quantified by Equation 1.8.

$$\boldsymbol{R = A\sigma^{\frac{5}{6}} \exp\left(-\frac{B}{\sigma}\right)} \quad \textbf{Equation 1.8}$$

This suggests that at low values of supersaturation, no growth will occur, with a sharp rise in growth rates with fractional increases in supersaturation, owing to the negative inverse exponential term.

1.4.3 Burton Cabrera Frank (BCF) model

In practice however, growth rates are observed at low values of supersaturation; this can be attributed to small dislocations or defects in the crystal surface. Of particular interest is the screw dislocation as this can provide a step for continuous growth in a spiral fashion (Figure 1.8); these screw dislocations are particularly common when growth has occurred on an external surface such as a seed crystal.

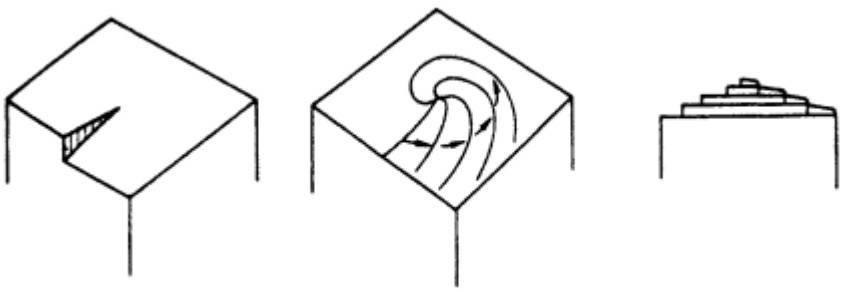

Figure 1.8: The development of spiral growth, originating from a spiral dislocation[13]

Once a screw dislocation has formed, growth is no longer occurring on a flat face and therefore further nucleation is not needed to continue the growth process. Therefore, growth can continue at much lower supersaturations than are possible by the simple birth and spread model. The spiral growth shown in Figure 1.8 has been directly observed in a number of materials including NaCl and KCl[16] and L-arginine trifluoroacetate[17] using techniques such as atomic force microscopy (AFM) (shown in Figure 1.9).

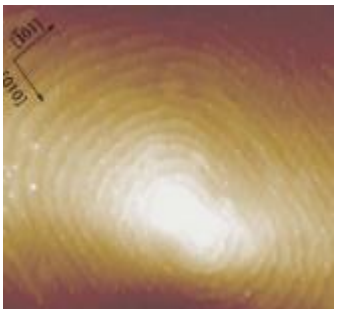

Figure 1.9: Spiral growth in L-arginine trifluoroacetate crystals, visualised using AFM

As with the birth and spread model, a mathematical expression is used to show the growth rate (R) of the crystal (Equation 1.9).

$$R = A\sigma^2 \tanh\left(\frac{B}{\sigma}\right) \qquad \textbf{Equation 1.9}$$

1.4.4 Rough interface model

Since, without the presence of screw dislocations, growth on flat faces is an energetically unfavourable process, sites with higher interaction energies such as steps or kinks need to be generated. A dimensionless parameter, α (Equation 1.10), or the surface entropy factor can be introduced, which defines the ease with which a surface is able to form these new sites with multiple binding interactions.

$$\alpha = \frac{\zeta \Delta H_f}{RT} \qquad \textbf{Equation 1.10}$$

Where ζ is the anisotropy factor and is related to the number of nearest neighbour sites.

Limits and boundaries exist for the value of α that defines the type of growth that will occur under certain conditions. For values of α<3, continuous growth is observed; the surface will contain many kink and step sites to ensure multiple binding interactions are possible. Therefore, every growth unit that arrives at the surface will find a growth site and the growth rate is linearly proportional to supersaturation. For values of α between 3 and 5, there are fewer surfaces for multiple binding interactions. As such, not every growth unit arriving at the surface will find a growth site; those that

do not find a growth site will either diffuse back into solution or agglomerate to other adsorbed units to form surface islands. These islands result in steps and kinks on the original crystal surface, providing more binding interactions. The growth rate takes the form of Equation 1.8 and so growth obeys the birth and spread model outlined above within this α range. For values of α>5, the growth obeys that of the BCF model outlined above and spiral growth occurs.

1.5 Crystal morphology

The overall shape of the crystal, often termed habit or morphology, is an important parameter to consider in the manufacture of fine chemicals and is a property that is controlled through the crystallisation process. It is common practice to distinguish between the equilibrium and kinetic morphology: the former is the morphology the crystal adopts when the reaction has reached equilibrium, and corresponds to the crystal structure that minimises the surface free energy, while the latter is the morphology adopted when the crystal is formed under kinetic control. Crystal morphology has significant effects on a variety of downstream processing steps such as flowability and filtration. Figure 1.10 compares the filtration of block and plate crystals; it can be seen that with the block crystals, the solution is able to flow freely through the crystals, whereas with the plate crystals, they pack in an impermeable layer and hence cause problems with filtration by blocking solution flow.

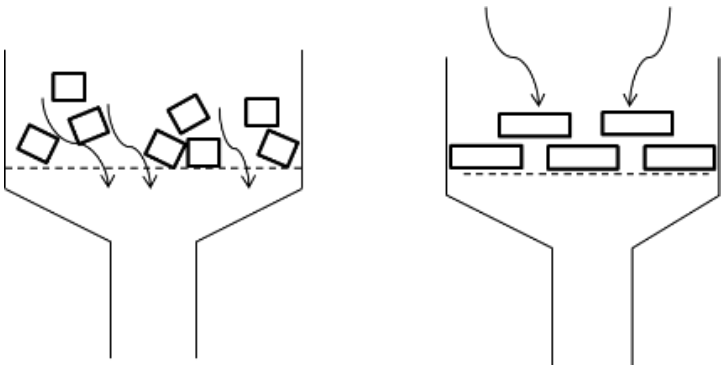

Figure 1.10: Filtration of block-like crystals (left) and plate-like crystals (right)

There exist methods that can be used in order to predict crystal morphology, however many of these are based on the crystal structure alone and will not take into account the effect of external factors such as choice of solvent or presence of additives. Both these factors have been shown to have considerable effect on the morphology of crystals produced from crystallisation experiments. The effect of solvent on the morphology of a variety of compounds is well reported in the literature, including but not limited to ibuprofen[18], p-aminobenzoic acid[19], meta-nitroaniline[20] and paracetamol. [21] Similarly, the effect of additives on the morphology of crystals is also well reported

in the literature and has been demonstrated for a variety of compounds including succinic acid[22], urea[23] and paracetamol. [24]

1.6 Crystallisation methods

In order for crystallisation to occur, a method of generating supersaturation within the system must be found. Crystallisation from solution is the most commonly employed method within the pharmaceutical industry.[25] Melt crystallisation is an alternative; however this is rarely employed owing to the low thermal stability of many active pharmaceutical ingredients (APIs).

1.6.1 Cooling crystallisation

During a cooling crystallisation experiment, knowledge and understanding of the solubility is crucial. Figure 1.11 shows a typical cooling profile used within a cooling crystallisation experiment. In the absence of any seed crystals, a period of cooling occurs in order to transform the process from the undersaturated region (1) to the supersaturated region (2). At point 2, nucleation will occur with a corresponding drop in solution concentration upon formation of crystals precipitating out of solution. With this drop in concentration, the system will move into the region defined by the metastable zone width (MSZW) (2→3). If the system is then cooled within the metastable zone, either through a stepped cooling profile or tracing the lower solubility curve, only growth and no further primary nucleation will occur. Designing a cooling profile as outlined above will help to produce a product with consistent particle attributes, namely particle size distribution and polymorphic form.

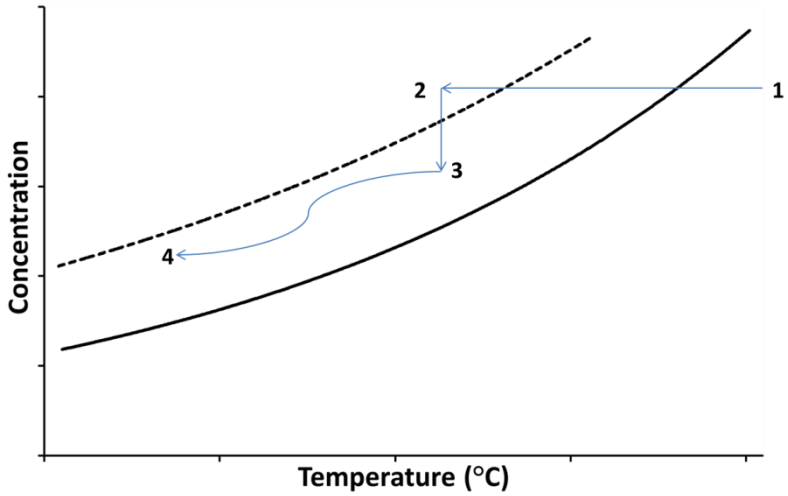

Figure 1.11: A typical solubility diagram showing the variation of concentration with temperature during a cooling crystallisation experiment

It is important to note that the metastable limit varies substantially under different crystallisation conditions. The presence of additives or impurities can alter the metastable zone width as well as

factors such as cooling rate. Faster cooling rates often do not allow equilibrium to be reached and hence nuclei form under kinetic rather than thermodynamic control; the crystals do not have time to rearrange into the most stable arrangement. Hence, faster cooling rates give rise to wider MSZWs. As such, operating the system close to equilibrium will favour the formation of more stable solid forms; metastable polymorphs are more likely to be formed through faster cooling rates. Cooling crystallisation is the basis of many continuous crystallisers (see section 1.7).

1.6.2 Evaporative crystallisation

Evaporative crystallisation is commonly employed if there is not a significant change in system supersaturation upon cooling. In an evaporative crystallisation experiment, the supersaturation of a system is generated through solvent evaporation. In a small-scale environment, an undersaturated solution is left at a certain temperature which causes evaporation of the solvent (1, Figure 1.12), thus increasing the saturation of the solution. When enough solvent has evaporated, the solution will cross the metastable zone width, to point 2 (Figure 1.12), and enter the supersaturated region. This induces spontaneous nucleation into the system.

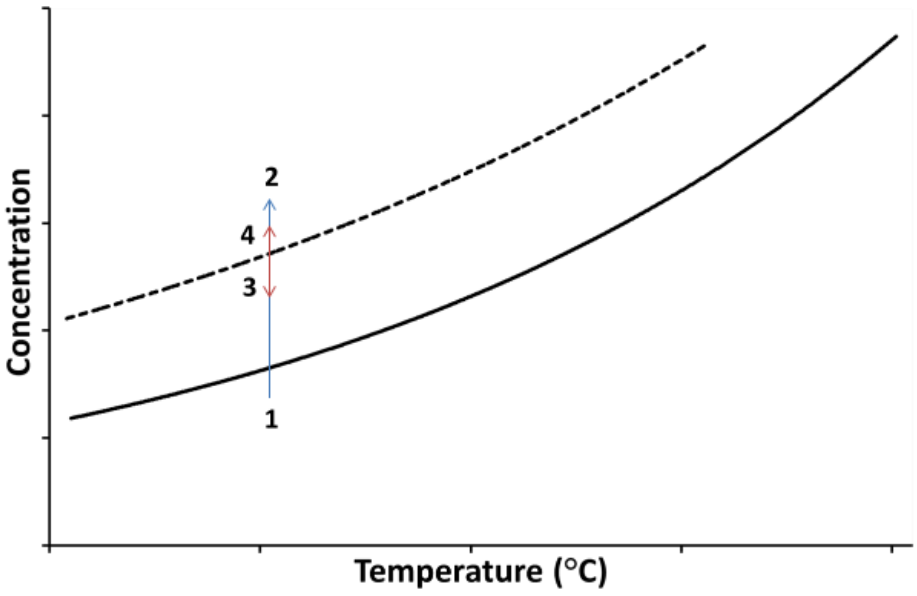

Figure 1.12: A typical solubility diagram showing the variation in temperature during an evaporative crystallisation - the blue arrow shows evaporation and the red arrow shows concentration

As crystallisation proceeds, the concentration of the solution will consequently decrease (2→3), however further evaporation of solvent will increase this again (3→4). Therefore the concentration will vary along the red line indicated in Figure 1.12 depending on the solvent and temperature at which evaporation is occurring.

Traditionally, in terms of pharmaceuticals and fine chemicals, evaporative crystallisation is useful for small-scale, discovery crystallisations. The main barrier to implementation of evaporative crystallisation into the pharmaceutical industry is the inability to control the supersaturation in a system sufficiently carefully, which can lead to inconsistent particle attributes. However, industrial scale evaporative crystallisers are marketed, many of which are steam heated, such as the Oslo-Krystal evaporating crystalliser and the wetted-wall evaporative crystalliser.[26]

1.6.3 Antisolvent crystallisation

In antisolvent crystallisation, a solvent, in which the solute displays poor solubility, is added to an undersaturated solution of the solute in order to increase the level of supersaturation within the system. The antisolvent added works to decrease the solubility of a substance in solution, hence resulting in crystallisation.

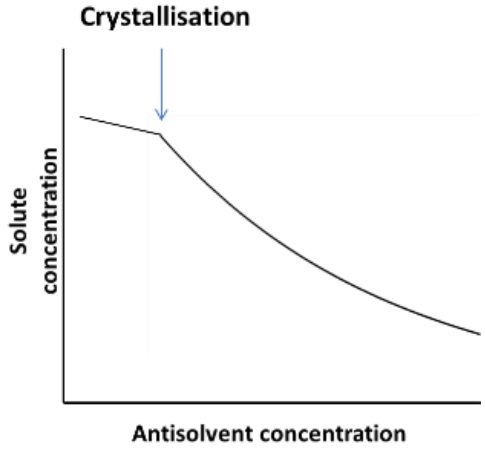

Figure 1.13: The variation in solubility of the solute with increasing antisolvent concentration in a typical antisolvent crystallisation

Antisolvent crystallisation is a commonly used method to produce solubility enhanced forms of Biopharmaceutics Classification System (BCS) Class II and IV drugs (low solubility-high permeability and low solubility-low permeability respectively). In particular, there are numerous examples of the use of antisolvent crystallisation to produce nanoparticles of poorly water-soluble drugs; these micronised nanoparticles are shown to increase the dissolution rate by a significant increase in the relative surface area and hence increase the bioavailability of these drugs.[27-30] Antisolvent crystallisation has also been used to obtain metastable polymorphs; examples include indomethacin[31], abecarnil[32] and L-histidine[33].

1.6.4 Reactive crystallisation

Reactive crystallisation occurs when two or more compounds react within the solution phase to give a product that is less soluble than the parent compounds in the particular solvent system chosen. This decrease in solubility, or increase in saturation, results in crystallisation. The rate at which supersaturation is generated in the system is dependent on the rate of reaction between the two components. Within the pharmaceutical industry, a common approach to reactive crystallisation is by changing the pH.[34]

1.6.5 Seeded crystallisation

As nucleation has a stochastic nature, many processes look to avoid spontaneous nucleation by introducing seed crystals into the crystallisation process, limiting nucleation to secondary nucleation at lower values of supersaturation. As such, seeding is commonly employed in order to obtain greater control over the solid form produced during crystallisation and obtain narrower particle size distributions. Seed crystals of the desired product are introduced when the growth solution is in the metastable zone (Figure 1.14); the solution is then cooled in line with the lower solubility curve. As a general rule, seeds are introduced one third of the way into the metastable zone; any higher in temperature (closer to the solubility line) and the seeds will dissolve, any lower in temperature (further into the MSZ) and there is a chance spontaneous nucleation will occur. The right of Figure 1.14 shows a typical temperature-time profile for a seeded crystallisation. Once the seeds are added, there is a hold period in order to ensure no dissolution of the seeds.

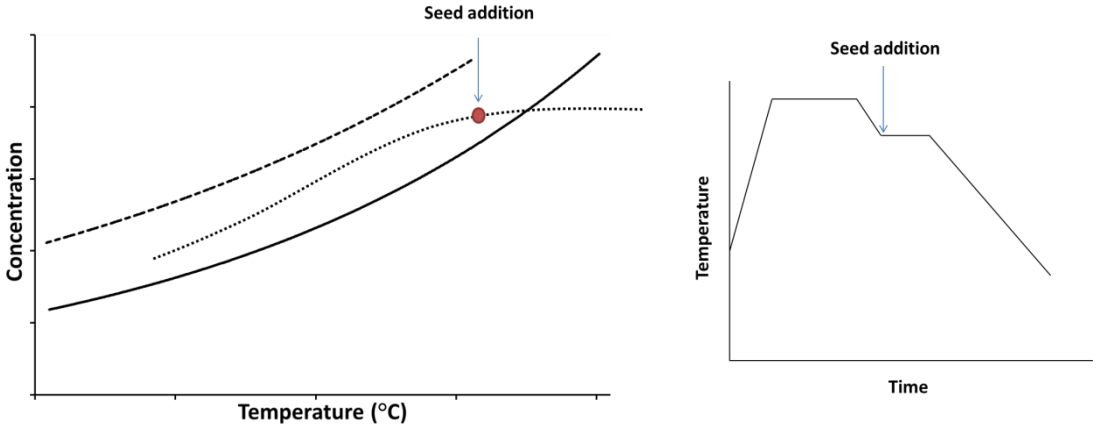

Figure 1.14: A typical solubility curve showing the change in concentration with temperature during a seeded cooling crystallisation (left) and a typical seeded crystallisation temperature profile (right)

Addition of seeds can be through a suspension or as dry seeds. Adding the seeds dry can cause problems with particle dispersion and agglomeration, especially if the seeds are particularly hydrophobic, however if trying to crystallise a metastable form where slurrying in solvent will cause conversion to a more stable form, addition of dry seeds may be desirable. Addition of seeds in a

suspension mitigates the problems with dispersion experienced with dry seeds. They can be added in a saturated solution in the same solvent as the crystallisation or as an antisolvent. The use of suspensions is particularly beneficial in continuous processes where a suspension can be continually pumped in throughout the course of the crystallisation.

There are a number of examples of the use of seeding within the pharmaceutical industry to gain polymorphic control within the system. [35-39] Abu Bakar *et al* [39] coupled seeding with temperature cycling in order both to gain polymorphic control and obtain a narrow particle size distribution of the antibacterial drug sulfathiazole. The use of temperature cycling results in faster dissolution of fines (very small crystalline particles of undesirable morphology) and accelerated growth of larger particles on cooling, increasing the kinetics of Ostwald ripening (the process whereby smaller crystals dissolve and the generated supersaturation aids the growth of larger crystals). This allows for tighter control of the particle size distribution.

1.6.6 Monitoring the crystallisation process

It is clear that control is one of the most critical elements of a successful crystallisation process. In order to exert such control most effectively, it is important to monitor crystallisation processes, to diagnose conditions and allow for these to be optimised throughout the process. The most effective way of monitoring the crystallisation process is through the use of inline process analytical technology (PAT); examples include focussed beam reflectance measurements (FBRM), infrared (IR) spectroscopy, UV-Vis spectroscopy, Raman spectroscopy and particle visualisation measurements (PVM). The experimental details of the techniques used in this work are outlined in Chapter 2. Monitoring of the crystallisation process allows real-time analysis of the product being produced and allows necessary adjustments to the operating conditions in order to obtain specific product attributes.

UV-Vis and IR spectroscopy are both techniques used to monitor the concentration of a particular species throughout the crystallisation process. In multi-component systems, where the different species have different spectra, specific peaks characteristic of each component can be tracked throughout the crystallisation process, enabling the formation or disappearance of the various components to be studied.

Raman spectroscopy is also commonly employed in the monitoring of crystallisation processes. It has the benefits of being an *in-situ*, non-destructive technique that requires little sample preparation and is relatively insensitive to aqueous solutions. The use of Raman spectroscopy is of particular use in the identification of polymorphic forms and transitions throughout a

crystallisation; examples include the non-steroidal anti-inflammatory (NSAID) drug flufenamic acid[40], the anticonvulsant drug carbamazepine[41] and the amino acid L-cysteine[42]. Raman spectroscopy has also been combined with thermal techniques such as differential scanning calorimetry (DSC) and hotstage microscopy (HSM) to aid in the monitoring of thermally-induced polymorphic transitions.[43-44]

Commonly, a number of PAT techniques are combined to monitor changes during crystallisation. The cooling crystallisation of paracetamol has been monitored simultaneously with IR and FBRM.[45-46] Both techniques confirm a solution mediated phase transition (see section 1.8.2) from form II to form I upon nucleation. FBRM analysis shows a decrease in the number of counts attributed to fines within the system and a consequential increase in larger particles. Photomicrographs show the change from a needle-like morphology (characteristic of paracetamol form II) to octahedral morphology (characteristic of paracetamol form I). Subtle differences in the IR spectra of the two polymorphic forms can be seen when tracking the IR signal throughout the crystallisation.

A similar analysis was undertaken with the anticonvulsant carbamazepine, which has four reported polymorphs. [47] Here, FBRM, ATR-FTIR and Raman spectroscopy were used to monitor polymorphic changes during a cooling crystallisation. FBRM combined with microscopic images helped to show polymorphic changes based on clear differences in crystal morphologies. ATR-FTIR and Raman microscopy were used to complement these techniques as each polymorph has significantly different IR and Raman spectra. Similarly, FBRM, PVM, PXRD and Raman spectroscopy were used to monitor the polymorphic changes of D-mannitol from the metastable δ form to the thermodynamically stable β form. [48]

1.7 Continuous crystallisation

Traditionally, crystallisation of active pharmaceutical ingredients (APIs) has been undertaken in large, stirred batch tank reactors which can suffer from poor heat and mass transfer upon scale-up from the laboratory to industrial scales. As such, there has been a large amount of industry and academic interest in moving these processes into a continuous environment.[49-52] Continuous crystallisation offers the advantages of more effective heat and mass transfer as well as reduced downtime between batches, less batch-to-batch variation and greater control over particle attributes such as particle size distribution and polymorphic form. Due to the nature of most continuous crystallisers, they also make the scale-up from laboratory to industry easier. The main advantages and disadvantages of continuous crystallisation techniques are outlined in Table 1.1.

Table 1.1: The advantages and disadvantages of continuous manufacturing of crystalline fine chemical products

Advantages	Disadvantages
Improved and heat mass transfer	High capital costs
Reduced reactor downtime between batches	Manufacturing sites already have batch equipment installed, however possibility of modification
Better control over particle attributes such as polymorphic form and crystal size distribution	No 'one size fits all' - equipment used will depend on system being studied
Reduced space requirements	
Reduced batch-to-batch variation	

A number of different continuous crystallisation platforms are available; those utilised in this work will be explained further in Chapters 4 and 5, however an overview will be given here. A simple batch crystalliser can be modified into a single-stage mixed suspension mixed product removal (MSMPR) crystalliser. In this, there is a continual addition and removal of solution/slurry; a feed vessel is often present, set at a higher temperature than the MSMPR to allow for a cooling gradient to be established and for crystallisation to occur. MSMPRs are often employed with more vessels; this will increase residence time and means smaller vessels can be used for the same total reaction volumes. Having smaller vessels will mitigate problems with mixing and heat transfer often experienced in large stirred tank reactors. Transfer between vessels in a multi-stage MSMPR can be *via* peristaltic pumps or as more recently demonstrated through vacuum transfer[53]; the former can often cause damage to particles, while the latter can cause problems with solvent evaporation. An MSMPR design can be further modified to give a periodic mixed suspension mixed product removal (PMSMPR) system. Unlike the continuous addition and removal of solution in conventional MSMPRs, PMSMPRs are characterised, as the name suggests, by the periodic addition and removal of solution from a single or multi-stage cascade[54]; this periodic nature allows for periods of dwelling within the reaction vessel to increase residence time within the crystalliser. The use of MSMPRs for the continuous crystallisation of a variety of compounds has been demonstrated including paracetamol form I[54-55], albuterol sulfate[56], cyclosporine[53] and preferential crystallisation of the enantiomers of threonine.[57]

Although vessels used in MSMPR designs tend to be smaller than batch crystallisation vessels, they will still experience problems with the uniformity of mixing and heat transfer throughout the course of the crystallisation. As such, over recent years there has been much interest in the use of oscillatory flow reactors (OFRs) as a method of continuous crystallisation[58-61], in particular continuous oscillatory baffled crystallisers (COBCs).[49, 62-63] A typical COBC set-up is shown in Figure 1.15 and will be described fully in Chapter 5.

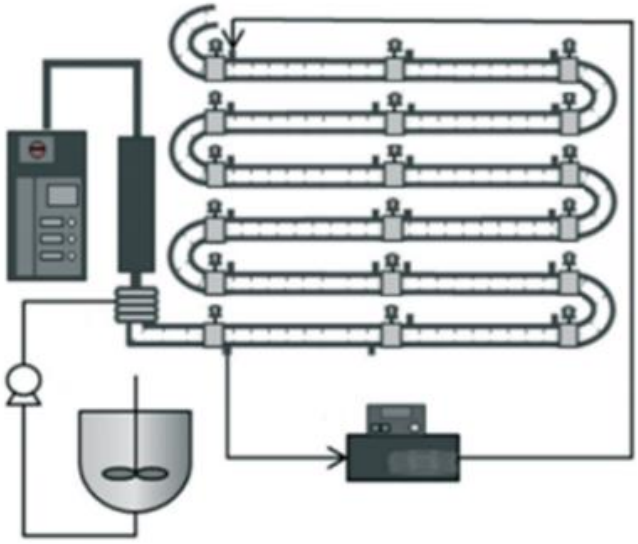

Figure 1.15: A typical COBC set-up[65]

In OBRs, a series of equally spaced baffles are present contained within a jacketed straight; these baffles result in the generation of eddies within the system which provides efficient mixing. Due to their relatively small internal diameters (typically 15 mm, but some have been developed that are smaller[64]), the heat transfer from the jackets is highly efficient and the mixing throughout the crystalliser is more uniform.

Continuous crystallisation has been demonstrated in the COBC of β-L-glutamic acid[65], a co-crystal of α-lipoic acid and nicotinamide[66], lactose[62] and a proprietary compound in production[49]. Although possessing a relatively small internal diameter, the volume of the COBC can be high, depending on the overall length of the crystalliser; this is ideal for industrial scale production, but less suitable for lab-scale production. As such, there have been reports of the development of lab-scale flow devices which operate with much smaller reaction volumes. One example is the kinetically regulated automated input crystalliser (KRAIC)[67] developed at the University of Bath; this is an open tubular crystalliser that operates on the principle of segmented flow (a more detailed overview is given in Chapter 5).

1.8 Polymorphism

Polymorphism is the ability of the same molecule to adopt different packing arrangements in the solid state; analogous to elemental allotropes. Approximately 80 % of marketed pharmaceuticals display polymorphic behaviour[68], with different polymorphs often displaying markedly different physical properties. Broadly, polymorphism can be subdivided into packing and conformational polymorphism; packing polymorphism arises from different bonding motifs resulting in different molecular packing arrangements, whilst conformational polymorphism arises from different molecular conformations often caused through rotation within the molecule. 5-methyl-2-[(2-nitrophenyl)amino]-3-thiophenecarbonitrile, also known as ROY owing to its red, yellow and orange crystalline forms, has 10 polymorphic forms and is an extreme example of conformational polymorphism. ROY adopts different conformations in each of its polymorphs due to the variation of the angle marked θ in Figure 1.16. [69]

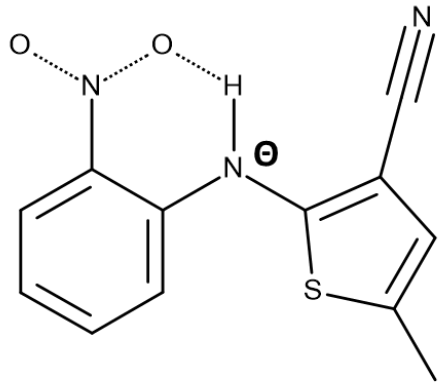

Figure 1.16: The molecular structure of ROY

The different properties often displayed by polymorphs can have substantial benefits in terms of favourable physical properties such as solubility[70-72], of importance for Active Pharmaceutical Ingredients (APIs) and other solid molecular materials. The case of the anti-HIV drug Ritonavir[73] provides a prime example to why knowledge of polymorphism and the ability to control this polymorphic form is of utmost importance in all stages of drug development; loss of control over production of the more soluble (less stable) polymorphic form of this compound had serious consequences for its manufacture (see Chapter 3). There are multiple accounts of methods of controlling the stable polymorphic form of APIs[74-76]; however the deliberate targeting of metastable polymorphic forms, with enhanced physical properties, is largely unreported, and has rarely been achieved on scale. Much previous work in targeting metastable polymorphic forms has focussed on small-scale discovery environments (mg quantities) [77-79], and where scale-up has been attempted, sample stability has been poor; for example the use of polymer additives to obtain paracetamol

form II gave samples stable for only five hours[80] and spray drying of acedapsone gave samples stable for only six hours.[81]

1.8.1 Thermodynamics of polymorphism

The relative stabilities of different polymorphs relate to the free energy; the polymorph with the lowest free energy, under a given set of experimental conditions, is termed the stable polymorph and any other polymorphs with higher free energies are metastable (Figure 1.17). Metastable forms often display enhanced physical properties such as solubility or compressibility[70, 82-83], however the system will have a tendency to reduce its free energy through transformation to the stable form, obeying Ostwald's Law of Stages (see section 1.8.2 below).

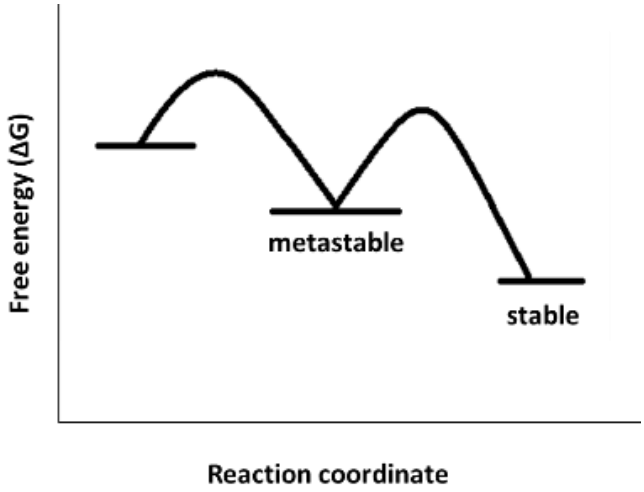

Figure 1.17: The energy landscape of stable and metastable polymorphs

Different polymorphic forms will have different crystal lattices, with the non-covalent interactions being the predominant difference; it is these differences in non-covalent interactions that result in different packing arrangements in the solid state. Due to the differences in non-covalent interactions, different polymorphs will display different molar heat capacities (C_m). Integration of these heat capacities at constant pressure with respect to temperature gives the enthalpy (H^{T1}) and entropy (S^{T1}) of the system at a given temperature T_1 (Equations 1.11 and 1.12).[84]

$$H^{T_1} = \int_0^{T_1} C_{m,p}dT + H^0 = U^{T_1} + PV = E^{T_1}_{Lattice-energy} + E^0_{zero-point\ energy} + PV \qquad \textbf{Equation 1.11}$$

$$S^{T_1} = \int_0^{T_1} \frac{C_{m,p}}{T} dT + S^0 \qquad \textbf{Equation 1.12}$$

The internal energy of the system (U^{T1}) is made up of contributions from both lattice energy and zero-point energy. In 1979, Burger and Ramberger[85] applied Equations 1.11 and 1.12 to polymorphic systems; polymorph A is more stable than polymorph B at absolute zero in this

consideration. These allow for the differences in enthalpy ($\Delta H_{B\rightarrow A}^{T_1}$) and entropy ($\Delta S_{B\rightarrow A}^{T_1}$) between two polymorphs to be calculated (Equations 1.13 and 1.14).

$$\Delta H_{B\rightarrow A}^{T_1} = \int_0^{T_1} \Delta C_{m,p\ (B\rightarrow A)} dT + \Delta H_{B\rightarrow A}^{0} \qquad \textbf{Equation 1.13}$$

$$\Delta S_{B\rightarrow A}^{T_1} = \int_0^{T_1} \frac{\Delta C_{m,p\ (B\rightarrow A)}}{T} dT + \Delta S_{B\rightarrow A}^{0} \qquad \textbf{Equation 1.14}$$

The third law of thermodynamics states that at absolute zero the entropy of a perfect crystal is zero and so the ΔS term will vanish. Similarly, if the polymorphs display packing polymorphism rather than conformational polymorphism the ΔH term will be dictated by the difference in lattice energy as the difference in zero-point energy will be small. As such, the difference in Gibbs free energy between the two polymorphs can be expressed as in Equation 1.15.

$$\Delta G_{B\rightarrow A}^{T_1} = \left(\int_0^{T_1} \Delta C_{m,p\ (B\rightarrow A)} dT + \Delta H_{B\rightarrow A}^{0}\right) - T_1 \left(\int_0^{T_1} \frac{\Delta C_{m,p\ (B\rightarrow A)}}{T} dT\right) \qquad \textbf{Equation 1.15}$$

Equation 1.15 assumes a monotropic relationship between the two polymorphs (i.e. no phase transition has occurred between T_1 and absolute zero). If the two polymorphs are enantiotropically related, extra terms will be included in the enthalpy and entropy changes to account for this, however the expression in Equation 1.15 would hold up to the point of the polymorphic transformation. Equation 1.15 is useful as it shows the difference in free energy between polymorphs can be calculated using heat capcity (C_m) and enthalpy; both of these can be measured through calorimetry methods.

Plotting the change in free energy with temperature gives an indication as to whether two polymorphs are enantiotropically or monotropically related (Figure 1.18). Two polymorphs are said to be enantiotropically related if there exists a transition point at which one polymorph converts to the other in a solid state transition. This transition temperature must be below the melting temperature of the two polymorphs for the polymorphs to be enantiotropically related. Similarly, two polymorphs are monotropically related if this transition point does not exist (the one noted in Figure 1.18 is a 'virtual transition temperature').

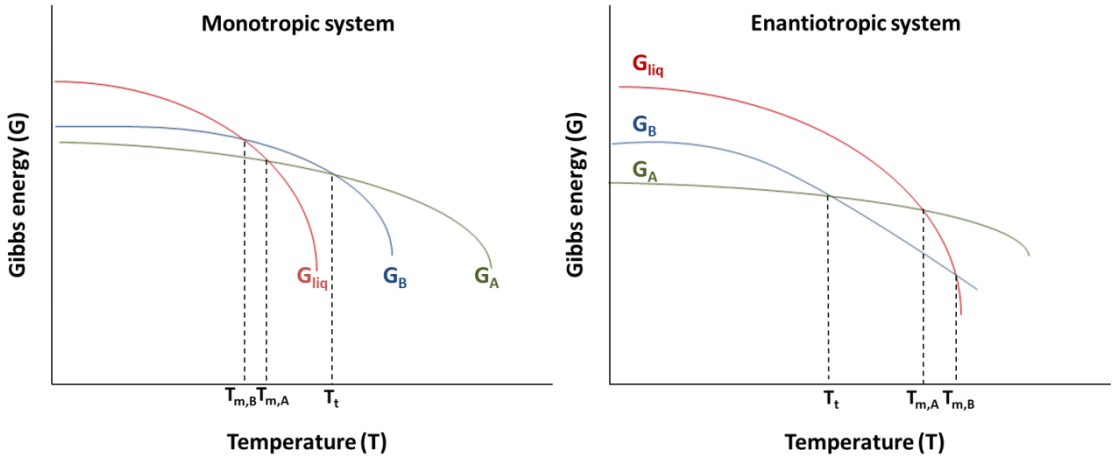

Figure 1.18: Gibbs free energy changes with temperature for monotropically (left) and enantiotropically (right) related polymorphs

A quick way to determine whether two polymorphs are enantiotropically or monotropically related is through consideration of their solubility curves. In a monotropic system, the two solubility curves of each polymorph do not cross. In enantiotropic systems, the relative solubility of each polymorph is temperature dependent and the two solubility curves will intersect; the point of intersection is the phase transition and the temperature at which this occurs is the transition temperature (Figure 1.19).

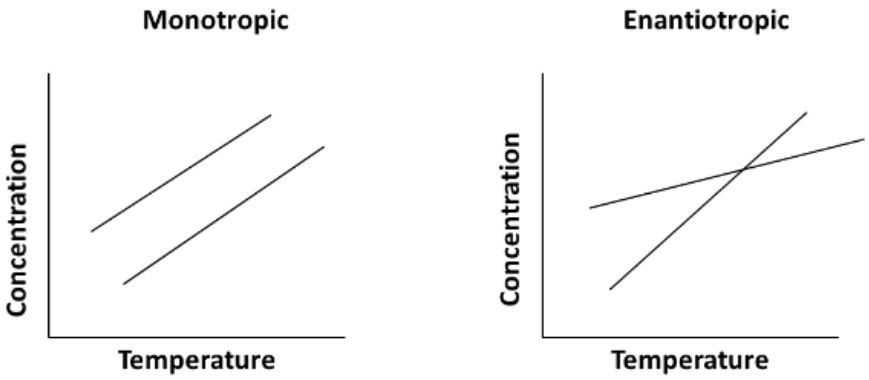

Figure 1.19: Concentration-temperature diagrams for a monotropic and an enantiotropic system

1.8.2 Solution mediated phase transitions

Polymorphic systems in solution will adhere to Ostwald's Rule of Stages[86]; the least stable polymorph will nucleate first, which will then dissolve and the stable polymorph will crystallise. The process of dissolution and crystallisation is known as a solution mediated phase transition, the kinetics of which are discussed in detail below.

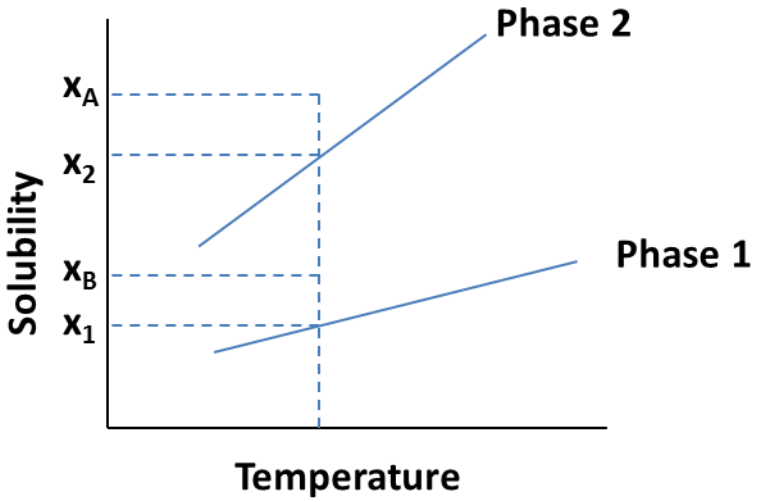

Figure 1.20: Phase diagram

Figure 1.20 shows a phase diagram for a monotropic system (or equally an enantiotropic system in which the transition temperature falls such that the two solubility curves do not cross); phase 1 represents the stable polymorph and phase 2 a metastable polymorph. At a given temperature, a solution with a composition such that the solubility is x_B is only supersaturated with respect to the stable phase 1, whereas a solution with a composition such that the solubility is x_A is supersaturated with respect to both phase 1 and phase 2; as such either phase can crystallise. Ostwald's Law of Stages states that the metastable polymorph (phase 2) will be the first to crystallise. At this point, the solution composition drops to x_1 which corresponds to the solubility of phase 1. However, although the majority of the nuclei formed will be of the metastable phase 2, it is plausible that some nuclei of the stable phase 1 will have formed as the solution has been supersaturated with respect to this phase throughout the crystallisation so far. The formation of these nuclei start the transformation process; as these nuclei grow, the solution concentration drops to that of x_1 which corresponds to the solubility of the stable phase 1 and becomes undersaturated with respect to the metastable form 2. The resultant effect is the dissolution of phase 2 crystals, which generates the necessary supersaturation for the growth of phase 1. This dissolution/growth process continues until the composition of solution is entirely phase 1. The total transformation can be considered as a sum of growth time (τ_G) and dissolution time (τ_D) (Equation 1.16).

$$\tau = \tau_G + \tau_D \qquad \textbf{Equation 1.16}$$

There exist two extremes: where $\tau_D >> \tau_G$ the solution mediated phase transition is under dissolution control and where $\tau_G >> \tau_D$ the solution mediated phase transition is under growth control. Measurement of the desupersaturation profile over the course of the crystallisation can help with

kinetic interpretation. Most solution mediated phase transitions can be classified by one of four main trends (Figure 1.21). [87]

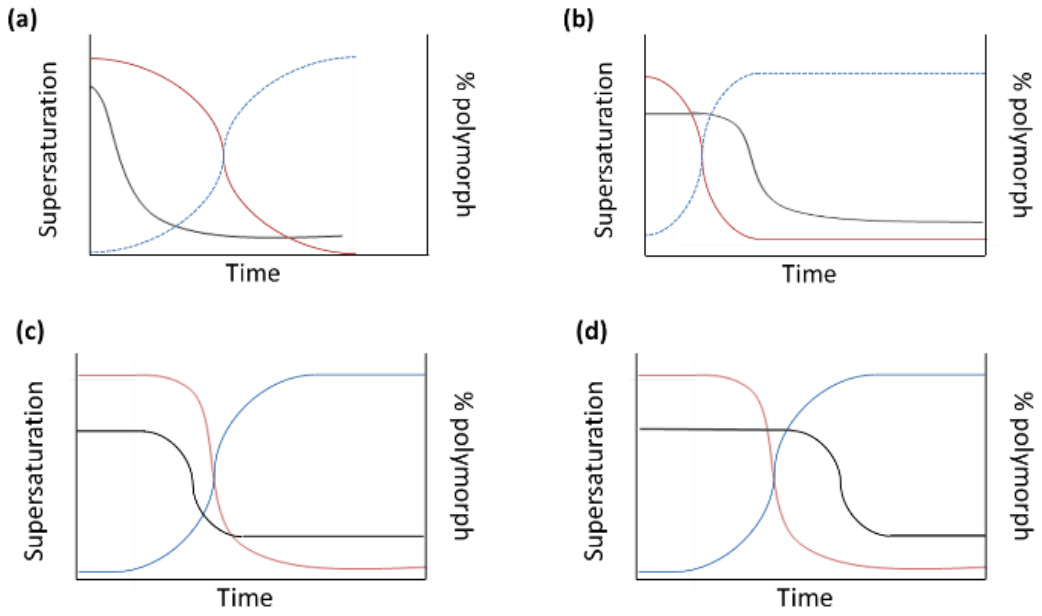

Figure 1.21: The four observed trends in solution mediated phase transitions (black – supersaturation, red – metastable polymorph, blue – stable polymorph)

In scenario (a), once there is any conversion to the more stable polymorph, the supersaturation profile starts to decrease immediately. This indicates that growth of the stable phase is faster than dissolution of the metastable phase and so is termed as a 'dissolution controlled polymorphic transformation'. This is often the case when the solid-liquid surface area is much smaller for the metastable form (larger particles take longer to dissolve) in comparison to the stable form. The opposite would be true for a seeded system. In scenario (b), the supersaturation plateaus at the solubility of the metastable form before a drop; this plateau in supersaturation represents an equilibrium being established between the amount of metastable material dissolving and the amount of material needed for growth of the stable form. The drop in supersaturation is seen when very little metastable solid remains in suspension. This is termed a 'growth controlled polymorphic transition'. This scenario has been shown to hold for the solution mediated phase transition of carbamazepine.[87] Scenarios (c) and (d) are similar to (a) and (b) respectively with the addition of an induction time to the onset of nucleation of the stable form. The difference between the plateau region seen in scenario (b) is that very little is occurring in this plateau as there is no transformation to the stable form. In scenario (c), once the stable form has nucleated, it follows the same path as scenario (a) and is called a 'nucleation-dissolution controlled polymorphic transformation'. This scenario has been observed in the system of tolbutamide.[88] The same is true for scenario (d) with regards to the plateau region and after this it follows the same pattern as scenario (b), hence being

termed a 'nucleation-growth controlled polymorphic transformation'. This scenario has been shown for piracetam[87] and famotidine. [89]

1.8.3 Solid state polymorphic transformations

Polymorphic transitions are also possible in the absence of solvent, taking place in the solid state. The kinetics of this type of transformation have been outlined in detail by Cardew and Davey in 1983[90] , building on the work of Avrami[91]; the latter assumed 'germ nuclei' to be randomly distributed throughout the solid which then grow within the metastable phase until the transformation is complete. It was concluded that ratio of growth rate and nucleation rate (τ_G/τ_N) is key in determining the kinetics of the solid state polymorphic transformation. The work by Avarmi holds for large values of this ratio, while the work by Cardew and Davey expands this for low values of this ratio. As such, it is often the case that the presence of the more stable polymorph in the solid can seed the conversion from metastable to stable form in the solid state. In early work this was seen for the polymorphic transformation from form IV→III for ammonium nitrate and the calcite→argonite transition in calcium carbonate.[92] More recently, this relationship has been observed for the form II→I transformation of paracetamol. [93]

Any two polymorphs displaying an enantiotropic relationship will undergo a solid-state phase transformation upon heating or cooling or with the addition of pressure. Often thermal analysis techniques such as differential scanning calorimetry (DSC) are used to observe these changes. Reported examples of solid-state polymorphic transitions include: caffeine[94], sulfamerazine[95], API CG3[96] and agomelatine. [97]

1.9 Multicomponent crystallisation

The use of second components within the crystallisation process can seem counterintuitive; crystallisation is a process used to help purify a compound and introducing a second component is counteracting this. More recently, however, second components are increasingly being included in the crystallisation process to help improve physicochemical properties of active ingredients: this can be achieved either by forming a molecular complex (co-crystal) with enhanced physical properties[98-101] or by helping to direct formation of a solid form with a certain property such as a preferred polymorph[102-104] or morphology. [22, 105-106] The design of multicomponent crystallisation processes, in which the two molecular components are chosen due to the likelihood that they will interact, is often aided by consideration of the approach of crystal engineering.

1.9.1 Crystal engineering

Crystal engineering can be described as '*the rational design on functional molecular solids*'.[107] Knowledge of a variety of intermolecular interactions, alongside computational tools and algorithms, allows for the prediction of possible bonding motifs to design solids that may have desirable physical properties. In the context of crystallisation, the same principles can be used to predict likely intermolecular interaction between components. The use of hydrogen bonding remains at the forefront of crystal engineering strategies, however the development of strategies employing alternative intermolecular interactions such as halogen bonding has become more prevalent within recent years.[108-109]

Crystal engineering is used in the design of a variety of materials for different applications including ensuring protein incorporation into crystal lattices [110], the design of crystals with non-linear optical applications [111] and the design of metal organic frameworks for use in gas storage.[112-113]

1.9.1.1 Hydrogen bonds

Due to their strength and directionality, hydrogen bonds are the most commonly employed intermolecular interaction exploited in crystal engineering. Their ubiquitous nature is demonstrated in the fact that hydrogen bonds are responsible for the double-helical structure of DNA[114-115], the crystal structure of ice[116] and the structure of fabrics such as nylon[117-119] and cotton.[120]

A hydrogen bond (A-H···B) is an electrostatic interaction that occurs when a hydrogen atom is bound to an electronegative atom such as O, N or F. This induces a partial positive charge on the hydrogen, resulting in an attraction to an atom that displays a partial negative charge or a free-bonding lone pair of electrons (B). The atom attached to the hydrogen (A) is the hydrogen bond donor and the atom that forms the interaction with the hydrogen is the hydrogen bond acceptor (B).

Table 1.2 highlights the properties of hydrogen bonds that classify these interactions as strong, moderate or weak hydrogen bonds; in strong hydrogen bonds, not discussed in this work, there is evidence of some electron sharing across the short bond, giving some covalent character.

Table 1.2: Hydrogen bond properties (adapted from[121])

	Strong	**Moderate**	**Weak**
A-H···B interaction	Largely covalent	Largely electrostatic	electrostatic
Bond lengths	A-H ≈ H···B	A-H < H···B	A-H << H···B
A···B (Å)	~2.2-2.5	~2.5-3.2	~3.2-4.0
Bond angles (°)	175-180	130-180	90-150
Bond energy ($kJmol^{-1}$)	62-167	16-62	4-16

Exploitation of crystal engineering is facilitated by the availability of a range of capabilities geared towards its use. For example, the Mercury program within the Cambridge Crystallographic Data Centre (CCDC) software has a range of tools available to aid in the prediction of possible hydrogen bonding motifs. The IsoStar option analyses the Cambridge Structural Database and protein data bank to find common interactions for a fixed central group and varying contact groups. These interactions are overlaid to form a scatter plot which highlights the propensity of functional groups to form certain interactions. However, IsoStar only considers individual functional groups rather than whole molecules.[122] Information from IsoStar can then be used to produce a full interaction map (FIM), which considers multiple functional groups in an entire molecule. These FIMs also take into account steric and environmental factors of the whole molecules involved in the crystal structure. FIMs are helpful when considering the relative stabilities of polymorphs. This is illustrated for the API sulfathiazole in Figure 1.22 . The FIM generated for a metastable polymorph (form I; SUTHAZ01) of sufathiazole shows that not all predicted hydrogen bonding interactions are satisfied by an area of electron density; the circled hydrogen bonding interaction is one such interaction that does not correlate with an area of predicted electron density. In comparison, the FIM for the stable polymorph (form V; SUTHAZ05) of sulfathiazole shows all interactions satisfied by areas of electron density (the same intermolecular hydrogen bonding interaction as for Form I is circled for comparison).

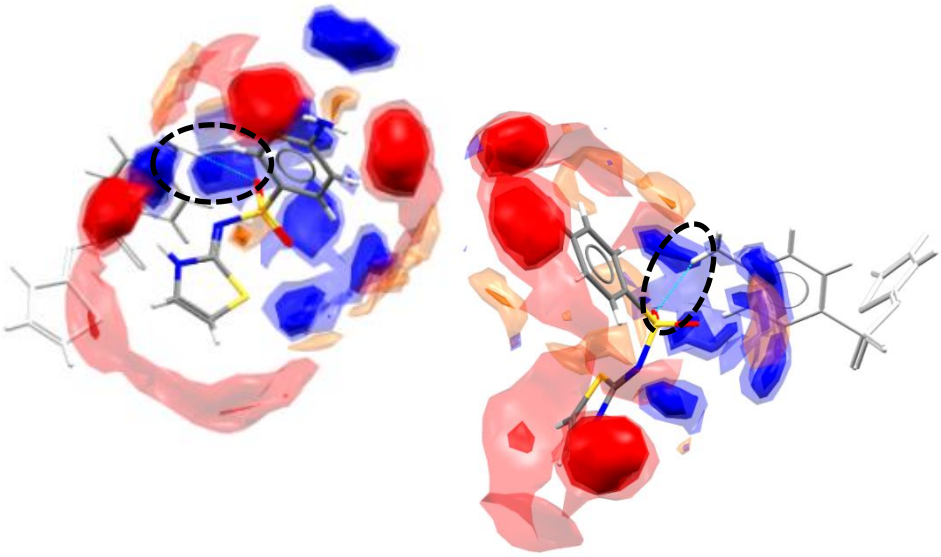

Figure 1.22: Full interaction maps for sulfathiazole form I (left) and form V (right); the greyed out molecules are formed through hydrogen bonding interactions. Generated from CSD references SUTHAZ01 and SUTHAZ05, respectively.

Similarly, analysis of the hydrogen bonds within the metastable polymorphic form of Ritonavir could have predicted the likely presence of a more stable polymorphic form as was indeed discovered after the drug was in production.[73, 123] In the stable Form II, all strong donors and acceptors have been satisfied, indicating its favourable stability.

1.9.1.2 π-π interactions

Although weaker than hydrogen bonds, π-π interactions (or pi-stacking) are also important intermolecular interactions. For example, the aromatic rings in amino acids undergo multiple π-π interactions in RNA binding. [124] Hunter and Sanders proposed a simple model of two interacting π systems; each π system consists of a positively charged σ-framework sandwiched between two negatively charged π-electron clouds. [125] The possible interactions that these two systems can have with one another are shown in Figure 1.23.

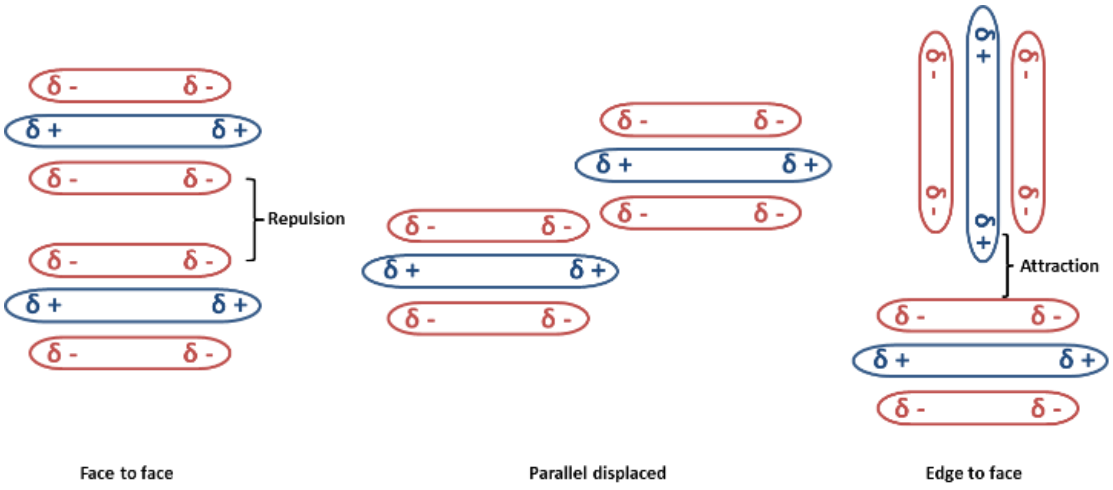

Figure 1.23: The different types of electrostatic interactions between two aromatic systems

The model proposed by Hunter and Sanders states that when one of the two systems possesses a strongly electron-withdrawing group, the preferred packing will not be edge to face. In this case, the electron-withdrawing group draws the electron density away from the core; hence, there is a central area of electron deficiency, promoting face to face packing in preference (Figure 1.24).

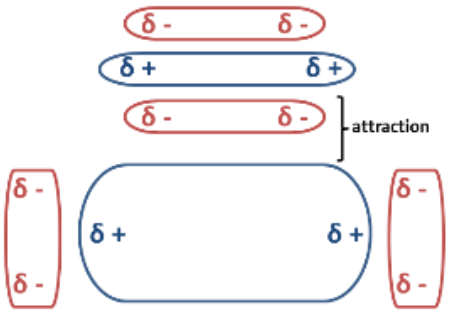

Figure 1.24: Attraction through face to face packing when one of the systems contains an electron withdrawing group

In the case of alternating electron-rich and electron-poor aromatics, there is the possibility of a charge transfer absorbance band. [126] Analogous to energy levels within molecules, the highest occupied molecular orbital (HOMO) of the system can be considered to be located mainly on the electron rich aromatic and the lowest unoccupied molecular orbital (LUMO) located mainly on the electron poor aromatic. Hence, excitation of an electron from the HOMO to the LUMO can occur. As the HOMO-LUMO gap between the two aromatics is smaller than that in each of the individual aromatics, a longer wavelength absorbance is often seen. This results in a shift from UV absorbance to visible absorbance; the origin of colour in this type of system can be partially attributed to π-π stacking.

1.9.1.3 Supramolecular synthons

To define the control of intermolecular interactions in a manner analogous to covalent bonds in organic synthesis, Desiraju coined the term supramolecular synthon to describe the '*structural units within supermolecules which can be formed and/or assembled by known or conceivable synthetic operations involving intermolecular interactions*'.[127] These synthons can either be composed of two identical functional groups (homosythons) or two different functional groups (heterosynthons), as shown in Figure 1.25.

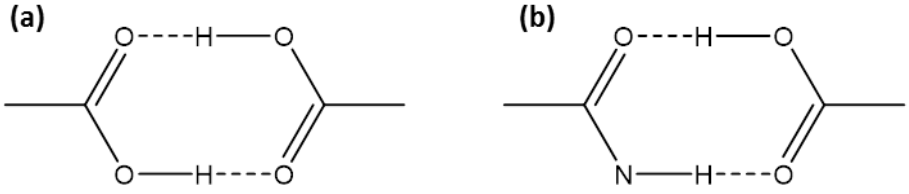

Figure 1.25: (a) a supramolecular homosynthon in the form of a carboxylic acid dimer, (b) a supramolecular heterosynthon in the form of an amide-carboxylic acid dimer

The hydrogen bonding patterns present in molecular packing arrangements can become complicated to describe, with often many interactions present. Graph set notation, developed by Etter, can be used to aid the description of hydrogen bonding motifs in three dimensions.[128] The notation is based on the number of proton donors and acceptors, subscripts and superscripts respectively, within the motif and whether the hydrogen bonds are intramolecular (S) or intermolecular; the latter can be distinguished as finite (R and D) or infinite (C). As an example, the dimer motifs in Figure 1.25 can each be described by the $R_2^2(8)$ graph set.

1.9.1.4 Co-crystallisation

Crystal engineering facilitates the design of new molecular materials enabling the possibility of enhancing a variety of physicochemical properties. One method of crystal engineering is through the use of co-crystallisation; this is a method whereby intermolecular interactions are used to 'join' an active ingredient such as a pharmaceutical with a benign co-former molecule with complementary functional groups chosen to enable interactions such as hydrogen bonding. In this use of crystal engineering, incorporation of the co-former molecule into the crystal structure is used to direct the structure towards more favourable packing arrangements.

Co-crystallisation has been used to a significant degree in the pharmaceutical industry; and in this context there are other multiple component systems that are commonly exploited; these include simple salts of the API. A co-crystal comprising two molecular components can, of course, also form a salt, in the case where there is, for example, proton transfer between the two, leaving each charged. For molecular co-crystals, the definition of the terms co-crystal and salt and the continuum that exists between the two is a highly debated topic throughout academia and industry. [129] For the purposes of this work a co-crystal can be defined as '*solids that are crystalline single phase materials composed of two or more different molecular and/or ionic compounds generally in a stoichiometric ratio which are neither solvates nor simple salts'*.[130] The same work highlights the FDA classification of salts as '*any of numerous compounds that result from replacement of part or all of the acid hydrogen of an acid by a metal or a radical acting like a metal; an ionic of electrovalent crystalline solid'.* The difference between these two types of solid forms is illustrated in Figure 1.26.

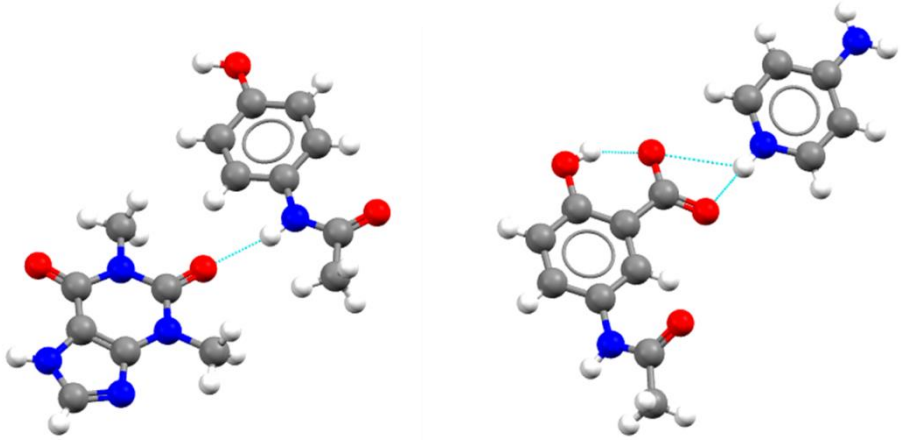

Figure 1.26: A co-crystal of theophylline and paracetamol (CSD REF: KIGLUI) and a salt of 4-aminopyridine and 5-acetylamino salicylic acid (CSD REF:CELXOI), with proton transfer from the carboxylic acid to the pyridine nitrogen

By the use of crystal engineering it is possible to predict possible structures through a variety of criteria such as analysis of common hydrogen bonding motifs. The nature of these hydrogen bonds (and whether proton transfer is likely to have occurred between the two molecular moieties involved) can also be predicted using the generally accepted pKa rule. This rule can be used to predict whether a salt or co-crystal will form; that is a salt will form (proton transfer favoured) if ΔpKa (pKa (base) – pKa (acid)) is greater than three, and a co-crystal will form if ΔpKa <0. [131] The area between this gives rise to the salt – co-crystal continuum. Although ΔpKa is strictly speaking a solution property, predictions from the pKa rule have been found to have some validity and to be a useful tool.

Co-crystallisation is a tool which allows physical properties of an active material to be tuned such as colour for a variety of optical applications [132], or to provide enhanced physical properties for active pharmaceutical ingredients (APIs). The latter can include enhancement of solubility, compressibility, dissolution rate, thermal stability and flowability, with a few examples outlined below.

Alpha lipoic acid (ALA) is an antioxidant that has uses in the treatment of diabetes and chronic fatigue. The disulfide bond in its structure is susceptible to cleavage when exposed to light or elevated temperatures above its melting point of 65 °C. Co-crystallisation with the Generally Regarded As Safe (GRAS) co-former nicotinamide has produced a molecular complex with enhanced thermal stability and solubility relative to the ALA starting material, whilst retaining the therapeutic properties of ALA. [133]

Loperamide hydrochloride is used in the treatment of diarrhoea and displays low solubility at the pH of the gastrointestinal tract where it is absorbed. An improvement in this solubility would

improve its efficacy. Bruni *et al* showed that by co-crystallising loperamide hydrochloride with glutaric acid, an increase in solubility of a factor of six (from 10.1mg/100ml to 63.5mg/100ml) can be achieved. [134] Multiple other examples of co-crystallisation for solubility increase have been reported throughout the literature.[135-139]

Co-crystallisation has also been used to alter a variety of mechanical properties of active ingredients. Co-crystallisation of caffeine with 4-chloro-3-nitrobenzoic acid has shown the possibility to use this method to increase the tensile strength of brittle active ingredients. [140] Materials with greater flexibility generated through methods such as this could be used in applications such as photovoltaic materials and chemical sensors. In another example of the altering of mechanical properties, co-crystallisation of paracetamol with the co-former trimethylglycine has resulted in increased compressibility upon tabletting.[141] Furthermore, the possibility to engineer co-crystals that display a layered arrangement of molecules within the crystal structure could allow for improved compressibility.

1.9.2 Hydrates

Solvated forms of crystal structures are found when a solvent from the crystallisation step is incorporated into the crystal lattice through the formation of intermolecular interactions. Owing to its small molecular size and ability to form multi-directional hydrogen bonds, water is often incorporated into the crystal structure, resulting in the formation of a hydrate.[142] It is estimated that one third of all pharmaceutical solids can form hydrates. [143] The formation of hydrates in the pharmaceutical industry can be both advantageous and disadvantageous.

In aqueous solvent systems, hydrated forms are often the most stable, displaying reduced solubility in comparison to their anhydrous counterpart.[144] They also pose the risk of dehydration in storage, risking loss of crystallinity or change in crystal form and efficacy. [145] Furthermore, hydrated forms of pharmaceuticals can also result in different crystal morphologies, potentially complicating downstream processing steps if these were to suddenly appear in manufacture.

However in the case of a polymorphic system whereby reliable formation of individual polymorphs was problematic, hydrate formation could offer a route to solid form control.

1.9.3 Additives within crystallisation

Over recent years there has been an increased interest in the use of additives included within the crystallisation process in order to direct specific particle attributes such as polymorphic form and particle morphology. Here an additive encompasses either small, size-matched molecules or

polymers. In contrast to the case of co-crystallisation, additives are often not incorporated into the solid product structure, and are often able to be used at very low concentrations.

In polymorphic systems, additives can work to hinder solution mediated phase transitions or to promote or hinder growth of a certain polymorphic form. The use of structurally similar additives has been well explored in the control of polymorphism in l-glutamic acid. [146-150] The metastable α form has been produced with a variety of amino acids[146, 148]; the presence of bulky side chains in l-phenylalanine and l-tyrosine were shown to be key in the stabilisation of the α-polymorph. Monomeric and polymeric derivatives of 5-aminoisophthalic acid were also used as additives to inhibit the growth of the stable β-polymorph. [149] Davey *et al* reported the stabilisation of the metastable α-form through conformational mimicry through a combination of modelling and experimental techniques. [150] The effect of additives on solution mediated phase transitions has been examined for carbamazepine[151-152] and a proprietary compound[153]. Here, the additives are thought to increase the solubility of the stable form, reducing the driving force for the transformation process from the metastable to stable form. Many new or previously elusive polymorphic forms have been discovered using attempted co-crystallisations, these forming in preference to the target co-crystal; examples include felodipine[103, 154], fluconazole[79], nicotinamide and isonicotinamide.[78]

Additives have also been used to alter the morphology of crystals whilst maintaining the polymorphic form. Klapwijk *et al* recently investigated the effect of a polymer additive on the crystallisation of succinic acid.[22] It was found at low polymer concentrations the polymer inhibited the growth of certain faces of the crystal, resulting in a more block-like morphology; this block morphology is more desirable for downstream processing than the traditional plate-like morphology usually adopted from crystallisation from water. Similarly, Simone *et al* investigated the effect of benzoic acid on the crystallisation of ortho-aminobenzoic acid.[155] It was found that benzoic acid acts as a growth modifier, resulting in a change from prisms to needles upon increasing concentration of benzoic acid.

The use of insoluble additives for heterogeneous nucleation and their effect on polymorphism has also been investigated widely in the literature; for example silica particles and carbon powder were used in order to ascertain the most stable form of an unnamed active ingredient[156]. Polymorph control through heterogeneous nucleation has been investigated in isonicotinamide, by employing a number of porous and regular surfaces[11], and in paracetamol[10]. Other systems studied where different additive approaches have been used include the use of spherical agglomerates in the

crystallisation of paracetamol[157] and the use of nanoscopic pores and polymers in the crystallisation of aspirin.[158]

1.10 Aims of research

The overarching theme of this work will be the use of multi-component crystallisation techniques to control the solid form of pharmaceutical materials. The ability to control the solid form of pharmaceutical materials and to be able to develop robust crystallisation processes to impart this control is of great interest to both academia and industry. The work presented in this thesis will investigate two different techniques to exert solid form control through crystallisation.

The first, and main, focus of the work will look at obtaining metastable polymorphic forms through multi-component templating techniques, using additives to promote formation of a desired solid form. Work will use the model system of paracetamol (PCM) and the distinction between its two main polymorphic forms, looking to design a large scale route to the metastable polymorph that displays enhanced physical properties. Previous work in this area has been limited to small scale evaporative crystallisation discovery environments. With this work emerging from the EPSRC Future Manufacturing Research Hub in Continuous Manufacturing and Advanced Crystallisation (CMAC), eventual aims will be to transfer systems into a variety of continuous crystallisation platforms set-up both at the University of Bath and within CMAC partner institutions.

The second strand of the work presented here will look at hosting of pharmaceuticals that display poor stability, with the aim of increasing said stability through incorporation into a host molecule *via* intermolecular host-guest association. Although work has been done to investigate the use of host materials to increase the solubility of a variety of APIs, their use in controlling the stability of these materials is still a new concept, with limited reports in the literature.

2 Experimental methods

Experimental details specific to particular investigations carried out during this project are presented within the main results chapters (Chapters 3-6); however details of the theory and experimental procedure for commonly used methods are presented here.

2.1 Solubility Measurements

Solubility measurements were performed at the University of Strathclyde using the Technobis Crystal 16 (Figure 2.1).

Figure 2.1: The Technobis Crystal 16

The technology employed within the Crystal 16 uses turbidity measurements to give clear and cloud points for the solution understanding. In the Crystal 16, up to 16 vials of the sample solution are subjected in parallel to a heating and cooling temperature programme. For each of the vials a temperature *vs* transmissivity vs time plot is generated and analysed in the CrystalClear software (Figure 2.2) in order to determine clear and cloud points. The clear point is where the solution allows for 100 % light transmission i.e. all particles having dissolved. The cloud point is where this transmittance no longer has a value of 100 % indicating precipitation of particles out of solution. From this, metastable zone widths (MSZW) can be determined and cooling crystallisation experiments designed; it is important to note that the MSZWs depend on a variety of crystallisation conditions including cooling rate, stirring and scale and so can only be used as a guideline for experimental design.

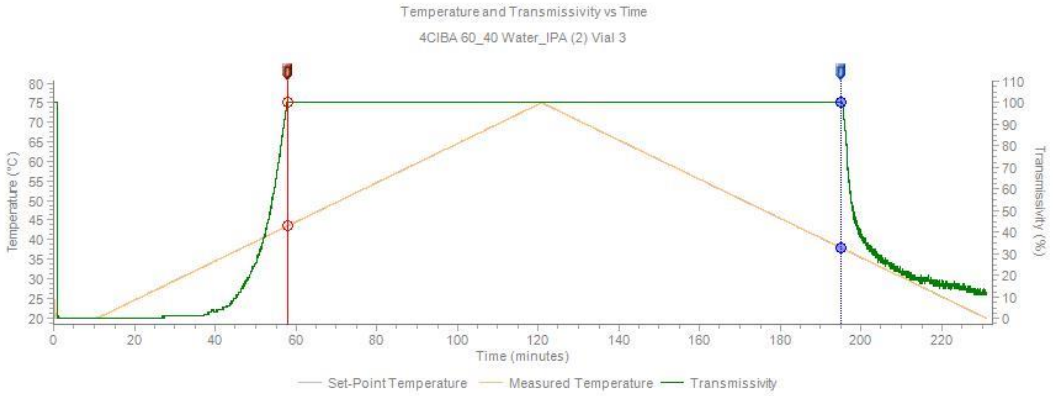

Figure 2.2: A temperature *vs* transmissivity *vs* time plot for a vial in a Crystal 16 experiment

As used in the present work, in general four 1.5 cm^3 vials of varying concentrations of the compound to be measured were heated from 20 °C to 75 °C and then cooled from 75 °C to 5 °C, *via* a peltier thermoelectric device, at a rate of 0.1 °C min^{-1} with a magnetic bottom stirring speed of 800 rpm. If a lower boiling point solvent such as ethanol (bpt = 78 °C) was used, the cooling profile was adjusted accordingly to prevent vaporisation of solvent, which would reduce the accuracy of the measurements. Data were processed using CrystalClear v.1.0.1.614 from Avantium Technologies.

2.2 Cooling crystallisations

Cooling crystallisation experiments were carried out using the Polar Bear Plus crystalliser from Cambridge Reactor Design (Figure 2.3). The Polar Bear Plus crystalliser provides a platform for simultaneous controlled cooling of up to 28 1.5 cm^3 vials in a temperature range of 150 °C to -40 °C *via* a peltier thermoelectric device with bottom magnetic stirring. It has interchangeable inserts that allow gradual scale up of systems from 1.5 cm^3 vials to 20 cm^3 vials up to 250 cm^3 round-bottomed flasks (RBFs).

Figure 2.3: The Polar Bear Plus with interchangeable inserts (right)

Overhead stirring can be implemented in conjunction with larger scale experiments in RBFs utilising a separate motor and shaft (detailed in Chapter 3) in order to provide more effective mixing at

these larger scales. Full details of cooling profiles employed for experiments are given in the relevant Chapters.

2.3 Single crystal X-ray diffraction (SCXRD)

2.3.1 The crystalline state

In order to study the key physicochemical properties of crystalline materials such as pharmaceuticals, a fundamental understanding of the underlying solid-state crystal structure is necessary. Broadly, the area of crystallography is the study of the atomic structure of ordered materials. A crystalline solid can be defined as a highly ordered, symmetrical lattice consisting of identical points (lattice points) arranged in a periodic manner in three dimensions; the lattice points form a highly regular arrangement which underpins the regularity of crystal structures. Joining together eight neighbouring lattice points forms a three-dimensional parallelogram (the unit cell). The unit cell is defined by three sides (*a, b, c*) and three angles (α, β, γ) as shown in Figure 2.4. The unit cell is the smallest repeating volume of the lattice that is representative of the crystal. The crystal is assembled by repeating the unit cell and its contents by translation along all three spatial dimensions.

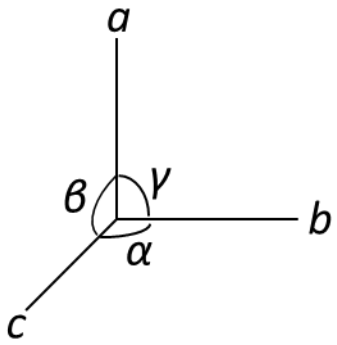

Figure 2.4: The unit cell axes showing the length and angle parameters

There are four types of unit cells dictated by the positioning of the lattice points, in particular the possible inclusion of additional lattice points: primitive (P), body-centred (I), base-centred (C) and face-centred (F) (Figure 2.5).

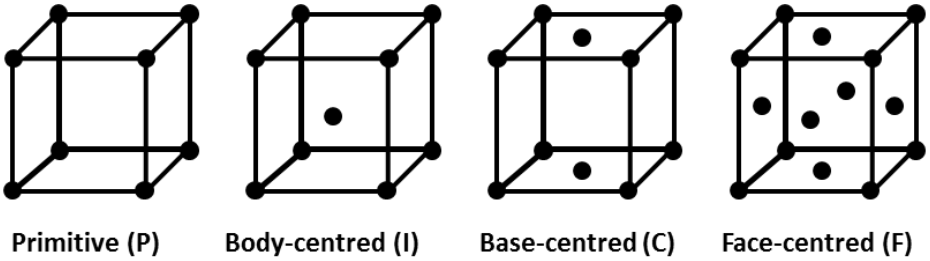

Figure 2.5: The four types of unit cell. Each lattice point is represented by a filled circle

Reflection and rotation symmetry elements result in constraints on the geometry of the unit cell and these constraints give rise to the seven crystal systems. The combination of the four unit cell types and the seven crystal systems gives the 14 Bravais Lattices.

Table 2.1: The restraints on the seven crystal systems that result in the 14 Bravais lattices [159]

Crystal system	Unit cell parameters	Lattice types
Triclinic	$a \neq b \neq c$; $\alpha, \beta, \gamma \neq 90°$	P, I, F
Monoclinic	$a \neq b \neq c$; $\alpha = \gamma = 90°, \beta \neq 90°$	P
Orthorhombic	$a \neq b \neq c$; $\alpha = \beta = \gamma = 90°$	P
Tetragonal	$a = b \neq c$; $\alpha = \beta = \gamma = 90°$	P, I
Rhombohedral	$a = b = c$; $\alpha = \beta = \gamma \neq 90°$	P, I, F, C
Hexagonal	$a = b \neq c$; $\alpha = \beta = 90°$; $\gamma = 120°$	P, C
Cubic	$a = b = c$; $\alpha = \beta = \gamma = 90°$	P

Whilst joining the lattice points in three dimensions results in formation of a unit cell, a two-dimensional array can be defined to produce lattice planes which can be indexed in two ways; using Weiss indices or Miller indices. Weiss indices are the intercepts of these planes with the cell axes and so can be fractions. Miller indices are the inverse of Weiss indices and are described as integers. In three dimensions, each Miller index (*h, k, l)* corresponds to a set of parallel planes with a characteristic plane spacing, 'd_{hkl}'.

In a crystal structure, there are also symmetry elements internal to the unit cell which add to the structure defined by the lattice symmetry. Six symmetry element types are possible; four non-translational and two translational; these act on the unit cell contents and define the internal symmetry. The translational elements are glide planes and screw axes. Glide planes consist of a reflection followed by translation; this can result in more efficient packing of molecules in comparison to a simple reflection. This is because the translation results in a half a repeat unit displacement of the mirror images in comparison to simple reflection where images are directly opposite one another where repulsive forces dictate a minimum separation distance of these images. A screw axis consists of rotation followed by translation and similarly can maximise packing efficiency with respect to a simple rotation. These symmetry elements act upon the smallest

volume of highest symmetry within the unit cell, termed the asymmetric unit, to generate the unit cell contents.

The combination of these six symmetry elements with the 14 Bravais lattices result in the generation of 230 possible arrangements, each of which is termed a space group. The 230 space groups are unevenly distributed across the fourteen Bravais lattices and they represent the only ways in which identical objects can be packed within a crystal structure. In practice, for the type of molecular systems relevant to pharmaceutical crystallisation, only a small number of these space groups, usually those of relatively low symmetry, are relevant.

2.3.2 X-ray diffraction

X-rays lie on the electromagnetic spectrum, with wavelengths of the same order of magnitude as typical interatomic spacings. Hence, X-rays are ideal for probing the internal structure of crystalline materials on the atomic scale.

The electrons in an atom scatter the X-rays and the strength of scattering is dependent on the number of electrons in the atom, its atomic number. The scattering of X-rays from electrons is known as Thomson scattering.[160] W. L. Bragg showed that X-ray diffraction can be regarded as a reflection from sets of parallel lattice planes, each of which contain a series of regularly distributed lattice points, analogous to the reflection of light by a mirror; as such the angle of incidence is equal to the angle of reflection. The Bragg construct shown in Figure 2.6 is used to derive Bragg's Law (Equation 2.1) for constructive interference between waves reflected from parallel lattice planes and hence leading to measurable intensity when Bragg's law is satisfied.

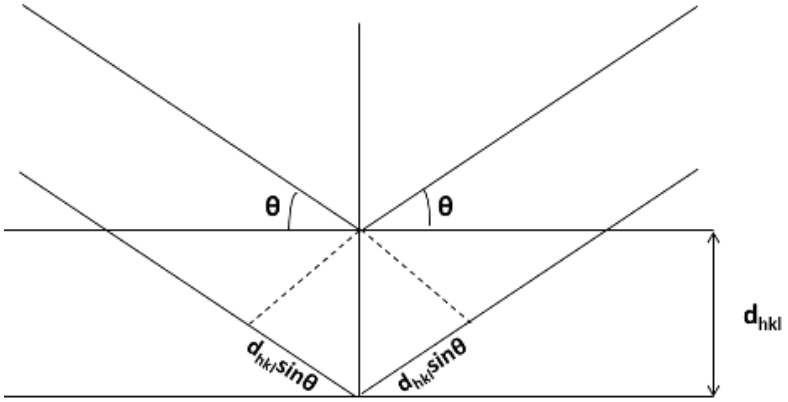

Figure 2.6: The Bragg construct used to show the diffraction of X-rays from sets of parallel lattice planes with a d spacing = d_{hkl}

$$\textbf{path difference} = 2d_{hkl}\sin\theta = n\lambda \qquad \textbf{Equation 2.1}$$

Bragg's law defines the necessary conditions to observe a reflection intensity, however it is purely geometric and does not define the intensity of the reflection; the latter is obtained from experimental data and is related to the unit cell and crystal contents. In the Bragg interpretation, the resultant wave is formed through constructive interference of the scattered waves from electrons on the lattice planes. The variation in intensities within an X-ray diffraction pattern is due to the variation in these resultant waves, thus must be related to the scattering from the atoms and molecules in the unit cell – the molecular structure. [161] The atomic scattering factor, f_j for the j^{th} atom, gives the extent to which that atom will scatter X-rays; the intensity of this scattering will vary with angle within the diffraction pattern; different atoms have different electron clouds which will scatter X-rays differently. The atomic scattering factor at a Bragg angle of 0° is equivalent to the atomic number of the atom. At low Bragg angles, the scattering power of the atom is thus proportional to the number of electrons, however this relationship diverges at higher Bragg angles as the scattering power of the atom diminishes.

An X-ray diffraction experiment measures the intensity of a series of reflections (diffraction spots) at varying positions. Each spot corresponds to diffraction from a set of Miller planes (*h, k, l)*. Rearrangement of Bragg's Law shows that there is an inversely proportional relationship between sinθ and *d.* A diffraction pattern is hence constructed in units of 1/*d* and so is said to be in reciprocal space; this concept is used in order to provide an understanding of the relationship between the position of spots and the unit cell. Simply, the distance of each spot on the diffraction pattern from the centre is proportional to sinθ and 1/*d*. Hence, materials with large unit cells, and hence larger *d* spacing, display compressed diffraction patterns and *vice versa*.

The relationship between the diffraction spots and atoms and their positions in the unit cell can be examined through information about reflection intensities and how these relate to electron densities. The diffraction pattern produced through experimental methods is related to the position of atoms through Fourier transforms defining the quantity known as the structure factor, F_{hkl} (Equation 2.2).

$$F_{hkl} = \sum_{j=1}^{j=n} f_j exp2\pi i(hx_j + ky_j + lz_j) \qquad \textbf{Equation 2.2}$$

Where f_j is the atomic scattering factor of the j^{th} atom and (h,k,l) are the reciprocal space coordinates and (x,y,z) the direct coordinates of the j^{th} atom, respectively.

Fourier transformation of the structure factor (Equation 2.3) in turn produces an electron density map which allows for the location of atoms (particularly those with higher atomic numbers) to be

determined. The structure factor can be defined as '*a mathematical function describing the amplitude and phase of a wave diffracted from crystal planes characterised by Miller indices*'.[162]

$$\rho(xyz) = \frac{1}{V}\sum_{h,k,l} F_{hkl}.\exp[-2\pi i(hx + ky + lz)] \qquad \textbf{Equation 2.3}$$

Where ρ(xyz) is the electron density at point x,y,z in direct space, (h,k,l) are reciprocal space coordinates and (x,y,z) are direct space coordinates.

The magnitude of the structure factor F_{hkl} is the square root of the intensity of each spot in the diffraction pattern (I_{hkl}) (Equation 2.4).

$$I_{hkl} = |F_{hkl}|^2 \qquad \textbf{Equation 2.4}$$

Equation 2.4 gives rise to the phase problem: the magnitude of F_{hkl} can be determined; however the sign or phase cannot be determined from the experiment. This is a problem as crucial information for the determination of electron density is contained within the phase, as is evident from Equation 2.3. The phase problem is overcome within the structure solution stage of X-ray structure determination; the method of overcoming the phase problem is dependent on the atoms present in the unit cell. Patterson methods are used when there is a heavy atom present in the structure. Here, the observed structure factors are squared to produce a Patterson map, which does not require knowledge of the phases; a Patterson map has peaks that correspond to vectors between pairs of atoms and so shows the positions of atoms relative to each other. The peaks are proportional to the square of the atomic numbers of the atoms present. Direct methods are used when lighter atoms are present, for example in purely organic materials. This process works on a 'best approximation' to determine the phases through statistical relationships between combinations of reflections. A successful direct method structure solution used in the large majority of organic structure determination usually yields the location of most non-hydrogen atoms in the structure. Following this, Fourier recycling methods are used, together with structural refinement, to locate any missing atoms; for good quality data this will include the hydrogen atoms in the structure.

Crystal structure refinement is carried out using least squares analysis. This procedure is based on the fact that once a set of approximate atomic identities and positions are known, defining the molecule within the crystal structure, a set of calculated structure factors can be obtained (from Equation 2.2). These can then be compared with the calculated structure factors, and a least squares process involving improving (refining) the atomic parameters/positions and atomic vibrations (thermal parameters) can be carried out, aiming to minimise the difference between

observed and calculated structure factors. The R factor is a calculation of the agreement between the calculated and observed structure factors, evaluated through the structure factor magnitudes; defined in Equation 2.5, the value of which should decrease throughout the refinement process. A good refinement is typically indicated by an R factor of less than 5 %.

$$R = \sum \frac{||F_{obs}| - |F_{calc}||}{|F_{obs}|} \qquad \textbf{Equation 2.5}$$

2.3.3 Experimental

Single crystal X-ray diffraction experiments were performed using Rigaku Oxford Diffraction (formerly Agilent Technologies) instruments, utilising the set-up shown in Figure 2.7. Both a Supernova and XCalibur diffractometer were used in the work presented in this thesis; the difference is that the Supernova is dual source (able to operate with both Mo-K_α and Cu-K_α radiation) and has higher intensity through the use of microfocus beams, whilst the XCalibur only operates with Mo-K_α radiation. Both instruments are equipped with a graphite monochromator, four-circle kappa goniometer and an Eos S2 detector. The four circle allows for movement of the goniometer through all diffractometer positions (κ, φ, ω, 2θ) to provide collection of a complete set of diffraction data. Each diffractometer is equipped with an Oxford Cryosystems Cryostream 700 series to provide a flow of liquid nitrogen to the sample for precise temperature control at both high and low collection temperatures.

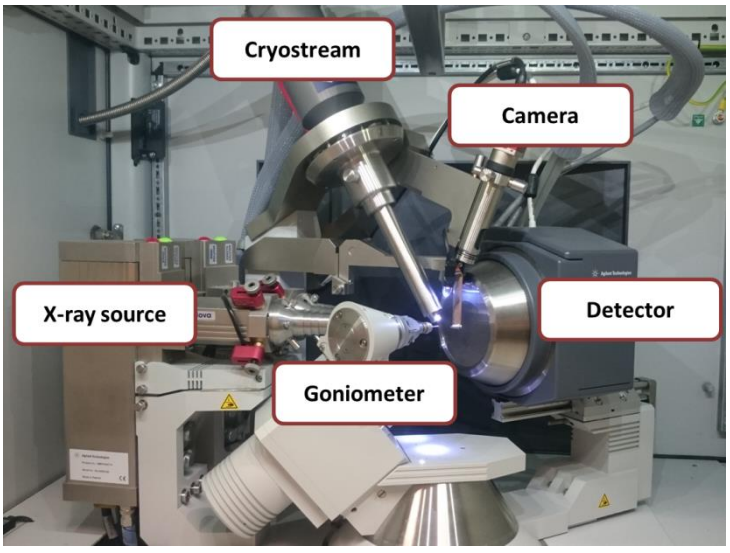

Figure 2.7: The Rigaku Oxford Diffraction Supernova set-up with key features labelled

Data collection and processing were carried out using CrysAlisPro software.[163] Diffraction data were processed through the XPREP software to verify the space group and eliminate poor reflections to allow a higher quality refinement. All crystal structures were solved using direct methods (SHELXS

for the crystal structure of PCM-II or SHELXD for the hosting complex outlined in Chapter 6) and refined with SHELXL in the WinGX interface.[164]

2.4 Powder X-ray diffraction (PXRD)

2.4.1 Theory

Although extremely useful for telling the composition of individual single crystals, SCXRD is not a suitable method for the analysis of large quantities of polycrystalline material that would be generated from a large scale batch crystallisation experiment. Analysis of polycrystalline materials produced from such experiments is conducted using powder X-ray diffraction (PXRD) analysis. Every compound will have a distinct PXRD pattern making it a good fingerprinting technique to quickly elucidate what has been produced in a given experiment.

In a powder sample, the varying arrangement of the micro crystals comprising the polycrystalline sample will result in differing orientations of the lattice planes. At any one detector angle, some of these lattice planes will be orientated at the correct Bragg angle to result in diffraction, as defined by Bragg's Law. Due to the random orientations of the crystals in the samples, the diffraction from the sample is scattered in multiple directions, with diffraction from each set of lattice planes within a polycrystalline sample seen as a cone of diffraction (Figure 2.8).

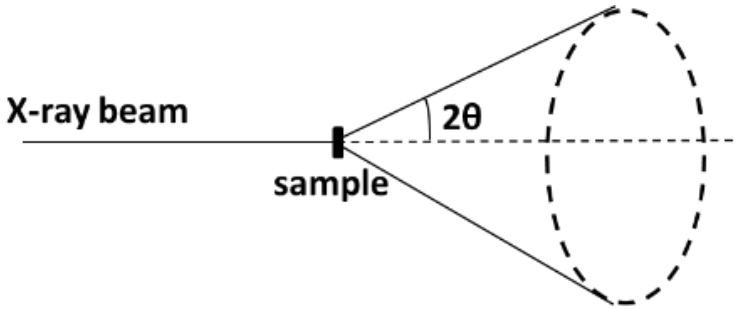

Figure 2.8: The cone of diffraction produced from a polycrystalline sample

On a two-dimensional detector placed perpendicular to the X-ray beam, these diffraction cones will appear as a series of concentric rings (Debye rings). Plotting the 2θ angle against the integrated intensity of these rings leads to a one-dimensional diffraction pattern.[159]

When comparing an experimental PXRD pattern to one calculated from a single crystal structure, the most important feature is the peak positions as these directly relate to the unit cell parameters and hence act as an ideal identifier of the crystal structure present. Peak intensities, which relate to the positions of the atoms in the unit cell, can often vary between experimental and calculated

patterns due to preferred orientation effects that can arise depending on the method of sample preparation used. Hence, unless full quantitative phase analysis is carried out using methods such as Rietveld refinement, the intensity can often only be used indicatively.

2.4.2 Experimental

Unless otherwise stated, PXRD data was collected at the University of Bath in flat-plate mode using a Bruker D8 Advance laboratory diffractometer equipped with monochromatic Cu-K_α radiation (λ = 1.54056 Å), the set-up of which is highlighted in Figure 2.9.

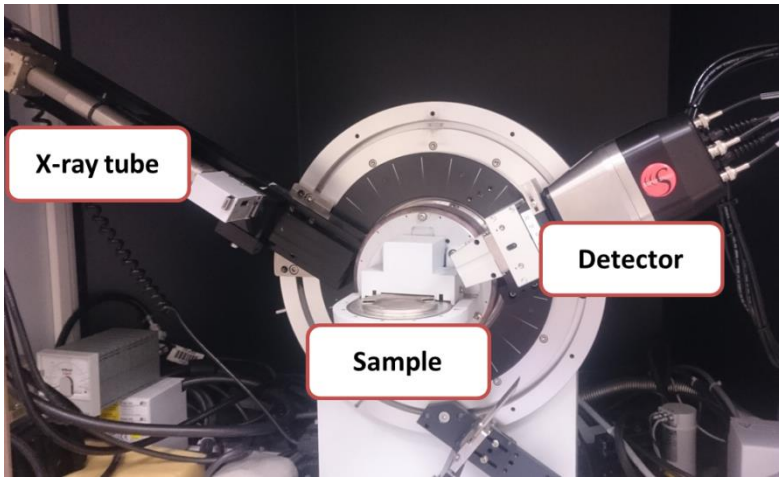

Figure 2.9: The experimental set-up of the D8 Advance diffractometer, with key features labelled

A small amount of powder was placed on a glass slide and pressed down to form a flat layer, using another glass slide. The glass slide was mounted onto the sample holder using non-diffracting plasticine. Samples were scanned between 5 ° and 40 ° 2θ with a 0.01° step size, 0.3 secs per step and a rotation speed of 15 rpm; rotation of the sample holder was used to negate preferred orientation effects.

2.5 Differential Scanning Calorimetry (DSC)

2.5.1 Theory

Differential Scanning Calorimetry (DSC) is a method of thermal analysis used to help provide qualitative and quantitative information on thermal events in a sample subjected to a set heat/cool profile. Both a reference pan (typically a closed empty aluminium pan) and a closed aluminium pan containing the sample are subjected to the same linear temperature programme. The difference in heat flow to the sample and to the reference at the same temperature is recorded as a function of temperature. This difference should remain the same until a thermal event occurs in the sample; an endothermic event would result in the rate at which the sample temperature would rise being

lower than that of the reference and so heat needs to be applied to the reference in order to maintain a constant temperature profile and *vice versa* for an exothermic event. [165] DSC can monitor various thermal changes within the sample; the main events typically observed in such a scan and their appearance in DSC patterns are shown in Figure 2.10 (note: this plot shows exothermic events up).

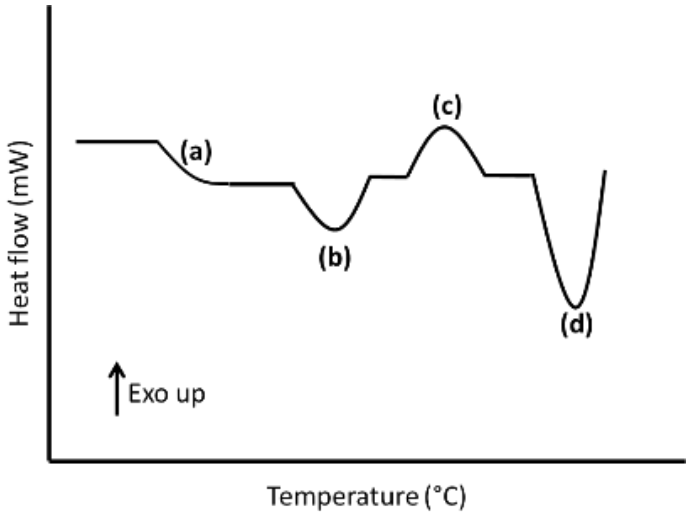

Figure 2.10: Thermal events in a DSC trace showing (a) a glass transition (change in baseline level), (b) a desolvation/phase transition (endothermic), (c) a re-crystallisation (exothermic) and (d) a melt (endothermic)

2.5.2 Experimental

All Differential Scanning Calorimetry (DSC) studies, with exception of the examination of samples produced in the MSMPR work at AstraZeneca, were carried out using a Thermal Advantage Q20 DSC from TA Instruments, equipped with Thermal Advantage Cooling System 90 and operated with a dry nitrogen purge gas at a flow rate of 18 cm^3 min^{-1}. The samples were placed in sealed Tzero aluminium pans and a heating rate of 5 °C min^{-1} was used. Data were collected using the software Advantage for Qseries (Ver. 5.40 software © 2001-2011 TA Instruments-Waters LLC). For the MSMPR samples DSC studies were carried out using a Thermal Advantage Q2000 from TA Instruments. Up to 3 mg of material was contained in an aluminium pan, fitted with a lid, and heated over the temperature range 25−200 °C at a constant heating rate of 5 °C min^{-1}. Data were collected using the software Advantage for Qseries (Ver. 5.40 software © 2001−2011 TA Instruments-Waters LLC).

2.6 Thermogravimetric analysis (TGA)

2.6.1 Theory

Thermogravimetric analysis (TGA) is a technique used to measure mass losses in a sample upon heating. A sample is weighed into a pan, with this weight being equivalent to 100 % mass. Percentage changes in mass from events such as loss of solvent or decomposition can be seen from a change in the % mass; correlation of this percentage mass loss to atoms within the molecule can aid with quantification of thermal events in a sample (Figure 2.11). For this reason, TGA is often combined with DSC in order to obtain a full picture of the thermal changes in a sample upon heating. [166-168] Crucially, TGA will not show melting events and so can be used to distinguish between events in a DSC that could theoretically be attributed to more than one event (e.g. distinguishing desolvation from melting).

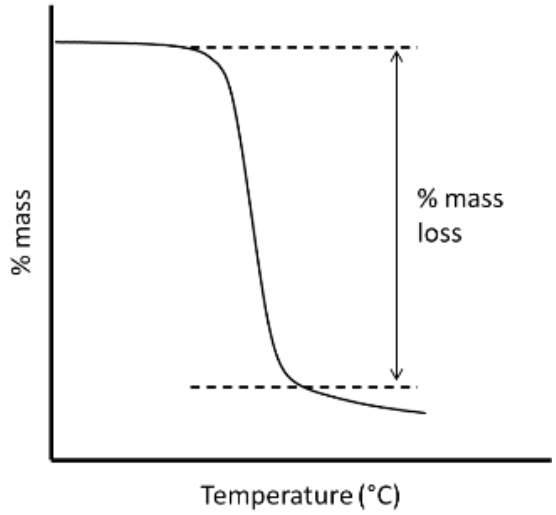

Figure 2.11: A typical TGA trace, showing mass loss from a decomposition event

2.6.2 Experimental

TGA data was obtained using a Perkin Elmer TGA 4000 Thermogravimetric Analyser. Analyses were performed using samples sealed in crimped aluminium sample pans. Data points were collected every second at a ramp rate of 5 ˚C min^{-1} in a flowing 40 mL min^{-1} argon stream.

2.7 Raman Spectroscopy

2.7.1 Theory

Raman spectroscopy is a type of vibrational absorption spectroscopy whereby a monochromatic beam of radiation is shone at a sample and the energies of the scattered radiation are measured. Most of the radiation will pass through the molecule without being scattered, but a small

proportion will be scattered, without the scattered frequency being altered from the incident frequency, this is known as Rayleigh scattering. However a small amount of the scattered light will exchange energy with the sample (in vibrational Raman, gaining or losing energy to vibrational modes), thus will be scattered with a lower or higher frequency than the incident radiation. When the scattered radiation has a lower frequency (lower wavenumber) than the incident radiation it gives rise to Stokes lines, with a higher frequency (higher wavenumber) giving rise to anti-Stokes lines. [169]

Raman spectroscopy is another method, in addition to PXRD, often used to help distinguish different polymorphic forms of the same material. Differences in hydrogen bonding between polymorphic forms would result in different vibrational frequencies of the associated bonds, which can manifest as different Raman spectra. Similarly, changes between a single component and multi-component material would be visible through Raman spectroscopy, owing to the different vibrational frequencies between hydrogen bonded moieties and free functional groups.

2.7.2 Experimental

Offline Raman spectra were acquired using a Renishaw InVia confocal Raman microscope using a red laser (λ = 785 nm) and a 4 second acquisition time. Experimental details for the Raman PhAT probe used in scaled batch crystallisation experiments are given in Chapter 4.

2.8 Process analytical technologies (PAT)

2.8.1 Focussed Beam Reflectance Measurement (FBRM)

FBRM is a laser-based technique used to measure the chord length distribution of particles suspended within a liquid. The chord length correlates to the particle size, however is not a direct measure of particle size. Internal lenses within the probe focus the laser beam to a focal point. The focussed beam probes particles in solution by scanning in a circular path (Figure 2.12 (a)). As this beam scans individual particles in suspension, the backscattered light is detected by the probe; the length of this pulse corresponds to the size of the particle (Figure 2.12 (b)). The length of each backscattered pulse is multiplied by the scan speed in order to obtain the chord length of the particle. Thousands of chord lengths are measured per second and these are plotted against the frequency of each chord length (counts) to give a chord length distribution (Figure 2.12 (c)). [170]

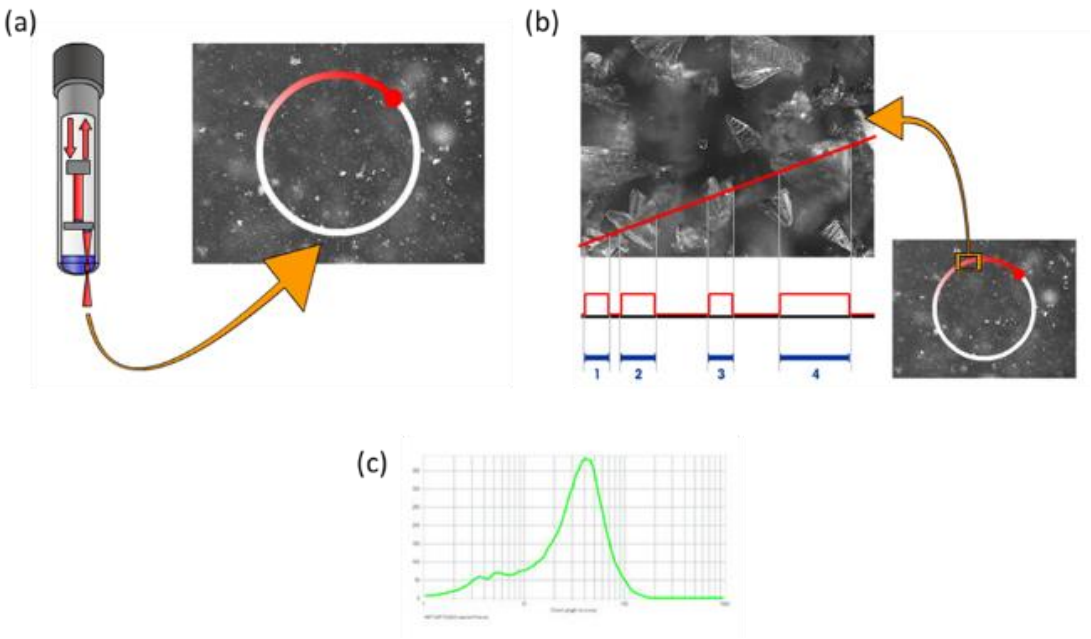

Figure 2.12: The measurement of chord length distribution through FBRM (a) a focussed laser beam scanning in a circular path, (b) the measurement of suspended particles in the circular path, (c) the resulting chord length distribution

FBRM is a useful technique for detecting onset of nucleation in systems as well as providing crucial information when using seeding techniques. However, particle size information from chord length distributions should be treated with caution; chord length distributions can be significantly skewed by crystals that display a high aspect ratio, such as needles.

Full experimental details for the FBRM used in scaled batch experiments are given in Chapter 4.

2.8.2 Raman probe

Raman probes apply the principles of Raman spectroscopy described above to monitor a crystallisation process non-invasively, giving real time information on the solid form produced throughout the process. Probes can be immersion based (i.e. submerged in a solution like a FBRM probe) or non-contact based such as the PhAT probe employed in this work.

One of the main benefits of monitoring crystallisation processes with a Raman probe is their insensitivity to aqueous solutions. However, other crystallisation solvents can swamp spectra, resulting in poor resolution of peaks from the product.

2.9 SEM

2.9.1 Theory

Scanning electron microscopy (SEM) is a technique used to obtain high resolution images of solid particles in terms of their morphology, surface features and topography and is often used to

complement optical microscopy images. Electrons are emitted from an electron gun and accelerated towards the sample, which has been coated in a thin film of a metal in order to prevent charge build up on the surface. The electron beam hits the sample and can interact with the sample to generate backscattered electrons, secondary electrons or X-rays. Backscattered electrons have a similar energy to the incident electron beam, losing very little energy on interaction with the sample. They originate from deep within the sample and provide compositional information. Secondary electrons have a lower energy than the incident electron beam, losing energy on interaction with the sample. They originate from within a few nanometres of the surface, and as such provide sensitive surface information. When interaction of the electron beam with the sample results in the ejection of an electron from the outer shell, the excess energy produced can be emitted as an X-ray. These give information about the elemental composition of the sample. [171]

2.9.2 Experimental

As different SEMs were used depending on where the work was performed, full experimental details are given in the relevant Chapters.

2.10 NMR

2.10.1 Theory

When a nucleus is placed in a strong magnetic field, the spin states of nuclei with a non-zero nuclear spin, such as ^{1}H and ^{13}C, can align themselves with or against the magnetic field resulting in a split in these normally degenerate energies. By applying an external radio-frequency (RF) field of correct frequency, the spin state of a nucleus can be changed from the stable state (aligned with the magnetic field) to the unstable state (aligned against the magnetic field); this is known as resonance. Depending on the local bonding environment of the nucleus (i.e. the local chemical environment), a slightly different external RF field frequency would be required to cause the nucleus to resonate; this is due to local shielding effects diminishing the effective magnetic field by a small amount. It is this difference in RF magnetic field that an NMR experiment measures. From the differences in frequency required for resonance, the chemical environment in which the nucleus sits can be determined.

2.10.2 Experimental

Routine NMR analysis was performed by dissolving the sample in D_2O and using a Bruker Avance 500 MHz spectrometer, with all spectra recorded at 298 K. Data were processed using ACD labs.

Chapter 6 details various different NMR methods used for host-guest complexes, the experimental details of which are given in the Chapter.

3 Small-scale batch crystallisation of paracetamol form II

Some of the results presented in this Chapter have been published in a themed issue (Pharmaceutical Solids) of Chemical Communications:

L.R. Agnew, D.L. Cruickshank, T. McGlone and C.C. Wilson, 'Controlled production of the elusive metastable form II of acetaminophen (paracetamol): a fully scalable templating approach in a cooling environment', *Chem. Commun.,* 2016, 52, 7368-7371

3.1 Introduction and Aims

Paracetamol (PCM) (Figure 3.1) is a well-known antipyretic and analgesic active pharmaceutical ingredient (API) which has been studied extensively in the solid state.[82, 172-174] It exists in five known polymorphic forms, two of which can only be accessed under high pressure conditions.[175] Until recently, Form III (PCM-III) has been highly elusive, however recent work has shown the possibility to isolate PCM-III using Ostwald's rule of stages.[176] The work in this thesis focusses on the two main polymorphic forms of PCM: the thermodynamically stable form I (PCM-I, CSD REF:HXACAN30) and metastable form II (PCM-II, CSD REF:HXACAN31)). PCM-I crystallises in the monoclinic space group $P2_1/n$, with PCM-II crystallising in the orthorhombic space group Pbca.

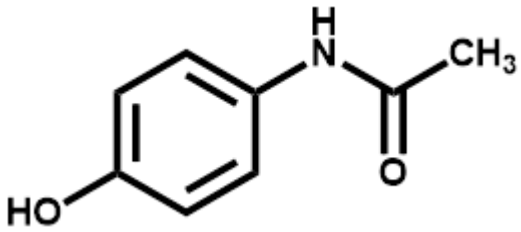

Figure 3.1: The molecular structure of paracetamol

PCM-I and PCM-II are a prime example of packing polymorphism, with PCM-I adopting a herringbone packing arrangement and PCM-II adopting a layered structure (Figure 3.2). In both polymorphs, each paracetamol molecule forms four hydrogen bonding interactions: the hydroxyl group acts as both a donor and acceptor forming an O-H···O hydrogen bond to the carbonyl group and an O···H-N hydrogen bond to the amide N-H, with the amine and the carbonyl forming the complementary interactions.

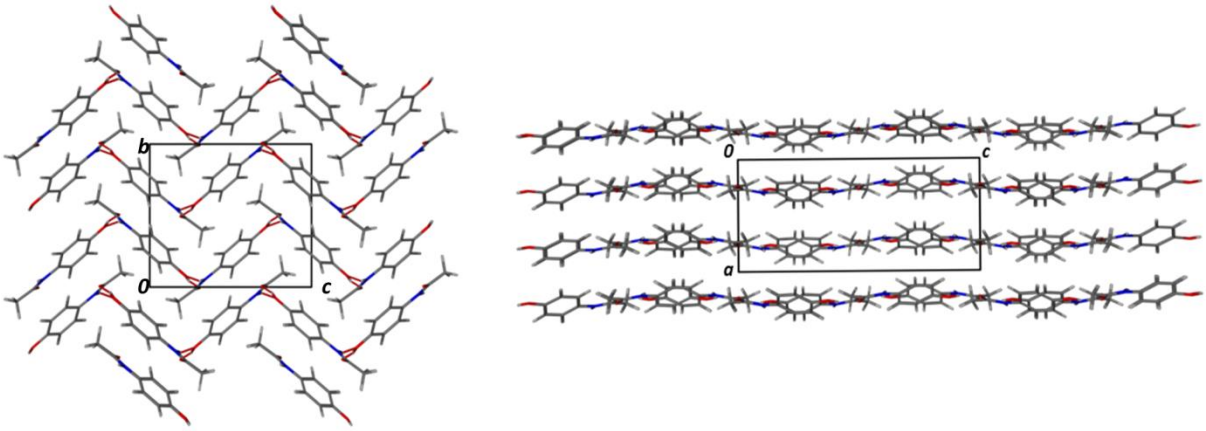

Figure 3.2: The crystal structures of PCM-I (left) and PCM-II (right), showing the clear difference in their packing arrangements

The two polymorphs are easily distinguishable through powder X-ray diffraction (PXRD) analysis (Figure 3.3), their space groups and unit cell parameters producing entirely distinct patterns; in particular there is a low angle peak at 10° 2θ in PCM-II that provides rapid, easily observed, distinction between the two polymorphs. Raman spectroscopy can also be used to distinguish between polymorphs, which will be detailed further in Chapter 4.

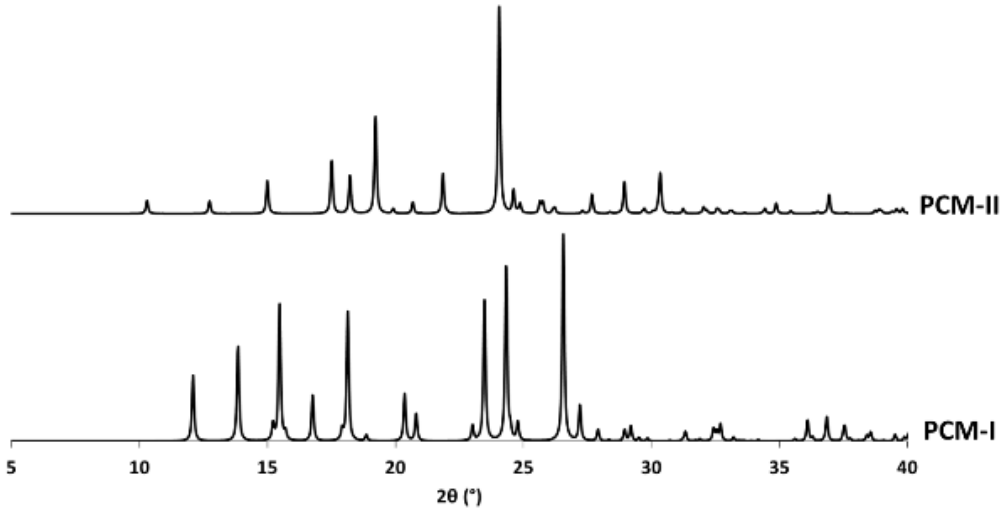

Figure 3.3: PXRD patterns for PCM-I and PCM-II

The two polymorphs display an monotropic relationship.[177] However, in some samples produced in this work, a solid state conversion from form II to form I is observed upon heating in a temperature range of 130-140 °C. This transition is visible through differential scanning calorimetry traces, when carried out with a slow scan speed (Figure 3.4). This phenomenon has been observed and explained

by Nichols and Frampton.[172] They observed that when crystallised from the melt, the DSC trace shows one sharp endothermic peak at 157 °C, indicating the monotropic relationship of the two polymorphs. However, when crystallised from solution, a small endothermic peak at 157 °C, corresponding to a phase transition from PCM-II to PCM-I, followed by a sharp melt at 171 °C, corresponding to the melt of PCM-I, are observed. They postulate that solution based methods produce samples of PCM-II which are not polymorphically pure, with the presence of this small amount of PCM-I being responsible for the first endothermic event. Alternatively, the fast precipitation of PCM-II crystals from solution based methods could result in more defects on the crystal surface, which could induce the transformation between the two forms.

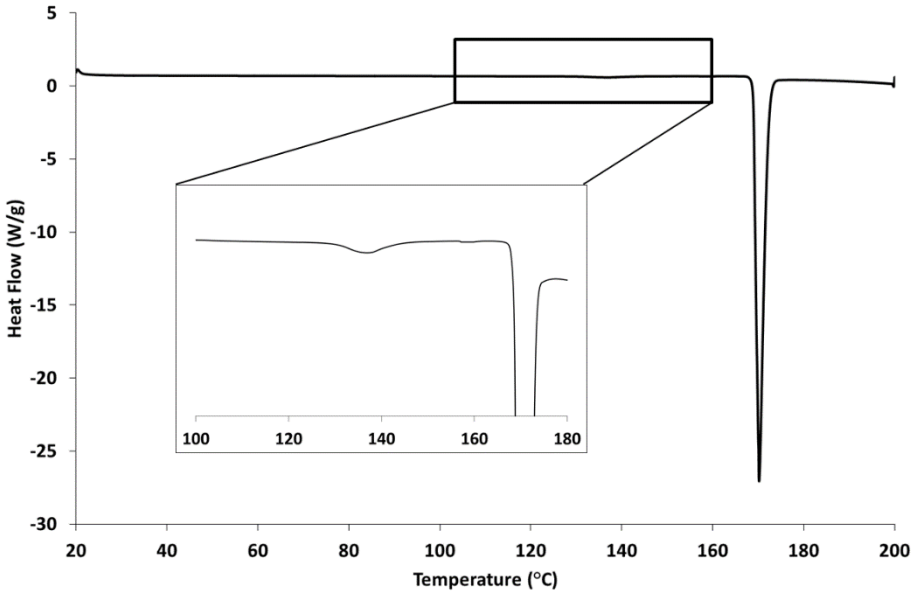

Figure 3.4: DSC trace of PCM, with the transition between 130 and 140 °C highlighted. This subtle transition is best observed using a slow temperature scan rate

Calculation of the Bravais-Friedel-Donnay-Harker (BFDH) morphology for each of the two polymorphic forms of PCM shows that PCM-I adopts equant block crystals with the herringbone arrangement growing perpendicular to the (002) plane, while PCM-II forms a more elongated diamond, again with the hydrogen bonded layers growing perpendicular to the (002) plane (Figure 3.5). It is commonly reported in literature that PCM-I adopts a block like morphology while PCM-II adopts a needle morphology.

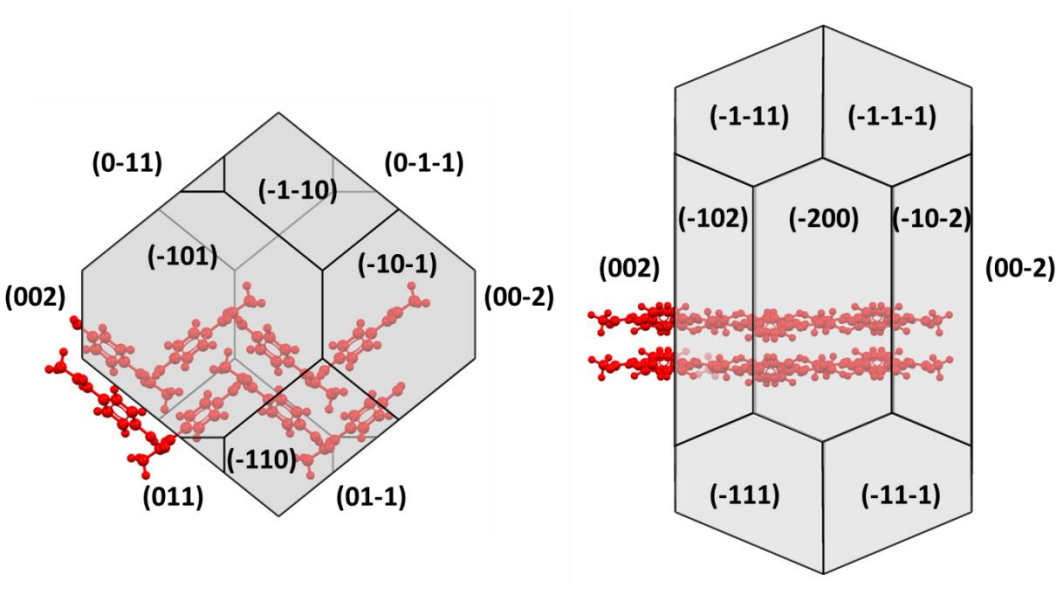

Figure 3.5: BFDH calculated morphology of PCM-I (left) and PCM-II (right)

However, calculations of the BFDH morphology are based on crystallographic parameters and use only knowledge of the unit cell and corresponding symmetry operations; they do not take into account any external factors such as solvent, supersaturation or presence of additives or impurities, nor do they take account of the internal molecular arrangement. As such, a lot of work has been carried out to investigate the effect of different parameters on the morphology of PCM. Prasad *et al* reported the change in morphology of PCM-I from columnar to plate-like upon increasing solution supersaturation.[178] The effect of a variety of structurally similar additives, including p-acetoxyacetanilide (PAA), methyl paraben (MP), 4-acetamidobenzoic acid (4-ABA), metacetamol (MCM) and orthocetamol (OCM), on the morphology of PCM-I has been reported[178-179], with the effects being classified as blocking, docking or disrupting depending on the mechanism of action and uptake of the additive into the PCM crystal. For example, due to the extra steric bulk of the ester group, PAA is a good blocking molecule; it does not have a proton donor to continue the hydrogen bonded chain and so blocks growth along the (002) face. MCM is considered to be a good docking molecule, meaning it can be included within the crystal lattice due its complementary hydrogen bonds to PCM. PAA is also considered to have a disrupting effect on the emerging nucleus, reducing its stability and inhibiting growth.

The differing morphologies of the two polymorphs has allowed for the use of in-line process analytical technologies to monitor the polymorphic transformation upon cooling a saturated solution of PCM. Here, focussed beam reflectance measurement (FBRM) was used to observe the change from a needle-like morphology (characteristic of PCM-II) to an octahedral morphology (characteristic of PCM-I), when crystallised from ethanol.[180]

The layering in PCM-II results in better compaction properties in comparison to PCM-I[82] , while PCM-II also displays increased solubility (Figure 3.6), as determined by the Technobis Crystal 16 (as outlined in Chapter 2). In light of these benefits of PCM-II in terms of solid state properties, it would be advantageous if a method could be established for the large scale production of PCM-II, producing samples that display good stability with respect to the transformation to the stable PCM-I; this has been the aim of this work.

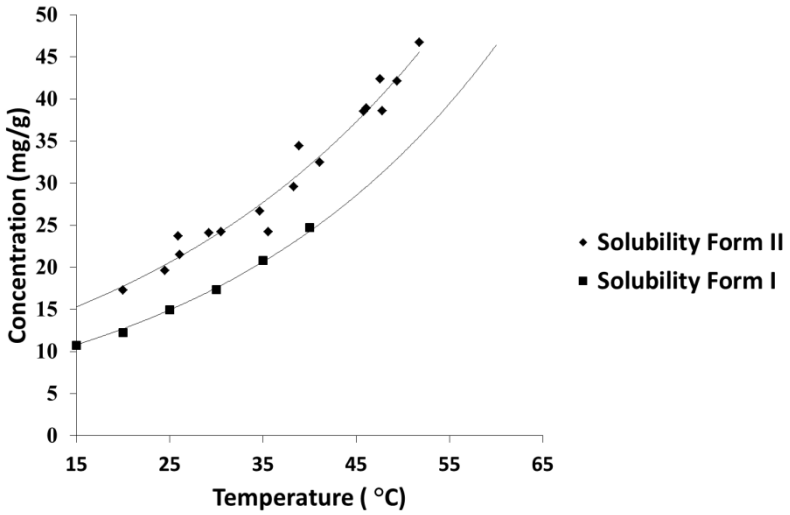

Figure 3.6: Solubility diagram showing the increased aqueous solubility of PCM-II over PCM-I, determined by turbidity measurements in the Technobis Crystal 16

Previous routes to obtaining metastable form II include reaction coupling[181], swift cooling[182], enforcing Ostwald's rule of stages[183], use of polymer additives[80], heterogeneous nucleation[10] and multicomponent "templating" approaches.[104] The last of these has shown the possibility to template form II with a variety of benzoic acid (BA) derivatives; in this context, a template is defined as a co-former included within the crystallisation process that leads to the adoption of a particular polymorphic form of an API, without itself being present in the final crystal structure. However, this was only achieved in an evaporative crystallisation environment. As the final goal is to transfer the production of PCM-II to continuous crystallisation platforms, many of which utilise cooling crystallisation, transfer to a cooling environment is a crucial first step. The work presented here looks at the production of metastable form II, with *p*-substituted halobenzoic acid derivatives (4-bromobenzoic acid (4-BrBA), 4-chlorobenzoic acid (4-ClBA), 4-fluorobenzoic acid (4-FBA)) as templating molecules, in a cooling crystallisation environment. The *p*-substituted benzoic acid derivatives were shown to produce form II most reliably in evaporative studies and so were chosen as initial additives. Here, this designed approach is developed by also using a variety of structurally similar molecules (Figure 3.7), all only previously studied in the relation to their effect on the morphology of PCM-I, as potential templating molecules for PCM-II production. The structurally

similar molecules investigated include metacetamol (MCM), orthocetamol (OCM), *p*-acetanisidide (PACN), methyl paraben (MP), 4-acetamidobenzoic acid (4-ABA) and 3'-amino-4'-methoxyacetanilide (3A4MA) as potential templating molecules for PCM-II production.

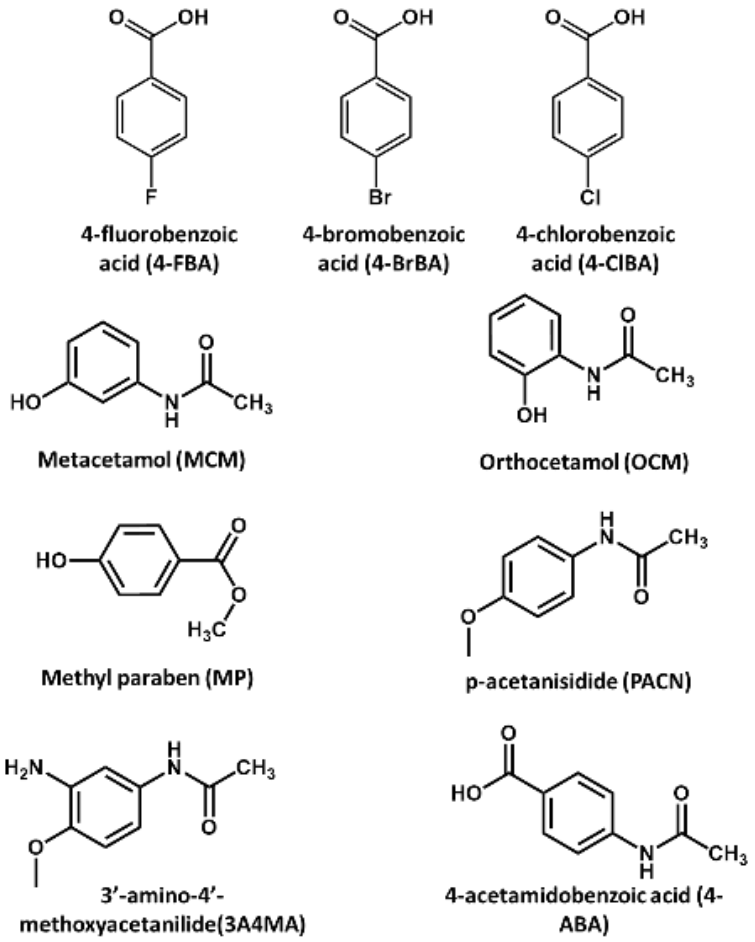

Figure 3.7: The molecular structures of the template molecules employed in this work

3.2 Materials and methods

PCM, 4-BrBA, 4-ClBA, 4-FBA, MP and 4-ABA were purchased from Sigma Aldrich. MCM, OCM, PACN and 3A4MA were purchased from TCI Ltd. All reagents were used without further purification. Laboratory grade solvents purchased from Sigma Aldrich and VWR were used throughout.

3.2.1Solubility measurements

Solubility measurements of PCM, MCM, OCM, 4-FBA, 4-BrBA and 4-ClBA in 60:40 (v/v) H_2O:IPA were carried out using the Technobis Crystal 16 at the 1 ml scale. Vials containing varying concentrations of each component were subjected to a heat-cool cycle at a rate of 0.5 °C min^{-1} with a magnetic bottom stirring rate of 800 rpm. Clear and cloud points were determined using the Crystal Clear software from Avantium Technologies.

3.2.2 Cooling crystallisations

Solubility analysis on paracetamol and the template molecules allowed for experimental design, in particular a cooling profile suitable for the system. The cooling profile used throughout all crystallisations is shown in Figure 3.8.

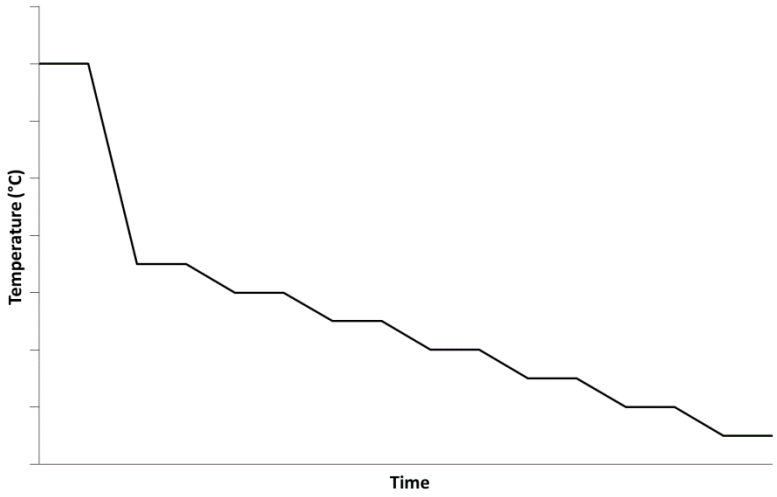

Figure 3.8: The stepped cooling profile employed in cooling crystallisation experiments

Dwelling periods of one hour were used throughout the cooling profile, as shown in Figure 3.8, to allow for equilibration of solution and give more control over the crystallisation process; similar to how induction time measurements are performed, holding a saturated solution at a certain temperature for an extended period of time would allow for nucleation at higher temperatures and aim to reduce the likelihood of unwanted products 'crashing out'.

Cooling crystallisation experiments were performed using the Polar Bear Plus crystalliser from Cambridge Reactor Design. Small scale experiments were all performed with magnetic bottom stirring to agitate the solution, the speed of which was dependent on the template molecule used. Full details of concentrations and experimental parameters are given in sections 3.3, 3.4 and 3.5. Products at the end of the crystallisation were filtered and solids analysed through PXRD analysis.

In each crystallisation performed, a control vial containing PCM in the absence of any template molecule was included. In all cases, the crystallisation carried out in this control vial resulted in the production of PCM-I.

3.2.3 Seeding experiments

Seeding experiments were performed in pure water as solvent in order to reduce the solution mediated phase transformation kinetics, with the aim of stabilising the metastable PCM-II. The

cooling profile employed throughout these seeding experiments is shown in Figure 3.9. A 15 minute hold period was utilised after addition of seeds to check that the added seeds do not dissolve; such dissolution would trigger the solution mediated phase transformation hence resulting in the production of PCM-I.

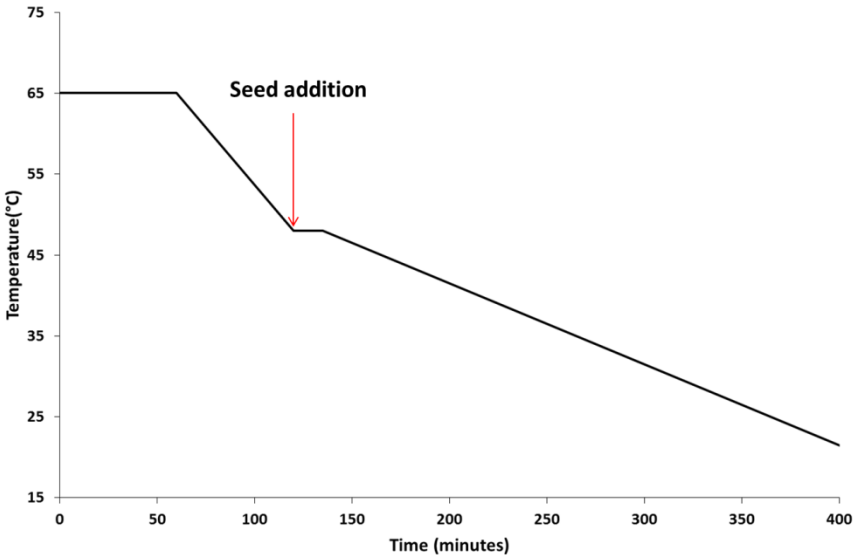

Figure 3.9: The seeding profile employed

A PCM concentration of 35 mg/g of solvent was used throughout all experiments in a 50 ml volume, with an overhead stirring rate of 400 rpm. This concentration of PCM was chosen as it corresponds to a saturated solution of PCM-II in the water solvent system at a temperature of 35 °C. Dry form II seeds were added at the beginning of the hold period and any obvious dissolution observed by eye.

3.2.4 Characterisation techniques

SEM analysis of the solid product from the crystallisations of PCM in presence of 4-FBA and PCM in presence of MCM at small scale was used to visualise crystal morphology more accurately than microscope images. The samples were prepared by vacuum filtration and subsequent drying at room temperature. They were then mounted and stored under vacuum. A Quorum QT Chrome Coater (UK) with a film thickness of 20 nm was used to coat the samples. The images were then obtained via use of the FESEM (JOEL 6301F SEM (Japan) with a Saturn Imaging System (Belgium)). SEM analysis of PCM-II in the presence and absence of metacetamol hydrate was undertaken at AstraZeneca in Macclesfield. Samples were mounted on an aluminium stub with a carbon tab and were gold coated with a Quorum Q150R sputterer to a target film thickness of 10 nm. The images were obtained using a Hitachi TM-1000 with an accelerating voltage of 15 kV.

Variable temperature PXRD (VT-PXRD) analysis was carried out at AstraZeneca in Macclesfield. The samples were mounted on a silicon wafer mount and analysed using a Bruker D8 Advance diffractometer (λ = 1.5418 Å) equipped with a LYNXEYE detector. Samples were measured in reflection geometry in θ - 2θ configuration over the scan range 4° to 40° 2θ with a nominal 0.5 second exposure per 0.02° increment. The effective exposure per step was 96 seconds. The X-rays were generated by a copper long-fine focus tube operated at 40 kV and 40 mA. The sample was heated inside a TTK 450 sample chamber using a TCU 110 Temperature Control Unit, both supplied by Anton-Paar Ltd. The temperature profiles used are shown in Table 3.1 and Table 3.2.

Table 3.1: Experimental parameters for the VT-PXRD study or PCM-II with metacetamol hydrate present

PCM-II + Metacetamol hydrate			
Temperature step	**T_{start} (°C)**	**T_{end} (°C)**	**Heating Rate (°C min^{-1})**
1	25.0	25.0	-
2	25.0	60.0	5
3	60.0	75.0	2
4	75.0	84.0	2
5	84.0	95.0	2
6	95.0	110.0	2
7	110.0	123.0	2
8	123.0	150.0	2
9	150.0	156.0	1
10	156.0	175.0	2
11	175.0	180.0	2

Table 3.2: Experimental parameters for the VT-PXRD of PCM-II

	PCM-II		
Temperature step	**T_{start} (°C)**	**T_{end} (°C)**	**Heating Rate (°C min^{-1})**
1	25.0	25.0	-
2	25.0	77.5	5
3	77.5	89.8	2
4	89.8	98.0	2
5	98.0	107.3	2
6	107.3	113.5	2
7	113.5	120.5	2
8	120.5	146.3	2
9	146.3	151.8	2
10	151.8	159.8	2
11	159.8	172.4	2

3.3 Crystallisation with benzoic acid derivatives

Initial solubility analysis of paracetamol and the 4-substituted halobenzoic acids in 60:40 H_2O:IPA solvent (Figure 3.10) allowed for design of cooling profiles; the 4-substituted derivatives were

chosen as they gave PCM-II most reliably and reproducibly in evaporative studies. [104] Due to the fast transformation time from PCM-II to PCM-I in this solvent system, turbidimetric or gravimetric solubility analysis could not be performed on PCM-II. As such, the solubility of PCM-II was calculated through the use of ratios[144], based on the solubility of both PCM-I and PCM-II in water and the solubility of PCM-I in 60:40 H_2O:IPA. The ratio between the two lines of best fit in H_2O was found to be related to temperature (x) through the expression

$$\text{Ratio}\,\frac{\text{II}}{\text{I}} = 1.45e^{-0.0027x}$$

Substitution of x at different temperatures and addition to the concentration value of PCM-I in 60:40 H_2O:IPA results in the solubility curve shown in Figure 3.10.

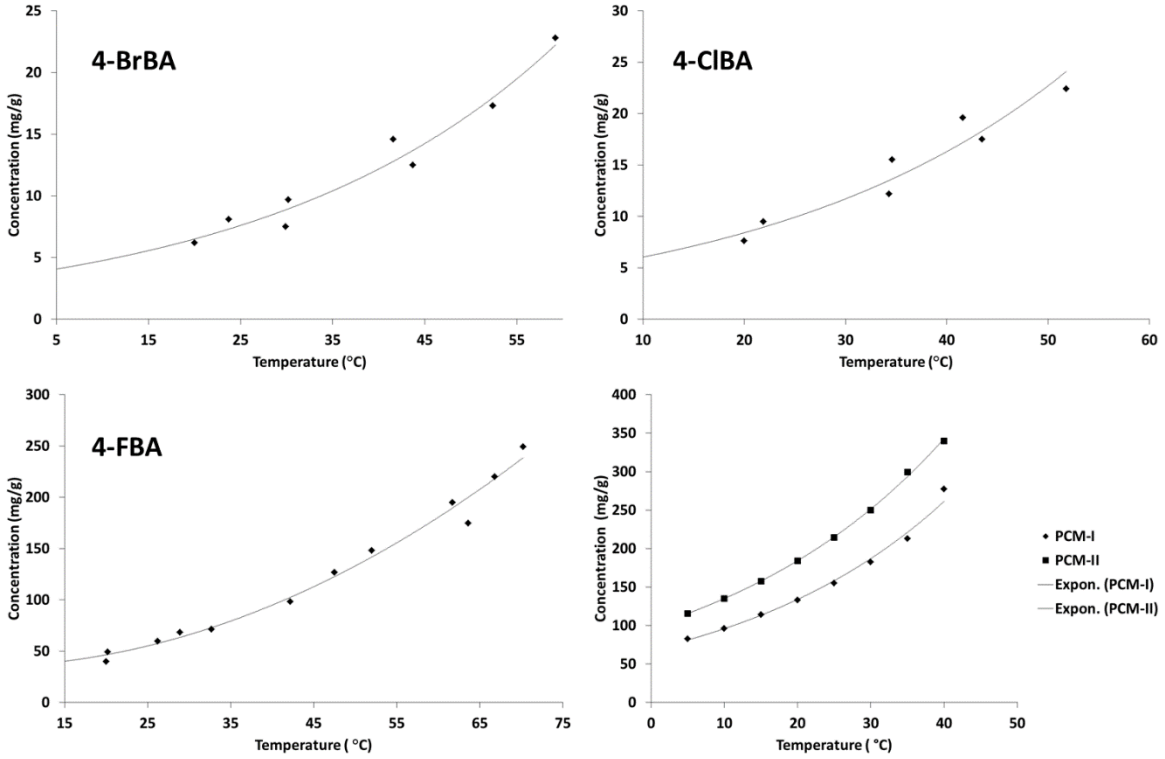

Figure 3.10: Solubility curves for 4-BrBA, 4-ClBA, 4-FBA and both polymorphs of PCM in a 60:40 H_2O:IPA solvent system

Cooling crystallisations were designed to ensure the co-former molecule remains in solution at the end of the crystallisation, with the concentrations of co-former molecules chosen to correspond to an undersaturated solution at the final temperature of 5 °C (i.e. for 4-FBA no concentrations above 40 mg/g were used, for 4-BrBA and 4-ClBA no concentrations above 5 mg/g were used).

Initial crystallisations using a concentration of PCM of 350 mg/g gave a solid product of PCM-I. However, a pink hue of the liquor in the vial, and its absence in the blank crystallisation vial, prompted this to be decanted and evaporated. Analysis of the evaporated product showed the

presence of PCM-II. For subsequent experiments, the concentration of PCM was decreased in order to decrease the supersaturation ratio of the system, allowing for more controlled nucleation; the concentration of PCM was chosen to ensure the system still remained supersaturated with respect to PCM-II in order to try and induce crystallisation of this polymorphic form.

Table 3.3: Cooling crystallisation conditions that have produced PCM-II with benzoic acid derivatives

Experiment set	Concentration PCM (mg/g)	Co-former	Wt.% co-former	Stirring speed (rpm)	Cooling rate (°C min^{-1})	Scale (ml)
1	300	4-ClBA	1.0	800	0.02	1
2	300	4-ClBA	1.7, 2.3, 4.0	800	0.02	1
3	250	4-BrBA	0.4, 1.6, 2.4	800	0.02	1
4	250	4-ClBA	1.2	800	0.02	1
5	250	4-BrBA	1.2, 2.0, 2.4	400	0.02	1
6	250	4-ClBA	1.2, 1.6	400	0.02	1
7	250	4-FBA	4.8	400	0.02	1
8	250	4-FBA	0.8, 2.0, 2.8	800	0.05	1
9	250	4-ClBA	0.6	800	0.05	1
10	250	4-FBA	3.4	400	0.02	1

Investigations were conducted with all three 4-substituted derivatives in varying concentrations, with varying PCM concentrations, stirring speeds and cooling rate, with Table 3.3 highlighting the conditions through which PCM-II was produced. The highlighted rows indicate conditions under which the production of PCM-II is fully reproducible; these conditions were used to produce enough PCM-II for solubility analysis. The production of PCM-II was confirmed through PXRD analysis and the absence of any co-former molecule in the solid product through DSC and NMR analysis.

The poor reproducibility of some of the experiments can be attributed to the small vials in which the crystallisations were carried out. In these small volumes, presence of varying amounts of impurities, such as dust or surface imperfections, between vials would have a greater effect than in a larger bulk solution where on average these would even out.

In general, it can be seen that those experiments where 4-BrBA and 4-ClBA were used, which display considerably lower solubility in comparison to 4-FBA, a higher stirring rate of 800 rpm was needed in order to direct the formation of PCM-II. The use of these higher stirring rates can be attributed to the fact that these conditions provide greater mass transfer required for these lower

concentrations. For cases where this does not hold true (Experiment Set 5 and 6), it can be seen that PCM-II production was only achievable at the higher concentrations of co-former molecules, where it had been seen at lower concentrations under the same conditions with a faster stirring rate.

The cooling rate used here for the production of PCM-II would not be conducive to transfer into continuous crystallisation platforms; to achieve a cooling rate this slow in a continuous crystallisation environment would require very long crystallisers consisting of many straights (in the case of the COBC) or vessels (in the case of an MSMPR). As such, investigations with faster cooling rates of 0.1 °C min^{-1} and 1 °C min^{-1} were performed, however all experimental parameters investigated with these cooling rates resulted in the production of pure PCM-I.

3.3.1 Seeding experiments

Attempted scale-up of the production of PCM-II using halobenzoic acid template molecules has been largely unsuccessful. Experiments were performed at both 5 ml and 10 ml scale, however only the production of PCM-I was observed under all conditions attempted. It can be postulated that this is due to the low solubility of the template molecules combined with the naturally reduced mass transfer experienced upon scale-up.

As such, seeding experiments at the 50 ml scale, in both the absence and presence of template molecule, were conducted to investigate another method for large-scale production of PCM-II.

Table 3.4: Experimental parameters investigated for seeding experiments. For templated experiments within the Table, 4-FBA was used

Seed loading (%)	Template present (Y/N)	Cooling rate before seed addition (°C min^{-1})	Cooling rate after seed addition (°C min^{-1})	Seeding temperature (°C)	Nucleation time (mins)	Solid product
5	N	0.5	0.1	55	7	Form I
5	N	0.5	0.1	53	4	Form I
5	Y	0.5	0.1	48	5	Form I
10	Y	0.5	0.1	46.5	0	Form I
5	Y	0.3	0.1	48.5	2	Form I
5	Y	0.3	0.1	48.0	6	Form I
5	Y	0.3	0.1	47.8	2	Form I
5	Y	0.3	0.1	47.9	3	Form I

Table 3.4 highlights the experimental parameters investigated for the seeding experiments. The two experiments performed in the absence of any templating molecule were unsuccessful, yielding only PCM-I and so succeeding experiments were performed with 4-FBA as a template molecule in a 1:30 (4-FBA:PCM) ratio; this ratio ensured that no 4-FBA was present in the final solid product. Initial experiments with a 5 % seed loading showed obvious seed dissolution followed by visible crystallisation in the hold period, indicating the seed was added too early and the supersaturation generated by dissolution resulted in crystallisation. PXRD analysis on the filtered solid product showed the production of PCM-I. As such, the seed loading was increased to 10 % and the temperature of seed addition decreased. However, although no visible seed dissolution was observed, this resulted in instantaneous nucleation. It can be suggested that the seed was added at the point of highest supersaturation in the system, close to nucleation, resulting in this instantaneous nucleation. Again analysis of filtered solid product showed the presence of PCM-I. For subsequent experiments, the cooling rate before seed addition was decreased from 0.5 °C min^{-1} to 0.3 °C min^{-1}; it was hoped that this slower cooling rate would allow the solution to equilibrate more to give more control over the point of nucleation in the system and aid with addition of seeds at the correct temperature. However, four experiments with seed addition at different temperatures all resulted in the production of pure PCM-I.

The lack of success in producing PCM-II in attempted scale-up crystallisations with benzoic acid derivatives as templating molecules prompted work with some structurally similar template molecules.

3.4 Crystallisation with metacetamol

Metacetamol is a structural isomer of paracetamol and displays a much higher solubility in a 60:40 H_2O:IPA solvent system than the benzoic acid derivatives; the solubility curves in two different solvent systems are shown in Figure 3.11. It was hoped that this solubility increase would mean higher concentrations of template molecule could be used, aiding in the scaled-up production of PCM-II, but still achieving the desired outcome of no template molecule being present in the final solid product.

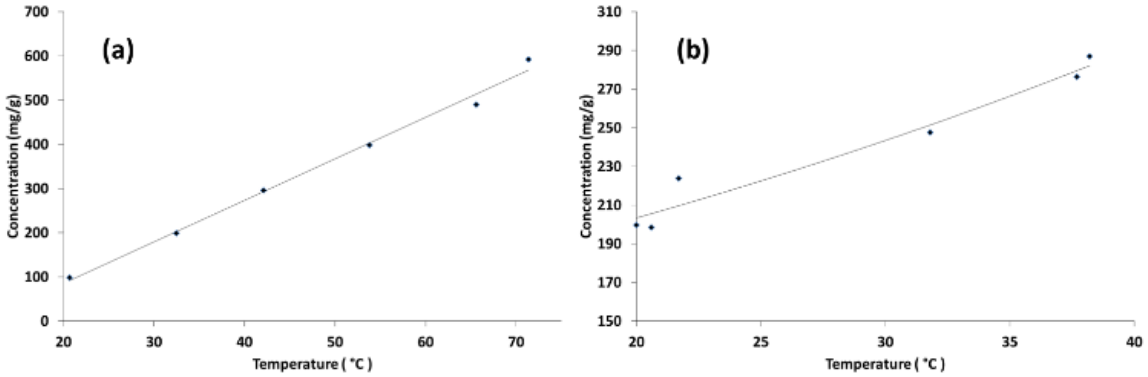

Figure 3.11: Solubility curves of metacetamol in (a) 60:40 H_2O:IPA and (b) EtOH

As with the halobenzoic acid crystallisations, a concentration of PCM of 250 mg/g was used, and concentrations of metacetamol again chosen so that this component was undersaturated with respect to the solvent system. Initial experiments at the 1 ml scale allowed for determination of which solvents and concentrations of MCM were likely to produce PCM-II and these were used to inform future larger scale experiments. These initial experiments investigated three different solvent systems (60:40 H_2O:IPA, EtOH and IPA) with percentages of MCM between 1 and 25 w/w %. PCM-II was produced from both 60:40 H_2O:IPA and EtOH, but its appearance was never observed in the product from IPA; use of IPA was therefore not investigated further after these experiments.

A systematic study was conducted at the 10 ml scale to investigate the reproducibility of the production of PCM-II in the two selected solvent systems under varying crystallisation conditions. Table 3.5 highlights the experimental conditions under which PCM-II has been obtained reproducibly.

Table 3.5: Crystallisation conditions for the reproducible production of PCM-II using MCM as a template molecule

Solvent	Cooling rate (°C min^{-1})	Cooling profile	Wt.% MCM
60:40 H_2O:IPA	0.02	Stepped	10, 25
EtOH	0.02	Stepped	5, 10, 25
60:40 H_2O:IPA	0.2	Stepped	5, 10, 15, 25
EtOH	0.2	Stepped	5, 10, 15, 25
60:40 H_2O:IPA	1	Stepped	10, 15, 20, 25
EtOH	1	Stepped	10, 15, 20, 25
60:40 H_2O:IPA	1	Linear	10, 20, 25
EtOH	1	Linear	10, 20, 25

The reproducible production of PCM-II was observed through a variety of crystallisation conditions. Those crystallisations performed with a cooling rate of 1 °C min^{-1} are of most interest as this cooling

rate would be more conducive to what would be achievable in a continuous crystalliser. At higher percentages of metacetamol, some vials showed the presence of small quantities of an extra crystalline form within the PCM-II solid (Figure 3.12); this extra form was confirmed by PXRD to be metacetamol hydrate (MCM·H_2O), as reported by Pulham *et al.*[184] Despite water being used in one of the solvent systems, the hydrate was more prevalent in the ethanol crystallisations. The presence of MCM·H_2O was eliminated through truncation of the cooling profile at a temperature of 20 °C.

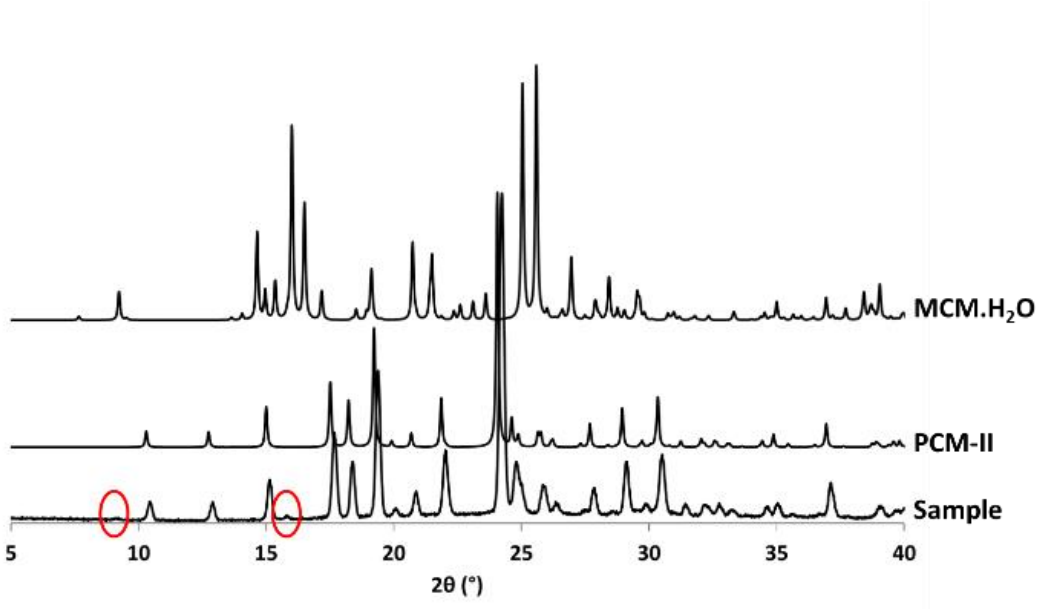

Figure 3.12: PXRD analysis confirming the presence of predominately PCM-II, with circled peaks showing the presence of small quantities of MCM.H_2O. The y-axis displays intensity in arbitrary units.

The ability to obtain PCM-II through a linear cooling profile is of great interest in terms of its transfer to continuous crystallisation platforms. However, as a consequence of not having the periods of dwelling to allow the solution to equilibrate, combined with a widening of the metastable zone width (MSZW) in the presence of MCM, crystallisation did not occur until lower temperatures. This effective crash cooling resulted in the crystallisation of MCM in the solid product (Figure 3.13). It can be suggested that the control exerted through the stepped cooling profile is needed to direct the formation of MCM·H_2O, which is not exerted through a quick linear cooling profile. As such, for scale-up experiments (see Chapter 4), the stepped cooling profile was employed in order to mitigate against the crystallisation of either MCM or MCM·H_2O.

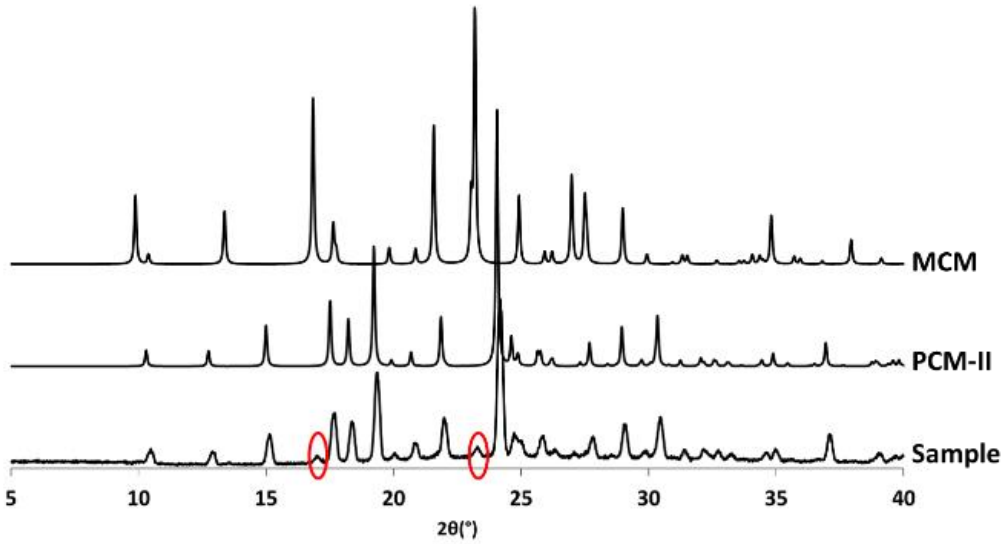

Figure 3.13: PXRD analysis showing the presence of small quantities of MCM from linear cooling experiments (circled in red). The y-axis displays relative intensity in arbitrary units.

Analysis of the yields of the crystallisations showed lower yields from the ethanol solvent system: an expected result due the enhanced solubility of PCM in this solvent. The yields from ethanol crystallisations were typically around 35 %, with those from 60:40 H_2O:IPA ranging between 60 and 70 % (Full experimental yields are shown in Appendix A3). The lower yields and the higher propensity for hydrate formation in an ethanol solvent system meant that investigations into the scaling potential of PCM-II production with MCM as a template were conducted in a 60:40 H_2O:IPA solvent system (see Chapter 4).

Use of DSC, PXRD, SCXRD and NMR spectroscopy confirm the absence of any MCM·H_2O in the solid sample. SCXRD analysis was performed to confirm whether any MCM has been included into the crystal lattice, a distinct possibility owing to the structural similarity of PCM and MCM. Single crystals from crystallisations were analysed by a full structure determination. The refinement parameters are good and the crystal structure shows no extra electron density that could correspond to a solid solution being formed (Figure 3.14).

R_{int}	0.027
Completeness (%)	99.8
GooF	1.068
R_1 (observed)	0.0411
R_1 (all)	0.0547
wR_2 (all)	0.0989

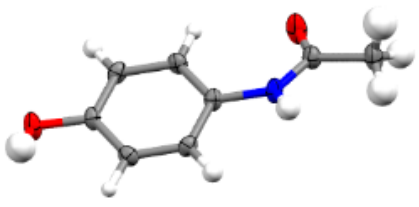

Figure 3.14: Refinement parameters and a molecule of paracetamol showing small thermal ellipsoids at a 50% probability level

Interestingly, evaporative crystallisation of PCM with MCM in a 1:1 ratio in five different solvents (ethanol, methanol, IPA, acetonitrile and acetone) yielded a physical mixture of PCM-I and MCM (Figure 3.15). It can be suggested that this is the case due to the static nature of an evaporative crystallisation vial; cooling crystallisation experiments demonstrated the importance of efficient mixing within the reaction vessel in order to direct the formation of PCM-II.

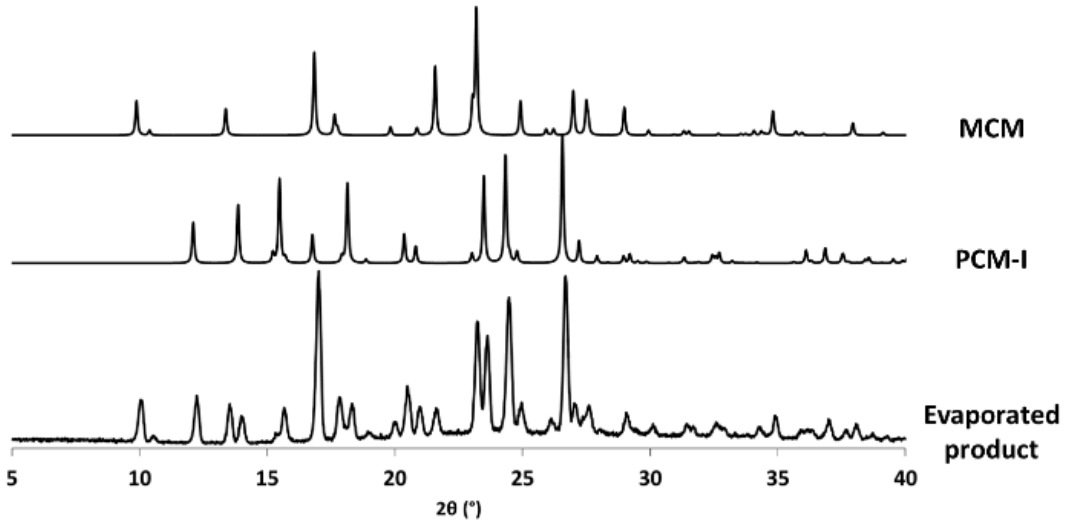

Figure 3.15: PXRD analysis of PCM/MCM evaporative crystallisations showing the formation of a physical mixture of PCM-I and MCM. The y-axis displays relative intensity in arbitrary units.

Investigations were also conducted in order to try to 'reverse' the templating effect, i.e. template metacetamol form II (MCM-II) with paracetamol, as the literature shows that MCM-II has similar characteristics to those of PCM-II.[184] Due to their similar solubilities in the 60:40 H_2O:IPA solvent system, the concentration of MCM of 300 mg/g was used with wt.% of PCM between 5 and 25 %. The dominant product in all crystallisations was MCM-I. However, at higher percentages of PCM, there are peaks evident in the PXRD patterns that correspond to the formation of PCM-II (Figure 3.16). Further experiments were performed with an increased MCM concentration of 400 mg/g, however this yielded the same result as those with the lower MCM concentration, with no evidence of MCM-II in the final solid product.

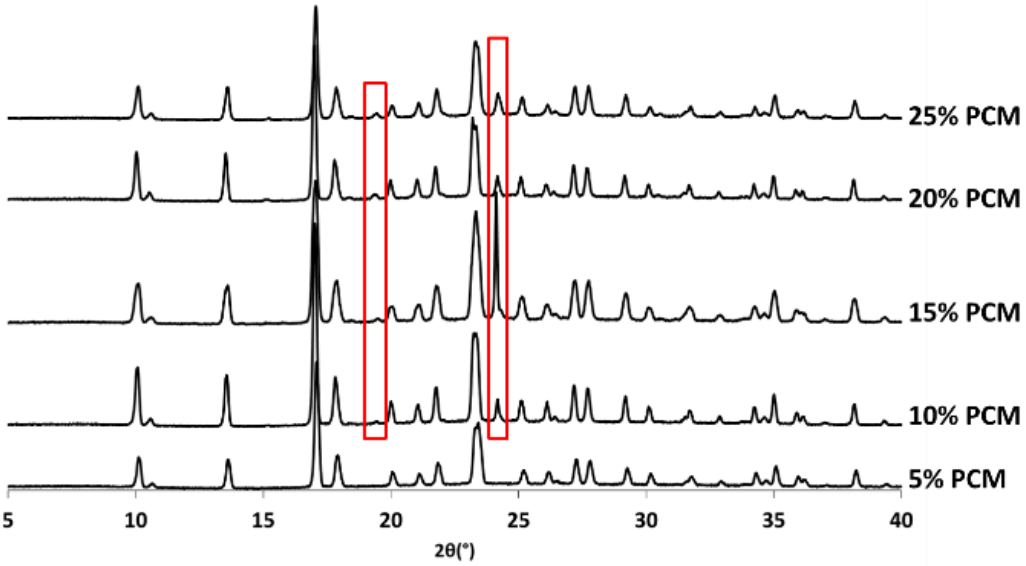

Figure 3.16: PXRD patterns showing the formation of some PCM-II (peaks in red boxes) within MCM samples. The y-axis displays relative intensity in arbitrary units.

3.4.1 Metacetamol hydrate (MCM·H_2O)

The appearance of small quantities of metacetamol hydrate (MCM·H_2O) in some of the crystallisation products prompted further investigations into its presence and properties by using analytical techniques. The presence of MCM·H_2O within PCM-II samples resulted in a DSC trace as shown in Figure 3.17.

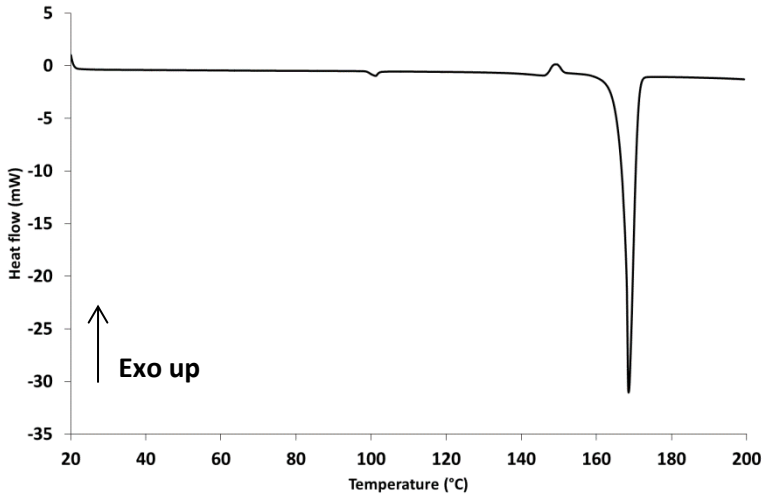

Figure 3.17: DSC trace of a PCM-II sample with trace amounts of MCM·H_2O present

The endothermic peak at 100 °C can be attributed to loss of water; however, the origin of the event at 150 °C (endotherm followed directly by exotherm) was unclear. As such VT-PXRD analysis was performed on a sample of pure PCM-II (Figure 3.18) and a sample of PCM-II with metacetamol hydrate present (Figure 3.19).

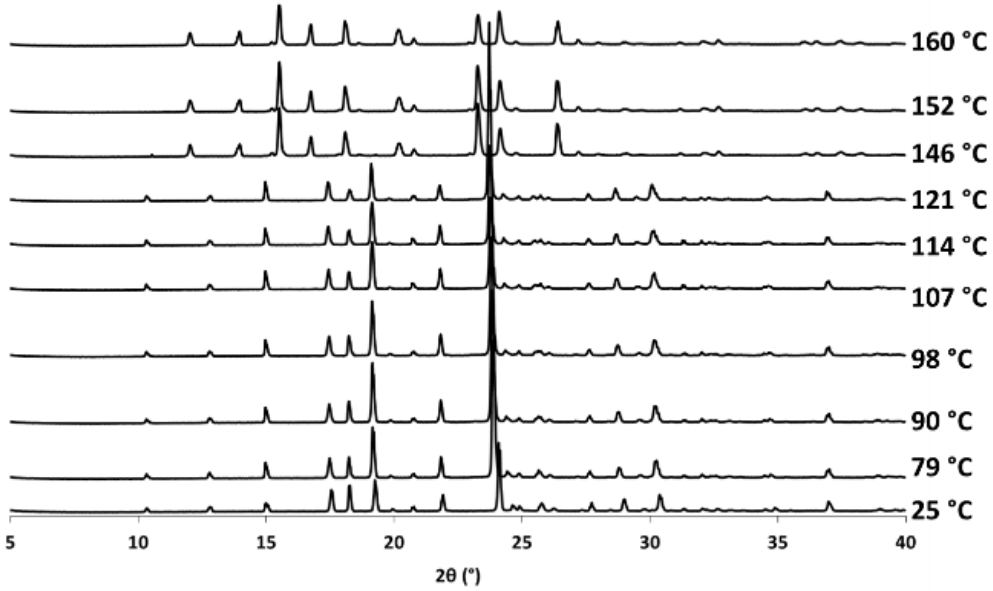

Figure 3.18: VT-PXRD of a sample of pure PCM-II showing the transition from PCM-II to PCM-I between 121 °C and 146 °C. The y-axis shows relative intensity in arbitrary units.

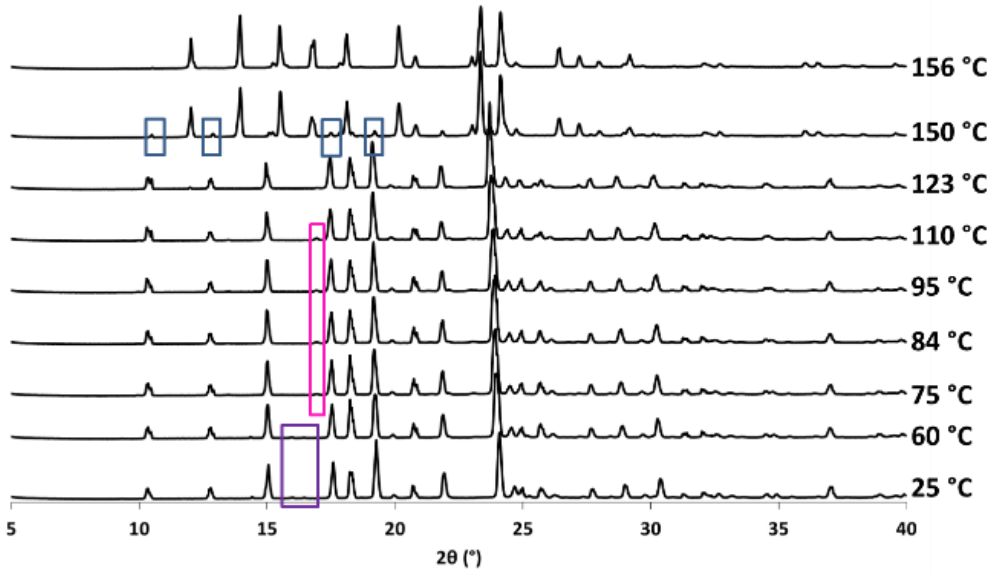

Figure 3.19: VT-PXRD for a PCM-II containing small amounts of MCM·H_2O. The y-axis displays relative intensity in arbitrary units.

Figure 3.18 clearly shows the phase transition from PCM-II to PCM-I between 121 °C and 146 °C. However, the VT-PXRD for PCM-II with some MCM·H_2O present is slightly more complicated. At room temperature there are two peaks at 2θ = 15.5° and 2θ = 16° (shown inside the purple box in Figure 3.19) that correspond to MCM·H_2O. Upon heating beyond 60 °C, these peaks are lost and there is the appearance of a peak at 2θ = 17° (shown inside the pink box in Figure 3.19); these peaks correspond to MCM. Therefore, it can be concluded that this is the dehydration step. Between 123 °C and 150 °C, the metacetamol melts and there is a partial transformation from PCM-II to

PCM-I. Unlike in the sample with no hydrate present, where this transformation is complete, there are still a few PCM-II peaks present in the PXRD pattern at 150 °C (shown inside the blue boxes in Figure 3.19). It could be suggested that the metacetamol melt acts to stabilise the PCM-II against the transformation to PCM-I. The transformation is only complete when extra energy is supplied to the system by further heating; once heated beyond 150 °C the transformation is driven to completion and the remaining sample is pure PCM-I, which then melts at ~ 170 °C.

3.4.2 SEM

SEM image analysis was undertaken in order to compare the morphologies of the samples of PCM-II produced with each individual template molecule; the shape of the crystals could help to elucidate a mechanism through which the template molecule acts, that affects the growth of PCM-II. Figure 3.20 shows the comparison between the samples of PCM-II produced in the presence of 4-FBA and MCM. It can be seen that crystals produced in the presence of 4-FBA are more elongated than those produced in the presence of MCM, which display a more block-like morphology. Block crystals are more favourable in terms of ease of downstream processing steps[185] and so use of MCM to produce PCM-II is again advantageous; samples of PCM-II produced in the absence of any template molecules have been reported to adopt a needle like morphology. The varying sizes of the crystals from each sample can be attributed to the use of magnetic bottom stirring in the crystallisations and its corresponding grinding motion, leading to fracturing of the forming crystals.[186-187]

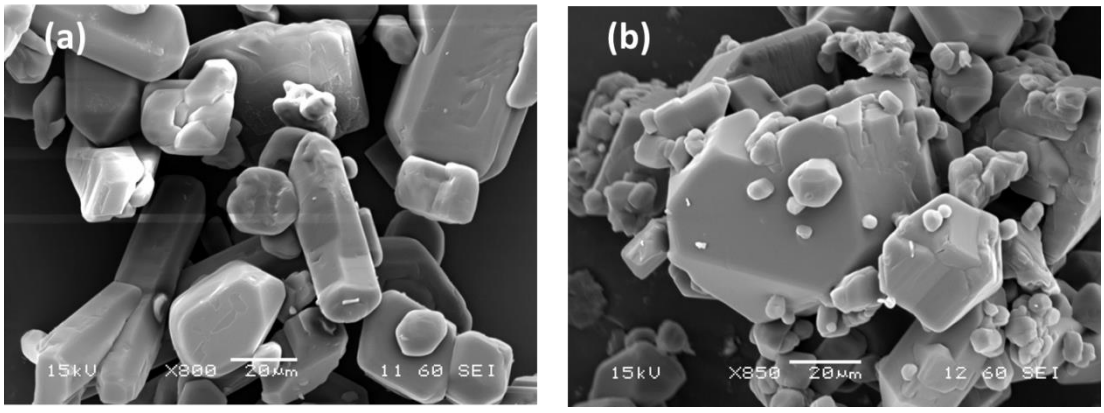

Figure 3.20: SEM images showing the morphology of samples produced in the presence of (a) 4-FBA and (b) MCM (both from a 60:40 H_2O:IPA solvent system)

SEM analysis was also used to compare any morphological differences between samples of pure PCM-II and samples of PCM-II that contained low levels of MCM·H_2O (Figure 3.21). The samples analysed were produced from crystallisations on the 100 ml scale (the details of which will be outlined in Chapter 4).

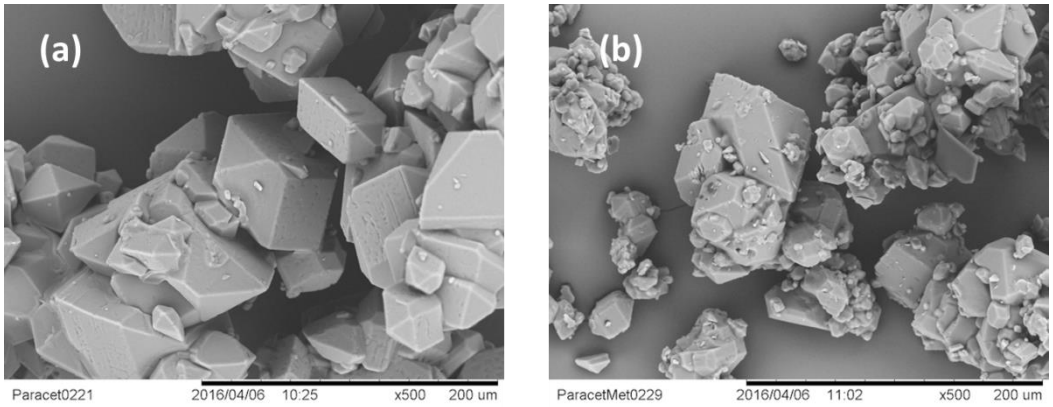

Figure 3.21: SEM images showing the morphology of samples produced for samples of (a) pure PCM-II and (b) PCM-II with small quantities of MCM·H_2O

It can be seen from Figure 3.21 that samples of pure PCM-II adopt a block, prismatic morphology. This same morphology is evident in samples that contain MCM·H_2O, however on the surface of these crystals are smaller crystals. It can be postulated that these crystals are metacetamol hydrate. It is reported in literature that metacetamol acts as a 'docking' molecule[178-179], adsorbing onto the growing crystal surface, further supporting the fact that these crystals could be MCM·H_2O. A technique such as Raman mapping of the surface would be required to confirm this.

3.5 Crystallisation with other structurally related compounds

Owing to the success of MCM as a templating molecule for PCM-II production, a variety of other structurally similar molecules to PCM were investigated for their templating abilities. Initial work was carried out with orthocetamol (OCM) at the 1 ml scale; much of this work was performed by L. Wayment (MChem 2015/16) under the direction of the author. Solubility analysis on OCM was performed in three solvent systems (Figure 3.22) to allow determination of the concentrations to be used for the templating investigations. Initially a slow cooling rate of 0.02 °C min^{-1} was employed with 400 rpm magnetic bottom stirring. Weight percentages of OCM (as a proportion of the weight of PCM) from 1.2-4 % for 60:40 H_2O:IPA, 2-6 % for IPA and 1-6 % for EtOH were initially investigated.

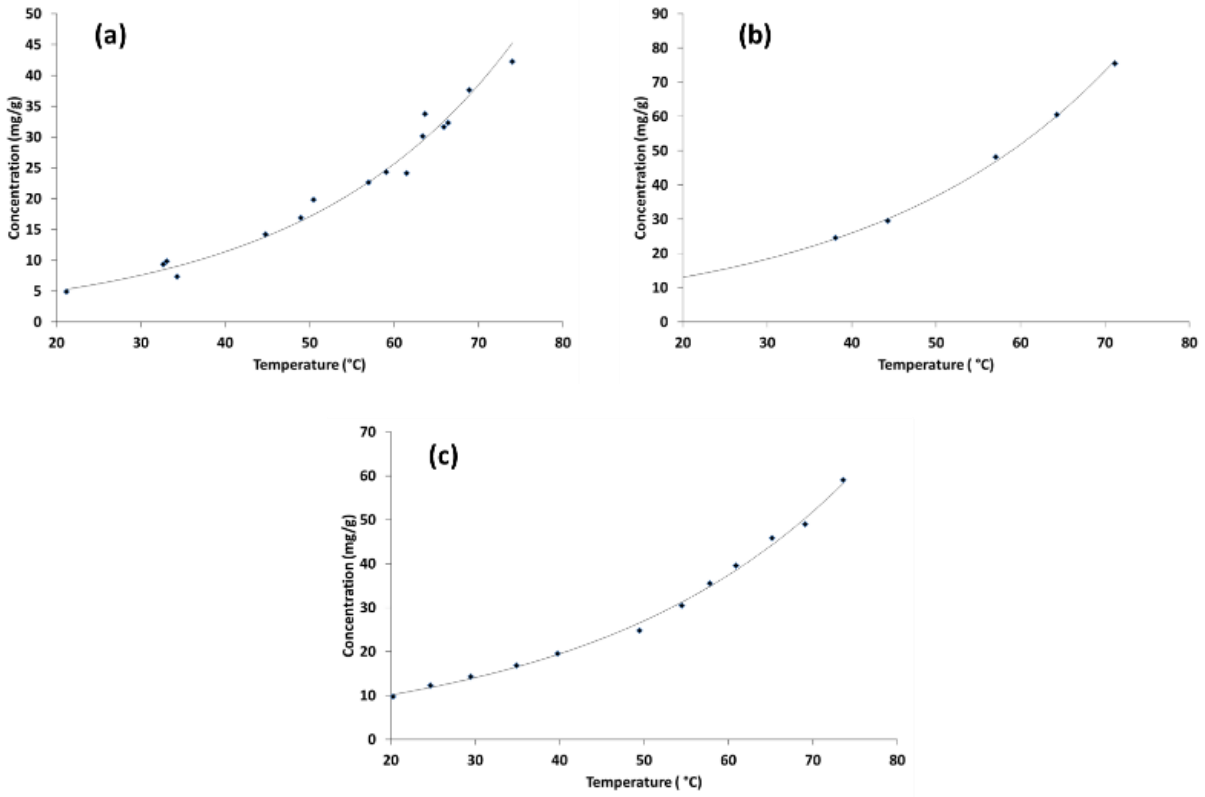

Figure 3.22: Solubility curves for OCM in (a) 60:40 H_2O:IPA, (b) EtOH and (c) IPA solvent systems

The use of 60:40 H_2O:IPA as solvent combined with both 2 % and 3 % OCM as a template resulted in the production of a mixture of PCM-II and PCM-I, as confirmed through PXRD analysis (Figure 3.23).

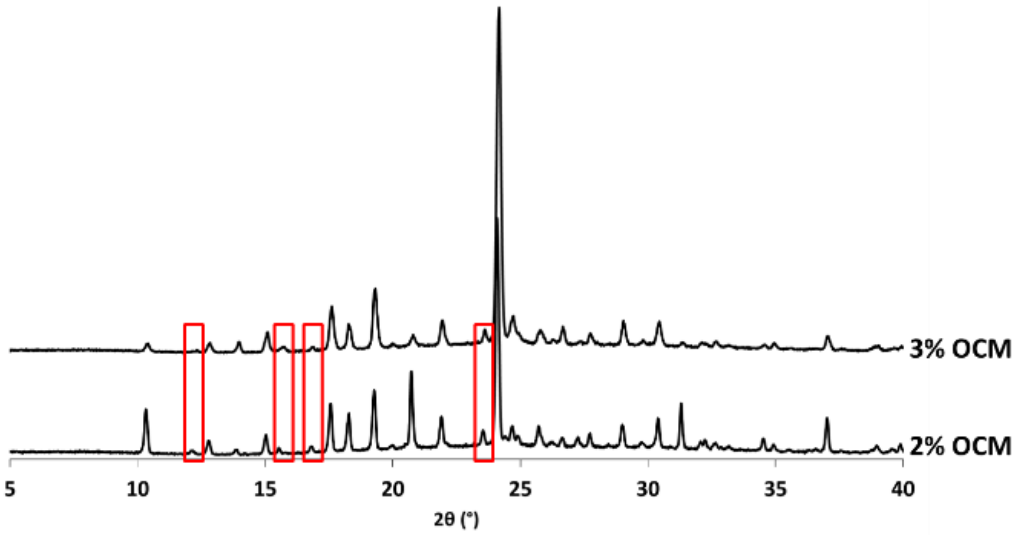

Figure 3.23: PXRD analysis showing a mixture of PCM-II and PCM-I being formed with 2 % and 3 % OCM (the peaks boxed in red are those that correspond to PCM-I). The y-axis displays relative intensity in arbitrary units.

For succeeding experiments, the stepped cooling profile was truncated at a temperature of 20 °C to try to mitigate the formation of PCM-I; if the system was crystallising at a higher temperature and being left until 5 °C for filtration, this period of dwelling could result in the solution mediated phase transformation being initiated. Weight percentages of OCM of 2 %, 2.4 %, 2.8 % and 3 %, each in triplicate, were subjected to a 70-20 °C stepped cool at a rate of 0.02 °C min^{-1}. The three vials containing 2.4 % OCM all gave PCM-II, with no trace of PCM-I in the solid product. Despite crystallisations being performed on the same scale, the two concentrations of OCM (2 % and 3 %) that previously gave PCM-II, albeit with small quantities of PCM-I, reproducibly gave PCM-I in this set of experiments. Using such low percentages of OCM on a small scale can result in inaccuracies in weighing, combined with difficulties in reproducibility on the small-scale, as explained previously. These inaccuracies could account for the difference in results from this set of experiments.

The slow cooling rate of 0.02 °C min^{-1} used in these experiments is not conducive to transfer to continuous crystallisation platforms and as such investigations with a faster cooling rate of 0.2 °C min^{-1} were undertaken. Again, weight percentages of OCM of 2 %, 2.4 %, 2.8 % and 3 %, each in triplicate, were subjected to a stepped cooling profile. Here, the use of 2.4 % OCM resulted in a mixture of PCM-II and PCM-I, with 2.8 % OCM giving samples of pure PCM-II (Figure 3.24), within the limits of detection of PXRD. However, reproducibility of these results has been poor and further experiments would be required to fine-tune the conditions suitable for the production of PCM-II reproducibly; this will be the subject of future work.

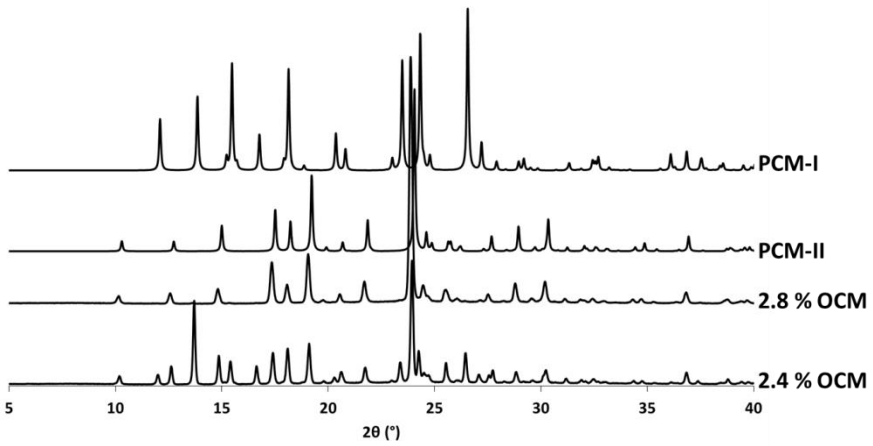

Figure 3.24: PXRD analysis confirming the production of a mixture or PCM-II and PCM-I with 2.4 % OCM, but the production of pure PCM-II with 2.8 % OCM. The y-axis displays relative intensity in arbitrary units.

Attempted scale-up of the templated production of PCM-II using OCM as a template molecule have been unsuccessful, encountering the same combined low solubility and poor mass transfer effects as was found for the benzoic acid derivatives described above.

As such, investigations were conducted with other structurally similar, size-matched components to PCM: p-acetanisidide (PACN), 3'-amino-4'-methoxyacetanilide (3A4MA), 4-acetamidobenzoic acid (4ABA) and methyl paraben (MP). Much of this work was carried out by S. Wright (MChem 2016/17) under the supervision of the author. Many of the compounds investigated have been shown to affect the morphology of PCM-I in low concentrations, but their use as additives to encourage the production of PCM-II is unreported. Due to equipment availability, solubility analysis was unable to be performed on these compounds and so concentrations of template molecules were chosen on a trial and error basis after initial crude solubility studies. Owing to previous problems experienced with transfer from the 1 ml solvent scale to higher volumes in larger vessels, all initial crystallisations were carried out at the 3 ml scale. Further, due to time constraints and the eventual goal of scaled production, very slow cooling rates were not examined in this work and were limited to 1 °C min^{-1} and 0.1 °C min^{-1}. Initial crystallisations utilised weight percentages (of the mass of PCM) of the template molecules between 5 and 25 %. The majority of these crystallisations resulted in the production of pure PCM-I, with the exception of MP that showed some PXRD peaks characteristic of another crystalline form. These peaks did not correspond to PCM-II or MP and it is possible that a new molecular complex may have been formed. As such, evaporative crystallisation experiments containing PCM and MP in varying ratios, in different solvent systems were set up and the products analysed. However, under the conditions investigated, all crystallisations yielded one of the two starting materials. The origin of these extra peaks is subject of future work.

For succeeding experiments, the concentrations of each of the template molecules were increased, examining percentages between 30 and 60 %. Under all conditions examined, the use of PACN, 4-ABA and MP has resulted in the production of PCM-I with some template molecule in the resulting solid product; the presence of these peaks in the PXRD meant the concentrations of these components could not be increased any further. However, use of 40 % 3A4MA combined with a cooling rate of 1 °C min^{-1} resulted in the production of PCM-II with some peaks in the PXRD from the starting material and no evidence for the presence of PCM-I (Figure 3.25).

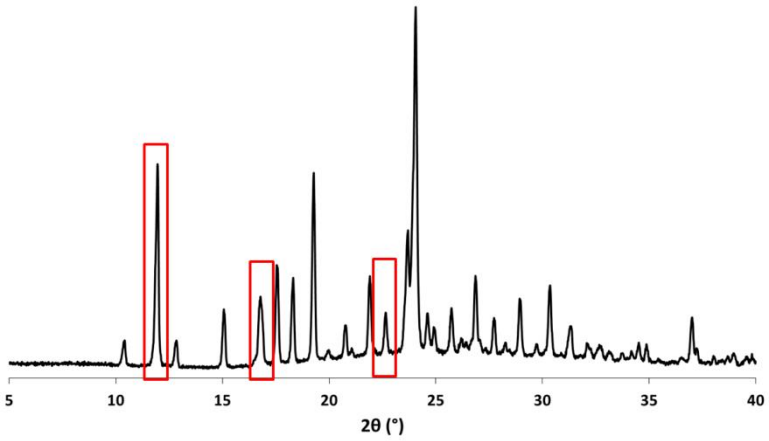

Figure 3.25: Production of PCM-II in the presence of 3A4MA as a template, with peaks from this template boxed in red. The y-axis displays relative intensity in arbitrary units.

Reproducibility of the production of PCM-II on the 3 ml scale was investigated by examining the concentration range between 35 and 45 % of 3A4MA. In order to mitigate the crystallisation of 3A4MA, initial crystallisations were cooled to 25 °C (instead of 20 °C as in previous crystallisations), and were left stirring at this temperature for a period of 2 hours until crystallisation occurred. Analysis of the product showed, instead of PCM-II, the production of pure PCM-I in the absence of any 3A4MA. It can be suggested that by forcing crystallisation at 25 °C this resulted in a faster solution mediated phase transition (SMPT) to PCM-I and PCM-II was unable to be stabilised. As such, the same crystallisations were repeated, but instead truncating the cooling profile at a temperature of 20 °C. Analysis of the powder produced from these experiments showed the production of PCM-II at percentages of 3A4MA of 35 % and 40 % thus supporting the interpretation that the SMPT from PCM-II to PCM-I is suppressed at this lower temperature. However, small quantities of the template molecule were detectable in the product through PXRD analysis. DSC analysis of this sample shows a similar behaviour to that observed from the product containing metacetamol hydrate (Figure 3.26).

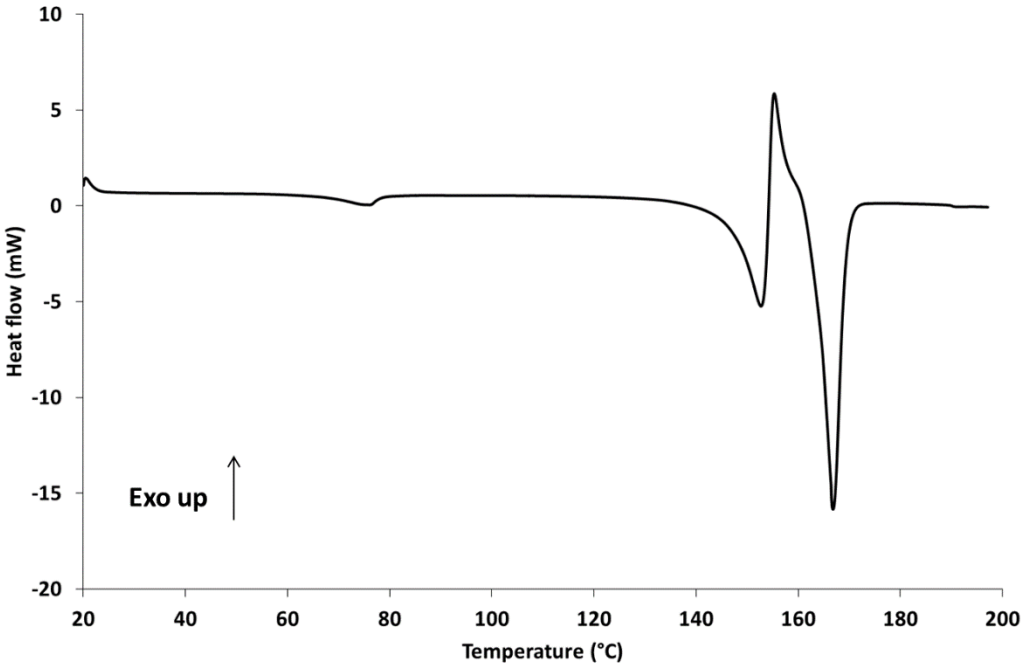

Figure 3.26: DSC trace of a sample of PCM with some 3A4MA present

VT-PXRD was also performed on the sample at AstraZeneca in Macclesfield in order to elucidate the nature of the endothermic and exothermic events in the DSC trace (Figure 3.27).

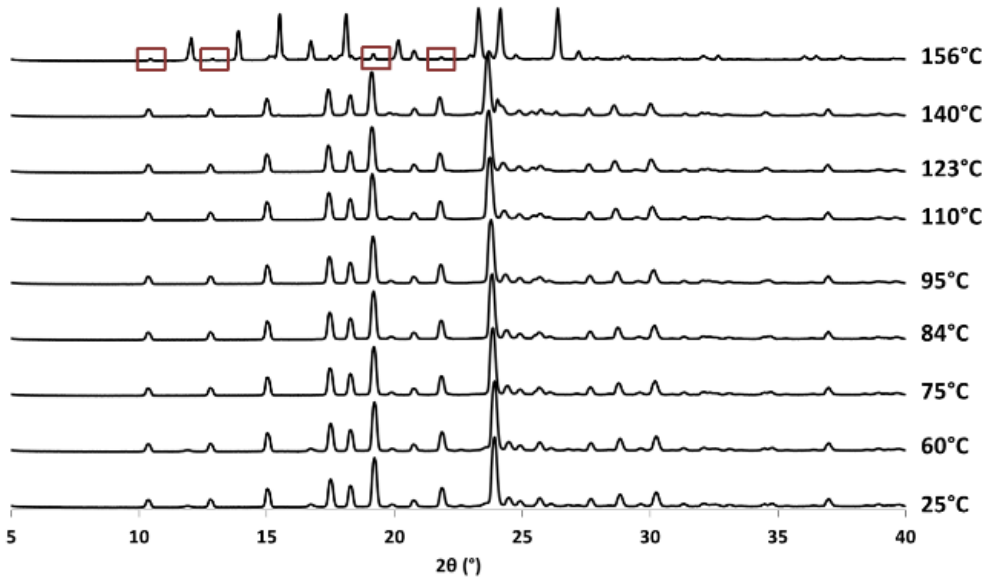

Figure 3.27: VT-PXRD patterns of a sample of PCM-II with small quantities of 3A4MA present. The y-axis displays relative intensity in arbitrary units.

The VT-PXRD, shown in Figure 3.27, shows some interesting features. At 25 °C and 60 °C, the pattern contains mainly PCM-II, with some peaks corresponding to 3A4MA at ~12°, 17° and 22.5° 2θ. Upon heating above 60 °C (corresponding the first small endothermic event in the DSC), the

peaks corresponding to 3A4MA disappear, with all patterns from 75 °C to 123 °C showing only the presence of PCM-II. Interestingly, the melting point of 3A4MA is not usually observed in DSC until 120 °C, with no corresponding thermal event seen in Figure 3.27. It could be that a solvated form of 3A4MA has been formed in the crystallisations, and upon desolvation at temperatures above 60 °C the crystal structure collapses and crystallinity is lost, meaning peaks from this compound are no longer observed in the PXRD pattern. Between 140 °C and 156 °C a phase transformation from PCM-II to PCM-I is seen. However, this is only a partial transformation as peaks from PCM-II are still visible in the spectra at 156 °C (boxed in red in Figure 3.27); a behaviour seen where small quantities of metacetamol hydrate are present in PCM-II samples. This further suggests that small quantities of these structurally similar molecules within PCM-II samples are acting to stabilise the metastable PCM-II against the polymorphic transformation.

Attempts have been made to investigate the scaling potential of the templated production of PCM-II with 3A4MA at the 50 ml solvent scale. Utilising the concentrations of 3A4MA used in small-scale batch crystallisations resulted in the production of PCM-I (Table 3.6, Experiment 1). As such, the concentration of 3A4MA was increased (Table 3.6, Experiment 2 and 3) in order to counteract the reduced mass transfer seen upon scale-up. However all crystallisation conditions examined have resulted in the production of PCM-I with 3A4MA in the solid product.

Table 3.6: Experiments performed with 3A4MA at the 50 ml scale. A concentration of PCM of 300 mg/g was used throughout

Experiment	% 3A4MA	Cooling rate (°C min^{-1})	Solid product
1	35	1	PCM-I
2	40	1	PCM-I + 3A4MA
3	45	1	PCM-I + 3A4MA

Investigations have also been conducted into the possible templating effect of polymers in the production of PCM-II. These experiments were undertaken with two different polymers that possess similar functional groups to PCM; polymers are typically used in very low concentrations which would be more desirable than the use of, for example, 25 w/w % of the structurally similar MCM as a templating molecule in terms of overall product purity. Crystallisations with polyacrylic acid (PAA) and polyvinyl alcohol (PVA) at the 3 ml solvent scale, under a variety of crystallisation conditions, whereby the concentration of each polymer was varied between 0.25 and 1 w/w % at a cooling rate of 1 °C min^{-1}, did not result in the production of PCM-II in any instance, with PCM-I

being formed in all crystallisations. Polymers that contained aromatic rings, which would further mimic the structure of PCM, were not used due to their poor solubility in the solvents investigated in this work. Polymers like this, such as nylon 6, have been shown to produce PCM-II through heterogeneous templating (i.e. on surfaces) approaches in literature studies but further work is required to establish if they can template in a solution mediated process. [10]

3.6 Mechanistic information

Upon cooling a saturated solution of PCM, Ostwald's Law of Stages is obeyed, with the metastable PCM-II crystallising first, which then undergoes a solution mediated phase transformation (SMPT) to PCM-I. Having this knowledge, it was thought that the template molecule might be acting to interfere with this SMPT, either by stabilising the metastable PCM-II or hindering the nucleation or growth of PCM-I. To test this hypothesis, PCM-II was slurried in the presence of varying percentages of MCM at the temperature at which the SMPT would normally occur (i.e. the point of nucleation in the system); from batch crystallisations at the same scale this was found to be 35 °C. A 60:40 H_2O:IPA solvent system was used with 400 rpm magnetic bottom stirring employed for a period of 24 hours. The resultant solid was filtered and analysed through PXRD (Figure 3.28).

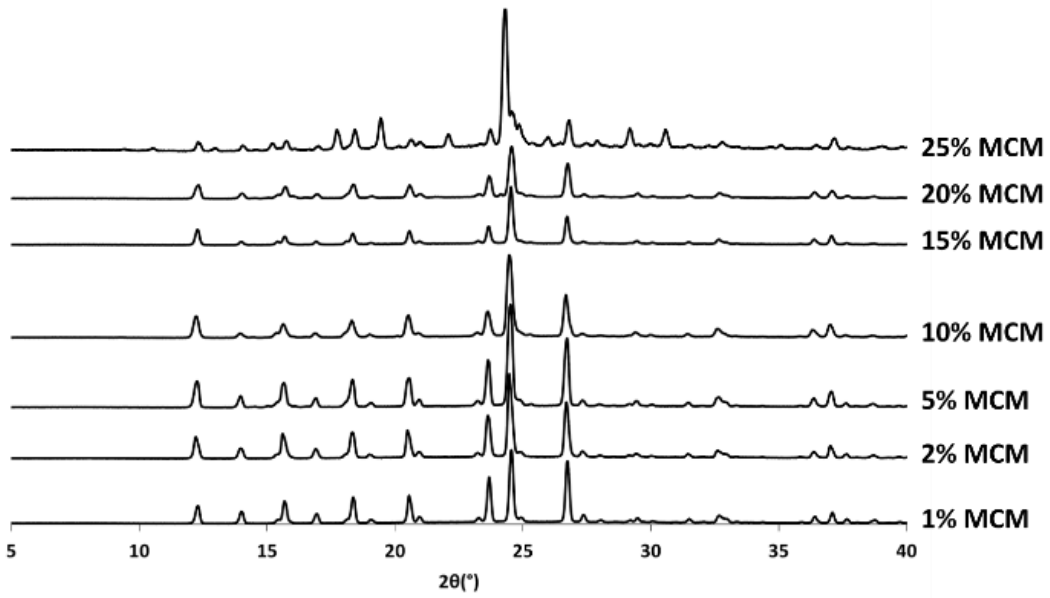

Figure 3.28: PXRD patterns of the filtered solid at the end of slurrying experiments in the presence of varying percentages of MCM. The y-axis displays relative intensity in arbitrary units.

Analysis of the PXRD patterns shown in Figure 3.28 shows that for percentages of MCM between 1 % and 20 %, complete conversion to PCM-I is observed over the 24 hour period. However, for 25 % MCM, the concentration used for the batch production of PCM-II, the PXRD pattern is still largely dominated by peaks corresponding to PCM-II, with only partial conversion to PCM-I being

observed. This observation shows that at sufficiently high concentrations, MCM is significantly retarding the rate of the SMPT.

Although use of additives is a common concept found in literature, their use has been largely limited to the control of morphology[105, 188] or their effect on the growth of a stable polymorphic form[179, 189], with only limited reports on their use in the controlled production of metastable or elusive polymorphic forms[102, 190] and even fewer on their mechanism of action in this case. Mukura *et al* examined the effect of structurally related impurities on the solution mediated phase transformation of an API, monitoring the transformation with PXRD and computationally modelling the uptake of the impurities into the API.[153] They concluded that the retardation effect of the impurities is due to kinetic stabilisation of the metastable polymorph through inhibition of the nucleation of the stable polymorph. They also noted that the driving force for the SMPT is the solubility difference between the stable and metastable forms and linked this to the effect of the impurities on the solubilities of the API. They postulate that the impurities could act to increase the solubility of the stable form, hence reducing the solubility difference (i.e. reducing the free energy difference) between the two forms and consequently the driving force for the SMPT, hence stabilising the metastable polymorph. Work by Qu *et al* [151] also showed that additives can act to increase the solubility of the stable form preferentially over that of the metastable form, enhancing the credibility of the above argument. As such, the effect on the solubility of varying percentages of MCM on two different concentrations of PCM was investigated (Table 3.7); recorded in Table 3.7 is the temperature at which the concentration of PCM and the corresponding percentage of MCM dissolves when subjected to a standard solubility experiment (outlined in Chapter 2). A higher temperature of dissolution would indicate a reduced solubility of that solid composition.

Table 3.7: The effect of varying percentages of MCM on the solubility of PCM-I, at two different concentrations

Concentration PCM (mg/g)	Wt.% MCM	Temperature of dissolution (°C)
250	0	38.7
250	15	49.9
250	20	45.4
250	25	44.7
250	30	45.0
300	0	44.2
300	15	52.1
300	20	51.6
300	25	49.7
300	30	56.8

It is clear from Table 3.7 that the presence of MCM actually acts to decrease the solubility of PCM, a result that might be expected due to the large quantities of MCM that are being used, a stark contrast to the small (<1 %) quantities used in the literature work. Interestingly, at both concentrations of PCM, the solubility in the presence of 25 % MCM (the concentration used throughout all batch crystallisation experiments) is increased in comparison to other percentages of MCM, but still decreased in comparison to the solubility in the absence of MCM. However, the decrease in solubility in the presence of MCM poses an interesting question that could elucidate a mechanism of action. If the MCM is acting also to decrease the solubility of PCM-II, then the barrier to dissolution, with dissolution being the first step in the SMPT, will be greater. This would reduce the driving force for the SMPT, hence stabilising the metastable PCM-II. Put another way, if the solubility of PCM-II is lowered, then crystallisation may not drop the solution concentration into the undersaturated region of the solubility phase diagram, meaning no dissolution of PCM-II can occur. If this dissolution does not occur, the SMPT cannot begin.

The concentrations of the template molecules employed in this work, especially when scaled to larger volumes, are relatively large in comparison to traditional additive concentrations, which typically employ concentrations below 10 %.[22, 189, 191-192] The reason that additives are typically able to act at such low concentrations is the fact that the concentration of active growth sites on a surface is low and so only small quantities are required to fill these sites. [2] As such, one would expect the templating effect to work at much lower concentrations of MCM if it was purely a growth effect.

It has been documented that high impurity loadings decrease the nucleation and growth rate coefficients for the stable form, increasing the transformation time (i.e. slowing down the SMPT)[153], which could act as a further explanation as to why the concentrations need to be so high in order to direct the production of PCM-II. Further, in order to elucidate whether the effect was a nucleation or growth effect, the crystallisation containing PCM and MCM was seeded with PCM-I. At two seed loadings (1 % and 5 %) the product of these crystallisations was PCM-I. This indicates that the MCM is acting to affect nucleation rather than growth; if the MCM was purely acting to promote growth of PCM-II over PCM-I, there would have been some PCM-II in this solid product.

In order to hinder the growth of PCM-I, the template molecules approaching the surface of the PCM-II crystals must be able to mimic a PCM molecule in terms of the interactions it makes at the surface. Using the calculated BFDH morphology from Mercury, the (002) face is the plane to which hydrogen bonded layers in PCM-II grow parallel (see above, Figure 3.5). Calculation of this plane in the Mercury software shows that the functionality lying on this surface is the carbonyl group of the amide (Figure 3.29). As such, to mimic a PCM molecule and continue this hydrogen bonding, the template molecule must first and foremost contain a hydrogen bond donor that is likely to be able to form a hydrogen bond to this carbonyl. Looking at the template molecules investigated in this work (Figure 3.7), all those templates that have successfully resulted in the production of PCM-II satisfy this requirement. This logic can be used to explain why p-acetanisidide does not result in the successful production of PCM-II; the ether functionality in place of a hydrogen bond donor means this molecule would not continue the hydrogen bonding in PCM-II.

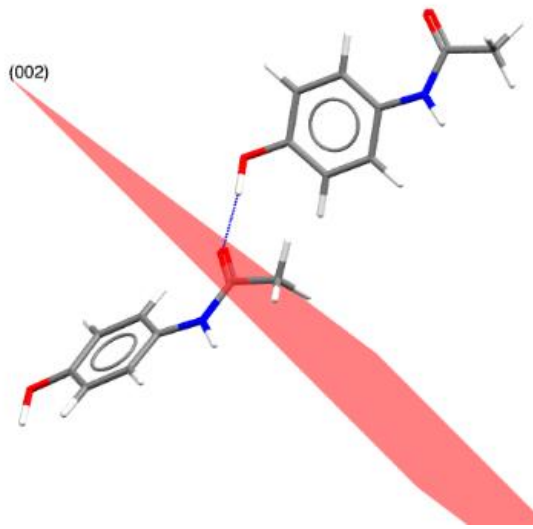

Figure 3.29: The (002) plane in PCM-II showing the carbonyl group lying on this plane

The next layer of PCM-II molecules, growing parallel to the (002) plane, is formed through N-H···O interactions (circled in red in Figure 3.30). Therefore the absence of this moiety in the template

molecule would hinder the continued growth of PCM-II. This reasoning can then be used to explain why methyl paraben also does not result in the production of PCM-II.

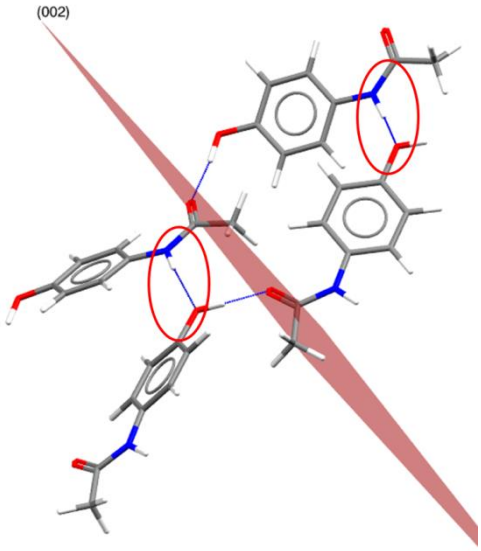

Figure 3.30: N-H···O interactions forming the next layer of molecules in PCM-II

However, based on these observations, it would suggest that 4-ABA would be a good molecule to direct the formation of PCM-II, differing only from PCM by substitution of the alcohol group for a carboxylic acid. It was noticed that at higher concentrations of 4-ABA, the template molecule crystallised preferentially over PCM. It may simply be that due to its low solubility and higher propensity to crystallise over PCM, 4-ABA is unsuitable as a template molecule; as demonstrated above, relatively high quantities of template are needed and if these quantities cannot be successfully achieved then the templating ability will be poor. All other templating molecules employed in this work have the correct moieties to continue the hydrogen bonding pattern and so could promote the growth of PCM-II. The difficulties in the reproducibility and scaling of the 3A4MA system could be explained by the added steric bulk from the ether functionality that may hinder the continuation of the hydrogen bonding depending at what angle the molecule approaches the growing crystal surface.

For MCM, the templating molecule that has been utilised in all further batch scale-up and continuous experiments reported in this work (see Chapters 4 and 5), analysis of the crystal packing similarity using the CCDC's Mercury software enables comparison of the two crystal structures (Figure 3.31); this was unable to be performed for the other template molecules due to single crystal data not being available or lack of structural similarity in the case of the benzoic acid derivatives.

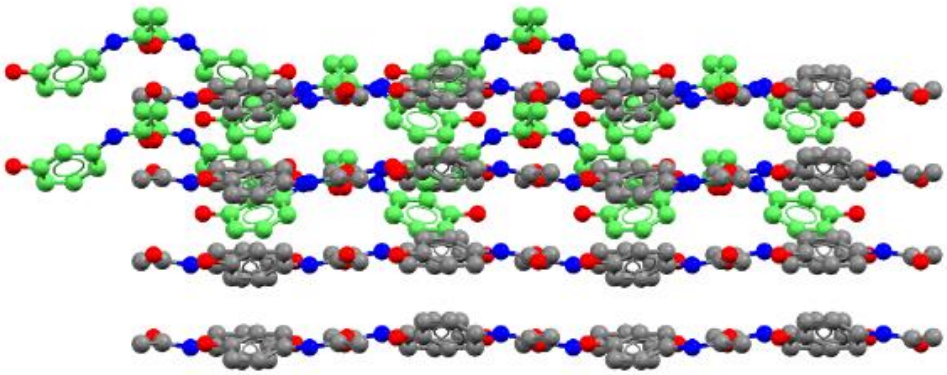

Figure 3.31: Crystal packing similarity of PCM-II (grey) and MCM (green) - hydrogen atoms have been removed for clarity

It can be seen that the packing between the molecules is virtually the same, differing only by the torsion of the aromatic ring, supporting MCM's superior ability as a template molecule. However, MCM's enhanced ability to template PCM-II in comparison to the other templating molecules investigated can also be attributed to its enhanced solubility, meaning more of the template molecule can be used.

3.6.1 Stability of samples

It is well documented that the presence of any of the stable PCM-I within PCM-II samples will seed the conversion from PCM-II to PCM-I. The PCM-II samples produced in this work from the MCM and 4-FBA templated studies are currently stable for a period of 24 months (Figure 3.32), indicating the polymorphic purity of the samples produced through this templating method.

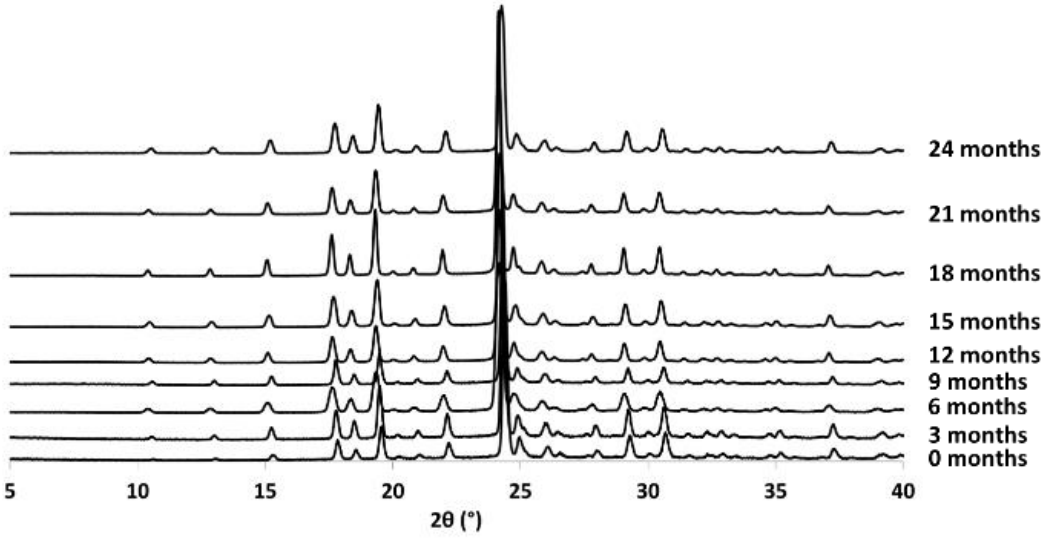

Figure 3.32: PXRD patterns showing a sample stability of 24 months. The y-axis displays relative intensity in arbitrary units

Although the PCM-II to PCM-I solid-state polymorphic transformation is well-documented, the speed of the transformation and quantification in relation to the percentage of PCM-I within a PCM-II sample is previously unreported. As such, doping experiments were performed whereby varying percentages (ranging from 1-50 %) of PCM-I were included within PCM-II samples and left in a closed vial. Aside from initial stirring with a spatula to distribute the PCM-I evenly throughout the sample, the samples were left in a non-agitated environment to ensure any polymorphic transformation was only due to the presence of PCM-I in the sample. Analysis of the solid product each week allowed for determination of a transformation time. Those samples containing more than 5 % PCM-I within were difficult to interpret as it was not possible to distinguish peaks present from the PCM-I simply being in the solid or from conversion; the limit of detection of PXRD using the instrument available is ~5 % and so the powder pattern recorded at the beginning of the stability studies to act as a reference contained peaks from PCM-I. Further, as the PXRD set-up is flat plate, preferred orientation effects are often seen and so peak heights cannot be used to help in this determination and full quantitative phase analysis was not undertaken. However, the analysis of the sample with 1 % form I seed loading provides some useful results (Figure 3.33); after a period of a month peaks from PCM-I are present in the PXRD pattern, indicating some conversion from PCM-II to PCM-I (1 % is well below the limit of detection of PXRD and so these peaks must, at least in part, be from converted PCM-I).

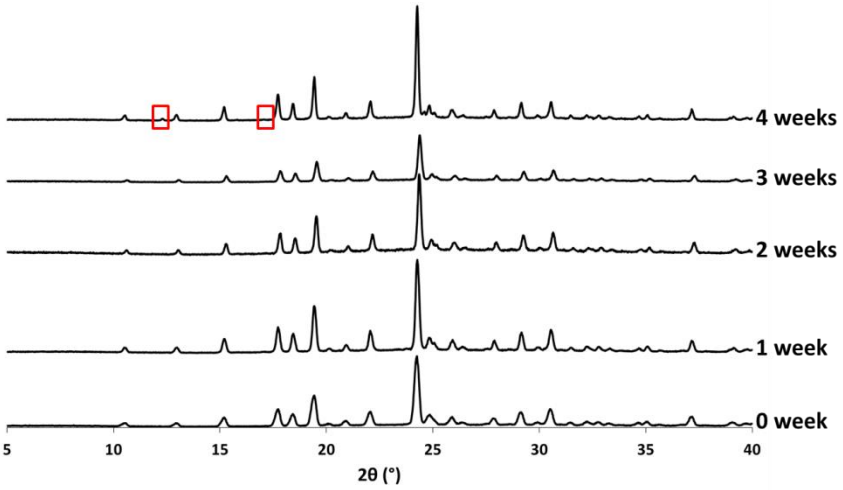

Figure 3.33: PXRD patterns over a one month period with a 1 % PCM-I seed loading, showing the appearance of PCM-I peaks after 4 weeks. The y-axis displays intensity in arbitrary units.

3.7 Conclusions

The production of metastable paracetamol form II (PCM-II), which displays enhanced physical properties of greater compressibility and higher solubility, has been investigated with three *p*-substituted halobenzoic acid derivatives and a variety of structurally similar, size-matched molecules as template molecules; here a template is defined as a molecule included in the crystallisation process that forces the adoption of a particular polymorphic form of a substance without itself being present in the final crystal product.

Based on previous literature evaporative work, initial crystallisations were carried out at the 1 ml scale using three *p*-substituted halobenzoic acid derivatives. Although all yielded PCM-II under varying experimental conditions, only the production of PCM-II with 3.5 wt.% 4-fluorobenzoic acid (4-FBA) and 0.4, 1.6 and 2 wt.% 4-bromobenzoic acid in a 60:40 H_2O:IPA solvent system were fully reproducible at this scale. The poor reproducibility of other experiments at this scale can be attributed to accuracy in weighing small quantities of template molecule. Attempted scale-up of the production of PCM-II using these derivatives were largely unsuccessful, postulated to be due to the low solubility combined with the naturally poorer mass transfer experienced at the larger scale.

As such, work was conducted using a variety of structurally similar molecules. Use of metacetamol (MCM) resulted in the reproducible production of PCM-II up to the 20 ml solvent scale (the further scaling of this system will be detailed in Chapter 4). Work with MCM showed the production of PCM-II at a relatively fast cooling rate (1 °C min^{-1}) in two different solvents (60:40 H_2O:IPA and

ethanol) through both a stepped and linear cooling profile; a stark contrast to the work with the benzoic acid derivatives that required a slow (0.02 °C min^{-1}), stepped cooling profile which would not be conducive to transfer to a continuous crystallisation environment. The use of MCM required higher percentages of template to be present, in comparison to the benzoic acid derivatives, with percentages as high as 25 % being employed to enable the production of PCM-II. Use of higher quantities of MCM resulted in the production of metacetamol hydrate (MCM·H_2O) in the solid product; however this was eliminated through truncation of the temperature profile at a temperature of 20 °C. Trace levels of MCM·H_2O resulted in a characteristic DSC pattern, with the nature of the thermal events in this pattern being quantified using VT-PXRD, showing dehydration followed by possible stabilisation of PCM-II in the melt of MCM. When comparing the crystal morphologies of PCM-II produced in the presence of 4-FBA and MCM, those with MCM showed a more block-like morphology, desirable in terms of ease of downstream processing; this is another reason why the templated production of PCM-II with MCM was explored further.

Other small scale studies showed the production of PCM-II using the templating molecules orthocetamol (OCM) and 3'-amino-4'-methoxyacetanilide (3A4MA). Initial experiments with OCM showed the production of a mixture of PCM-II and PCM-I with 2 wt. % and 3 wt. % OCM when cooled to a temperature of 5 °C at a rate of 0.02 °C min^{-1}. Investigations in this percentage region combined with truncation of the cooling profile at 20 °C resulted in the reproducible production of PCM-II with 2.4 % OCM in a 60:40 H_2O:IPA solvent system. Due to this cooling rate not being conducive to transfer to continuous crystallisation platforms, a faster cooling rate of 0.2 °C min^{-1} was investigated, with 2.8 % OCM resulting in the production of PCM-II. However, reproducibility at this cooling rate has been poor. Attempted scale-up of this system has been unsuccessful, encountering similar problems to the benzoic acid derivatives due to OCM's low solubility in the solvent system used. Initial experiments examining weight percentages of 3A4MA between 1 % and 25 % resulted in the production of PCM-I. However, upon increasing the percentage of 3A4MA to 40 %, utilising a stepped cooling profile and cooling rate of 1 °C min^{-1}, PCM-II was formed; however some 3A4MA was detected in the solid product. Attempts to mitigate the formation of 3A4MA by truncating the cooling profile resulted in the production of PCM-I. However, upon scale-up of this system to the 10 ml scale, utilising 35 % 3A4MA, pure PCM-II was produced in the absence of any 3A4MA.

Slurrying experiments, whereby PCM-II was stirred for a period of 24 hours with varying percentages of MCM at the temperature at which the solution mediated PCM-II to PCM-I phase transition usually occurs were used to try and elucidate a mechanism of action of the template

molecules. These experiments showed that for percentages of MCM between 1 and 20 %, full conversion back to PCM-I was observed. However, for 25 % MCM, only partial conversion to PCM-I was observed, with the filtered product PXRD still being largely dominated by peaks from PCM-II. As such, it was concluded that the presence of the template molecule was hindering the solution mediated phase transformation, stabilising the metastable PCM-II.

The samples produced through this templated crystallisation method display a stability of 24 months against the well-documented PCM-II to PCM-I solid state transformation, which is accelerated by the presence of even trace quantities of PCM-I in a PCM-II sample. Investigations into this transformation time through doping of PCM-II samples with varying percentages of PCM-I showed that the presence of 1 % PCM-I or greater started the conversion back to the thermodynamically stable PCM-I within a month. The stability of the PCM-II samples produced here further highlights the polymorphic purity of the samples produced through this method.

The transfer of the templated crystallisation of a metastable polymorphic form to a cooling crystallisation environment, as demonstrated in this chapter, is a key first step towards the continuous crystallisation of these metastable polymorphic forms, which often display enhanced physical properties. It represents a breakthrough in the manufacture of these metastable polymorphic forms with previously reported methods of obtaining these metastable forms being largely limited to small scale discovery environments, with samples displaying poor polymorphic stability with respect to the transformation to the thermodynamically stable form.

4 Scaled batch crystallisation of PCM-II and transfer to a MSMPR crystalliser

The work presented in this chapter has been published as part of a Crystal Growth and Design special issue of selected papers presented at the 12th International Workshop on the Crystal Growth of Organic Materials (CGOM12 Leeds, UK):

L.R. Agnew, T. McGlone, H.P. Wheatcroft, A. Robertson, A.R. Parsons and C.C. Wilson, 'Continuous Crystallization of Paracetamol (Acetaminophen) Form II: Selective Access to a Metastable Solid Form', ***Cryst. Growth Des.,*** **2017, 17(5), 2418-2427**

Small scale experiments (outlined in Chapter 3) highlighted a system that showed promising results in selective formation of a metastable form with scaling potential; the reproducible production of paracetamol form II (PCM-II) was achieved with use of the structurally similar metacetamol (MCM) as a template molecule. The aim of the further work presented in this Chapter was to attempt to scale this system, highlighting optimum conditions for PCM-II production and moving towards transfer to a variety of continuous crystallisation platforms.

4.1 Design of Experiments (DoE) at the 100 ml scale

4.1.1 Initial investigations into scaling potential in an RBF

In order to assess the suitability of the PCM/MCM system for a Design of Experiments at the 100 ml scale, initial investigations into the scaling potential of the system in a round-bottomed flask (RBF) had to be performed. The aim of these crystallisations was to identify conditions under which PCM-II could be produced, which could then be optimised and fine-tuned through use of a DoE approach, exploring the experimental limits of PCM-II production. Initial scaled-up crystallisations in an RBF were conducted using a magnetic bottom stirring rate of 800 rpm; this was increased from small scale experiments to take into account the reduced mass transfer that could be experienced on scale up. As observed in Chapter 3, the use of ethanol resulted in more PXRD peaks corresponding to the metacetamol hydrate phase and so a solvent system of 60:40 H_2O: IPA was used throughout all further experiments. Investigations with lower percentages of MCM (10-25 %) that resulted in the successful crystallisation of PCM-II at the small scale, employing both a slow (0.02 °C min^{-1}) and fast (1 °C min^{-1}) cooling rate resulted in the production of PCM-I at this scale. As such, the use of larger proportions of MCM was investigated (Table 4.1). The working volume of all

experiments was 50 ml. RBFs were subjected to the stepped cooling profile detailed in Chapter 3, cooling from 70 °C to 20 °C at 1 °C min^{-1} , unless otherwise stated.

Table 4.1: Experimental information for RBF crystallisations with magnetic bottom stirring

Experiment	Wt.% MCM (%)	Temperature of crystallisation (°C)	Product
RBF1	40	20	PCM-II + MCM·H_2O
RBF2	40	Did not crystallise	-
RBF3	35	13	PCM-II + MCM·H_2O
RBF4	30	15	PCM-II + MCM·H_2O

The use of magnetic bottom stirring, and the associated reduced mass transfer, required larger quantities of MCM to be used in order to direct the formation of PCM-II. Further, the widening of the metastable zone width experienced with larger quantities of MCM meant crystallisations had to be cooled below 20 °C, resulting in more MCM·H_2O in the solid product. As such, all further investigations were conducted with overhead stirring. In order to try to aid the crystallisation of PCM-II at higher temperatures, which will have the effect of mitigating the formation of MCM·H_2O, the concentration of PCM was increased to 300 mg/g for subsequent experiments (Table 4.2).

Table 4.2: Overhead stirring crystallisations of PCM/MCM

Experiment	Scale (ml)	Wt.% MCM (%)	Temperature of crystallisation (°C)	Product
RBF5	50	25	30	PCM-II + MCM·H_2O
RBF6	50	25	25	PCM-II + MCM·H_2O
RBF7	100	25	30	PCM-II + MCM·H_2O
RBF8	100	25	30	PCM-II
RBF9	100	25	30	PCM-II
RBF10	150	25	30	PCM-II + MCM·H_2O
RBF11	150	25	30	PCM-II + MCM·H_2O

For all experiments shown in Table 4.2, DSC was required to detect the small quantities of MCM·H_2O present. This reduction in the quantities of MCM·H_2O in the solid products combined with inconsistencies at the 100 ml scale prompted a Design of Experiments (DoE) study to be performed,

with the aim of fine-tuning the conditions needed to produce pure PCM-II in the absence of any MCM·H_2O.

4.1.2 Introduction to DoE

Traditionally, optimisation of a process is achieved through changing one factor at a time until a perceived optimum is found; this approach to experimentation is called one variable at a time (OVAT) or the COST approach (illustrated with black dots in Figure 4.1). It can often be an inefficient method of experimentation, requiring large numbers of experiments, and could result in missing the optimum conditions, especially if two different factors interact and are thus correlated. As such, many researchers now employ a Design of Experiments (DoE) approach to experimentation. DoE varies all factors simultaneously in a systematic manner to produce a model to describe the behaviour of the system with respect to these variables.[193-194] From this model, through selection of correct factors and meaningful responses, producing a statistically relevant model, can allow for prediction of future results from experiments not performed, allowing an optimum to be discovered without the need for extensive experimentation (Figure 4.1; red dots).

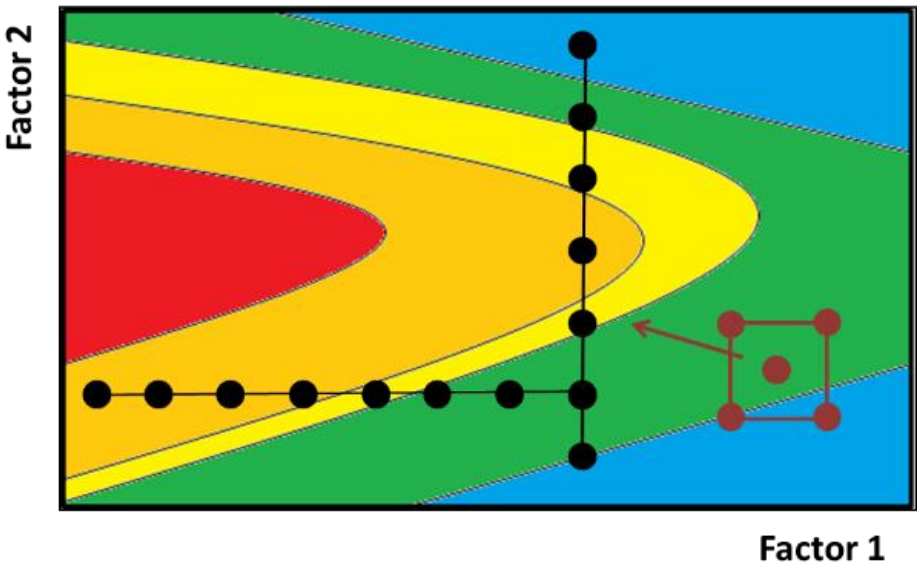

Figure 4.1: A visual representation of the COST approach (black dots) and the DoE approach (red dots)

There are three scenarios for which DoE is commonly employed: screening, optimisation and robustness testing.[195] Screening is used to identify important factors and the corresponding ranges for which they should be investigated. As the name suggests, optimisation is used to elucidate the factors that allow for optimal conditions for production of the desired product. Robustness testing analyses how small changes in operating conditions could affect the outcome of the experiment, for example if small amounts of an impurity were introduced into a crystallisation process. The DoE

approach has been used to determine important parameters in graphene synthesis[196], in the kinetic resolution of oxazinones[194] and to aid in the preparation of nano- and micro-particles with a desired size distribution. [197]

Consider a system that has k factors each with a high and low value, coded as +1 and -1 respectively. Then suppose a full factorial experiment is carried out with n= 2^k runs, with each run consisting of each factor set at either +1 or -1. The experiments make up a matrix within which all factors are varied over the two levels. For example a full factorial design with two factors (x_1 and x_2) consists of four runs with (x_1,x_2) = (1,1), (1,-1), (-1,1) and (-1,-1).[198] Each of the experimental conditions forms the corner of a square; similarly a full factorial with three factors would consist of eight experiments, with each condition forming the vertices of a cube.

Upon completion of the runs, data must be analysed in order to see the effect of factors on the responses. The data produced is fitted to one of three possible polynomial models: linear, interaction or quadratic. The type of model to which the data are fitted will depend upon the objective of the DoE. For screening and robustness testing objectives, linear and interaction models are commonplace. For an optimisation objective, quadratic models are used as these tend to be more flexible to complex response functions. In the present work, a screening objective was used and so an interaction model was employed. For the simple two factor full factorial design outlined above, the interaction model would take the form of Equation 4.1.

$$\boldsymbol{y = \beta_0 + \beta_1 x_1 + \beta_2 x_2 + \beta_{12} x_1 x_2 + \varepsilon} \quad \textbf{Equation 4.1}$$

Where y is the response, x_1 and x_2 are the two factors, the β terms are the model parameters and ε is the residual response variation not explained by the model. Partial least squares (PLS) regression is then used to fit the data to the model to allow determination of the β terms, quantifying the interactions between the factors.

The aim of the work presented here was to identify conditions under which PCM-II could be formed in high polymorphic purity, in the absence of any MCM·H_2O impurity. In order to explore a number of factors, in a designed and systematic approach, it was decided that a DoE approach was appropriate.

4.1.3 Materials and methods

Paracetamol (4'-hydroxyacetanilide; PCM) was purchased from Sigma Aldrich Chemie Gmbh (Steinheim, Germany). Metacetamol (3'-hydroxyacetanilide; MCM) was purchased from TCI Ltd. All

were used without further purification. Laboratory grade solvents purchased from Sigma Aldrich were used for all crystallisations.

4.1.3.1 Overhead stirring experiments in the Polar Bear Plus

Initial experiments utilising overhead stirring were conducted using the Polar Bear Plus crystalliser with an overhead motor and shaft (Figure 4.2). Investigations were carried out at both the 50 ml and 100 ml scale using a 100 ml and 250 ml round bottomed flask (RBF), respectively; the different RBF sizes were used to ensure effective mixing was experienced at the different scales. All initial experiments at this scale were performed using the stepped cooling profile shown to allow reproducible production of PCM-II on the small scale (Chapter 3).

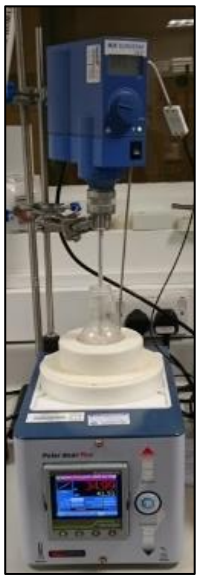

Figure 4.2: Polar Bear Crystalliser with overhead motor and shaft to provide overhead stirring to the system

4.1.3.2 Design of Experiments for optimisation of PCM-II production

The MODDE 11 Pro software was used to design a full factorial DoE with five factors: stirring rate, concentration of PCM, wt.% MCM, stirring time at the final temperature and final temperature. A full factorial design with five factors results in 32 experiments; three control experiments are also performed at the same 'mid-point' conditions to determine the reproducibility of the model, resulting in a total of 35 experiments. All the factors selected appeared to have an effect on the polymorphic form produced in initial experiments at the same scale. Appropriate high and low values for each of the factors were chosen; this resulted in varying the stirring rate between 200 rpm and 400 rpm, the concentration of PCM between 250 mg/g and 300 mg/g, the wt.% of MCM between 25 % and 30 %, the stirring time at the final temperature between 30 mins and 120 mins and the final temperature between 15 °C and 20 °C. Two responses, polymorphic form

and yield, were selected for the DoE. The MODDE software requires the responses to have a quantitative value. As such for the polymorphic form response, numerical values were assigned to each of the possible polymorphic form outcomes, with a 0 representing PCM-I, 1 representing PCM-II and 2 representing a mixture of PCM-II with some MCM/MCM·H_2O impurity present. Table 4.3 highlights the experimental parameters investigated in this DoE, alongside the responses measured. All experiments were performed at the 100 ml scale in a 250 ml RBF. Temperature control was provided by the Polar Bear Plus crystalliser and overhead stirring from an overhead motor and shaft (Figure 4.2). A stepped cooling profile with one hour dwell periods, as used in small scale experiments in Chapter 3, was used throughout all DoE experiments.

Table 4.3: Design of Experiments experimental parameters

Experiment Number	Run order	Stirring rate (rpm)	Concentration PCM (mg/g)	Wt.% metacetamol	Stirring time at final temperature (mins)	Final temperature (°C)	Polymorphic form	Yield (%)
N1	18	200	250	25	30	15	2	30
N2	31	400	250	25	30	15	2	43
N3	27	200	300	25	30	15	2	59
N4	4	400	300	25	30	15	1	57
N5	29	200	250	30	30	15	2	35
N6	1	400	250	30	30	15	2	36
N7	17	200	300	30	30	15	2	35
N8	32	400	300	30	30	15	2	48
N9	28	200	250	25	120	15	2	51
N10	2	400	250	25	120	15	2	56
N11	33	200	300	25	120	15	2	60
N12	23	400	300	25	120	15	2	65
N13	12	200	250	30	120	15	2	64
N14	26	400	250	30	120	15	2	46
N15	6	200	300	30	120	15	2	-[1]
N16	22	400	300	30	120	15	2	55
N17	19	200	250	25	30	20	2	29
N18	34	400	250	25	30	20	1	37
N19	5	200	300	25	30	20	2	30
N20	16	400	300	25	30	20	2	44
N21	8	200	250	30	30	20	2	37
N22	24	400	250	30	30	20	2	27
N23	15	200	300	30	30	20	2	35

[1] Solid was lost during the filtration process so yield was not included in the model

Experiment Number	Run order	Stirring rate (rpm)	Concentration PCM (mg/g)	Wt.% metacetamol	Stirring time at final temperature (mins)	Final temperature (°C)	Polymorphic form	Yield (%)
N24	10	400	300	30	30	20	1	46
N25	21	200	250	25	120	20	2	40
N26	25	400	250	25	120	20	1	39
N27	7	200	300	25	120	20	2	51
N28	13	400	300	25	120	20	2	41
N29	3	200	250	30	120	20	2	33
N30	11	400	250	30	120	20	2	48
N31	20	200	300	30	120	20	2	40
N32	9	400	300	30	120	20	1	46
N33	14	300	275	27.5	75	17.5	2	51
N34	30	300	275	27.5	75	17.5	2	49
N35	35	300	275	27.5	75	17.5	2	46

4.1.4 Results and discussion

PXRD analysis (Figure 4.3) shows that PCM-II was formed under all experimental conditions investigated in the DoE (polymorphic outcomes 1 and 2 in Table 4.3). Only one experiment showed the production of MCM·H_2O in the solid product at high enough levels to be detected by PXRD (N3; peaks corresponding to MCM·H_2O shown in the red box in Figure 4.3). In order to determine whether trace quantities of MCM·H_2O were present in the solid product, differential scanning calorimetry (DSC) analysis was performed on each of the samples after being left to dry in air overnight; this was to ensure any of the peaks attributed to solvent were from the internal crystal structure rather than any solvent left on the surface of the crystals. As shown in Chapter 3, the presence of a melt/recrystallisation event in the DSC before the final melt can be attributed to the presence of MCM or MCM·H_2O. Only five experiments result in the production of pure PCM-II, with experiment N4 resulting in the highest yield; as such a concentration of PCM of 300 mg/g coupled with 25 % MCM was used for all future experiments.

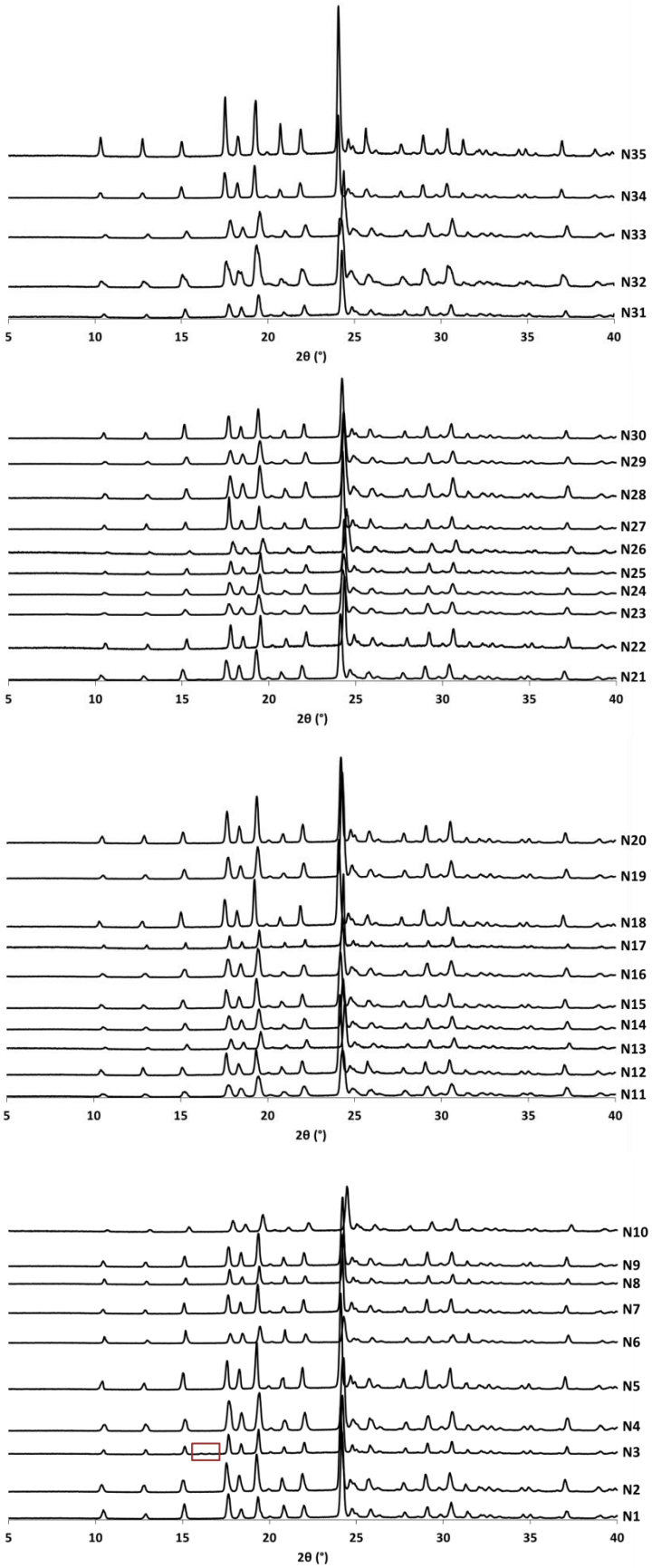

Figure 4.3: PXRD analysis on all 35 DoE experiments, y-axis shows intensity in arbitrary units. The shift in the pattern for N10 can be attributed to sample preparation.

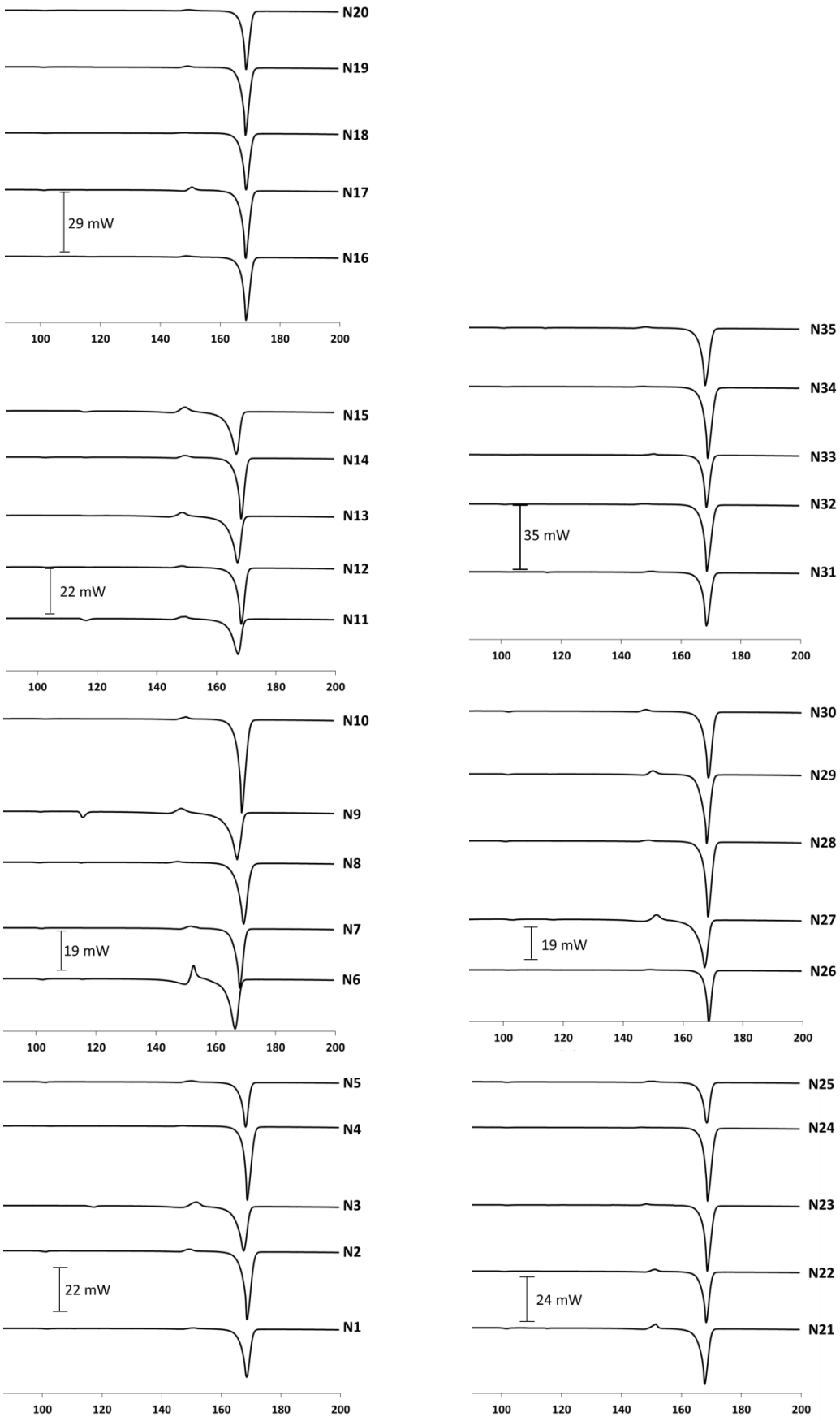

Figure 4.4: DSC analysis on the 35 DoE experiments, y axis showing heat flow in mW

Application of partial least squares regression to the data produced from these experiments gave the DoE summary of fit plot shown in Figure 4.5.

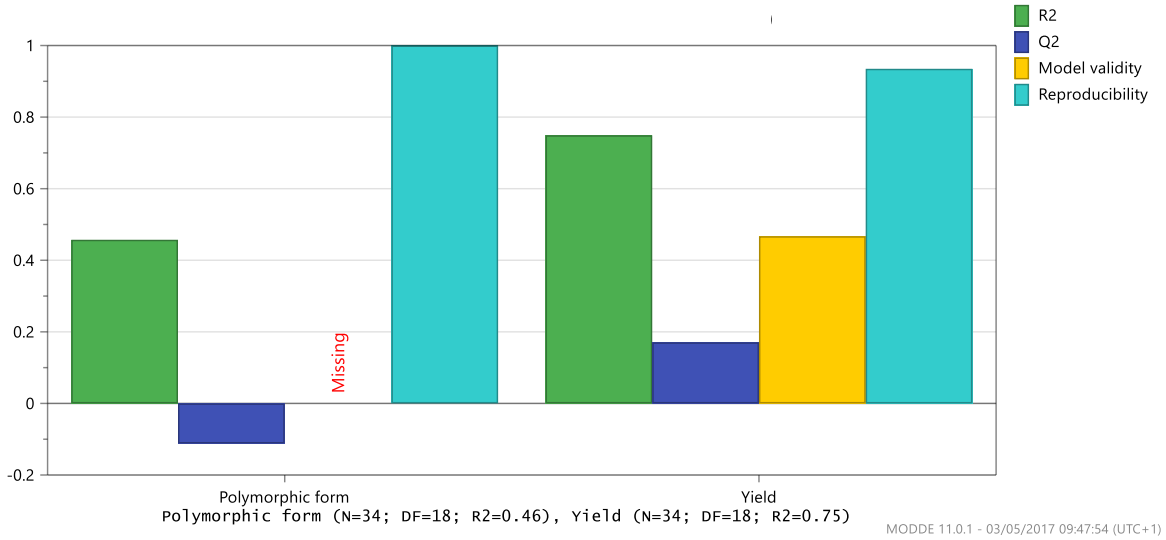

Figure 4.5: Summary of fit plot for the both the polymorphic form and yield response

There are four indicators used to produce the summary of fit plot: R2, Q2, model validity and reproducibility. R2 represents how well the model produced fits the data; the value of R2 needs to exceed 50 % to be informative, with a value over 75 % indicating a good model. Q2 gives an indicator as to how well the model predicts new data; an important parameter to consider if the purpose of the DoE is to allow prediction of future results. A useful model should have a high value of Q2, with a low Q2 resulting from either poor reproducibility or poor model validity. Good model validity has a value above 0.25, indicating there is no lack of fit of the model and the associated model error is within experimental error. The reproducibility represents the variation of the response under the same experimental parameters (pure error), compared to the total variation of the response over all experiments. [199]

As can be seen from Figure 4.5, the summary of fit plot for the yield response shows good reproducibility (93 %), a good R2 value (indicating a good model) and reasonable model validity. The value of Q2 is, however, low, likely due to the large number of factors investigated in the experiments. The low Q2 value prompted analysis of the factors using the variable importance plot (VIP) (Figure 4.6). Although the polymorphic form response has an excellent reproducibility, all other indicators show a poor model in terms of validity and ability to predict new data. This is likely due to having to represent polymorphic form, a qualitative response, as a quantitative value. The formulation of a DoE involves setting each of the responses at one of three levels: a minimum, an optimum and a maximum. This works well with responses that yield a numerical value, however in

the case of the polymorphic form response, numbers had to be assigned to each of the possible polymorphic form outcomes, with a level of 1 representing the optimal result of pure PCM-II, and 2 representing a mixture. As such there were no responses at values in between 1 and 2. Therefore, the formation of a histogram to determine the distribution of responses, which should display a normal distribution (i.e. rising and falling each side of a maximum in the traditional bell curve), only represents the two values of 1 and 2, skewing the distribution, resulting in a poor model. Furthermore, as there is perfect reproducibility for the polymorphic form response, the pure error will be zero. The reason for low model validity is due to the model error being significantly larger than the pure error, resulting in a lack of fit.

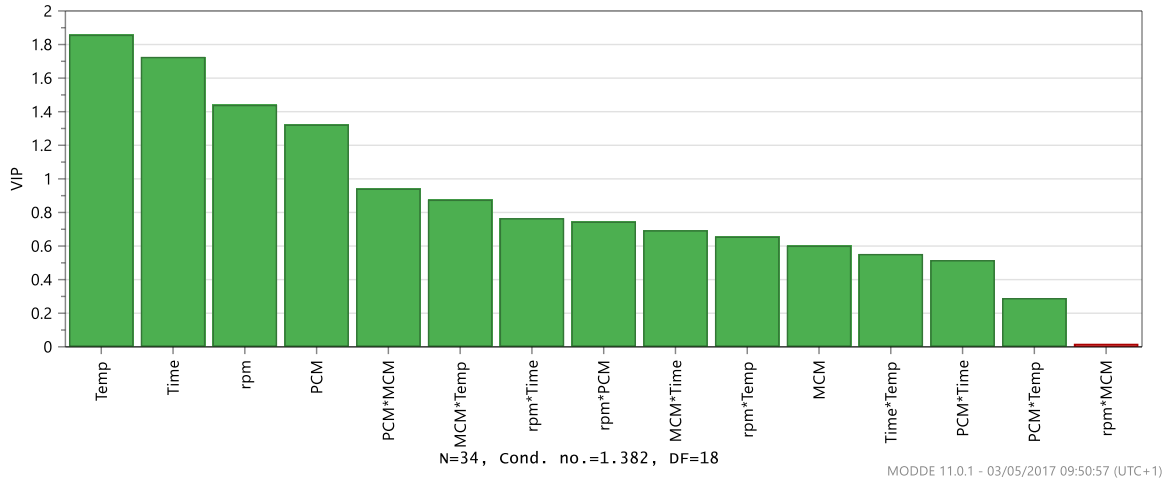

Figure 4.6: Variable Importance plot (VIP) highlighting the importance of factors and their interactions

The VIP plot (Figure 4.6) summarises the importance of the terms in the model and the interaction between individual factors. They are normalised such that a VIP of 1.0 corresponds to average importance. It is common practice to keep anything with a VIP>0.8, removing all factors that have a value lower than this. However, the MCM factor was retained, as removal of this factor would result in removal of the correlation PCM*MCM which can be seen to have an importance >0.8. Removal of the other factors with VIP < 0.8 resulted in the summary of fit plots shown in Figure 4.7.

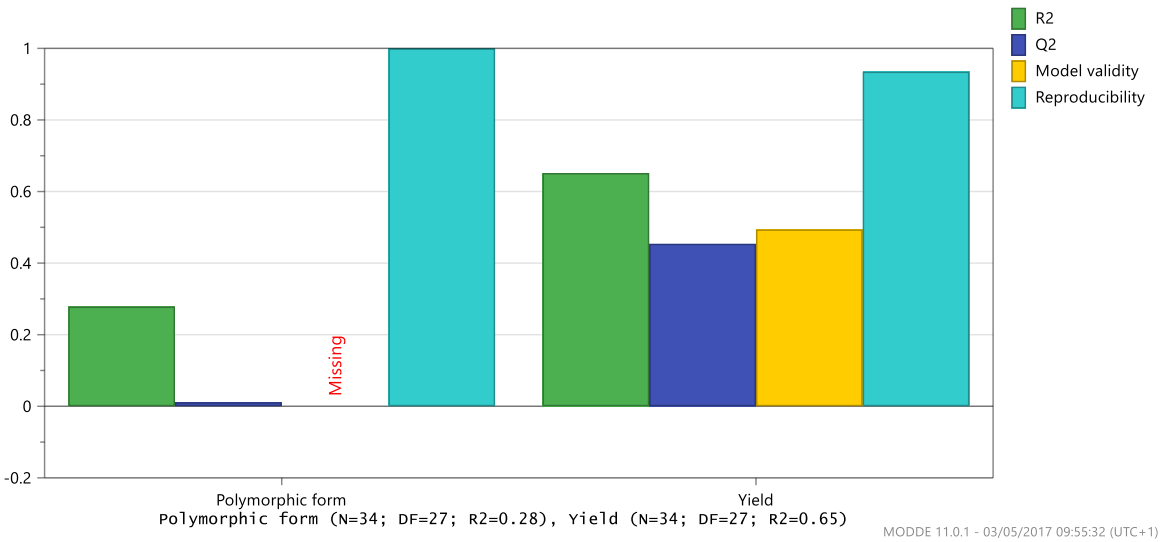

Figure 4.7: Summary of fit plots after removal of factors with an importance of <0.8

As can be seen from Figure 4.7, removal of these interactions from the model increases the value of Q2 for both of the responses. The inherent problem of qualitative values being represented quantitatively has not been altered through removal of the interactions, and so the model validity for the polymorphic form response remains missing. It was this refined model that was used to examine the coefficient plots for the two responses, allowing quantification of how changing different factors impacts the responses (Figure 4.8).

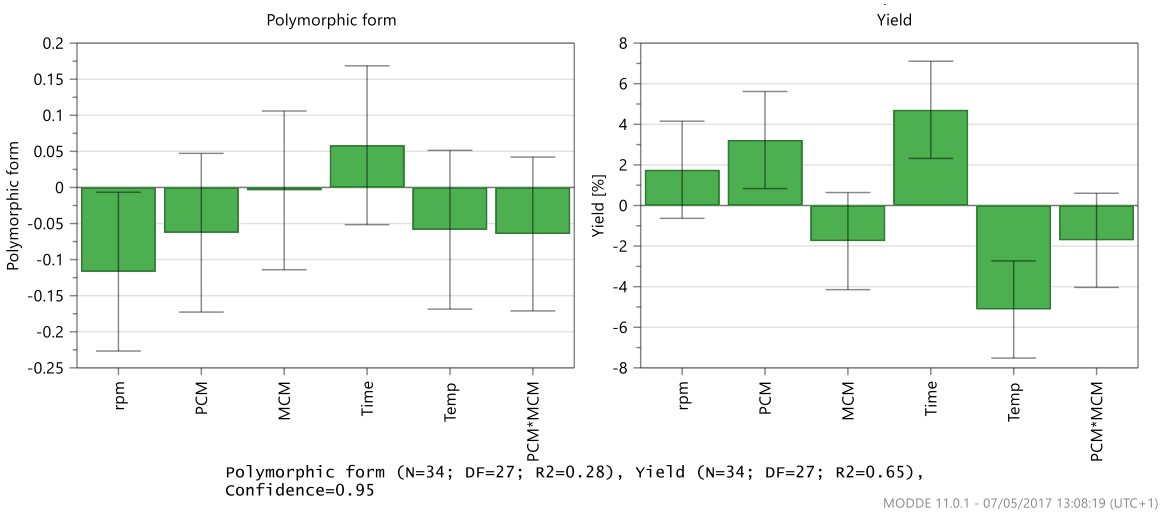

Figure 4.8: Coefficient plots for both the responses, quantifying the effect of each of the factors on each of the responses

The coefficient plot displays the regression coefficients with confidence intervals. The coefficients are scaled by the MODDE software in order to allow for direct comparison between all factors. The size of the coefficient represents the change in the response when a factor varies from 0 to 1, in coded units, while the other factors are kept at their averages. The coefficient is considered as significant (i.e. different from the noise), when the error bar does not cross the horizontal zero axis.

For the coeffcient plot for the yield response, it can be seen that increasing the concentration of PCM and the time at the final temperature results in an increase in the yield, with time having the greatest effect. This is what would be expected: increasing the time allows for more time for growth of crystals and increasing the concentration of PCM will cause the system to nucleate at an earlier temperature (as it is more saturated) and so has more time for growth to occur. It is interesting to note that the concentration of MCM with respect to paracetamol is not seen as significant. Initial experiments (outlined in Section 4.1.1) suggested that increasing the concentration of MCM results in a widening of the metastable zone; this widening would result in crystallisation at lower temperatures, giving less time for growth in the system and hence reducing the yield of crystallisation. It can be suggested that within the ranges explored in this DoE, this interaction was not as obvious and so was not considered important.

The results for the polymorphic form coefficient plot are slightly more difficult to interpret, due to the software requiring quantitative values. Therefore, any negative effect on polymorphic form on the coefficient plot actually corresponds to an increased propensity for forming PCM-II in the absence of MCM·H_2O. The only factor found to have a significant effect on polymorphic form is the stirring speed; increasing the stirring speed increases the propensity for the formation of pure PCM-II. In terms of the polymorphic purity of the samples produced, stability analysis under standard room temperature conditions has been investigated, through analysis of the PXRD patterns of the samples every three months. The PXRD patterns after a period of 15 months (Figure 4.9) show all samples still to be PCM-II, indicating the polymorphic purity of the samples produced; the presence of any PCM-I in these samples, as shown in Chapter 3, would seed the conversion back to the thermodynamically stable PCM-I within one month.

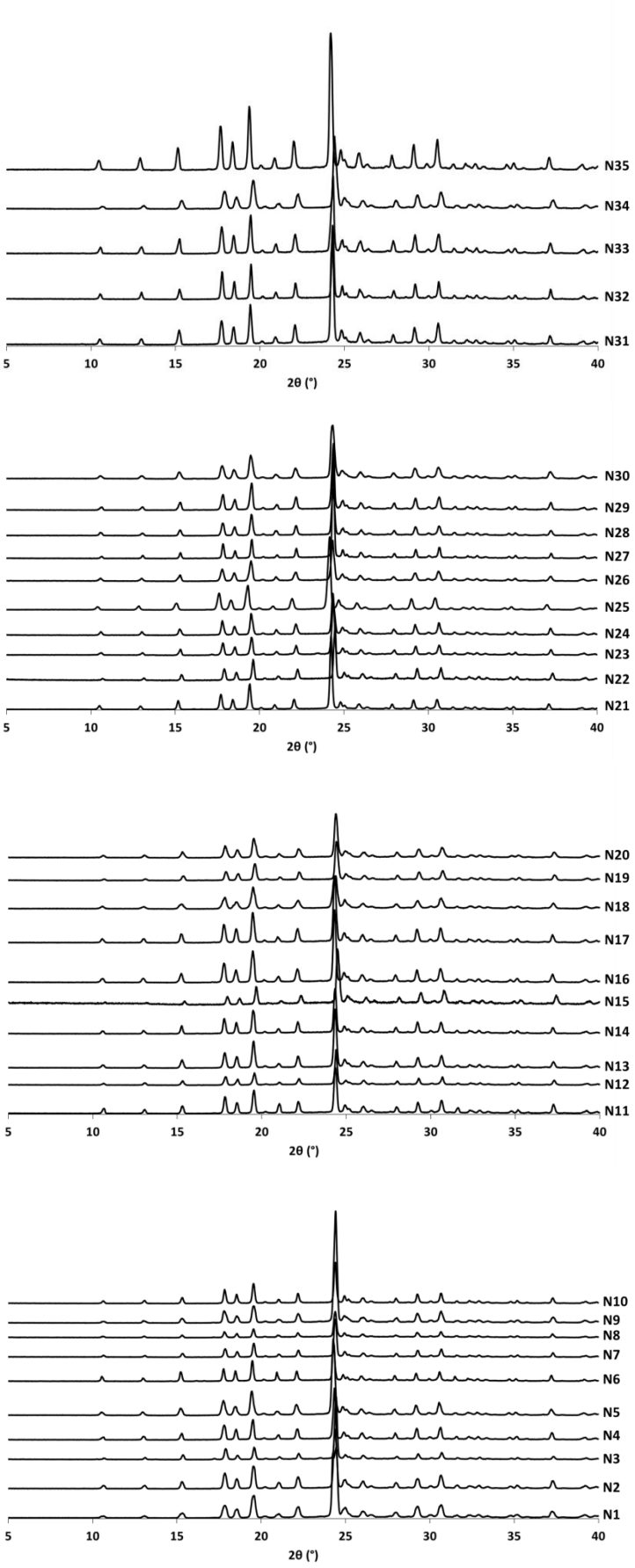

Figure 4.9: PXRD patterns showing the DoE samples after a period of 15 months; the y axis shows relative intensity in arbitrary units

4.1.5 Conclusions

A full factorial design with five factors Design of Experiments (DoE) investigation has been conducted in order to find the optimal conditions for the production of PCM-II in the absence of metacetamol hydrate (MCM·H_2O). The concentration of PCM, the wt. % of MCM, the final temperature of the cooling profile, the stirring rate and the stirring dwell time at the final temperature were investigated to observe their effect on two outcomes, polymorphic form and yield of crystallisation.

All experimental parameters investigated resulted in the production of PCM-II, the desirable polymorphic form. However, only five experimental conditions resulted in the production of PCM-II in the absence of any MCM·H_2O, at levels detectable through DSC analysis. As such, for all future experiments a concentration of PCM of 300 mg/g and 25 % MCM was used as these showed the production of pure PCM-II in the highest yield. The samples produced from all DoE experiments are currently stable for a period of 15 months, indicating the polymorphic purity of the PCM-II samples produced.

Inputting the responses to the MODDE software resulted in the production of a model which allowed for the effects of factors and interactions between factors to be examined. The yield response showed good model statistics, with the four indicators of R2, Q2, model validity and reproducibility indicating a reliable model. It was shown that a higher concentration of PCM and a longer dwell time at the final temperature of the cooling profile resulted in increased yields. The former would allow crystallisation earlier, resulting in a longer crystallisation time, allowing more time for growth and hence an increased yield. The latter would allow for increased time for growth, again resulting in an increased yield. However, due to an inherent problem with representing a qualitative response quantitatively, the polymorphic form response resulted in poor model statistics. However, general trends could be identified that showed that the stirring rate was an important factor, with a faster stirring rate showing a higher propensity for the production of pure PCM-II in the absence of any MCM·H_2O.

4.2 Scaled crystallisation in the OptiMax

4.2.1 Introduction and aims

The ability to scale systems beyond discovery scale is crucial if a manufacturing method within an industrial setting is to be established. However, with the reduction in mixing efficiency upon scale-up comes the possibility of supersaturation build-up in certain areas of the crystalliser, resulting in potentially different particle attributes and impurity rejection. [200-201] As such, much industrial and academic interest has been dedicated towards developing scalable crystallisation processes.

As many currently operational continuous crystallisers operate on the principle of cooling crystallisation, a large scale cooling crystallisation route to the target PCM-II first had to be developed, which will be the subject of this section. This work was performed in collaboration with Dr Thomas McGlone at the CMAC National Facility housed within the Technology and Innovation Centre at the University of Strathclyde.

4.2.2 Experimental

Initial cooling crystallisations were carried out at the 100 ml scale using the *Mettler Toledo EasyMax* (Figure 4.10), in order to check the transferability between the Polar Bear Plus and this platform, which both operate at the same working volume. One important consideration in this initial transferability investigation was to ensure that the results seen in the laboratory in Bath were not due to accidental seeding of the vessels. These crystallisations also allowed for optimisation of the positioning of the Raman PhAT probe above the crystallisation vessel in order to achieve the optimal spectra.

Figure 4.10: The Mettler Toledo EasyMax

Scaled-up batch experiments were conducted using the *Mettler Toledo OptiMax* (Figure 4.11). Crystallisations were monitored with Raman PhAT and FBRM probes. For all experiments, a *Mettler Toledo* FBRM probe (*G400* series) was used with *iC FBRM V4.3* incorporated in the *iControl V5.2* software. Each measurement was collected with a 2 s scan speed and a 15 s sampling interval.

A *Kaiser RXN2* Raman spectrometer with PhAT probe was used to monitor the polymorphic form produced throughout the process non-invasively. The PhAT probe had the laser beam optically expanded to give a 3 mm spot size, with a focal length of 12.5 mm. The beam was directed at the process through the top of the vessel. The laser wavelength of 785 nm was produced by an Invictus diode laser operated at 350 mW at the source, with a CCD detector cooled to −40 °C by a Peltier cooling system. In advance of any measurements a verification (which measures relative peak intensity and peak position against known peaks from a cyclohexane standard) using the external sample compartment accessory for the instrument was performed. Raman spectra were recorded using *iC Raman V4.1* software, also incorporated in the *iControl* software. Each Raman spectrum was recorded with two scans and a 30 s integration time resulting in one spectrum every 2 minutes.

A PCM concentration of 300 mg/g coupled with 25 wt.% MCM was used throughout all crystallisations. The temperature was lowered from 70 °C to 20 °C through the stepped cooling profile outlined in Chapter 3 at a cooling rate of 1 °C min^{-1}, with an overhead stirring rate of 400 rpm.

Figure 4.11: Mettler Toledo OptiMax with inline process monitoring using a Raman PhAT probe and FBRM probe

4.2.2.1 Characterisation techniques

PXRD patterns were collected on a *Bruker AXS D8-Advance* transmission diffractometer equipped with θ/θ geometry, primary monochromatic radiation (Cu $K\alpha_1$, λ = 1.54056 Å), a Vantec 1-D position sensitive detector (PSD), and an automated multi-position x-y sample stage. Samples were oscillated ±0.5 mm in the x-y plane at a speed of 0.3 mm s^{-1} throughout data collection, to maximize particle sampling and minimize preferred orientation effects.

Offline Raman spectra were collected at the University of Bath using a Renishaw InVia confocal Raman microscope. A red laser of wavelength 785 nm (Renishaw, diode laser, 370 mW at source) was used for all spectra, operated with a 50x lens and a spot diameter of ~1.9 μm.

4.2.3 Raman spectra for the polymorphs of paracetamol

To highlight the differences in Raman spectra between the two polymorphic forms of paracetamol, offline Raman spectra were collected for both polymorphic forms of PCM and for metacetamol (MCM) (Figure 4.12). The two PCM spectra are very closely related, with Table 4.4 highlighting the differences in each spectral region. The assignment of these Raman bands, combined with analysis of the crystal structures of the PCM polymorphs, shows that the bands where differences between the polymorphs are observed relate to Raman modes that would be different between the polymorphic forms; either through differences in hydrogen bonding, torsion angles or packing interactions. For example, the C-C-N-C torsion angle in paracetamol form I is ~22 ° and in form II is ~17 °; this difference could be responsible for the slight shift in peaks in the Raman spectra. The previous analysis by Szelagiewicz *et al* [202] did not account for the differences in spectra above 1260 cm^{-1}; in this region, the main difference is the splitting of the peak at 1624 cm^{-1} in PCM-II; in PCM-I there is no such splitting, with the peak only displaying a slight shoulder. This peak corresponds to the carbonyl stretch and the difference can be attributed to the slight difference in hydrogen bond lengths, and hence strengths, in the polymorphs. Despite its structural similarity to paracetamol, the Raman spectra for metacetamol shows easily discernible differences, with the strong peak at 1007 cm^{-1}, corresponding to the aromatic ring, being the most obvious.

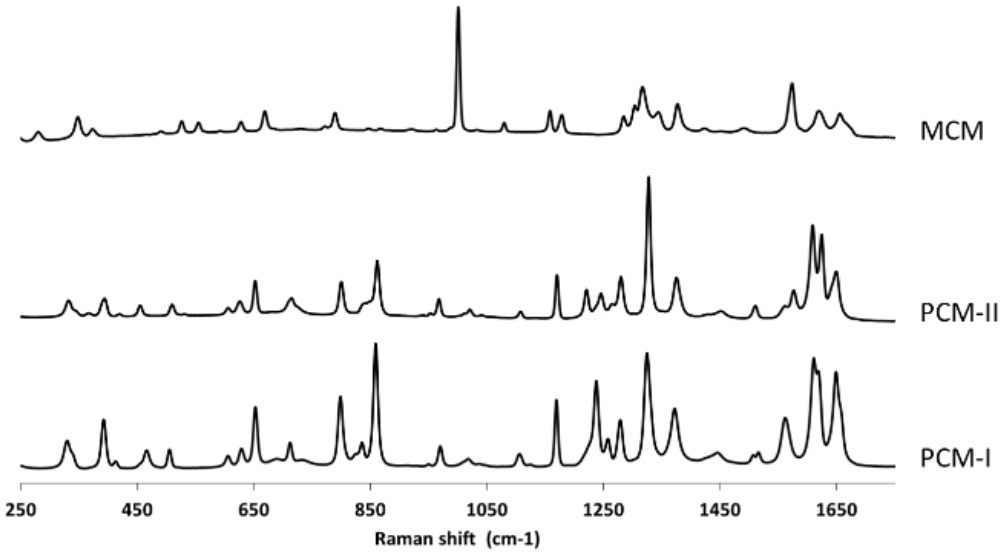

Figure 4.12: Offline reference spectra for PCM-I, PCM-II and MCM; the y axis shows intensity in arbitrary units

Table 4.4: Characteristic Raman bands differentiating PCM-I and PCM-II (adapted from Szelagiewicz et al.[202])

Raman shift (cm^{-1})	Form II (cm^{-1})	Form I (cm^{-1})	Functional group
1200-1260	1242 and 1218-1219	1254-1258 and 1233-1238	Amide
855-865	860	857-859	C-C ring stretch
790-810	797-798	795-798	C-N-C ring stretch
450-470	451-452	460-466	O-H vibration
200-220	200-201	207-215	C-C stretch (chain)

4.2.4 Results and discussion

An initial cooling crystallisation performed in the EasyMax showed the production of PCM-II to be transferable from the Polar Bear set-up at the same 100 ml scale, verifying the results obtained from the DoE. However, PXRD analysis indicated that there were still trace levels of MCM·H_2O in the solid product. It is likely that this is due to the different mixing conditions experienced in the EasyMax in comparison to the RBF due to different vessel shape and use of a different impeller. Owing to time constraints, further work was not conducted at this scale in order to optimise the system and focus was directed towards trying to scale the system further, utilising the OptiMax.

Initial experiments in the OptiMax were conducted using a working volume of 500 ml. The positioning of the Raman PhAT probe at the top of the vessel, through one of the holes in the lid, meant that this lower working volume resulted in a distance from probe to solution longer than any focal length obtainable with the varying spot sizes, meaning the spectra obtained from the Raman

probe were poor and largely dominated by fluorescence. As such, further experiments utilised a larger working volume of 800 ml.

Determination of the polymorph specific bands shown in Table 4.4 allowed for a peak in the Raman spectrum corresponding to PCM-II (1624 cm^{-1}) and one corresponding to PCM-I (1236 cm^{-1}) to be tracked throughout the crystallisation, to allow rapid elucidation of the polymorphic form being produced. At the point of nucleation in the system (characterised by the sharp increase in total FBRM counts in Figure 4.13), the peak characteristic of PCM-II increases and that of PCM-I drops off and remains level for the remainder of the crystallisation. The peak for PCM-I does not drop to a zero value as the probe still detects paracetamol dissolved in solution, with the signal for PCM-I and dissolved PCM being indistinguishable. The total FBRM counts remain roughly constant towards the end of the experiment, indicating steady state has been achieved.

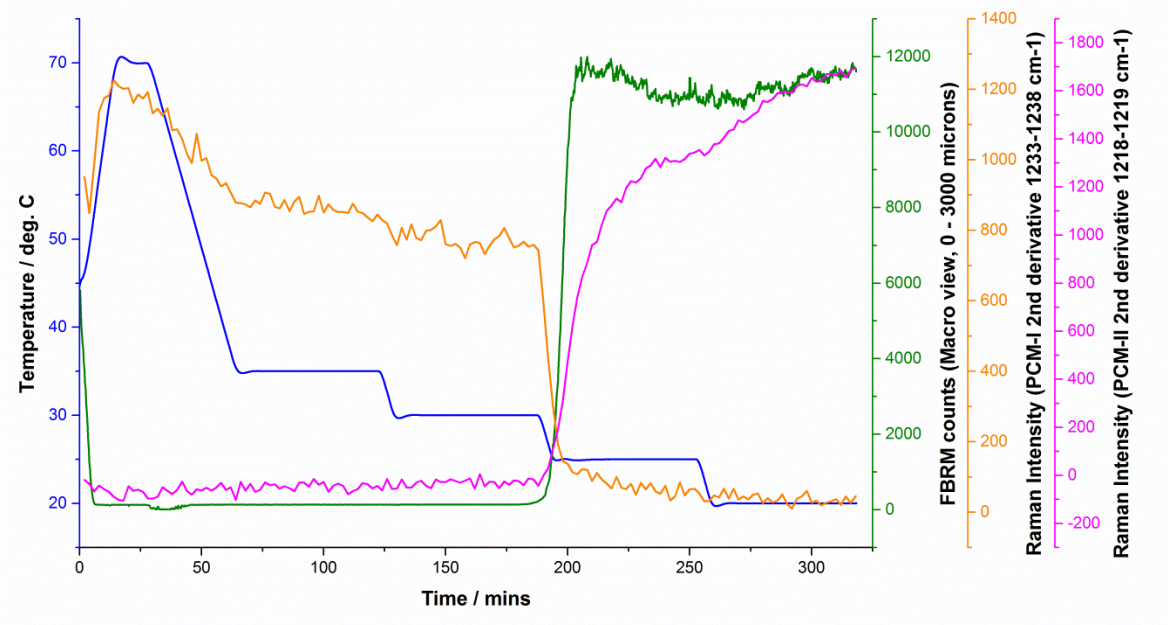

Figure 4.13: Trend output from 800 ml crystallisations in the OptiMax showing the temperature profile employed (blue), total FBRM counts (green), PCM-I Raman at 1236 cm^{-1} (orange) and PCM-II Raman at 1624 cm^{-1} (pink)

Figure 4.14 shows the change in the spectra produced from the inline Raman probe over the course of the crystallisation. The dominant production of PCM-II at the end of the crystallisation (300 mins) is confirmed by the characteristic splitting of the peak at 1624 cm^{-1}, circled in red in Figure 4.14. Table 4.5 also highlights the regions of difference specified in Table 4.4, again confirming the presence of PCM-II in all cases. However, the presence of extra peaks, circled blue in Figure 4.14, indicate the presence of another crystalline phase in the solid. Additional PXRD analysis (Figure 4.15) shows this to be metacetamol hydrate; this could not be shown by Raman data as phase pure samples of MCM·H_2O were unable to be obtained. This scaled-up batch crystallisation route allowed for the production of 120 g of PCM-II in a single process run with no evidence of the

presence of PCM-I. This high degree of scalability offers confirmation of the robustness of the process devised to produce PCM-II using MCM as a template molecule.

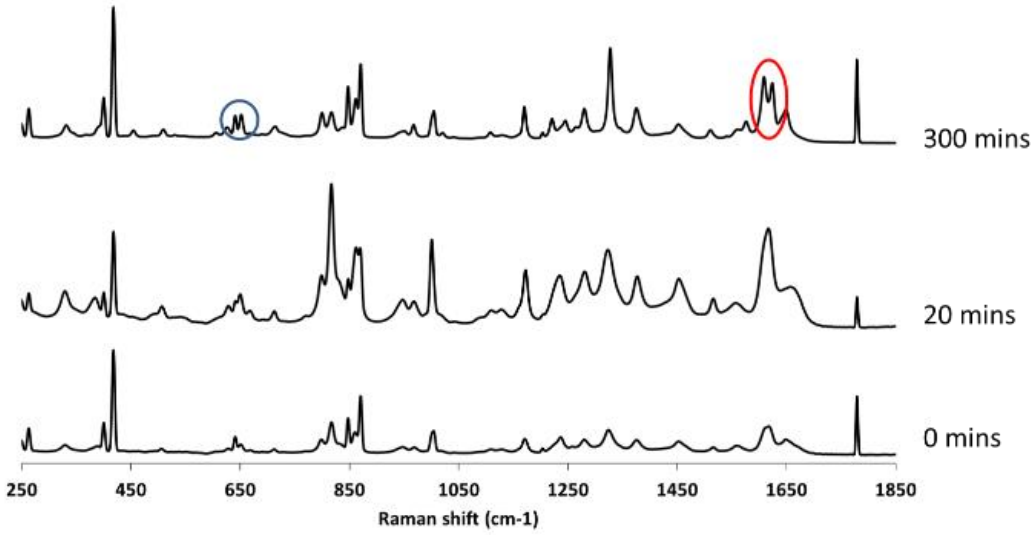

Figure 4.14: Raman spectra collected throughout the course of the crystallisation from the inline PhAT probe (0 mins - suspension, 20 mins - after dissolution of all solid, 300 mins - suspension of final product at end of crystallisation). The y-axis shows intensity in arbitrary units

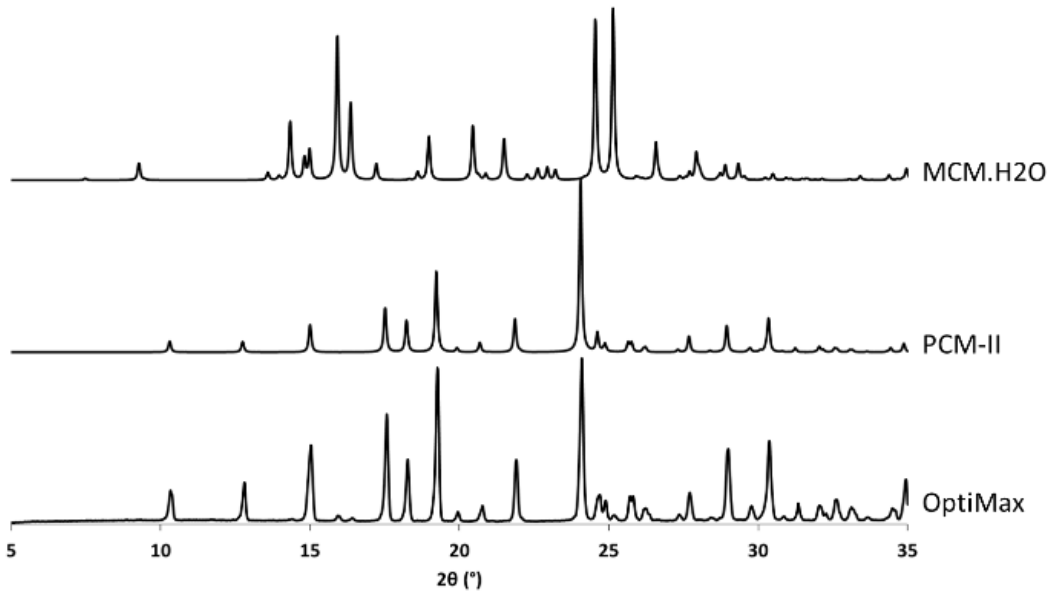

Figure 4.15: PXRD patterns confirming the presence of PCM-II in the OptiMax experiment, with small quantities of MCM·H_2O present; the y-axis shows intensity in arbitrary units

Table 4.5: Each of the spectral regions where differences between PCM-I and PCM-II are visible, showing the shape of the patterns from final product (green) to match PCM-II (orange) and not PCM-I (blue) in all regions

Spectral region (cm^{-1})	Raman
200-220	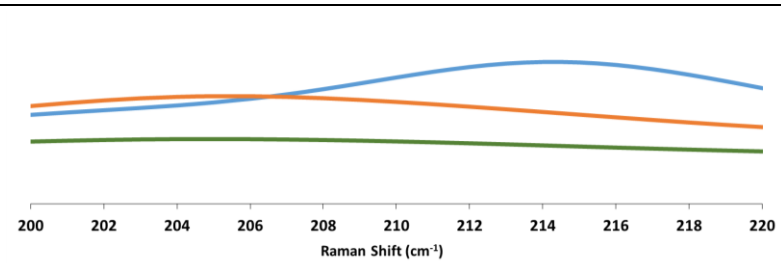
450-470	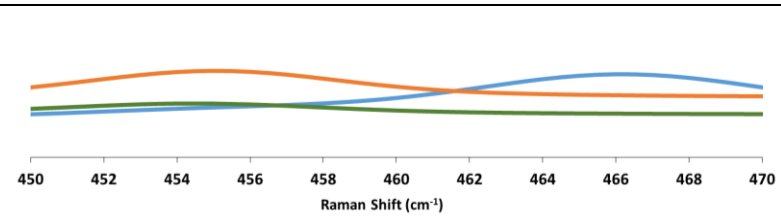
790-810	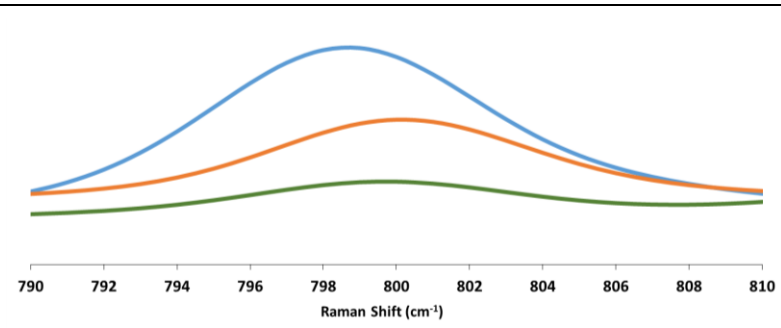
855-865	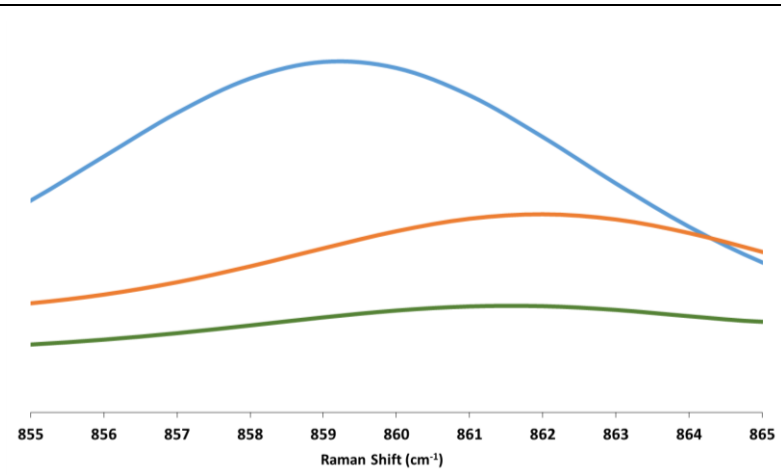
1200-1260	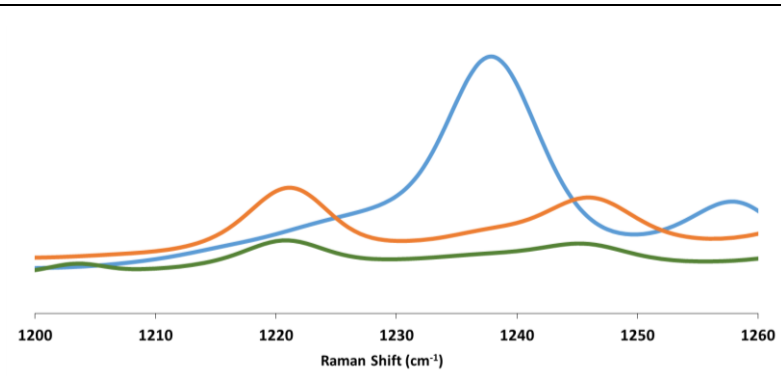

4.2.5 Conclusions

A scalable batch crystallisation route to PCM-II has been developed, allowing production of 120 g of PCM-II in a single process run. However, the solid produced on all scales investigated contains small quantities of metacetamol hydrate impurity, present at levels high enough to be detected through PXRD analysis. It can be suggested that the presence of this MCM·H_2O impurity is due to sub-optimal mixing conditions experienced upon scale to larger vessels, with mixing shown to be an important factor in the production of pure PCM-II in the Design of Experiments outlined in Section 4.1. The work was carried out at the University of Strathclyde and due to the time constraints of the visit, optimisation of the large scale batch crystallisation of PCM-II has not been achieved and would be the subject of any future work on this system. However, this work does present the design and implementation one of the only reported large scale productions of a metastable polymorphic form of an API.

4.3 Continuous crystallisation in a MSMPR

4.3.1 Introduction and aims

The drive towards continuous crystallisation processes is becoming more prevalent in an industrial setting. Although much academic research attention has been directed towards developing the huge potential offered by the use of tubular flow crystallisers, owing to their superior heat and mass transfer, to date the industrial application of continuous crystallisation procedures has been focussed on mixed suspension mixed product removal (MSMPR) crystallisers. A batch crystalliser can be modified to a single stage MSMPR by allowing continuous input and removal of solution/slurries, maintaining a constant working volume within the vessel. MSMPR's are the most commonly employed method of continuous crystallisation owing to their applicability to most systems and ability to achieve the long residence times that are needed to crystallise compounds displaying slow nucleation or growth kinetics; this is in contrast to plug flow reactors that require fast kinetics to allow growth in the relatively short residence times characteristic of such reactors.[52, 203] MSMPR systems operate at steady state rather than equilibrium and so residual supersaturation may be left in the mother liquor, resulting in yield reductions; however, this can be combatted through operation in recycle mode.[204]

The use of MSMPR systems is not limited to single stage vessels, with many employing multi-stage MSMPRs in a cascade.[53, 205] It is often the case that the first stage acts a nucleator vessel, producing nuclei of the desired product, with the second stage acting as a growth vessel to allow yield to be maximised.[74] Transfer between vessels can be made through peristaltic pumps, which can result in

damage to particles, or as demonstrated more recently, through vacuum transfer.[53, 190] The use of MSMPRs for the continuous crystallisation of a variety of compounds has been demonstrated including paracetamol form I[55], albuterol sulfate[56], cyclosporine[53] and preferential crystallisation of the enantiomers of threonine.[57] The continuous crystallisation of metastable α-glutamic acid has been reported in an MSMPR[206], the only other reported example of the continuous crystallisation of a metastable organic solid; the continuous crystallisation of inorganic solids has been reported widely in the literature. [207-210]

Unlike traditional operation of MSMPRs, characterised by the continual addition and removal of suspensions, there has been recent work directed towards the use of periodic mixed suspension, mixed product removal (PMSMPR) crystallisers.[54, 211] As the name suggests, these systems allow for the periodic addition and removal of suspensions at a high flow rate over short periods of time.[211] Having periods of dwelling within each vessel allows access to longer residence times and can help with obtaining steady state more rapidly. The use of a PMSMPR crystalliser has been demonstrated for paracetamol form I[54] and for obtaining control over the stable form of a polymorphic co-crystal. [211]

The aim of the work presented in this section is to transfer the templated crystallisation of PCM-II seen in a batch crystallisation environment to an MSMPR continuous crystallisation platform. Through operation of an MSMPR in periodic mode this system should better mimic the stepped cooling profile used in batch cooling crystallisation experiments (Chapter 3) than tubular flow crystallisers (outlined below in Chapter 5).

4.3.2 Experimental

4.3.2.1 Continuous crystallisation experiments

Continuous crystallisation experiments in an MSMPR system were carried out at the AstraZeneca site in Macclesfield; a two-stage MSMPR working in recycle mode was used throughout all experiments. The set-up consisted of a 500 ml jacketed feed/dissolver vessel and two 140 ml jacketed MSMPR vessels (Figure 4.16 and Figure 4.17), each operated at a working volume of 80 ml. To avoid crystal breakage on transfer between vessels, a vacuum transfer system was used to transfer solids from MSMPR 1 to MSMPR 2 and from MSMPR 2 back to the feed/dissolver vessel. A *Masterflex* peristaltic pump, equipped with *Masterflex* tubing was used to transfer the clear solution from the feed vessel to MSMPR 1.

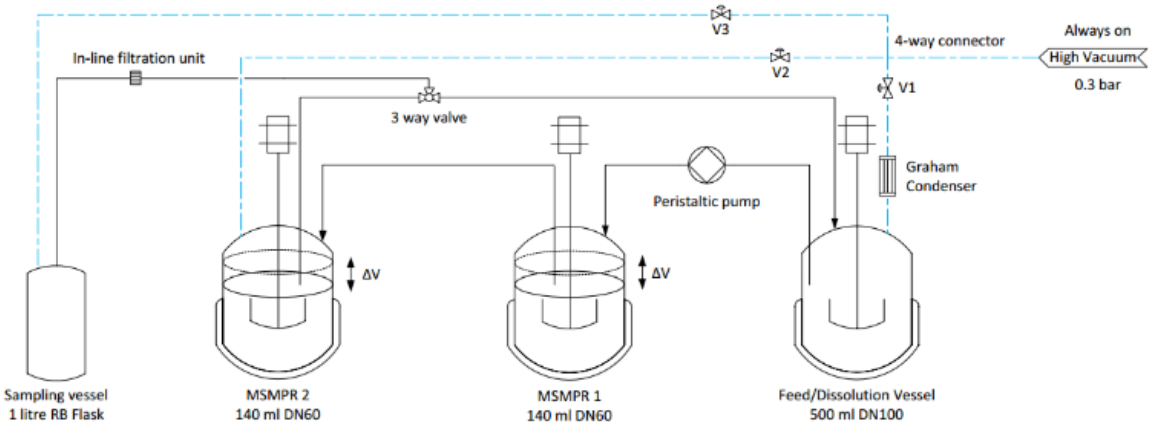

Figure 4.16: Schematic of the MSMPR set-up used

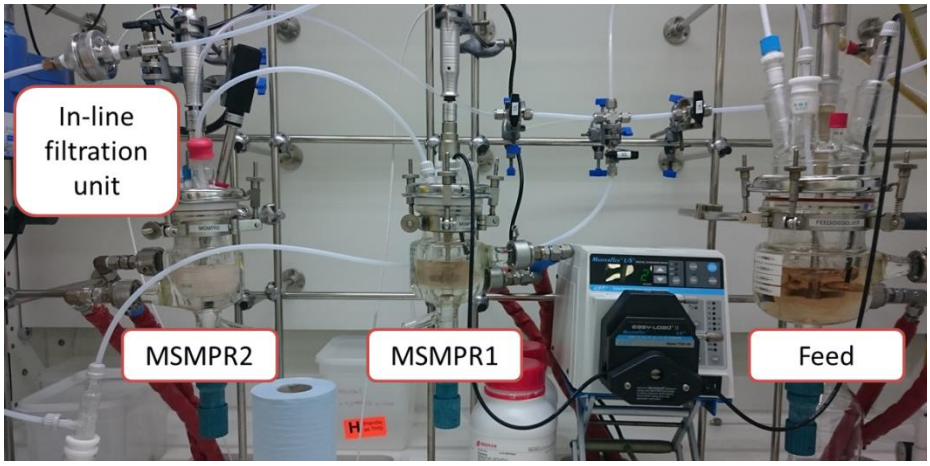

Figure 4.17: The MSMPR set-up at AstraZeneca Macclesfield used in this work with key features labelled

A dip tube was positioned in MSMPR 1 and MSMPR 2 to allow transfer of a calibrated volume (8 ml) between these two vessels and MSMPR 2 and the feed vessel, respectively. As the MSMPR was operated in periodic mode, this transfer was done through manual opening and closing of valves at set time intervals; if the system was to be operated in non-periodic mode, the valves would remain constantly open for the duration of the experiment. The time between transfers was dictated through the residence time within each vessel, with calculations being done based on ten transfers between the two vessels per residence time (RT).

Temperature control was provided by three *JULABO* heater/chiller units operated on control of thermocouple temperature rather than chiller internal temperature. The transfer tube from MSMPR 2 to the feed vessel was fitted with a three-way valve to allow sampling with an inline filtration unit. Filter papers in this filtration unit were changed every residence time to allow for a sample from each residence time to be taken.

Table 4.6 and Table 4.7 highlight the start-up calculations and operational parameters for each of the two residence times (30 minutes and 45 minutes) explored in this work. In all experiments a concentration of PCM of 300 mg/g with 25 wt.% MCM were dissolved in 410 ml of 60:40 (v/v) H_2O:IPA at a temperature of 60 °C with an overhead stirring rate of 250 rpm. Once dissolved, clear solution was pumped through the peristaltic pump at a specified flow rate to MSMPR 1, until a volume of 80 ml in MSMPR 1 was reached. At this point, valve V2 was opened and then closed to transfer 8 ml of solution/slurry to MSMPR 2. The two vessels were left stirring with an overhead stirring rate of 350 rpm for 4.5 minutes or 3 minutes (for a 45 minute and 30 minute residence time respectively). Valve V2 was then opened and closed to transfer 8 ml of solution to MSMPR 2. This process was repeated until the volume in MSMPR 2 reached 80 ml. At this point, both valve V2 (to transfer solution from MSMPR 1 to MSMPR 2) and valve V1 (to transfer solution from MSMPR 2 to the feed vessel) are opened simultaneously. As both vessels have now reached the desired operating volume, this simultaneous opening of V2 and V1 is done each time for the remainder of the experiment. Sampling of solution was done through opening of valve V1 at time points not corresponding to the opening of the valves for transfer of solution. At the end of the experiment, the contents of MSMPR 1 and MSMPR 2 were removed and filtered to isolate the solid for analysis.

4.3.2.2 Characterisation techniques

PXRD patterns and DSC traces were collected at AstraZeneca. The PXRD samples were mounted on silicon wafer mounts and analysed using a Bruker D4 X-ray diffractometer (Cu-Kα radiation, λ = 1.5418 Å) equipped with a LYNXEYE detector. Each sample was exposed for 0.32 s per 0.02° 2θ increment (continuous scan mode) over the range 2° to 40° in θ-θ mode. The X-ray generator was operated at 40 kV and 40 mA. DSC studies were carried out using a Thermal Advantage Q2000 from TA Instruments. Up to 3 mg of material was contained in an aluminium pan, fitted with a lid, and heated over the temperature range 25−200 °C at a constant heating rate of 5 °C min^{-1}. Data were collected using the software Advantage for Qseries (Ver. 5.40 software © 2001−2011 TA Instruments-Waters LLC). Imaging was performed on a Hitachi TM-1000 scanning electron microscope (SEM) operating with an accelerating voltage of 15 kV. Samples were mounted on an aluminium stub with carbon tab and gold coated in a Quorum Q150R sputterer to a target thickness of 10 nm.

Table 4.6: Operating parameters and start-up calculations for experiments operated with a 45 minute residence time

	OPERATING PARAMETERS					START-UP CALCULATIONS			
Vessel	**V_{MAX} (ml)**	**V_{MIN} (ml)**	**Operating volume (ml)**	**Flow rate (ml/min)**	**Residence time (min)**	**Initial Volume to pump (ml)**	**Time to pump initial volume**	**Transfer interval (mins)**	**Transfers per residence time**
Feed	500	200	250	1.8	140.6	-	-	-	-
MSMPR1	160	80	80	1.8	45.0	80.0	45.0	4.5	10
MSMPR2	160	80	80	1.8	45.0	80.0	90.0	4.5	10

Table 4.7: Operating parameters and start-up calculations for experiments operated with a 30 minute residence time

	OPERATING PARAMETERS					START-UP CALCULATIONS			
Vessel	**V_{MAX} (ml)**	**V_{MIN} (ml)**	**Operating volume (ml)**	**Flow rate (ml/min)**	**Residence time (min)**	**Initial Volume to pump (ml)**	**Time to pump initial volume**	**Transfer interval (mins)**	**Transfers per residence time**
Feed	500	200	250	2.7	93.8	-	-	-	-
MSMPR1	160	80	80	2.7	30	80.0	30.0	3.0	10
MSMPR2	160	80	80	2.7	30	80.0	60.0	3.0	10

4.3.3 Results and discussion

Table 4.8: Experimental Conditions and Output from MSMPR experiments

Exp	RT (mins)	T_{FEED} (°C)	T_{MSMPR1} (°C)	T_{MSMPR2} (°C)	Product	Supersaturation ratio (S)
AZ1	45	60	25	20	PCM-II + PCM-I + MCM·H_2O	1.63
AZ2	45	60	30	25	PCM-II	1.03
AZ3	45	60	30	25	PCM-II	1.03
AZ4	30	60	30	25	PCM-II	1.03

Table 4.8 highlights the experimental parameters investigated in the MSMPR continuous crystallisation experiments; note the supersaturation ratio is calculated at the point of nucleation, relative to PCM-II. As the effect of using this set-up on the metastable zone width (MSZW) of the crystallisation was not known, the temperature of the final MSMPR in experiment AZ1 was set at 20 °C, which considering batch crystallisation experiments nucleate at 30 °C, should allow for crystallisation in the system. Crystallisation in the system was observed initially in MSMPR 2 after the third transfer in RT2 (i.e. after 59 minutes), with a dense slurry being observed in MSMPR 2 by the end of RT3. The high solid loadings produced in this experiment resulted in settling of solid in the vacuum transfer lines (Figure 4.18); although in this experiment this did not result in blockage, over extended operation times this settling could become detrimental to the crystallisation process either through blockage of transfer lines or of possible conversion to the stable PCM-I and subsequent seeding.

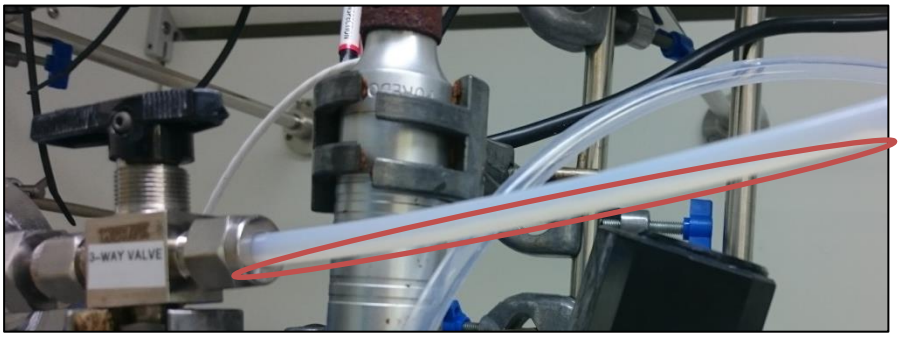

Figure 4.18: Settling of solid in vacuum transfer lines

Solid from each of the residence times along with the solid from both MSMPR vessels at the end of the crystallisation were analysed by PXRD (Figure 4.19), DSC (Figure 4.20) and SEM (Figure 4.21).

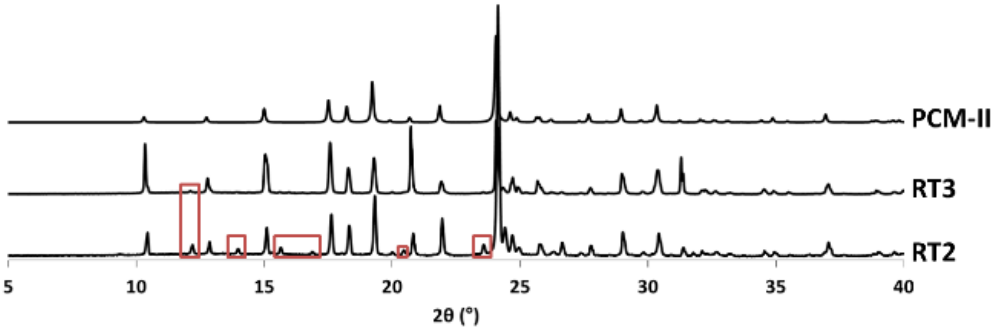

Figure 4.19: PXRD analysis of RT2 and RT3 of experiment AZ1 showing the production of predominately PCM-II with some PCM-I present (peaks corresponding to PCM-I boxed in red). The y-axis shows intensity in arbitrary units.

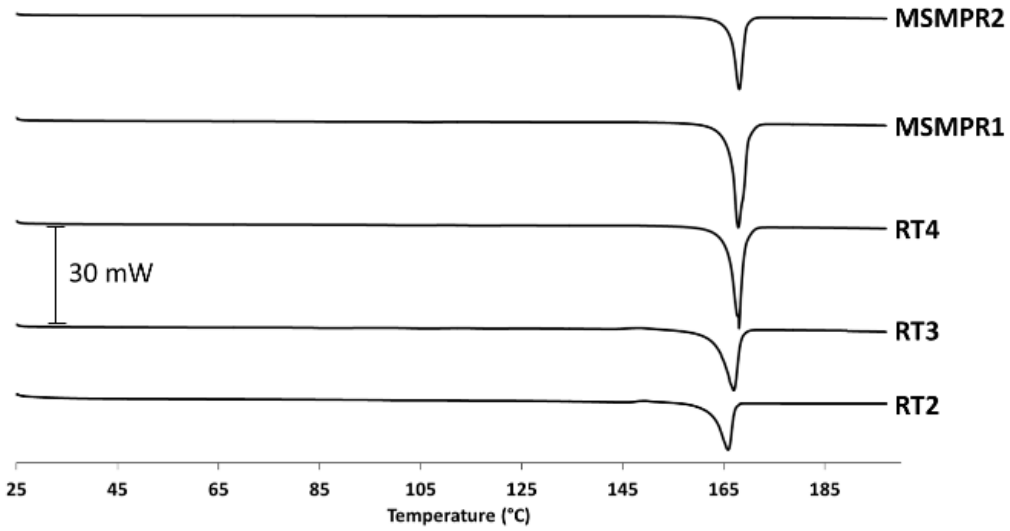

Figure 4.20: DSC analysis on the samples taken from experiment AZ1; the y axis shows heat flow in mW.

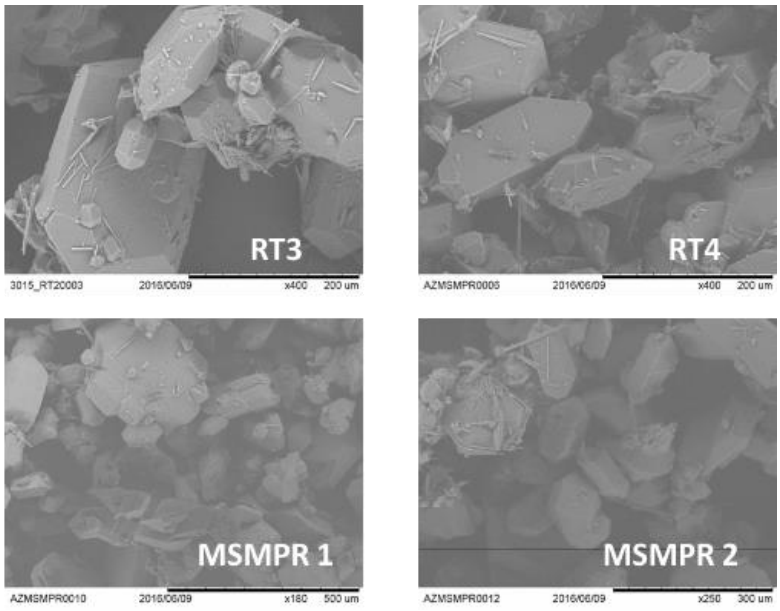

Figure 4.21: SEM images for the samples from experiment AZ1 (RT2 was not analysed due to the small amount of solid available).

PXRD analysis confirms the production of predominately PCM-II, however there are peaks corresponding to another crystalline form. These are not from MCM·H_2O, as would be expected, but correspond to the presence of PCM-I. Interestingly, looking at the SEM images, all residence times display large block like crystals that can be attributed to PCM-II. On the surface of these crystals are finer, needle crystals. It can be suggested that these needle crystals can be attributed to PCM-I; in contrast, SEM from batch crystallisation experiments show metacetamol hydrate to adopt a block morphology on the surface of PCM-II crystals (Chapter 3). Literature work has always suggested PCM-I adopts a hexagonal block-like morphology, with PCM-II adopting a needle-like morphology.[24, 180] Block-like morphologies are likely to have more desirable flow properties than needles and perform better in downstream processing steps such as filtration and charging in the drug product process, so this alteration in morphology of PCM-II offers an additional advantage to the templating approach adopted in this work. It can be suggested that this nucleation of PCM-I is due to crystallisation at a higher supersaturation ratio, which would result in less controlled nucleation. Further, as crystallisation was initially observed in MSMPR 2 when the volume was low, the different mixing dynamics at the volume may have induced nucleation of PCM-I. The DSC analysis does show small quantities of MCM·H_2O to be present in earlier residence times, through the presence of a thermal event at 145 °C.

As such, for future experiments (AZ2-4), the temperature of MSMPR 2 was increased to 25 °C and correspondingly the temperature of MSMPR 1 to 30 °C, reducing the supersaturation ratio at the point of nucleation, hence providing greater control over crystallisation. Experiment AZ2 and AZ3 were executed with the same experimental parameters, however experiment AZ3 was run for a longer period of time (*c.a.* 5 hours) to see whether the polymorphic form outcome could be retained over longer operation times. In both cases, crystallisation was observed whilst still filling MSMPR 2, in RT1. It can be suggested that crystallisation was observed earlier due to a reduction in cooling rate, narrowing the MSZ, as a result of increasing the temperatures of the two MSMPR vessels. Upon discharging remaining solid from the two MSMPR vessels, encrustation on the vessel walls was observed in MSMPR 2 (Figure 4.22).

Figure 4.22: Encrustation on the walls of MSMPR 2 in experiments AZ2 and AZ3.

Offline characterisation of the solid produced from each residence time and the discharged solid from each of the two MSMPR vessels shows the production of PCM-II (PXRD; Figure 4.23) in the absence of any metacetamol hydrate (DSC; Figure 4.24). This MSMPR run has thus been successful in producing phase pure PCM-II, with no impurity phases present in the solid product.

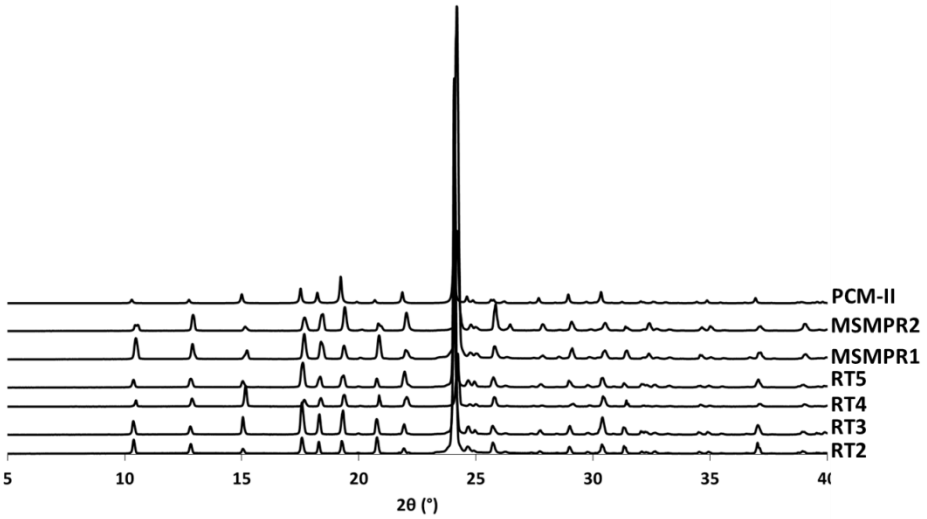

Figure 4.23: PXRD patterns showing the production of PCM-II in Experiment AZ3. The y-axis shows intensity in arbitrary units.

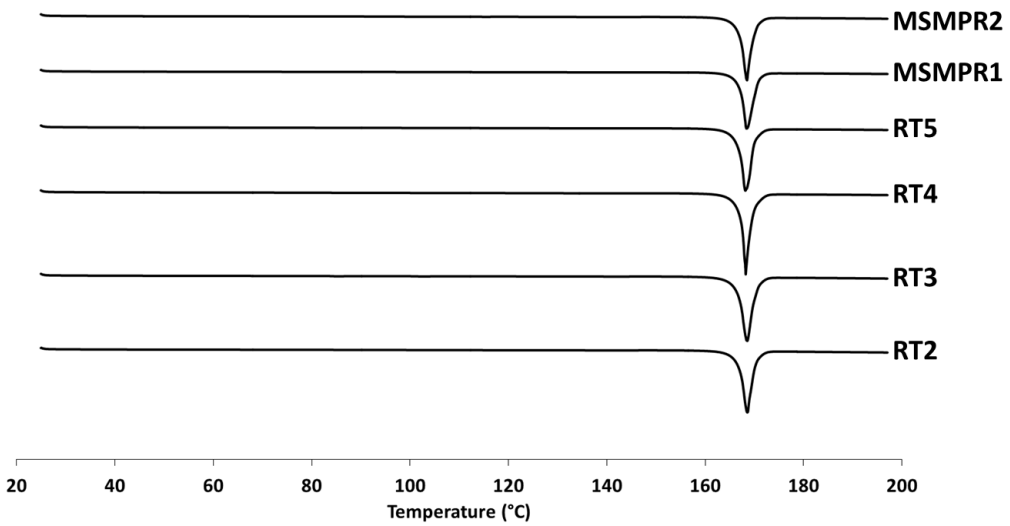

Figure 4.24: DSC traces for experiment AZ3, showing the absence of any MCM.H_2O. The y-axis shows heat flow in mW.

Due to time constraints, for the SEM analysis, images were only taken of the samples from each of the MSMPR vessels at the end of the experiment. These images (Figure 4.25) show the production of large diamond-shaped crystals of PCM-II. Since all analytical methods indicate the absence of any MCM·H_2O, the smaller crystals present in the SEM images can be attributed to either crystal breakage or to crystals that have not had as much time for growth; the latter explanation is more likely as these small crystals are seen more in MSMPR 1.

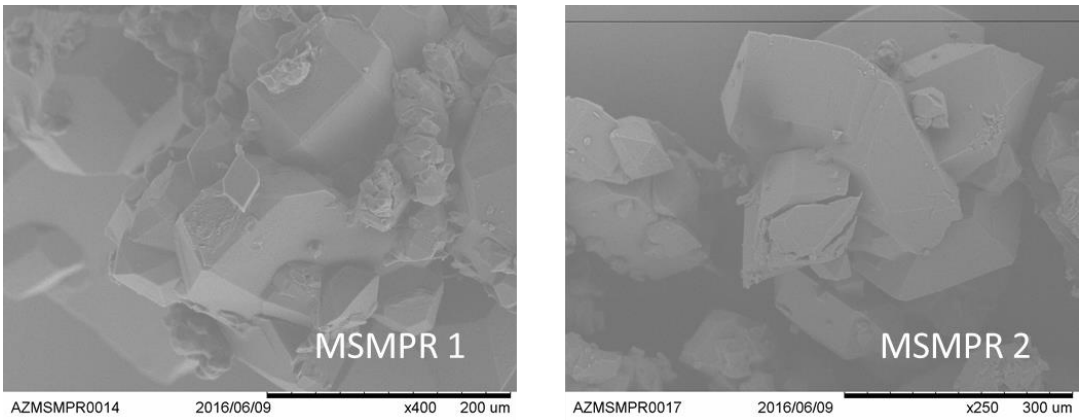

Figure 4.25: SEM analysis of samples from each of the MSMPR vessels in Experiment AZ3

The final experiment, AZ4, investigated a reduction in the residence time within the crystalliser to observe whether the polymorphic form outcome could be retained. Reducing the residence time, whilst maintaining the correct polymorphic form, would be beneficial as it would allow for shorter operation times and hence higher throughput, increasing plant productivity. After 30 minutes of operation, the solution in MSMPR 1 appeared turbid, indicating the onset of nucleation, with crystallisation following shortly. Crystallisation in MSMPR 2 was observed at the end of RT2. This difference in point of crystallisation can be attributed to the faster pumping rate of solution into

the MSMPRs associated with a shorter residence time, which could alter the kinetics of the crystallisation process. Blockage of the inline filtration unit (Figure 4.26) meant that a sample for RT3 was unable to be collected.

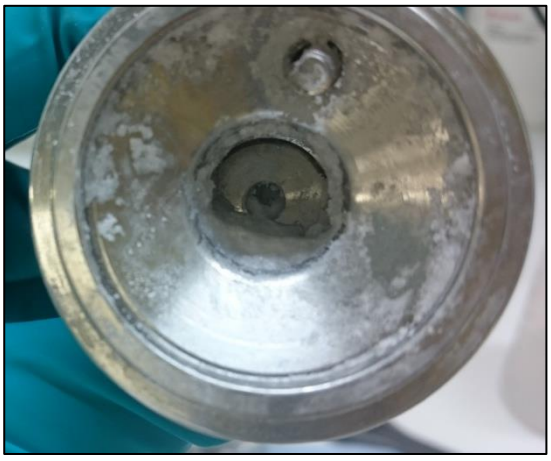

Figure 4.26: Blockage of the inline filtration unit in experiment AZ4

PXRD (Figure 4.27) and DSC analysis (Figure 4.28) shows the production of PCM-II in the absence of any MCM·H_2O. SEM analysis (Figure 4.29) again shows the production of large diamond shaped crystals, attributed to PCM-II.

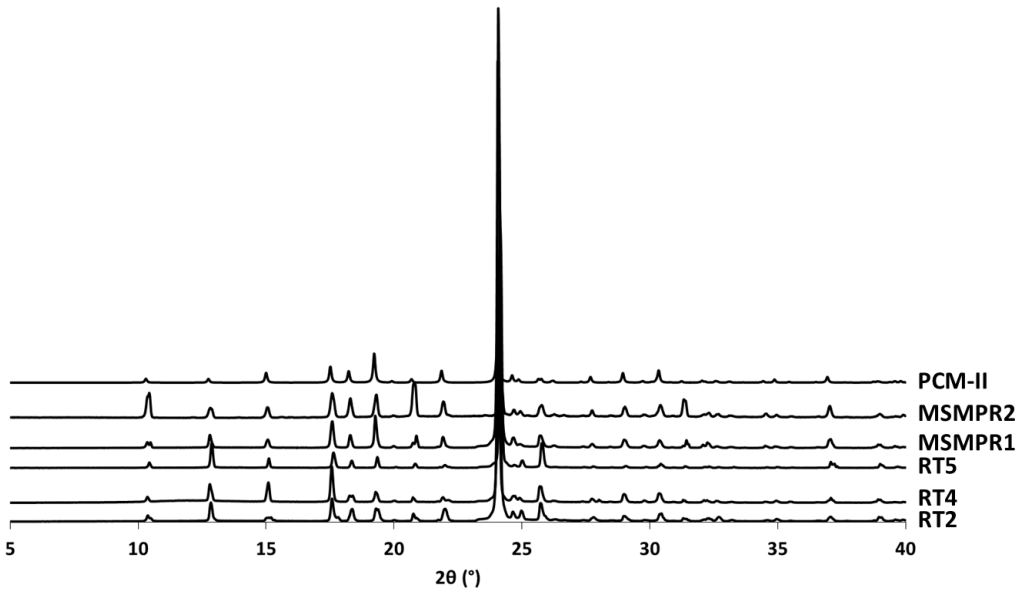

Figure 4.27: PXRD patterns of the solids produced in experiment AZ4; the y-axis shows intensity in arbitrary units

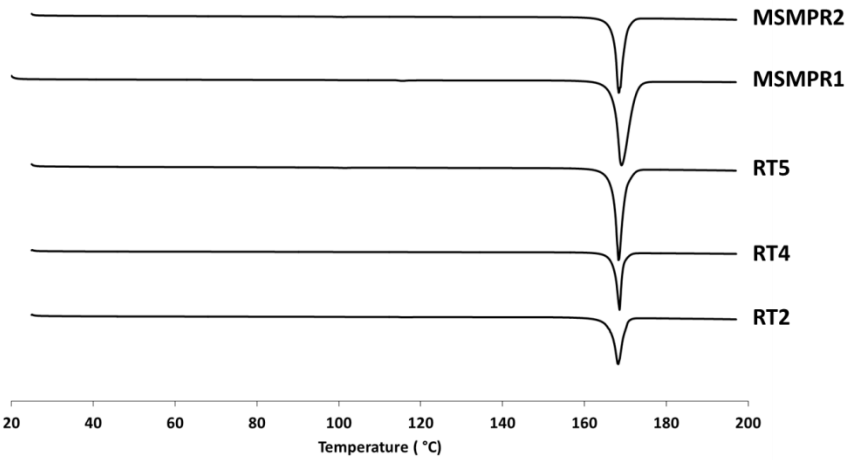

Figure 4.28: DSC traces for experiment AZ4, indicating the absence of any MCM·H_2O. The y-axis shows heat flow in mW

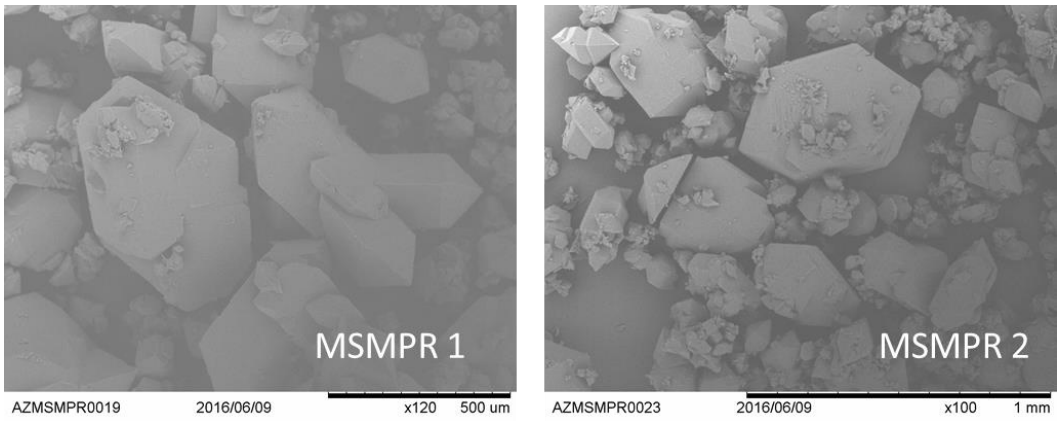

Figure 4.29: SEM analysis of samples from each of the MSMPR vessels in Experiment AZ4

The samples produced in experiments AZ2-4 display a high degree of polymorphic purity, with the samples stable as PCM-II for a period of a year at the time of writing (Figure 4.30), with no peaks indicating conversion back to the thermodynamically stable PCM-I. Using knowledge from the doping experiments outlined in Chapter 3, which showed that the presence of 1 wt.% or greater of PCM-I in a PCM-II sample would catalyse the process of conversion back to PCM-I within one month, it can be concluded that the samples produced in these experiments display a high polymorphic purity.

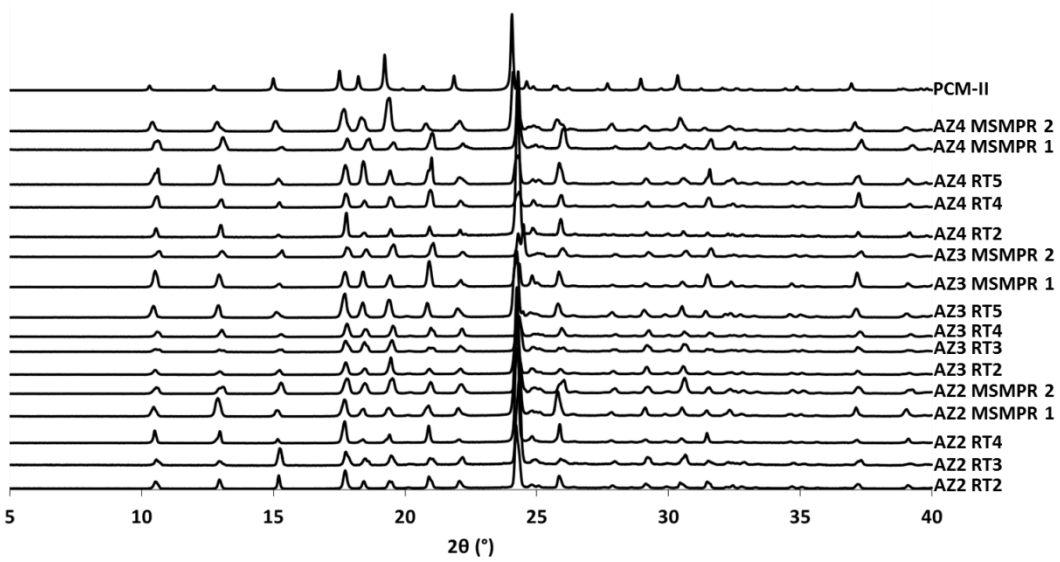

Figure 4.30: 12 month stability PXRD patterns for samples produced in experiments AZ2, AZ3 and AZ4; the y-axis displays relative intensity in arbitrary units

Similar stability analysis was performed on the samples from Experiment AZ1, where some samples showed the presence of PCM-I initially at the point of crystallisation. The 12 month stability analysis shows peaks corresponding the presence of PCM-I appearing in all samples (boxed in red in Figure 4.31); these peaks were not present in initial samples for RT4, MSMPR 1 and MSMPR2, confirming the peaks are due to the solid-solid PCM-II to PCM-I transformation.

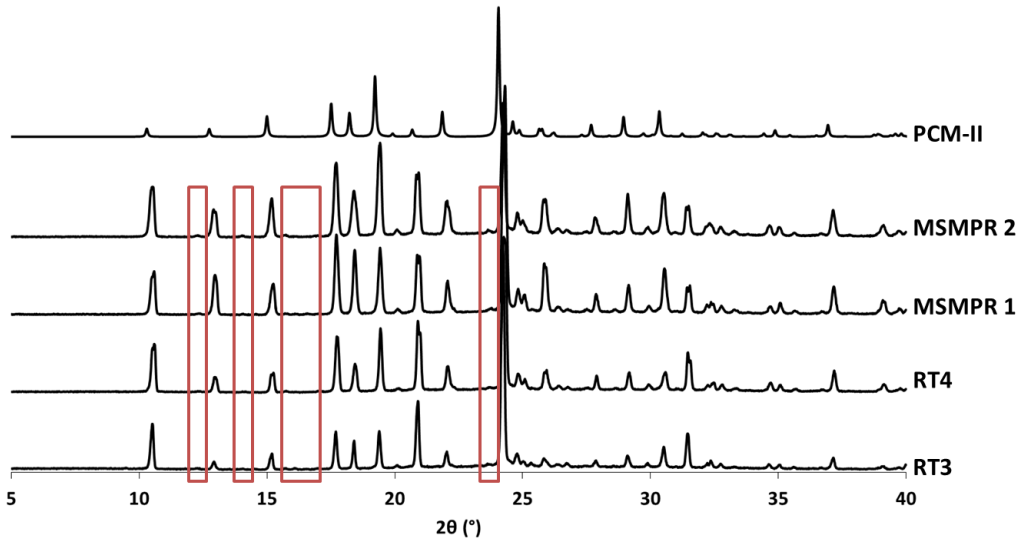

Figure 4.31: 12 month stability PXRD patterns for samples produced from AZ1 with peaks corresponding to PCM-I boxed in red; the y-axis displays intensity in arbitrary units

Literature has suggested that MSMPR systems tend to be useful for systems that display slower nucleation and growth kinetics; the presence of MCM in the crystallisation process widens the metastable zone width and increases the induction time to nucleation, resulting in slow nucleation kinetics, making the MSMPR crystalliser suitable for this system. Further, the Design of Experiments

outlined in Section 4.1 indicated the importance of stirring time at final temperature for increased yields of crystallisation. Operation of an MSMPR system in periodic mode would allow for these enhanced yields to be obtained, a contrast to flow crystallisers where growth time is limited by the residence time within the crystalliser due to the continuous flow of solution.

4.3.4 Conclusions

A two-stage periodic MSMPR operated in recycle mode, utilising vacuum transfer between the vessels, has allowed for the production of samples of PCM-II with high chemical and polymorphic purity. This crystallisation platform eliminates the metacetamol hydrate impurity that has been problematic in batch crystallisation environments and produces samples of PCM-II that display good stability with respect to the solid state transformation to the thermodynamically stable PCM-I. PCM-II has been successfully crystallised in three operational runs, with an initial experiment producing samples of PCM-II with trace quantities of PCM-I. This PCM-I was eliminated from succeeding experiments through alteration of the temperature profile, allowing more controlled crystallisation at a lower supersaturation ratio. The experiments investigated two different residence times and were operated for a maximum of *c.a.* 5 hours whilst retaining the polymorphic form outcome. These experiments represent the first reported continuous crystallisation of a metastable polymorphic form of an API.

Use of this MSMPR system in periodic mode better mimics the stepped cooling profile used in batch crystallisation experiments, giving more control over the crystallisation. The MSMPR set-up employed here is thus well suited for the crystallisation of PCM-II in the presence of MCM as it allows for the longer residence times required to crystallise systems which display slow nucleation kinetics.

4.4 Chapter Conclusions

A Design of Experiments (DoE) approach has been used in order to investigate the effect of five factors on the polymorphic form and yield outcomes in the batch crystallisation of PCM-II in the presence of MCM as a templating molecule at the 100 ml scale. These experiments showed that the time at the final temperature and concentration of PCM were important factors in the yield outcome; increasing the time and increasing the concentration of PCM resulted in the highest yields due to an increased time for growth. Due to the inherent problem of representing a qualitative polymorphic form outcome as a quantitative response, the model produced for this response displayed poor statistics. However, general trends could be identified and it was found that the stirring rate was the most important factor in the polymorphic form outcome, with a higher stirring

rate resulting in a higher propensity to form PCM-II in the absence of any MCM·H_2O impurity. This DoE investigation allowed for the optimal concentration of PCM and percentage of MCM for future experiments to be determined, as well as allowing for an explanation for some observations seen both in this Chapter and in Chapter 5 below.

Once the optimal concentration of PCM and MCM had been determined, work at the CMAC National Facility at the University of Strathclyde looked at scaling the production of PCM-II through this templated crystallisation. Initial investigations with the EasyMax, which operates at the same working volume as the DoE work performed at Bath, showed the production of PCM-II to be rapidly transferable between the two different platforms. Scaled-up experiments were conducted using the OptiMax operating at a working volume of 800 ml, with the crystallisation monitored through inline process analytical technologies: a Raman PhAT probe to monitor the polymorphic form and an FBRM probe to help track nucleation events. Tracking of a peak in the Raman unique to PCM-II showed the nucleation of this form at the point of nucleation of the system, characterised by an increase in FBRM counts. Raman data at the end of the crystallisation from the PhAT probe, combined with PXRD analysis, showed the production of PCM-II with some MCM·H_2O impurity present. It can be suggested that MCM·H_2O was present in large enough quantities to be detectable through PXRD due to less efficient mixing at the larger volume required at this larger scale; at an industrial scale this could be combatted through the use of multiple impellors along the shaft.

A two-stage MSMPR crystalliser, at AstraZeneca in Macclesfield, allowed for investigations into the continuous crystallisation potential of the templated production of PCM-II with MCM as a template molecule. The crystalliser was operated periodically in recycle mode, with an in-line filtration unit to provide sampling of the crystallisation, with vacuum transfer used to transfer solution/slurry between the vessels. Initial crystallisations whereby the temperature of MSMPR 1 and MSMPR 2 were set at 25 °C and 20 °C, respectively, resulted in the production of PCM-II with small quantities of PCM-I present. A further three experiments were performed with the temperatures of MSMPR 1 and MSMPR 2 at 30 °C and 25 °C respectively, investigating a residence time within each MSMPR of 45 minutes and 30 minutes. Both residence times resulted in the crystallisation of PCM-II with a high level of both polymorphic and chemical purity. Samples produced displayed good stability with respect to the solid state transformation to PCM-I, indicating a polymorphically pure sample. PXRD and DSC analysis did not detect any MCM·H_2O in any of the solid products from these three crystallisation experiments. Experiments were run for a maximum of five hours, with retention of the production of phase pure PCM-II throughout all residence times. Morphology analysis of the samples produced *via* SEM images show the production of a diamond-shaped, block morphology

for the samples of PCM-II; this would be favourable in terms of ease of filtration and downstream processability, an added benefit of this templated crystallisation method. These experiments represent the first reported successful continuous crystallisation of a metastable polymorphic form of an API, showing that the scalable production of these forms that display enhanced physical properties is now a distinct and real possibility.

5 Continuous flow crystallisation of PCM-II

Some of the work presented in this chapter has been published as part of a Crystal Growth and Design special issue of selected papers presented at the 12th International Workshop on the Crystal Growth of Organic Materials (CGOM12 Leeds, UK):

L.R. Agnew, T. McGlone, H.P. Wheatcroft, A. Robertson, A.R. Parsons and C.C. Wilson, 'Continuous Crystallization of Paracetamol (Acetaminophen) Form II: Selective Access to a Metastable Solid Form', ***Cryst. Growth Des.,*** **2017, 17(5), 2418-2427**

Although much industrial application of continuous crystallisation has been focussed on MSMPR crystallisers (as outlined in Chapter 4), owing to the ease of adapting existing batch crystallisation vessels, much academic interest in the area of continuous crystallisation has been dedicated towards the use of tubular flow crystallisers. These are of particular interest owing to their superior heat and mass transfer properties and may therefore offer significant opportunities for scalable continuous manufacturing processes based on crystallisation of molecular systems. [49, 51, 58, 65-66]

Flow chemistry for synthetic purposes has become more prevalent over the past few decades[212-213], reflecting interest in the opportunities offered by available and emerging technologies in this area. However, it is only within recent years that continuous flow crystallisation has attracted increased interest, with centres such as the EPSRC CMAC Future Manufacturing Hub and the joint MIT-Novartis Center for Continuous Manufacturing pioneering the way towards establishing the technical and scientific background required for the adoption of these manufacturing methods. The work in this Chapter will look at transferring the templated crystallisation of PCM-II described in Chapters 3 and 4 into two continuous flow crystallisation platforms.

5.1 Continuous crystallisation in the COBC

5.1.1 Introduction and Aims

The continuous oscillatory baffled crystalliser (COBC) (Figure 5.1), originally developed by NiTech Solutions[214], is a tubular crystalliser consisting of a series of jacketed straights and unjacketed bends, contained within which are periodically spaced baffles, intended to generate favourable mixing conditions (Figure 5.1, left). The platform utilises the method of cooling crystallisation in order to generate supersaturation in the system, with the temperatures of each of the straights controlled through a series of circulators.

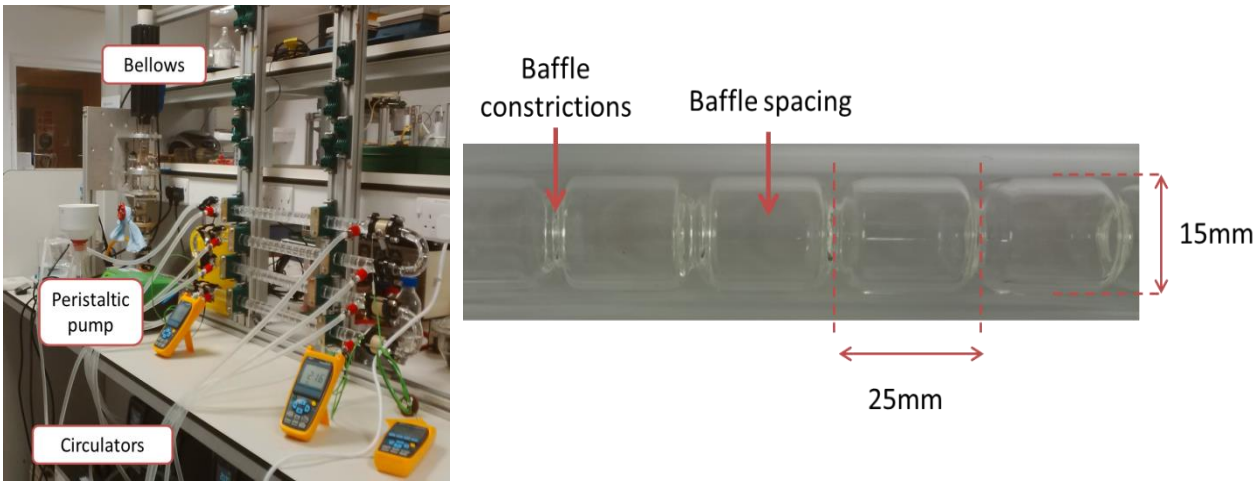

Figure 5.1: The compact 4-straight COBC set-up at the University of Bath (left) with the baffle geometry highlighted (right)

The peristaltic pump imparts net flow to the system; as the solution flows through the baffle constrictions, eddies are generated in the direction of flow (Figure 5.2, upstroke). Combining this net flow from the peristaltic pump and the oscillatory motion generated from the bellows results in the generation of these eddies in the direction opposite to the flow also (Figure 5.2, downstroke). Thus, eddies are generated on each side of the baffle constrictions. These eddies are responsible for the mixing observed within the COBC; each baffle spacing can be considered as a micro batch reactor. The small volumes of fluid within each micro batch reactor combined with the turbulence of mixing, resulting in greater homogeneity, gives the COBC its superior mass transfer characteristics compared with conventional batch crystallisers.

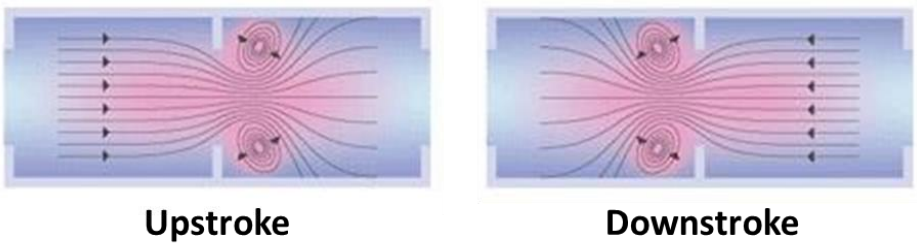

Figure 5.2: The generation of eddies within the baffles in a COBC [211]

As the mixing is governed by oscillation and not net flow, plug flow conditions are achieved even at low flow rates that are usually more conducive to laminar flow. The plug flow conditions ensure that all particles in the crystalliser experience the same environment in terms of temperature, mixing and residence time. The differences between plug flow and laminar flow are illustrated in Figure 5.3, with the arrows representing the velocity of a particle.

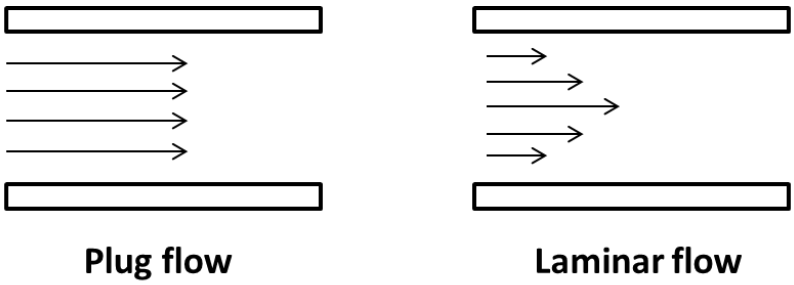

Figure 5.3: Plug and laminar flow through a pipe

Flow within the COBC is governed by three main equations which give rise to dimensionless constants used to describe flow conditions: the oscillatory Reynolds numbers (Re_o), the net flow Reynolds number (Re_n), and the Strouhal number (St).

$$Re_o = \frac{2\pi f \rho d \chi_0}{\mu}$$

$$Re_n = \frac{\rho u d}{\mu}$$

$$St = \frac{d}{4\pi\chi_0}$$

Where f = frequency of oscillation (Hz), ρ = density (kg m^{-3}), d = tubing internal diameter (m), χ_o = centre to peak amplitude (m), μ = viscosity (kg m^{-1} s^{-1}), u = mean velocity (m s^{-1}).

The ratio of the oscillatory Reynolds number to the net flow Reynolds number gives the velocity ratio, φ.

$$\varphi = \frac{Re_o}{Re_n}$$

General guidelines and limits exist for these quantities in order to direct operation under plug flow including $Re_o \geq 100$, St ≤0.5 and $Re_n \geq 50$. The velocity ratio should always exceed 1 (i.e. the oscillation velocity should be greater than the net flow velocity), with values between 2 and 10 advised for operation under plug flow conditions.[58]

The aim of this work was to transfer the templated crystallisation of PCM-II in the presence of MCM to a COBC set-up, optimising the conditions for its formation to obtain polymorphically and chemically pure product.

5.1.2 Experimental

Continuous crystallisation experiments were performed in a 15 mm internal diameter (DN15) COBC mounted in a vertical geometry (Figure 5.1). The feed vessel for the experiments was an unjacketed 5 L RBF fitted with an overhead stirrer, with heating provided by a hotplate *via* a DrySyn® former. For all experiments, a concentration of PCM of 300 mg/g and a 60:40 H_2O:IPA solvent system were used. Full experimental details are given in Table 5.2. Dissolved feed solution was transferred from the feed vessel to the main crystalliser *via* a Watson Marlow 520S peristaltic pump. The peristaltic pump used was calibrated with a variety of oscillation conditions in order to reproducibly obtain a flow rate of 50 ml min^{-1}. Optimal oscillation conditions were chosen based on previous work in the group with succinic acid (Dr A Klapwijk, 2016 PhD Thesis[215]), with which the author assisted, and on advice from the CMAC National Facility. The main COBC set-up consisted of varying numbers of jacketed straight sections (ranging from 4 to 12) and non-jacketed bends; the temperature of the jackets was controlled through four Grant R3 TX150 circulator systems filled with water. Three thermocouples were used to monitor the temperature of the reaction mixture throughout the crystallisation. In all crystallisations there was a good agreement between the jacket and solution temperature.

Before priming of the system, all jackets were set to their crystallisation temperature and allowed to equilibrate whilst the feed solution was dissolving. All air bubbles were removed from the system by initial priming with water. The system was then primed with the crystallisation solvent (60:40 H_2O:IPA) set at a temperature of 55 °C (the temperature of the feed solution). The inlet tube was then transferred to the heated feed vessel; temporary pausing of the oscillation and flow allowed for minimisation of any further air ingress into the system. Oscillation in the system was controlled through a bellows set up (note: due to pressure build up the bellows were operated only partially full).

Solids were collected through a tube connected to an outlet piece and separated immediately from solution through vacuum filtration. Solids were collected for each residence time (RT). In this work a distinction between residence time and solid residence time is made. Residence time is defined as the period of time spent within the crystalliser. The first residence time of all COBC experiments consists of replacing the priming solvent that is already in the crystalliser with saturated solution. Unless the system displays very fast nucleation kinetics, very little crystallisation would be seen in this first residence time. Solid residence time is calculated based on the residence time in which solid is first observed i.e. in most cases COBC RT2 = solid RT1.

5.1.2.1 Characterisation techniques

PXRD and DSC analysis were performed on all samples to determine the solid form produced and, based on key outcomes indicated from batch and MSMPR investigations presented in Chapters 3 and 4, to detect any trace quantities of MCM·H_2O.

Quantitative NMR analysis was performed with the Bruker Avance II+ 500 MHz spectrometer with BBFO probe at 298 K. Samples were dissolved in D_2O and spectra were referenced to the residual solvent peak (δ = 4.79 ppm). ^{1}H NMR of PCM and MCM were performed to act as reference samples and highlight differences in the spectra (Table 5.1). The differences in the two spectra are seen in the aromatic region, owing to the differing substitution positions in the two isomers.

Table 5.1: Chemical shift information for the NMR spectra of PCM and MCM

PCM			MCM		
δ (ppm)	**Splitting**	**Integral**	**δ (ppm)**	**Splitting**	**Integral**
Methyl protons					
2.14	Singlet	3	2.16	Singlet	3
Aromatic protons					
6.91	Doublet	2	6.75	Doublet	1
7.25	Doublet	2	6.96	Doublet	1
			7.02	Singlet	1
			7.29	Doublet of doublets	1

T_1 values were calculated and the highest value was the singlet in MCM at 7.02 ppm (with a coupling constant 2 Hz), T_1 = 9 seconds. The differences between quantitative ^{1}H NMR and standard ^{1}H NMR are the number of scans (to achieve sufficient signal-to-noise ratios to be able to integrate the MCM peaks with confidence) and the delay between scans, which should be at least five times the longest T_1. All quantitative ^{1}H NMR experiments were run with 200 scans each and a delay of 50 seconds. A peak corresponding to MCM (δ = 7.02 ppm) was integrated to allow quantification of the percentage of MCM present; the integral was compared to a PCM doublet which equated to a value of two protons.

Table 5.2: Experimental parameters for the COBC experiments

Experiment	Wt.% MCM	Oscillation					Flow rate (ml min^{-1})	RT (mins)	Straight Temperature (°C)													
		Frequency (Hz)	Amplitude (mm)	Re_o	Re_n	St			Feed	T_1	T_2	T_3	T_4	T_5	T_6	T_7	T_8	T_9	T_{10}	T_{11}	T_{12}
4-straight set-up																						
COBC 1	0	2	25	1538	46	0.09	50	12.23	55	35	25	20	15	-	-	-	-	-	-	-	-	-
COBC 2	0	2	25				50	12.23	45	30	27	25	22	-	-	-	-	-	-	-	-	-
COBC 3	25	2	25				50	12.23	60	35	30	25	20[†]	-	-	-	-	-	-	-	-	-
COBC 4	25	2	25				50	12.23	55	30	20	15	13	-	-	-	-	-	-	-	-	-
COBC 5	25	2	25				50	12.23	55	30	20	15	15	-	-	-	-	-	-	-	-	-
8-straight set-up																						
COBC 6	25	2	25	1538	46	0.09	50	21.84	55	30	30	20	20	15	15	15	15	-	-	-	-	-
COBC 7	25	2	25				50	21.84	55	30	30	20	20	15	15	15	20	-	-	-	-	-
COBC 8	25	2	25				50	21.84	55	30	30	20	20	20	20	20	20	-	-	-	-	-
COBC 9	18	2	25				50	21.84	55	30	30	20	20	20	20	20	20	-	-	-	-	-
COBC 10	18	2	25				50	21.84	55	30	30	25	25	25	25	25	25[‡]	-	-	-	-	-
COBC 11	18	2	25				50	21.84	55	30	30	23	23	23	23	23	23	-	-	-	-	-

[†] Temperature of T_4 reduced to 15 °C to induce crystallisation

[‡] Temperature of T_4 –T_8 reduced to 23 °C after 40 minutes

Experiment	Wt.% MCM	Oscillation					Flow rate (ml min^{-1})	RT (mins)	Temperature (°C)													
		Frequency (Hz)	Amplitude (mm)	Re_o	Re_n	St			Feed	T_1	T_2	T_3	T_4	T_5	T_6	T_7	T_8	T_9	T_{10}	T_{11}	T_{12}
12-straight set-up																						
COBC 12	18	2	25	1538	46	0.09	50	33.20	55	30	30	25	25	25	25	25	25	25	25	25	25	25
COBC 13	18	3	25	2307	46	0.09	50	33.20	55	30	30	25	25	25	25	25	25	25	25	25	25	25

5.1.3 Results and Discussion

5.1.3.1 Experiments with a four-straight COBC set-up

COBC 1 and COBC 2: Experiments with no MCM

Experiments COBC 1 and COBC 2 were performed in the absence of any MCM, acting as control crystallisations for future experiments. Conditions for COBC 1 were chosen based on batch crystallisation experiments, with temperatures chosen to ensure crystallisation would be observed in the system. After 14 minutes (i.e. within the first solid RT) crystallisation was observed in the third and fourth straight. By the end of the first solid residence time, encrustation was observed on baffle edges and walls (Figure 5.4).

Figure 5.4: Encrustation on the baffle walls in Experiment COBC 1

PXRD analysis of the harvested solid confirmed the presence of PCM-I, as would be expected in absence of any templating molecule. One further experiment (COBC 2) was performed in attempts to reduce the encrustation observed through increasing the temperature of the straights. Encrustation was reduced with this approach, but not eliminated completely. As the focus of this work was to try and obtain PCM-II through a templated crystallisation in the COBC, all future work in this area was directed towards this aim.

COBC 3 and 4: Initial investigations with a four-straight set-up

Crystallisation of PCM-II in the absence of MCM during batch cooling crystallisation experiments was observed at a temperature of 25 °C, as such the final straight temperature in experiment COBC 3 was set to 20 °C; a slightly reduced temperature to account for the relatively quick residence times experienced in the COBC, which could result in a longer induction time for nucleation. At the end of solid RT1, crystals were observed in the filter paper but not within the main crystalliser, indicating crystallisation occurred on the filter paper. As such, during the same experiment, the temperature of the final straight was reduced to 15 °C. This resulted in visible crystals in the exit piece of the crystalliser (Figure 5.5).

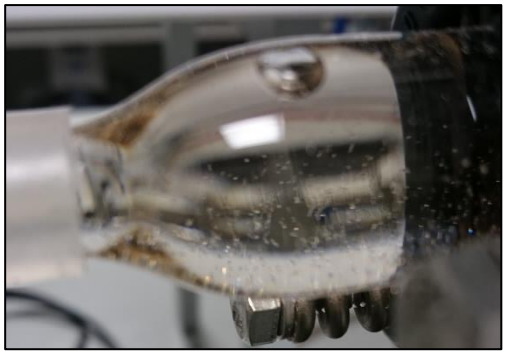

Figure 5.5: Crystallisation in the exit piece in experiment COBC 3

These crystals were collected on a second filter paper and subjected to PXRD analysis (Figure 5.6). Crystallisation was also observed in the Buchner flask; this is likely due to sudden crystallisation upon contact with the flask and saturated solution from RT1. This solid was separated from the mother liquor and analysed through PXRD (Figure 5.6).

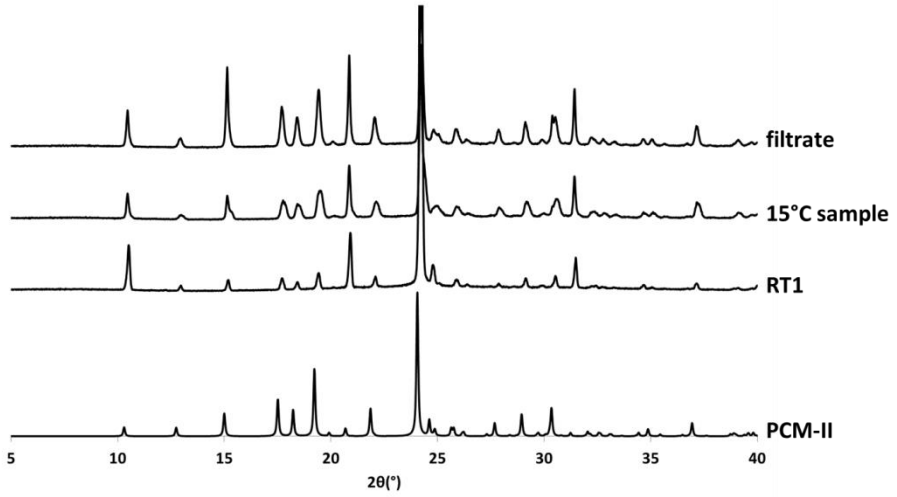

Figure 5.6: PXRD analysis of the samples for experiment COBC 3; the y-axis shows relative intensity in arbitrary units

PXRD analysis confirms the production of PCM-II, and the absence of PCM-I, in all three samples analysed. However, crystallisation yield was very poor and could not be measured. As such, for experiment COBC 4, the temperature of the final straight was reduced to 13 °C in order to induce crystallisation within the system. Crystallisation was observed in straight 4 in RT1, with crystals observed in straight 3, midway through RT2, indicating possible back-mixing within the system. The crystallisation was run for four residence times (*c.a.* 1 hour of operation), with solid from each residence time analysed through PXRD (Figure 5.7). The mass of solid produced in each residence time was recorded and yields of crystallisation calculated (Table 5.3). The yields of crystallisation are calculated based on the concentration of PCM in a known residence volume (residence volume is the volume of solution within the crystalliser in one residence time); for a concentration of 300 mg/g of PCM in 612 ml, a theoretical 100 % yield would be 183.6 g. The yields of crystallisation

can be seen to be low in comparison to the batch crystallisation of PCM-II (*ca* 50 %), likely due to the long induction time needed to crystallise PCM-II in the presence of MCM not being amenable to the short residence times seen in this system.

Table 5.3: Solid yields for experiment COBC 4

Residence time	Mass solid (g)	Yield (%)
RT1	20.7486	11
RT2	67.8748	37
RT3	61.0844	33
RT4	24.9980	14

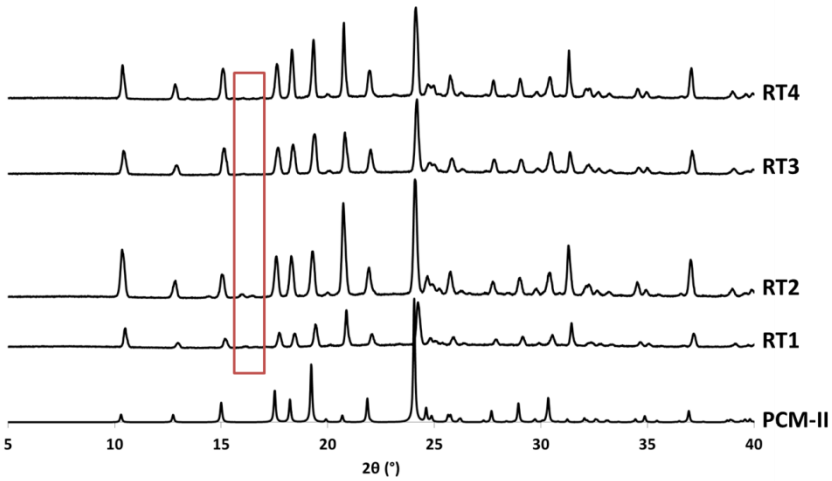

Figure 5.7: PXRD patterns from experiment COBC 4, showing the production of PCM-II with some peaks from MCM.H_2O present (boxed in red). The y-axis displays relative intensity in arbitrary units

PXRD analysis confirms the presence of PCM-II, however some peaks corresponding to MCM·H_2O (the main peaks from which are boxed in red in Figure 5.7) are also observed, confirming the presence of some MCM·H_2O in the solid product. This is likely due to the low temperatures needed to induce crystallisation in this compact four-straight set-up.

COBC 5: T_1 = 30 °C, T_2 = 20 °C, T_3 = 15 °C, T_4 = 15 °C

In order to mitigate the formation of MCM·H_2O in the final solid product (as seen in COBC 4), the temperature of the final straight was increased (from 13 °C to 15 °C) with the rationale that crystallisation at a higher temperature would stop the crystallisation of this unwanted impurity. However, as demonstrated in experiment COBC 3, having one straight at 15 °C resulted in a very poor solid yield. As such, the final two straights in this experiment were each set at 15 °C; the

rationale being that having a longer period of time at this temperature may allow for more crystallisation.

Little crystallisation was observed in RT1 (reflected in the low solid yield in Table 5.4), with crystallisation in the exit piece observed within RT2 (Figure 5.8). Crystals were only observed by eye in the final straight in RT3. It could be that the increase in temperature from the jacketed straights to the unjacketed exit piece provided the energy to overcome the barrier to nucleation, which would explain why solid was only observed in the exit piece initially.

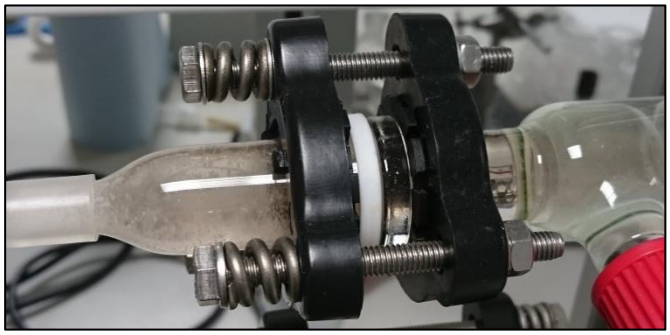

Figure 5.8: Crystallisation in the exit piece in Experiment COBC 5

Solids from each residence time were collected on separate filter papers and the weights of solid with corresponding yield calculated (Table 5.4). Solid yields can be seen to be lower in this experiment than from COBC 4, the higher temperature of the final straight resulting in less solid crystallising from solution.

Table 5.4: Crystallisation yields from Experiment COBC 5

Residence time	Mass of solid (g)	Yield (%)
RT1	2.56	1.4
RT2	26.65	14.5
RT3	34.87	19.0
RT4	22.28	12.1

PXRD analysis (Figure 5.9) of the solid from each of the residence times indicates the formation of PCM-II, in the absence of PCM-I, in all residence times, with increasing amounts of MCM·H_2O in later residence times.

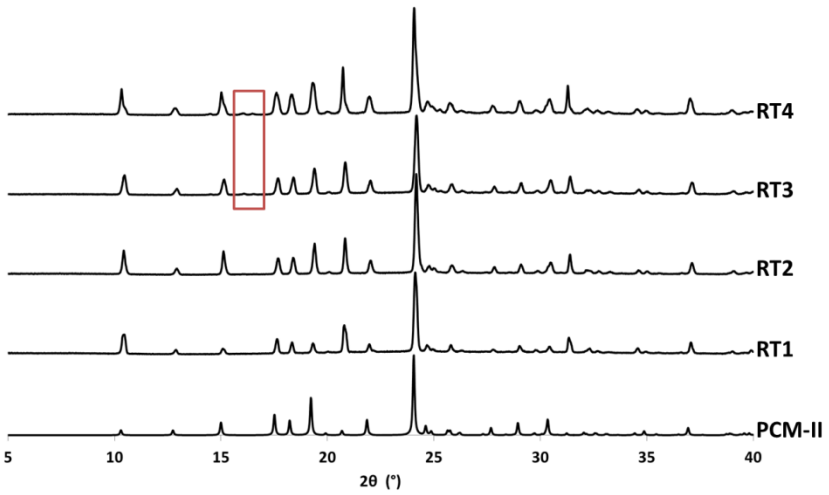

Figure 5.9: PXRD patterns for Experiment COBC 5 showing the production of predominately PCM-II, with some peaks (boxed in red) from MCM.H_2O. The y-axis displays relative intensity in arbitrary units

5.1.3.2 Experiments with an eight-straight COBC set-up

It was concluded from the experiments with the compact four-straight COBC set-up that crystallisation needed to take place at a higher temperature in order to eliminate the MCM·H_2O from the final solid product. The four-straight COBC set-up (total length - 3.58 m) did not provide a sufficiently long enough residence time at a higher temperature to induce crystallisation in the system. As such, the length of the COBC was doubled to an eight-straight set-up (total length - 6.38 m) for the next set of experiments whilst the net flow rate was maintained at the previous value, doubling the residence time within the crystalliser.

COBC 6

Initial experiments with this eight-straight set-up utilised a similar cooling profile to that of Experiment COBC 5, with the number of straights for each temperature doubled (Figure 5.10).

T1	30°C
T2	30°C
T3	20°C
T4	20°C
T5	15°C
T6	15°C
T7	15°C
T8	15°C

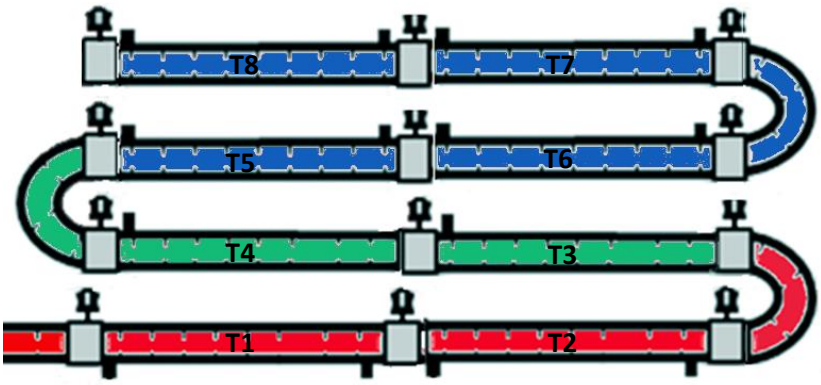

Figure 5.10: Temperature profile used for Experiment COBC 6

Crystals were observed in the filter at the end of the solid RT1; however it was not until solid RT2 that crystals were visible in the final two straights of the COBC. During solid RT2 and solid RT3 the amount of crystallisation was observed to increase. The experiment was run until the feed volume expired (at a time of 1hr 22 mins; after three solid residence times). As with previous experiments, samples were collected for each residence time to allow yield calculations (Table 5.5) and for analysis of solid form produced (Figure 5.11).

Table 5.5: Solid yields in Experiment COBC 6

Residence time	Mass of solid (g)	Yield (%)
Solid RT1	5.24	1.6
Solid RT2	8.87	2.7
Solid RT3	98.27	30.0

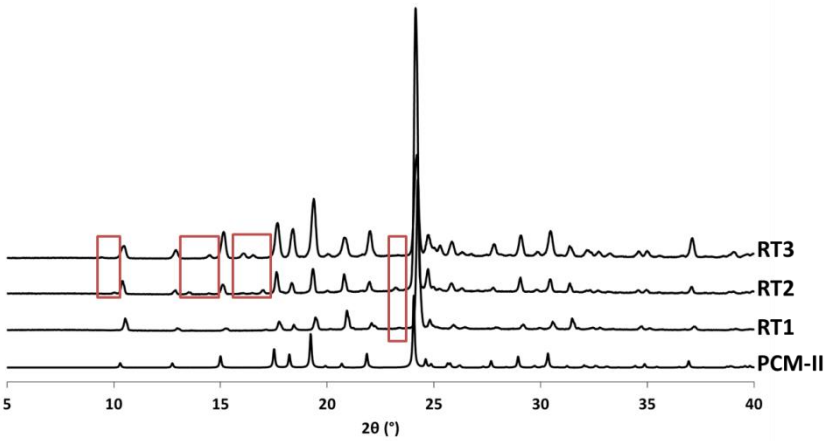

Figure 5.11: PXRD patterns for Experiment COBC 6 showing the production of PCM-II with some MCM.H_2O present (boxed in red). The y-axis displays relative intensity in arbitrary units.

Again, the long induction time to nucleation in this system is reflected in the poor solid yields for RT1 and RT2. PXRD analysis (Figure 5.11) shows the production of PCM-II, however there are peaks corresponding to MCM·H_2O present in the samples extracted from all residence times. It is likely that, due to the fact the system is crystallising at a temperature of 15 °C, this results in the crystallisation of MCM·H_2O, as was observed in the Design of Experiments outlined in Chapter 4.

COBC 7

The observation of crystallisation in the exit piece in Experiment COBC 5 was explained through possible nucleation due to an increase in temperature providing the energy to overcome the barrier to nucleation. Combining this knowledge with the observation in multiple experiments that

crystallisation at 15 °C resulted in the production of some MCM·H_2O in the solid product, an experiment was carried out whereby the final straight was heated to a higher temperature (Figure 5.12). It was thought that if nucleation was induced at 20 °C instead of 15 °C, PCM-II may be able to be crystallised in the absence of MCM·H_2O.

T1	30°C
T2	30°C
T3	20°C
T4	20°C
T5	15°C
T6	15°C
T7	15°C
T8	20°C

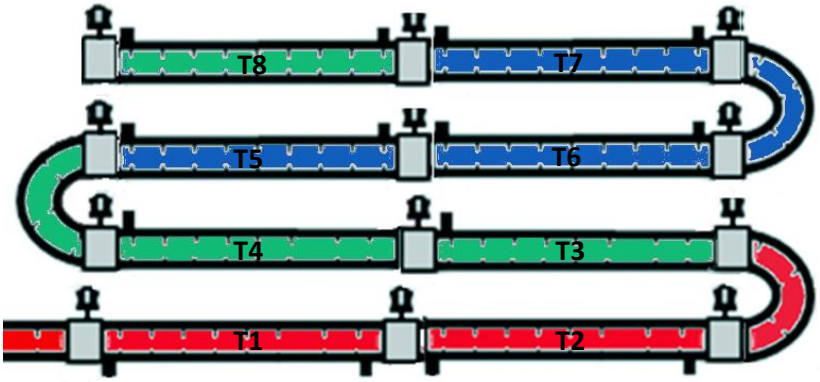

Figure 5.12: Temperature profile used in Experiment COBC 7

Within solid RT1, small amounts of crystallisation were observed in straight 8. By the beginning of solid RT2, crystals were appearing in straight 7, with a significantly higher slurry density visible in straight 8. Problems with filtration of the slurry were observed in this experiment due to crystallisation in the Buchner funnel as the remaining saturated solution was filtered from solid. This crystallisation indicates that the conditions within the COBC using this temperature regime do not lead to complete desupersaturation of the solution. The experiment was run for 1 hr 44 mins (4.84 residence times), at which point crystallisation was visible in straights 4 and 5, possibly due to back mixing of crystals from later straights. Solid was collected for each solid residence time to allow determination of yields (Table 5.6) and analysis of the solid form produced (Figure 5.13).

Table 5.6: Crystallisation yields for Experiment COBC 7

Residence time	Mass of solid (g)	Yield (%)
Solid RT1	1.23	0.4
Solid RT2	43.64	13.3
Solid RT3	88.08	26.9

The crystallisation yields reflect the observation that crystallisation was seen at an earlier time point during the crystallisation in comparison to previous experiments; however the yield for solid RT3 is less than that observed for the same residence time in Experiment COBC 6. Heating of the final straight clearly helped to induce nucleation in the system as the yield for RT2 for experiment COBC 7 is greater than in COBC 6, indicating earlier nucleation in the system. However, although nucleation

was induced into the system earlier, the yields of crystallisation for later residence times were reduced for COBC 7 in comparison to COBC 6 as the temperature of crystallisation was higher. The DoE outlined in Chapter 4 clearly shows how cooling to a temperature of 15 °C compared to 20 °C increases the yield of crystallisation.

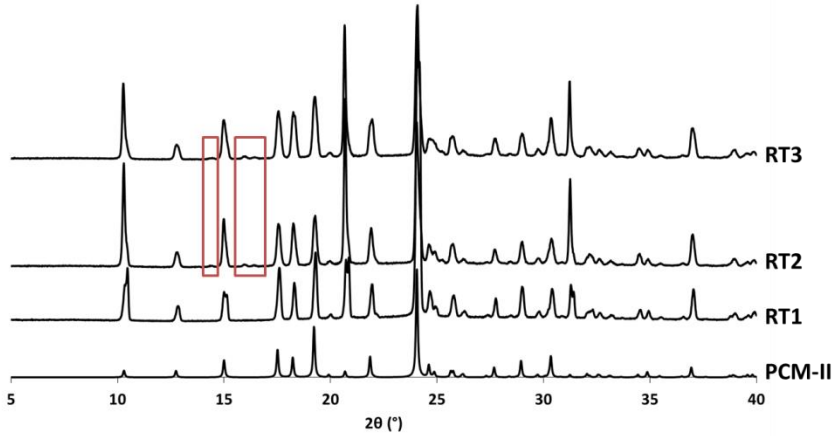

Figure 5.13: PXRD patterns showing the production of PCM-II with some MCM.H_2O (peaks boxed in red) in Experiment COBC 7. The y-axis displays intensity in arbitrary units

Analysis of the PXRD patterns (Figure 5.13) shows the production of PCM-II in all residence times, with some MCM·H_2O detectable in RT2 and RT3. Combining this data with observations from the experiment it can be concluded that in solid RT1, where no MCM·H_2O was detectable in the solid through PXRD analysis, crystallisation occurred only in the final straight set at a temperature of 20 °C. As such, it can be postulated that through facilitating crystallisation at 20 °C, MCM·H_2O can be eliminated from the crystallisation product. This is supported by observations from solid RT2 and solid RT3 where some MCM·H_2O was detectable in the solid through PXRD analysis; these samples result from crystallisation observed in straights set at a temperature of 15 °C.

COBC 8

As previous experiments have suggested a temperature of 20 °C is needed to induce crystallisation of PCM-II in the absence of any MCM·H_2O, the next set of experiments investigated the effect of keeping the final six straights at 20 °C.

T1	30°C
T2	30°C
T3	20°C
T4	20°C
T5	20°C
T6	20°C
T7	20°C
T8	20°C

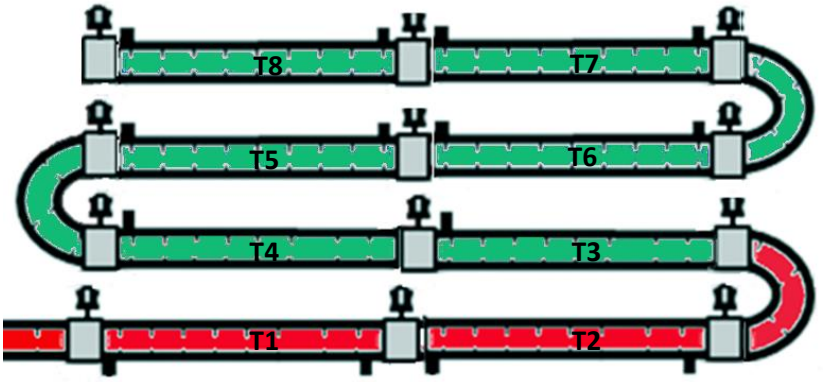

Figure 5.14: Temperature profile employed in Experiments COBC 8 and COBC 9

After 30 minutes of operation (i.e. midway through solid RT1) a few crystals were observed in the filter paper and in the final straight. By 62 minutes (towards the end of solid RT2), more crystals were observed in straight 8 and a few in straight 7; however it was noted that the suspension was much less dense than observed in previous experiments. This reduction in observed solid yield is supported by the calculated yields from filter paper masses (Table 5.7) and can be explained through the system having an increased induction time to nucleation at higher temperatures. As with Experiment COBC 7, problems with filtration due to crystallisation in the funnel were observed, indicating incomplete desupersaturation of the system within the COBC.

Table 5.7: Solid yields in Experiment COBC 8

Residence time	Mass of solid (g)	Yield (%)
RT1	1.63	0.5
RT2	1.23	0.4
RT3	69.25	21.1

Although solid yields were poor, PXRD analysis (Figure 5.15) does not indicate the presence of any MCM·H_2O in the solid harvested from each of the three solid residence times. As such, DSC analysis was performed to detect any trace levels of MCM·H_2O in the solids; these DSC scans did in fact indicate the presence of MCM·H_2O in all residence times, characterised by the melt/re-crystallisation event at 150 °C (Figure 5.16).

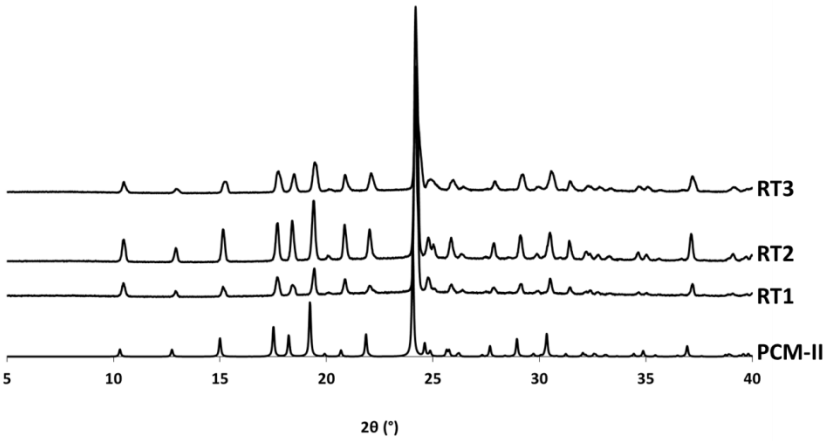

Figure 5.15: PXRD analysis showing the production of PCM-II in Experiment COBC 8; the y-axis displays relative intensity in arbitrary units

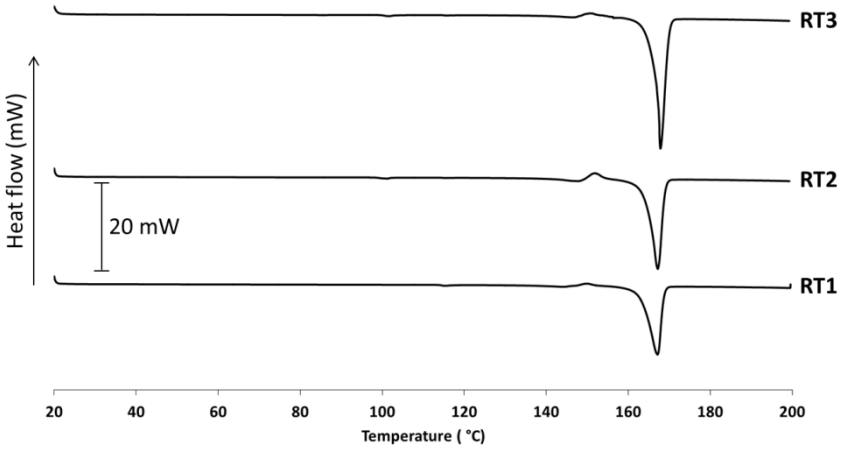

Figure 5.16: DSC analysis showing the presence of some MCM·H2O in all three residence times in Experiment COBC 8 (exothermic up)

COBC 9

Having the final six straights at 20 °C resulted in the crystallisation of trace amounts of MCM·H_2O and previous experiments had also resulted in low solid yields. It was therefore possible that increasing the temperature of these final straights further would result in very little crystallisation but would favour inducing nucleation of PCM-II in the system without nucleating MCM·H_2O. Therefore, the concentration of MCM used was decreased from 25 % to 18 %. In batch crystallisation experiments, the presence of MCM was seen to widen the metastable zone (MSZ), resulting in a delayed onset of nucleation. Therefore, by decreasing the concentration of MCM, the MSZ may be narrowed slightly, resulting in crystallisation at a higher temperature and hence eliminating the crystallisation of MCM·H_2O. Experiment COBC 9 used the same temperature profile as COBC 8 to allow direct comparison between the two experiments.

Crystallisation in the final straight was observed in RT1, after a period of 25 minutes, earlier than has been seen in previous experiments. This indicates that reducing the concentration of MCM has the desired effect of reducing the induction time to nucleation. However, this resulted in high solid loadings in the crystalliser (Figure 5.17), leading to eventual blockage of the unjacketed bends and poor suspension of solid.

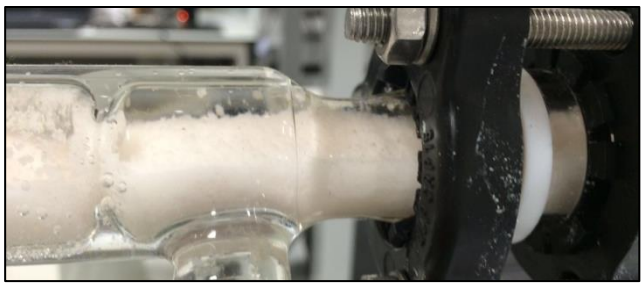

Figure 5.17: High solid loadings in Experiment COBC 9

Problems with filtration meant that accurate solid yields of crystallisation could not be determined for this experiment. However, samples were collected to allow for PXRD analysis; the outcomes for two separate samples are given for RT2 as the filtration problems resulted in filter papers being changed multiple times throughout the course of the experiment. The PXRD analysis (Figure 5.18) shows the production of PCM-II with some MCM·H_2O present in small quantities. There are two possible reasons for this MCM·H_2O being present at sufficiently high levels to be detected by PXRD. First, the high solid loadings in the crystalliser could have affected the mixing conditions; the DoE outlined in Chapter 4 highlighted the importance of mixing for the elimination of MCM·H_2O. Secondly, the filtration problems experienced in this experiment were due to crystallisation in the filter funnel; it is plausible that the MCM·H_2O detected in the PXRD is crystallising in the filter. Implementation of an inline Raman PhAT probe would allow for elucidation of whether this is the case.

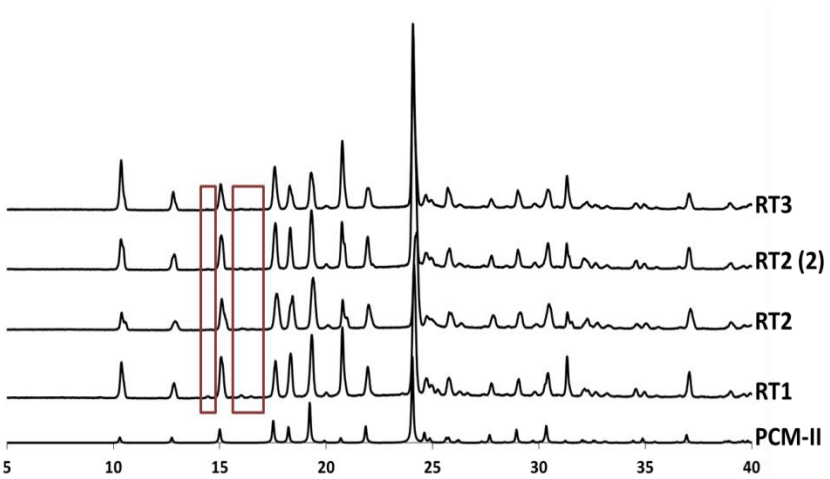

Figure 5.18: PXRD patterns confirming the production of PCM-II with trace MCM.H_2O (boxed in red) in Experiment COBC 9. The y-axis displays relative intensity in arbitrary units

COBC 10

Owing to the presence of MCM·H_2O in the solid for each of the residence times in COBC 9, in COBC 10 the effect of increasing the temperature of the final six straights from 20 °C to 25 °C was investigated with the aim of eliminating this impurity from the crystallisation in the COBC. The concentration of MCM remained at 18 %. By the end of solid RT1, very little crystallisation was observed, with only a few crystals in the filter and exit piece. As such, the temperatures of the final four straights (T4 – T8) were reduced to 23 °C to induce more crystallisation in the system. This step was successful in promoting further crystallisation; however this experiment experienced detrimental filtration problems due to crystallisation occurring in the filter as a result of the low solid yields produced within the main crystalliser, indicating incomplete desupersaturation of the system. Because of this, samples were not collected based on residence times, but instead were defined by the volume filtered before blockage in the filtration occurred. Six samples were collected throughout the course of the experiment, every 5 minutes for the last 30 minutes of the experiment, which was only able to be run for 1 hour due to these filtration issues. All six samples were subject to PXRD analysis (Figure 5.19).

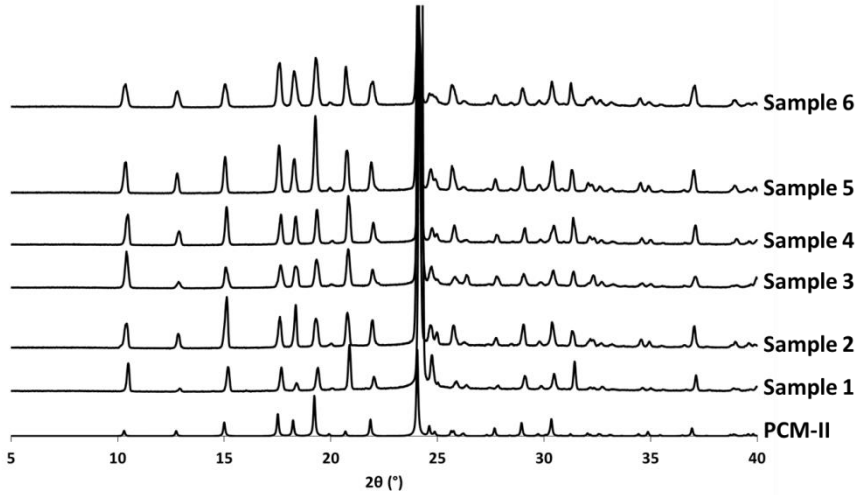

Figure 5.19: PXRD analysis of each of the six samples taken during the course of Experiment COBC 10; the y-axis displays relative intensity in arbitrary units

PXRD analysis (Figure 5.19) indicates that the production of PCM-II has been achieved in the absence of any MCM·H_2O. As such, DSC analysis was performed on the samples to determine whether MCM·H_2O was present in quantities not detectable through PXRD; due to the low mass of solid produced for Samples 1 and 2 only samples 3-6 were analysed through DSC (Figure 5.20).

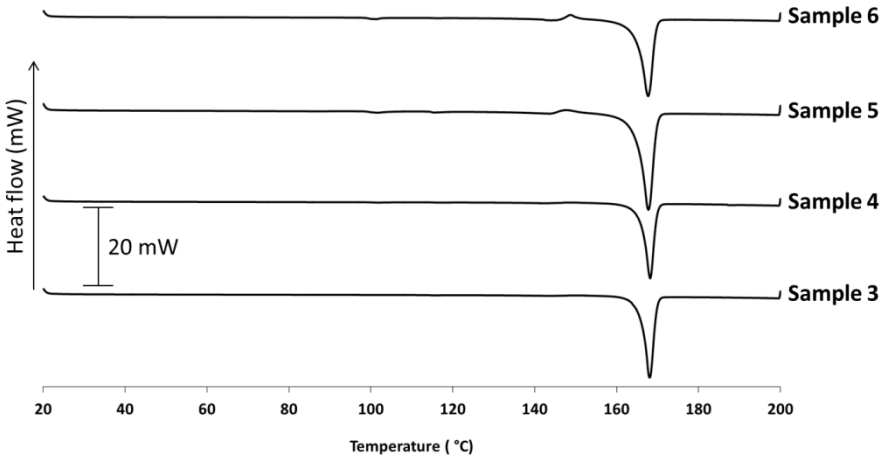

Figure 5.20: DSC analysis for samples 3-6 in Experiment COBC 10 (exothermic up)

DSC analysis shows the production of pure PCM-II in the absence of MCM·H_2O in Samples 3 and 4. However, the presence of MCM·H_2O is seen to increase with time, with Samples 4 and 5 displaying the characteristic melt/recrystallisation event at around 145-150 °C of MCM.H_2O (see Chapter 3). However, it could be that the MCM·H_2O is crystallising in the filter; due to the filtration problems experienced in this experiment, saturated mother liquor remained on top of the filter cake for

extended periods of time which could result in further crystallisation of either PCM-II or MCM·H_2O. As such, results from this experiment should be treated with caution, with the experiment being repeated in Experiment COBC 11.

COBC 11

Owing to the fact that in Experiment COBC 10, the temperature of the final four straights had to be reduced to 23 °C in order to induce any significant crystallisation in the system, for COBC 11 the final six straights were set at a temperature of 23 °C.

This temperature profile resulted in a successful experiment in terms of onset of nucleation; crystallisation was observed shortly into solid RT1 (at a time of 24 minutes) in straight 6. Nucleation in earlier straights is beneficial as it allows more time for growth, increasing yield, and more complete desupersaturation of the system. The crystallisation was run for three solid residence times (total operating time of 90 minutes) without any blockages or difficulties with filtration. Samples were collected for each residence time and solid yields calculated (Table 5.8).

Table 5.8: Solid yields for Experiment COBC 11

Residence time	Mass of solid (g)	Yield (%)
Solid RT1	42.19	12.9
Solid RT2	43.38	13.2
Solid RT3	55.73	17.0

Despite being more successful than the previous experiment, solid yields are still poor. It is likely that the eight-straight set up employed in this experiment does not allow for a long enough residence time within the crystalliser to allow for full desupersaturation of the solution, resulting in lower yields. However, the yields can be seen to be relatively consistent over the three solid residence times indicating the system is close to achieving operation at steady state; a parameter that is crucial for obtaining consistent particle property attributes. PXRD analysis was performed on each of the samples to determine the solid form of the product. This analysis confirms the production of PCM-II, however there are two peaks from MCM·H_2O in each of the three residence times (boxed in red in Figure 5.21).

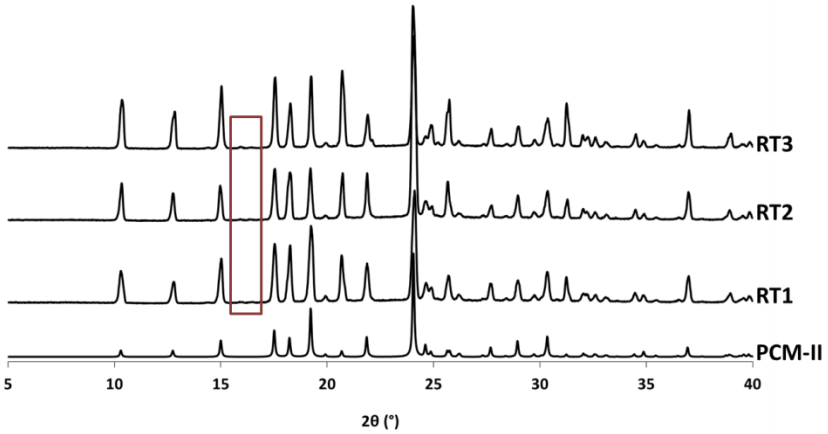

Figure 5.21: PXRD analysis for the solid produced in Experiment COBC 11 confirming the production of PCM-II with some peaks from MCM.H_2O (boxed in red). The y-axis displays relative intensity in arbitrary units

5.1.3.3 Experiments with a 12-straight COBC set-up

It was concluded from experiments using an eight-straight set-up that the residence time within the crystalliser was not long enough to induce nucleation at a temperature that eliminated MCM·H_2O from the solid product, whilst giving reasonable yields. As such, the COBC was further increased in length to a 12-straight set-up (9.7 m). Two experiments were performed using this set-up, utilising the temperature profile outlined in Figure 5.22.

T1	30°C
T2	30°C
T3	25°C
T4	25°C
T5	25°C
T6	25°C
T7	25°C
T8	25°C
T9	25°C
T10	25°C
T11	25°C
T12	25°C

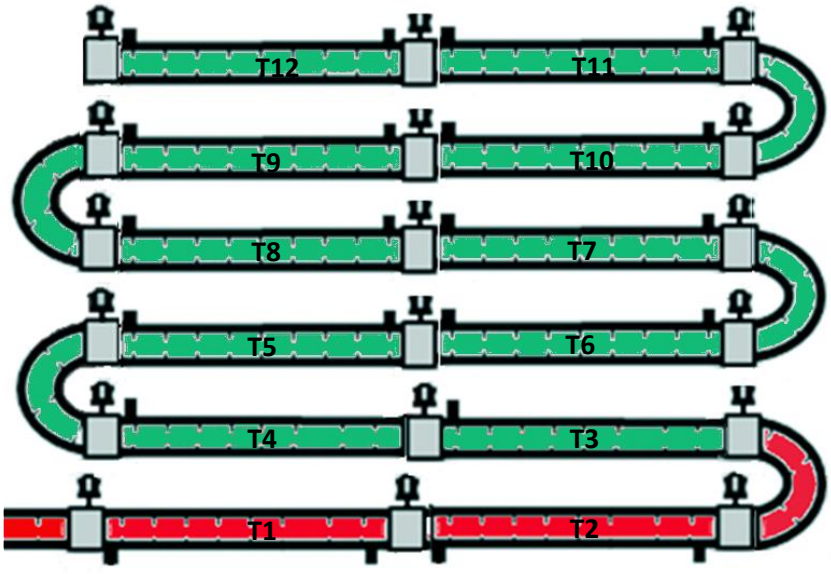

Figure 5.22: The temperature profile employed for the 12-straight COBC experiments (COBC 12 and COBC 13)

COBC 12

COBC 12 utilised the same net flow rate and oscillation conditions as all previous experiments performed. After a period of 49 minutes (half way through solid RT1) crystallisation was observed in the final two straights. At the end of solid RT1, crystals were visible in straights 9 and 10. However, the experiment was hampered by significant suspension problems in the final four straights and detrimental filtration problems. The suspension problems were likely due to oscillation dampening, suggesting different oscillation conditions or methods (e.g. a piston set-up rather than bellows) would be required in order to suspend the particles in this longer set-up. As the temperature of crystallisation was set to 25 °C in order to induce crystallisation in the absence of MCM·H_2O, it is likely that the addition of four extra straights was not enough to sufficiently desupersaturate the solution to prevent the filtration problems.

Due to the filtration problems, solids were not collected based on residence time but as in COBC 10 were defined on the volume filtered before the funnel became blocked. Four samples were taken throughout the 1 hr 25 minute operation (every 10 minutes from 50 minutes into the crystallisation) and analysed through PXRD and DSC (Figure 5.23 and Figure 5.24).

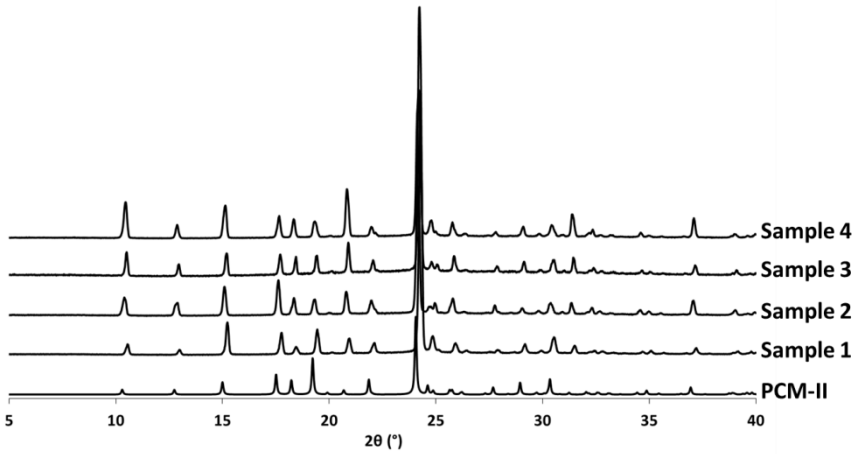

Figure 5.23: PXRD analysis for the samples taken during experiment COBC 12; the y-axis displays relative intensity in arbitrary units

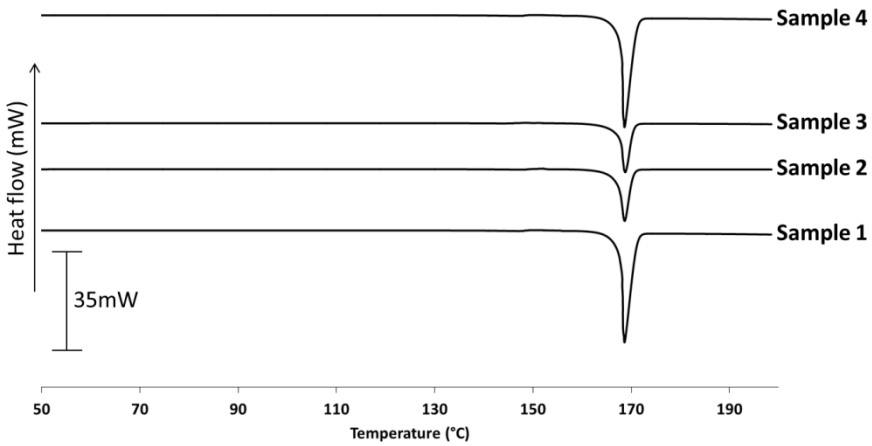

Figure 5.24: DSC analysis on the samples taken from Experiment COBC 12

PXRD analysis (Figure 5.23) confirms the presence of PCM-II, with no MCM·H_2O present at levels detectable through PXRD. As such DSC analysis was used to confirm whether any MCM·H_2O was present at levels below the detection limit of PXRD. This analysis (Figure 5.24) seemed to indicate the absence of any MCM·H_2O; however there is a small event around 150 °C that could correspond to the presence of this form. As such, quantitative NMR analysis was performed on each of the samples in order to quantify the levels of any MCM·H_2O that may be present in the sample. A peak at δ = 7.02 ppm corresponding to MCM (Table 5.1) was used to elucidate the percentage of MCM·H_2O in the samples. The presence of MCM·H_2O was detected in all samples at levels between 2 % and 3.5 % w/w (Table 5.9).

Table 5.9: Percentages of MCM·H_2O in PCM-II samples from quantitative NMR analysis

Sample	% MCM.H_2O
1	2.61
2	3.42
3	3.13
4	2.38

It is likely that the poor mixing experienced in the final four straights is responsible for the small quantities of MCM.H_2O detected in the final solid product, an observation supported by the DoE highlighted in Chapter 4. The poor filtration seen in this experiment could also be responsible for the presence of this impurity, which could have crystallised whilst saturated mother liquor sat on top of the filter cake.

COBC 13

In order to aid in the suspension of particles in later straights, the oscillation conditions were changed by increasing the frequency of oscillation; the amplitude could not be increased further due to limitations with the bellows construction. The temperature profile remained the same as that used in Experiment COBC 12. Crystallisation in the end piece and on the filter paper was observed at the beginning of solid RT1. Again, the experiment was hampered by poor filtration and poor suspension of particles, resulting in premature termination of the experiment after a period of 1 hour. Four samples were taken throughout the operating time, with each sample subjected to PXRD and DSC analysis to confirm the solid form produced in the experiment.

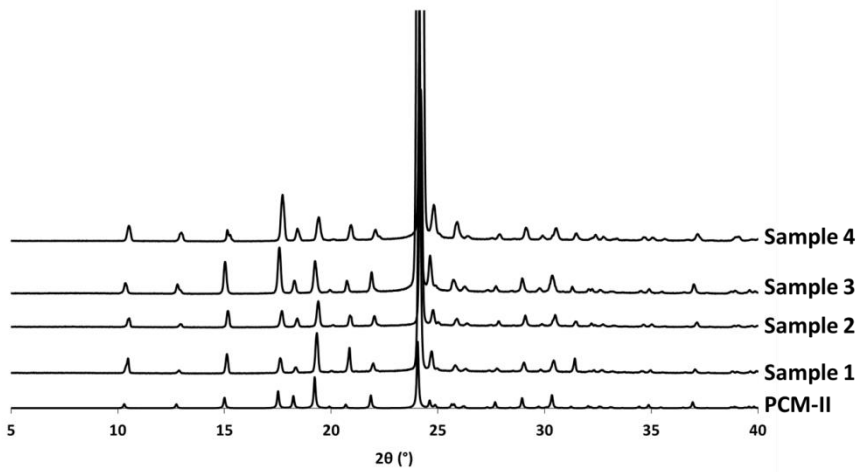

Figure 5.25: PXRD analysis of the samples taken in Experiment COBC 13; the y-axis displays relative intensity in arbitrary units

PXRD analysis (Figure 5.25) confirms the production of PCM-II in all samples taken. It also indicates the absence of any MCM·H_2O at levels detectable through PXRD analysis. As such, DSC analysis was performed in order to indicate whether trace levels of MCM·H_2O were present in the samples (Figure 5.26). The DSC of Samples 1 and 2 show a small thermal event at 150 °C (boxed in red in Figure 5.26), which corresponds to the presence of MCM·H_2O. The DSC traces of Samples 3 and 4 appear to only show one thermal event, the final melt at 170 °C. As MCM·H_2O was detected in the first two samples, quantitative NMR analysis was performed on Samples 3 and 4 in order to detect any trace MCM·H_2O in the solid samples (Table 5.10), the presence of which was confirmed in small quantities, at similar wt.% levels as found in COBC 12.

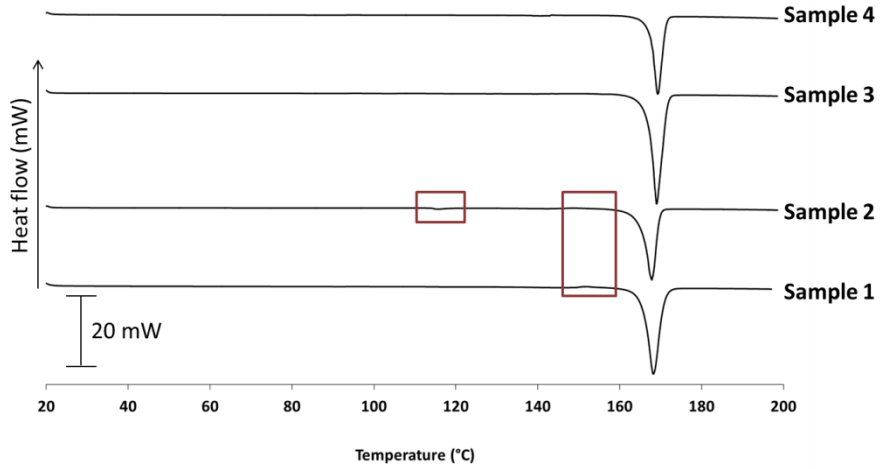

Figure 5.26: DSC analysis of the samples taken in Experiment COBC 13

Table 5.10: Quantitative NMR analysis on samples from COBC 13

Sample	% MCM.H_2O
3	1
4	2

5.1.4 Conclusions

In conclusion, metastable paracetamol form II (PCM-II) has been successfully crystallised in a reconfigurable COBC set-up. This represents the first example of a metastable polymorphic form of an API produced in a COBC.

Initial crystallisations in a compact four-straight set-up resulted in the first successful continuous crystallisation of PCM-II (these experiments preceded the MSMPR runs detailed in Chapter 4); however MCM·H_2O was present in the solid samples at high enough levels to be detectable by PXRD analysis (i.e. at least 5 % w/w). In order to induce crystallisation in the system, the temperature of the final straight was set to 13 °C. It can be postulated that the crystallisation of MCM·H_2O is seen by forcing the system to crystallise at 13 °C; the batch Design of Experiments investigation outlined in Chapter 4 supports this observation, showing the prevalence of MCM·H_2O at lower temperatures of crystallisation. The same result was observed when the final two straights were set at a temperature of 15 °C. It was concluded that the residence time within this compact set-up was not sufficient to induce crystallisation at temperatures that would result in elimination of the MCM·H_2O impurity. The flow rate could not be decreased any further as this would not be sufficient to suspend and pump particles within the crystalliser.

As such, the length of the COBC was increased to an eight-straight set-up, increasing the residence time within the system. Increasing the time at which the crystallising solution is held at a higher temperature should allow crystallisation of PCM-II at this temperature, in the absence of any MCM·H_2O impurity. Initial investigations with this eight-straight set-up utilised a 25 wt. % concentration of MCM. A variety of temperature regimes were employed in attempts to eliminate the hydrate impurity from the final solid product. Setting the final six straights to a temperature of 20 °C produced the most successful crystallisation, resulting in levels of MCM·H_2O only detectable through additional DSC analysis (i.e. not present at levels detectable through PXRD). However, solid yields of crystallisation were poor, possibly due to a widening of the metastable zone (MSZ) in the presence of MCM. Therefore, the concentration of MCM was reduced to 18 wt. % for all subsequent experiments. The cooling profile remained the same, with the final six straights set at 20 °C. This reduction in MCM concentration had the desired effect of decreasing the MSZ, inducing

crystallisation earlier in the system. However, this decrease in MSZ resulted in higher solid loadings within the crystalliser, resulting in eventual blockage of the unjacketed bends. Furthermore, the final PCM-II solid still contained trace levels of MCM·H_2O. As such, the temperatures of the final six straights were increased to 25 °C in the aim of inducing crystallisation in the absence of any hydrate impurity. No crystallisation was observed within the COBC in this temperature regime and the experiment was hampered by blocking of the filter funnel; it was thought that this blocking was due to incomplete desupersaturation of the solution within the main crystalliser. Therefore, to induce crystallisation and obtain more complete desupersaturation of the system, the temperatures of the final six straights were reduced to 23 °C. Although this resulted in crystallisation, blockage of the filter was still observed and the PCM-II solid still contained some MCM·H_2O. As such, it was concluded that a still longer set-up was needed in order to desupersaturate the system fully and induce crystallisation at a higher temperature to eliminate MCM·H_2O from the PCM-II solid product.

Two further experiments were conducted using a 12-straight COBC set-up, equating to a residence time within the crystalliser of *ca*. 30 minutes. Setting the final 10 straights at 25 °C resulted in crystallisation of PCM-II in the apparent absence of any MCM·H_2O. However, quantitative NMR analysis shows its presence at levels between 2 and 3.5 %. Suspension of particles in the final four straights was poor due to oscillation dampening. Increasing the frequency of oscillation had little effect on suspension. Experiments were again hampered by poor filtration due to crystallisation in the filter funnel. Any future experiments could look into operating in recycle mode, taking small samples for each residence time and transferring the tube back into the feed vessel in order to mitigate problems with filtration and allow for longer operation times.

Future work on this system would look to investigate longer COBC set-ups in order to increase the residence time within the crystalliser. This increase in residence time would allow for more complete desupersaturation of the system, mitigating the problems seen here with filtration. However, it has been noted in literature that COBC set-ups may not be the most suitable for systems that display slow nucleation and growth kinetics, like the PCM/MCM system explored in this work.

Despite all samples still containing trace quantities of MCM·H_2O it is very likely that through increasing the length of the COBC, phase pure samples of PCM-II could be produced. Furthermore, the process understanding gained from these experiments allowed for rapid transferability to the MSMPR platform described above in Chapter 4.

5.2 Continuous crystallisation in the KRAIC

5.2.1 Introduction and Aims

The COBC continuous crystallisation platform described above works on high-throughput volumes (typically L/h). Previously reported work for smaller volumes has focussed on micro-reactors (µL/h), which display small internal diameters prone to blocking with particles any larger than nanometre in size.[216-218] With a rise in concepts such as 'dial-a-particle' and the drive towards distributed manufacturing concepts, implying smaller manufacturing sites at point of use, the need for niche reactors that allow for crystallisation of particles with desirable physical properties in smaller volumes at the lab scale (mesoscale) is highly desirable. These lab scale reactors are also crucial in scaling up processes from discovery scale and moving towards larger manufacturing scales.[219] Furthermore, use of such mesoscale reactors allows for development of crystallisation processes using lower quantities of material; this is a key challenge in the pharmaceutical industry where process development has to occur with small quantities of material, especially in the early stages of development.

Mesoscale crystallisers are generally of tubular geometry utilising either static mixers or operating with segmented flow. [67, 220-221] Much previous work in this area has focussed on gas segmentation[222-225], however this results in solution wetting the walls of the crystalliser and formation of discrete air slugs (Figure 5.27). As the solution comes into contact with the walls, this can lead to problems with encrustation, which can result in eventual blockage of the crystalliser. By contrast, use of two immiscible liquids, whereby the carrier fluid preferentially wets the walls the crystalliser, resulting in the formation of discrete slugs of solution (Figure 5.27), would minimise contact between the solution and crystalliser walls, theoretically reducing encrustation in the system. The main barrier to implementation of liquid/liquid segmentation into mesoscale reactors is separation of the two phases at the end of the experiment.

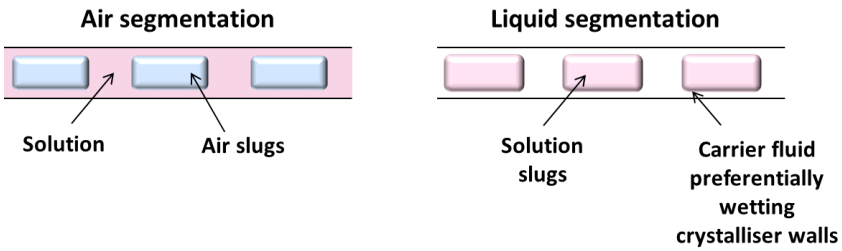

Figure 5.27: Schematic representing the differences between air and liquid segmentation

The mixing in each slug is provided by the characteristic recirculating motion (Figure 5.28); the edges of the slugs act as stagnation points which cause reversal of the direction of flow.[226] The two distinct edges of the slugs both providing this flow reversal result in the recirculating motions.

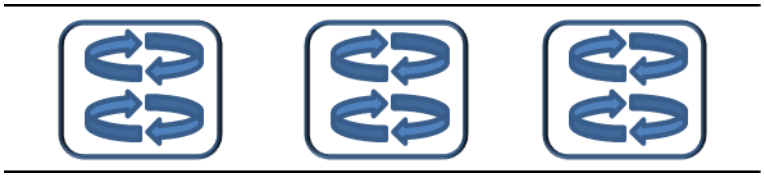

Figure 5.28: Recirculating motion within slugs which provide mixing to the system

The kinetically regulated automated input crystalliser (KRAIC; Figure 5.29) is a continuous crystallisation platform designed by Dr Karen Robertson (Wilson group PDRA). It is an open tubular crystalliser that operates on the principle of segmented flow. Owing to the inherent problems of encrustation experienced with air segmentation, due to solution touching the walls of the crystalliser, the KRAIC utilises an immiscible carrier fluid, a perfluropolyether polymer (Galden SV110). The carrier fluid is chosen as it is highly inert and preferentially coats the walls of the crystalliser, resulting in the formation of discrete slugs of solution.

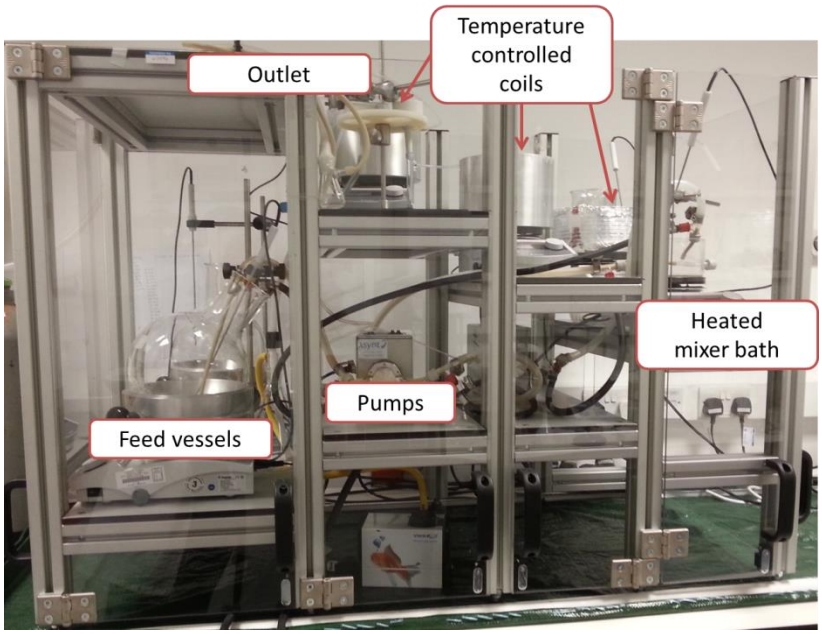

Figure 5.29: The KRAIC segmented flow crystalliser as set-up at the University of Bath

Feed solution is pumped *via* a gear pump to the mixer piece, where it is combined with carrier fluid and/or air, giving resultant segmented flow. From here, the solution desupersaturates with a gradually decreasing temperature gradient over three temperature controlled coils, resulting in crystallisation. Crystals are separated from solution and carrier fluid at the outlet.

The feed vessel is heated *via* a DrySyn® former with magnetic bottom stirring to aid dissolution of material. Jacketed tubing, equipped with flexible tubing jackets, transfers solution from the feed vessel to a mixer piece which is submerged in a heated water bath to mitigate encrustation of the mixer piece (Figure 5.30).

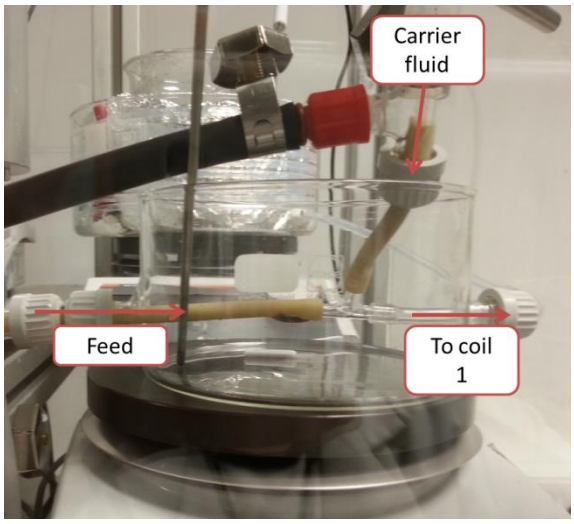

Figure 5.30: The mixer piece in the heated water bath

The three coils of the KRAIC are constructed of a single piece of fluorinated ethylene propylene (FEP) tubing, 15 m in length with an internal diameter of 3.2 mm. Coil 1 is contained within a glass dish, placed on a hotplate. Graphite powder provides a medium for heat transfer to allow efficient heating of the coil. Coils 2 and 3 are pressed against DrySyn® formers with air surrounding them, to allow a progressively reducing temperature gradient to be established. In its current set-up, the KRAIC does not allow for cooling of coils below ambient temperatures. As such, for systems which require cooling below ambient temperatures to induce nucleation, a cold tube can be introduced into the set-up; the portion of FEP tubing between the mixer piece and coil 1 is contained within larger diameter (9.5 mm ID, 12.7 mm ED) silicone tubing which is dynamically temperature controlled through the use of a heater/chiller (Figure 5.31).

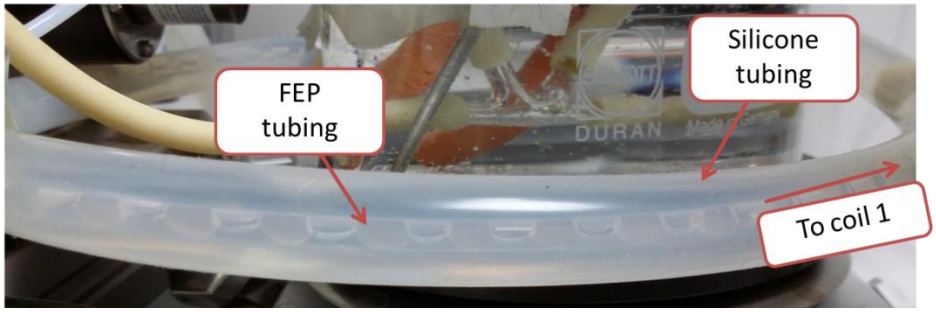

Figure 5.31: The cold tube attached to the KRAIC to allow cooling below ambient temperatures

A specialised end piece has been developed to aid in both the propulsion of crystals into the filter and allow for separation and recycling of the carrier fluid (Figure 5.32). As the slugs of solution reach the end of the crystalliser, a neutral solvent is pumped in; here a neutral solvent is defined as a miscible solvent that will neither induce further crystallisation nor result in dissolution of existing particles. The purpose of the neutral solvent is to mitigate any possible fouling issues by increasing the velocity of the solution, propelling crystals out of the tubing into the filter. After neutral solvent is added, the contents pass through the carrier fluid recovery section (inset Figure 5.32). A series of holes in the tubing allow for selective removal of the carrier fluid that preferentially wets the crystalliser walls and not the slurry. In the event solvent also migrates through these holes, the tubing end is placed into a separating funnel which will allow separation of the two immiscible fluids based on density. After separation of the carrier fluid, the remaining slurry is propelled from the crystalliser, aided by the downward slope of the mouth of the end piece. Here, crystals are immediately separated from mother liquor through vacuum filtration.

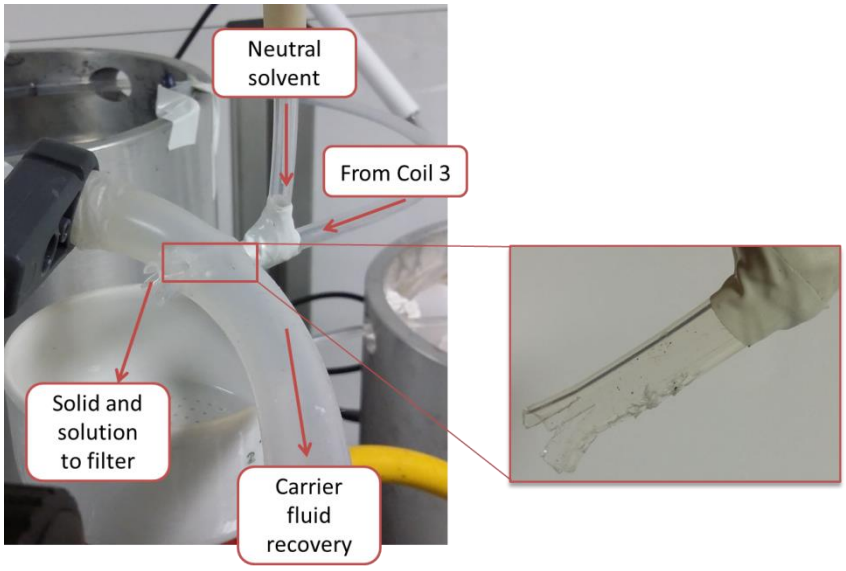

Figure 5.32: Novel end piece to allow separation of carrier fluid from solution flow

5.2.2 Experimental

A concentration of PCM of 300 mg/g with the corresponding percentage of MCM (Table 5.11) were dissolved in 1 L of 60:40 H_2O:IPA in a 5 L feed vessel, with magnetic bottom stirring to aid dissolution. 2 L of pure 60:40 H_2O:IPA was heated to the same temperature as the feed solution. The temperatures of the transfer tube, mixer bath, cold tube and coils were set at this point to allow equilibration before the beginning of the experiment.

Once at temperature, the pure solvent feed was used to prime the system for a period of 1-2 hours. It is during the priming step that flow rates of the feed, air and carrier fluid and mixer piece orientation are adjusted in order to obtain regular segmentation throughout the crystalliser. By priming with the same solvent as the crystallisation solvent, the solution slug properties are unlikely to deviate significantly through introduction of solution into the crystalliser.

Once primed, the transfer tube is moved from the pure solvent feed to the solution feed. The air bubble generated from this transfer is used to help determine the residence time in the crystalliser; here the residence time is measured from when the air bubble exits the mixer piece to when it exits the crystalliser i.e. the time spent by particles under segmented flow. Full details of all experimental parameters for each of the KRAIC experiments are given in Table 5.11.

The neutral solvent pumped in to the end piece was 60:40 H_2O:IPA at room temperature; cooling the neutral solvent below these temperatures resulted in unwanted crystallisation in the end piece.

Table 5.11: Continuous crystallisation experiments in the KRAIC

Experiment	Wt.% MCM	Conc. PCM (mg/g)	Cold tube (Y/N)	Mixer piece	Flow rate (ml min^{-1})			Residence Time	Set Temperature (°C)						
					Solution	Carrier Fluid	Air		Feed	Transfer tube	Mixer bath	Cold tube	Coil 1	Coil 2	Coil 3
KRAIC 1	25	300	Y	X	2.1	2.1	2.1	30 mins	55	55	55	15	30	20	20
KRAIC 2A	25	300	Y	K	2.1	2.1	2.1	30 mins	55	40	35	10	20	20	20
KRAIC 2B	25	300	Y	K	2.1	2.1	2.1	30 mins	55	55	40	13	20	20	20
KRAIC 3	18	300	N	Y	4.6	4.1	-	20 mins	55	55	40	-	ICE	30	20
KRAIC 4	25	300	Y	Y	4.6	6.3	-	12 mins 43 secs	55	55	40	8	20[§]	20	20
KRAIC 5	0	250	Y	X	3	2.1	0.2	18 mins 10 secs	50	45	40	10	20	20	20

[§] Ice placed inside coil 1 after 28 minutes to help induce crystallisation

5.2.3 Results and discussion

KRAIC 1

Initial experiments incorporating MCM as a template molecule utilised a cross mixer piece (Figure 5.33) to give tri-segmented flow within the main crystalliser coils. Due to residence time restrictions, stemming from pump operational limits and tubing length, and the widening of MSZ for the PCM/MCM system, it was deemed necessary to induce nucleation by use of a cold tube. A 0.50 m cold tube was incorporated into the set-up as detailed in section 5.2.1. It was anticipated that induction of nucleation in the cold tube could result in high solid loadings which could result in blockage of the crystalliser. As such, initial investigations adopted heating of the first coil to a temperature of 30 °C in order to mitigate this potential problem. However under the conditions investigated in this experiment, no crystallisation was observed, with inconsistent slug sizes seen throughout; regular slug sizes are crucial for consistent particle attributes, ensuring all particles experience the same conditions in terms of mixing and residence time within the crystalliser. The temperature of both the cold tube and the mixer bath were decreased to 5 °C and 35 °C respectively; however after a period of 2.5 hours, crystallisation was still not evident in the system and the experiment was halted.

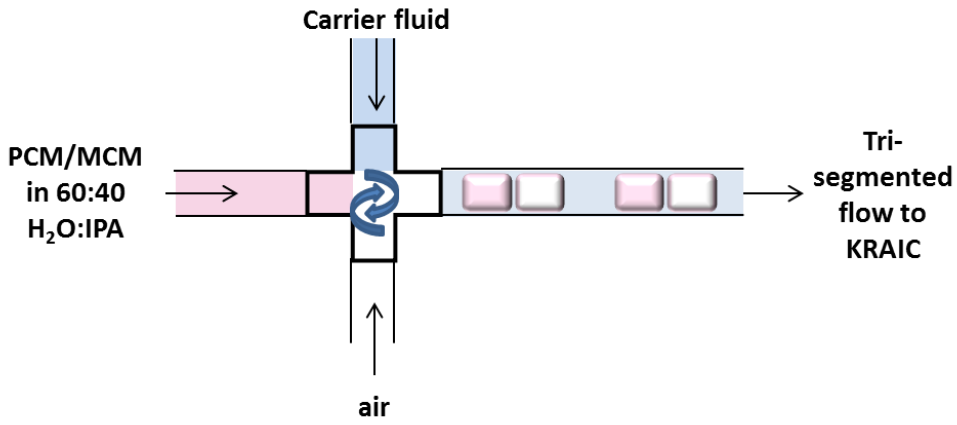

Figure 5.33: The cross mixer piece alignment used in KRAIC 1

As with the COBC, the KRAIC is a flow crystalliser and so the residence time is dictated by the length of the tubing and the net flow rate. The temperature control and profile obtained in the KRAIC is a function of tubing length and as this is fixed at a constant length the crystallisation cannot be run for longer periods of time as can be done for batch crystallisations. It can be suggested that the cold tube was not of sufficient length/ low enough temperature to induce crystallisation in the system. This combined with the short residence time (30 minutes) provided by the three coils were not sufficient to allow crystallisation in the system.

KRAIC 2A and KRAIC 2B

In order to address the issues with inconsistent segmentation observed in the crystalliser during experiment KRAIC 1, in experiment KRAIC 2A the mixer piece was changed to a K-mixer (Figure 5.34). Based on experiments presented above of inducing crystallisation in the COBC platform, the length of the cold tube was also increased to the same length as one COBC straight (0.75 m) in order to provide a greater residence time at the lower temperature, with the aim of inducing nucleation in the system. The temperatures of the jacketed tube linking feed to mixer piece, the mixer water bath and the first coil were also reduced, as detailed in Table 5.11.

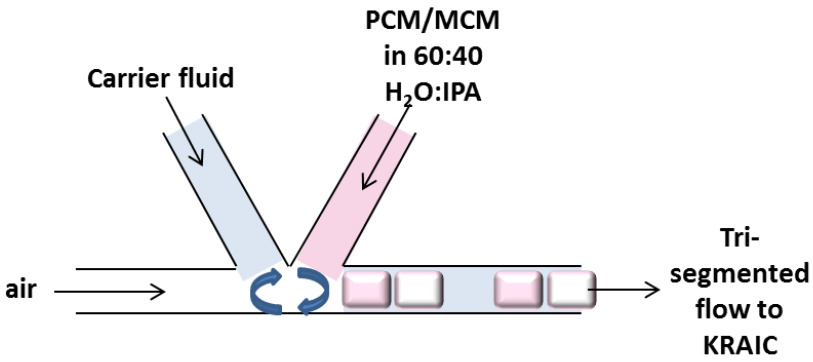

Figure 5. 34: The K-mixer piece alignment used in KRAIC 3A and 3B

After 5 minutes, crystals were observed in the cold tube (Figure 5.35), prompting the temperature of the cold tube to be increased to 13 °C after 11 minutes to mitigate the formation of blockages. At 21 minutes, there were signs of crystallisation in the mixer piece and so the temperature of the water bath and the jacketed tube before were increased without any stopping of flow. Due to the change in conditions within a run, the subheading KRAIC 2B is henceforth used for the experiment after these changes were implemented.

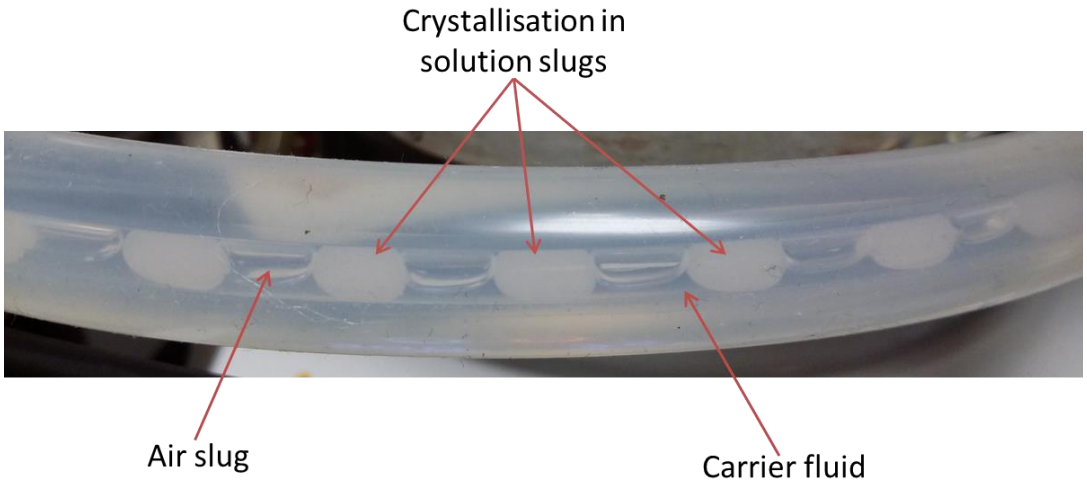

Figure 5.35: Crystallisation in the cold tube in Experiment KRAIC 2A

After the change of conditions, Experiment KRAIC 2B was run for a further 40 minutes, after which time the experiment had to be stopped in order to clear blockages caused by very high solid loadings throughout all three coils (Figure 5.36). It was observed that the joints connecting the cold tube to the main body of crystalliser tubing acted as another site of nucleation and sedimentation, further hindering the flow of slurry within the system.

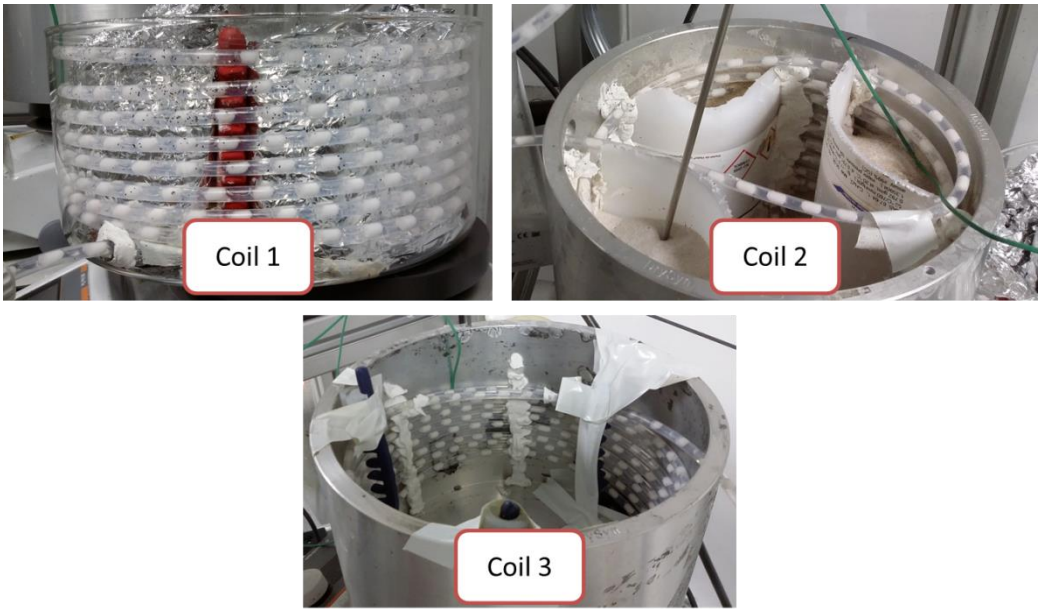

Figure 5.36: High solid loadings in the three coils in Experiment KRAIC 2B (images taken at 12 mins for coil 1 and 38 mins for coils 2 and 3)

Solid samples from Experiment 2A and 2B were taken and analysed through PXRD (Figure 5.37).

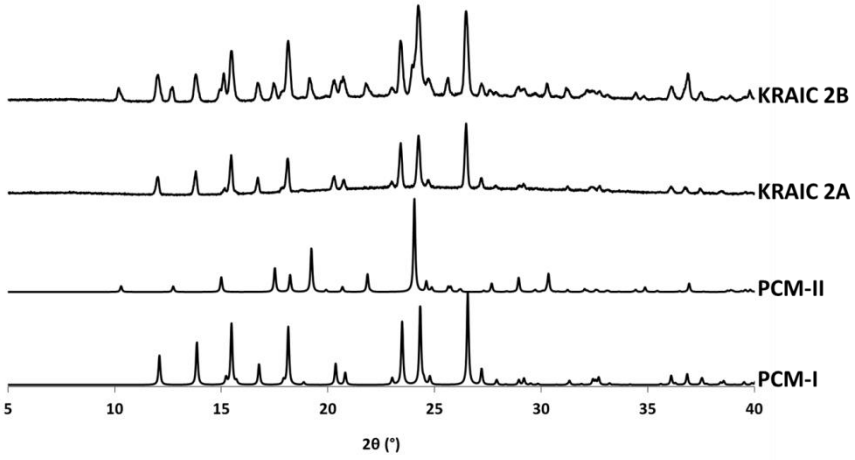

Figure 5.37: PXRD patterns for Experiment KRAIC 2A and KRAIC 2B; the y-axis displays relative intensity in arbitrary units

KRAIC 2A corresponds to the point of the crystallisation where encrustation was observed in the mixer piece, likely nucleating in the jacketed tube between the feed vessel and mixer, with PXRD analysis showing the production of PCM-I. Batch crystallisation experiments showed PCM-I crystallises at roughly 45 °C and so it can be suggested that the period of time the solution spent at this temperature resulted in the nucleation of this polymorphic form. Due to the fact that the crystallisation was not stopped between Experiment 2A and 2B, the PCM-I already produced was still present in the coils of the KRAIC and so some PCM-I was still present in the PXRD pattern for KRAIC 2B. However, once conditions were altered and crystallisation was controlled such that nucleation occurred within the main coils, PCM-II began to crystallise. As such, the PXRD pattern for KRAIC 2B shows a mixture of PCM-I and PCM-II. Due to the mixture of the two polymorphic forms and the focus of the work being on obtaining the metastable PCM-II, yields for this experiment were not calculated.

KRAIC 3

Owing to the observation that the joints between the cold tube and the mixer piece/main coil tubing acted as sites of nucleation for the crystallisation observed in Experiment KRAIC 2A and 2B, Experiment KRAIC 3 investigated removal of the cold tube and replacement with a bag of ice/water/salt inside coil 1. Coil 2 was slightly heated to 30 °C to mitigate significant blockages. Furthermore, a reduction in the number of available gear pumps meant that only two inputs into the mixer piece were possible; owing to the problems that can be experienced with air segmentation, the two flows used were solution and carrier fluid. As such, the mixer piece orientation was changed to a Y-mixer (Figure 5.38).

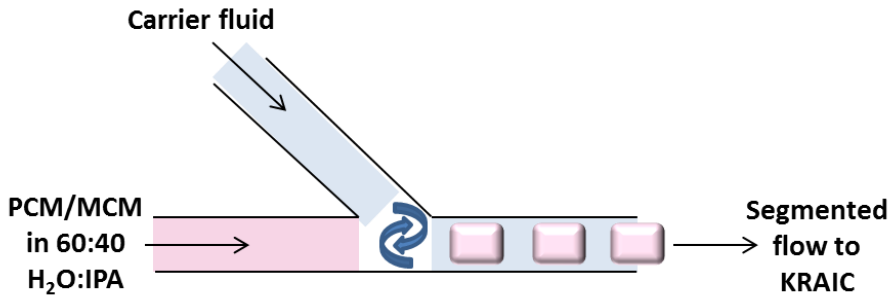

Figure 5.38: The Y-mixer piece utilised in Experiments KRAIC 4 and KRAIC 5

After the first residence time (20 minutes), no crystals were observed and so another bag of ice was placed in coil 2 to encourage nucleation. The residence time for this experiment is significantly less than those in previous experiments due to the increased flow rates needed to obtain even segmentation with the Y-mixer piece. This decreased residence time could explain why

crystallisation was not observed within the main body of the crystalliser. Although no crystals were observed in the slugs of solution, small crystals were captured on the filter paper. It can be suggested that due to the shortening of residence time within the crystalliser, the solution did not have enough time to fully desupersaturate so crystallisation occurred on the filter paper. That notwithstanding, analysis of these crystals showed the production of PCM-II in the absence of any PCM-I (Figure 5.39). Owing to the very low solid yields produced in this experiment, experimental yields could not be accurately determined.

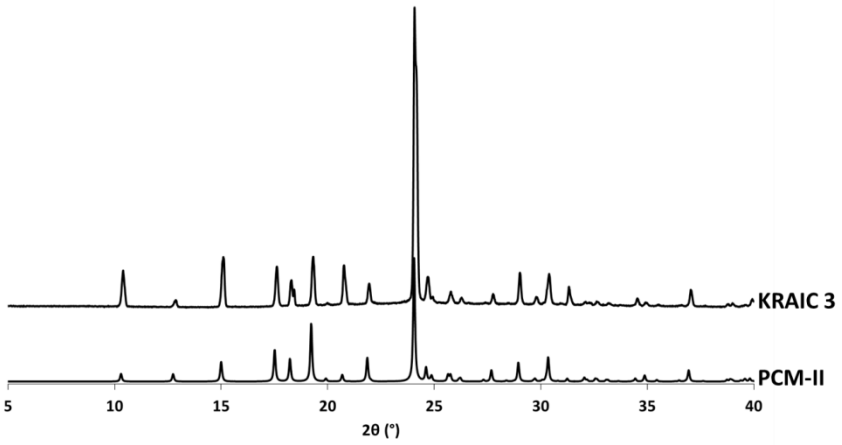

Figure 5.39: PXRD patterns showing the production of PCM-II in Experiment KRAIC 3; the y-axis displays relative intensity in arbitrary units

Despite best attempts to ensure that the bags of ice placed inside the coils resulted in effective cooling of all parts of the coil, the heat transfer could not be as effective as when the entire coil is surrounded by a cold tube. Further, over time the ice would melt, effectively increasing the temperature. As such, it can be surmised that, the temperature of the coil combined with the time spent at this temperature is not sufficient to induce nucleation in a system that displays slow nucleation kinetics such as the one investigated here; it is concluded that in order to induce consistent nucleation in the system, a cold tube is needed.

KRAIC 4

For Experiment KRAIC 4, a zero-volume union was used in order to connect the cold tube (1.14 m in length) to the main coil tubing, ensuring the join was not a possible site of nucleation. As far as possible the experimental parameters employed for Experiment KRAIC 2B (which resulted in the formation of PCM-II) were retained in KRAIC 4, with the exception of the mixer piece which remained as a Y-mixer (Figure 5.38), as deployed in Experiment KRAIC 3, and the flow rates (these were increased from Experiment 2B in order to obtain even segmentation with the Y-mixer piece). However, to keep parameters consistent with Experiment KRAIC 2B, tri-segmented flow was

achieved by delivering both air and carrier fluid from the same pump (set to 4.1 ml min^{-1}) *via* a valve upstream from the pump. The valve enabled a controlled proportion of air to carrier fluid to be achieved, here set at 50 % (a 1:1 v/v ratio). The temperature of the cold tube (reduced from 8 °C to 5 °C after 18 minutes), coil 1 (through addition of ice after 28 minutes) and mixer water bath (reduced from 40 °C to 35 °C after 60 minutes) were all reduced throughout the experiment to induce nucleation in the system. After one hour of operation, small crystals were observed in slugs approaching the exit piece, however were not visible in the filter paper. As such, the filter paper was changed to a paper that had a smaller (from 11 µm to 25 nm) pore size in order to collect these crystals. Samples collected were analysed by PXRD (Figure 5.40).

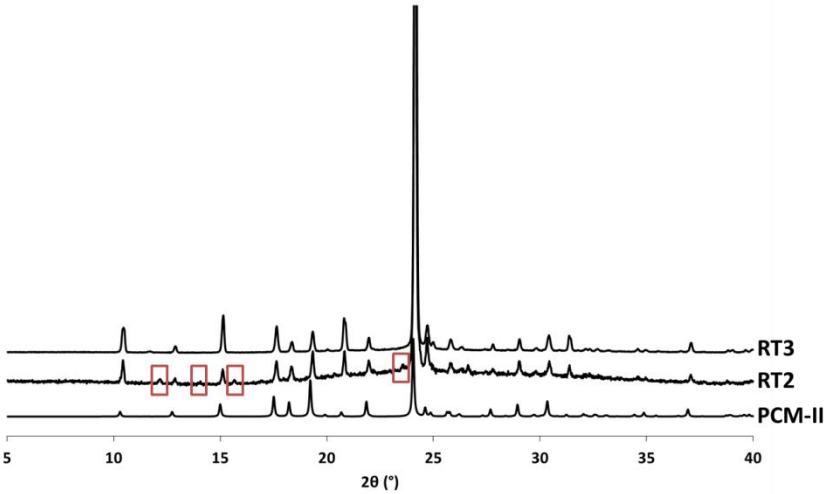

Figure 5.40: PXRD analysis for Experiment KRAIC 4 – those peaks corresponding to PCM-I in RT2 are boxed in red. The y-axis displays relative intensity in arbitrary units.

PXRD analysis (Figure 5.40) of samples from these filter papers shows the production of a mix of PCM-I and PCM-II in RT2, with pure PCM-II being produced in RT3. However, solid yields were extremely low and whilst sufficient for PXRD analysis, insufficient solid product was obtained for reliable yield calculations. Further optimisation of this crystallisation process would be required in order to produce PCM-II in higher yields. A longer residence time in the system would be required in order to allow crystallisation of a system which displays slow nucleation kinetics due to a wide metastable zone width such as the one studied in this work.

KRAIC 5

Experiment KRAIC 5 was run as a control experiment and investigated the crystallisation of PCM in the KRAIC in the absence of any template molecule. A lower concentration of PCM (250 mg/g) was used in comparison to the experiments with MCM present; in the absence of MCM a concentration of 300 mg/g would result in very high solid loadings which would block the small bore tubing of the

KRAIC. To ensure consistency between this experiment and those containing MCM, a cold tube of length 1.14 m was incorporated into the set-up.

Crystallisation was observed by the end of the second coil in RT1. There were problems with blocking of the carrier fluid recovery holes at the point of filtration, however these were alleviated easily. After an hour of operation, the experiment was halted due to blockage within the coils. Analysis of the solid form of the crystals produced through PXRD confirms the presence of PCM-I, with yields of crystallisation shown in Table 5.12.

Table 5.12: Yields from experiment KRAIC 5

Residence Time	Mass product (g)	Yield (%)
RT1	0.2760	2.04
RT2	0.8524	5.68
RT3	0.4259	3.96

5.2.4 Conclusions

The templated crystallisation of metastable PCM-II in the KRAIC has been observed, however further optimisation of the conditions is required in order to produce this metastable polymorphic form in appreciable yields. Segmented flow with an immiscible carrier fluid and air was used throughout the experiments.

The KRAIC design had to be adapted to incorporate a cold tube into the platform in order to induce any crystallisation in the system, as the current design does not facilitate controlled dynamic cooling of the three coils below ambient temperatures. Ice can be added to the inside of the coils; however this does not allow accurate and controllable temperature control to be achieved. The temperatures of each of the sections required initial optimisation after crystallisation was observed upstream of the mixer piece at a temperature which has been shown to be conducive to the crystallisation of PCM-I (see Chapters 3 and 4). Upon controlling the point of nucleation to occur within the cold tube, the target metastable PCM-II form was observed in the solid product. However, joints between the cold tube and main crystalliser tubing acted as sites of further nucleation resulting in high solid loadings which lead to eventual blockage of the small bore diameter tubing.

Repetition of experiments with the modified set temperatures of the mixer bath and cold tube (to ensure the stable PCM-I did not crystallise) resulted in crystallisation of small quantities of PCM-II. The crystals produced in this experiment were so small that a smaller pore size filter paper was

needed in order to harvest them for analysis. PXRD confirmed the presence of a mixture of PCM-II and PCM-I in the second residence time, with the product in the third residence time shown to be PCM-II. The mixing experienced within the KRAIC platform is significantly gentler than that observed in other systems (COBC, MSMPR, batch environments) and so it can be postulated that this relative decrease in mixing intensity could be responsible for the small quantities of PCM-I observed in the PCM-II solid. Furthermore, nucleation is being induced at a low temperature, due to limited time within the cold tube, and so this could be causing nucleation of the more stable polymorph. As such, future experiments should investigate increasing the length of this cold tube further to allow for both more nucleation and nucleation at a higher temperature that could mitigate the production of the stable PCM-I. A longer residence time within the main body of the crystalliser would also be desirable in order to increase the residence time within the system; however with the current experimental set-up this is not possible due to experimental limits of tubing length and net flow rate.

As the KRAIC operates at much lower volumes than the two continuous crystallisation platforms previously already explored in this work, it may be that use of this platform would be beneficial for those systems outlined in Chapter 3 that could not be scaled beyond the 1 ml volume.

5.3 Chapter conclusions

This chapter has demonstrated the use of two tubular continuous flow crystallisation platforms in the templated crystallisation of metastable PCM-II using MCM as a templating molecule. The KRAIC works on much lower working volumes (mL/h *vs* L/h) and smaller internal diameters (3.2 mm *vs* 15 mm) in comparison to the COBC. The mixing in the KRAIC is provided by bolus flow and is gentler than the eddies generated through oscillatory motion in the COBC.

PCM-II was formed in all instances in the COBC; however elimination of the metacetamol hydrate impurity proved problematic, with trace quantities present in all samples. In the case of the KRAIC, crystallisation had to be induced through a cold tube, resulting in the crystallisation of PCM-II with small quantities of PCM-I in the solid product, as detected through PXRD. Further, the gentle mixing in the KRAIC may not be sufficient for the elimination of PCM-I from PCM-II samples; small scale experiments performed in Chapter 3 highlighted the importance of mass transfer and mixing in the formation of PCM-II in smaller volumes. The elimination of PCM-I from the solid product is a key challenge to stop the conversion from PCM-II to PCM-I (see Chapter 3). As such, for the production of PCM-II, the COBC would be preferred between the two tubular crystallisers investigated.

However, it was noted that both crystallisers did not provide sufficient residence time to allow for substantial growth of product. With systems such as this, that display slow nucleation kinetics, flow systems would not be as desirable as, for example, crystallisation in a periodic MSMPR (PMSMPR) system. These PMSMPR systems allow for periods of dwelling during the crystallisation, increasing residence time and helping induce crystallisation into slow nucleating systems (Chapter 4).

6 Hosting of reactive pharmaceuticals

The research presented in Chapters 3-5 focussed on controlling the polymorphic solid form of molecules, in particular APIs, with paracetamol used as an exemplar in a range of investigations. One of the major drivers in such control is to produce solid forms with favourable physical properties. The work presented in this Chapter looks at using hosting in order to control the production of more stable solid forms of pharmaceutical molecules that can be classed as reactive in terms of, for example, thermal or hydrolytic stability. The principles used in designing such host-guest complexes are related to those used in selecting co-molecules, templates and additives – notably the choice of GRAS hosts and the aim of enhancing one of more key physical properties of the solid state system that will enhance the efficacy of the active ingredient.

6.1 Introduction and Aims

Cyclodextrins (CDs) have been chosen as the host materials for the stabilising of reactive target molecules, owing to their lack of toxicity and feasibility for use in drug preparations; they are GRAS molecules.[227] Cyclodextrins are organic molecules comprised of varying numbers of glucose units joined together in a ring through α-1,4 glycosidic bonds. There are three native cyclodextrins (Figure 6.1); alpha (α-CD), beta (β-CD) and gamma (γ-CD) comprised of 6, 7 and 8 glucose units respectively.

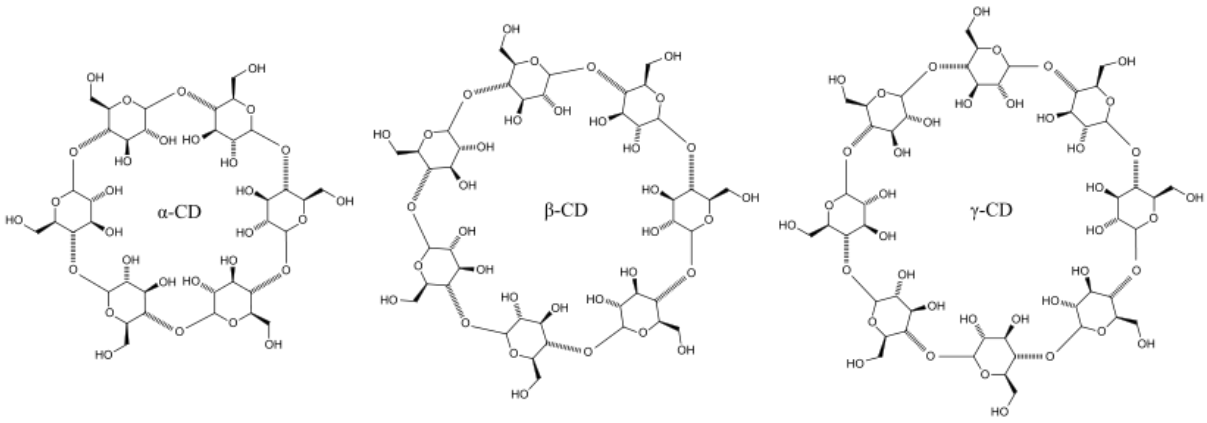

Figure 6.1: Structural diagrams of the three native cyclodextrins

The cyclodextrins consist of a hydrophobic interior cavity and hydrophilic exterior surface, and in their parent state contain water molecules loosely bound inside the cavity (Figure 6.2). Inclusion of guests within cyclodextrins is driven by an enthalpic and entropic gain from the release of water molecules from the cavity upon inclusion. The formation of a variety of intermolecular interactions and the release of conformational strain can also be considered driving forces for the inclusion of molecules inside the CD cavity.[228] An included compound is bound through a hydrophobic

interaction between the interior cavity and a hydrophobic guest molecule, however binding through hydrogen bonds from the secondary hydroxyl groups of the cyclodextrin is also possible; the included compound must be of comparable size to the cavity for inclusion to occur. The complexation process is reversible; the CD with included guest molecule is in dynamic equilibrium with the uncomplexed molecules as no covalent bonds are formed upon complexation. It has been shown that complexation of a cyclodextrin with another molecule increases the stability of cyclodextrins. [229-230]

Cyclodextrins, both native and derivatised, have been used extensively within the pharmaceutical sector to improve the aqueous solubility of a variety of poorly soluble drugs; furthermore, derivatised CDs are often used to increase the solubility of the parent CD.[231-234] Much less research has been reported on the use of cyclodextrins to host reactive pharmaceuticals[235], where reactivity encompasses both pharmaceuticals which are unstable at high temperatures or humidities and those that display a short half-life in the body.

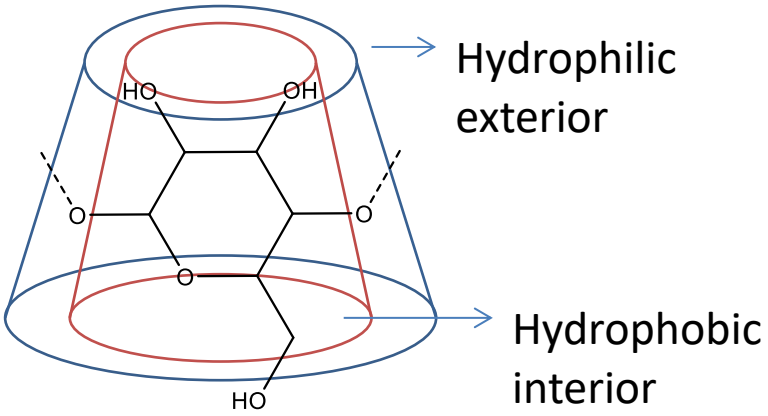

Figure 6.2: Schematic representation of a cyclodextrin molecule, illustrating the hydrophobic core and hydrophilic exterior

Two guest pharmaceutical molecules (APIs) have been the focus of this work: the antibiotic thiamphenicol (THM) and the antioxidant α-lipoic acid (ALA) (Figure 6.3). Thiamphenicol displays poor hydrolytic stability across the amide bond[236-237], while ALA displays poor thermal stability due to cleavage of the S-S bond, as shown in Figure 6.3.

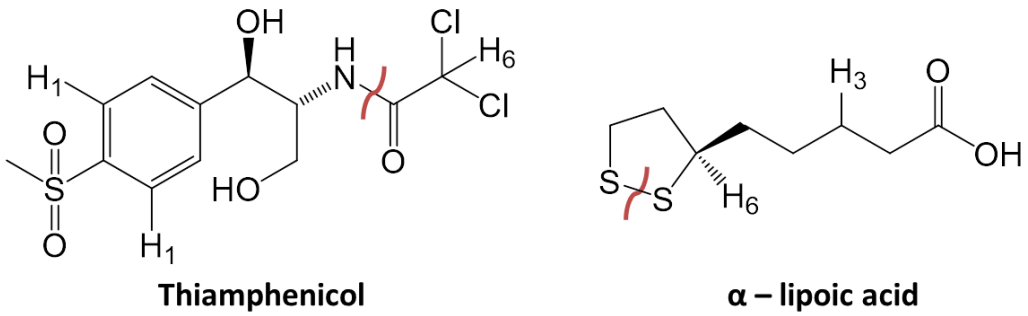

Figure 6.3: The chemical structures of thiamphenicol and α-lipoic acid, with the bonds that are the source of molecular instability highlighted

Literature has shown that incorporation of ALA into β-CD confers increased thermal stability of the ALA. [235] The aim of the work presented here on ALA would be to transfer this literature reported host/guest system, with proven stabilisation of the ALA, initially into cooling crystallisation environments. If this is successful, transfer into continuous crystallisation platforms will be targeted. Utilising the premise of hosting within cyclodextrins, attempts at incorporating thiamphenicol into a similar hosting system will be explored; hosting of this API in CDs is previously unreported. As water molecules are excluded from the hydrophobic cavity upon inclusion of a guest molecule, hosting of a hydrolytically unstable guest molecule inside this cavity could help to increase its stability against hydrolysis.

Transfer of these host/guest systems to cooling and continuous crystallisation environments for large scale production is unreported with current methods of production using the method of saturated aqueous solution.[238-240]

6.2 Experimental

6.2.1 Evaporative crystallisations

Evaporative crystallisation experiments were conducted as a screening method in order to obtain suitable single crystals of CD-thiamphenicol host-guest complexes for SCXRD. Equimolar amounts of thiamphenicol (10 mg) and each of the three parent cyclodextrins (27.3 mg α-CD, 31.8 mg β-CD and 36.3 mg γ-CD) were dissolved in minimal volumes of water in a 7 ml vial, with each crystallisation performed in triplicate. Water was chosen as an initial solvent as there is a risk of preferential inclusion of other solvents into the CD cavity over the guest molecule; in their native form as supplied, CDs contain water bound inside the cavity. For each of the crystallisations with each of the three CDs, the vials were fitted with a pierced lid and placed on temperature controlled hotplates at 25 °C, 40 °C and 50 °C to allow slow evaporation of the solvent.

6.2.2 Cooling crystallisations

Cooling crystallisations for both hosting systems at a variety of scales were conducted using the Polar Bear Plus Crystalliser. Ratios of the two components were determined based on the binding ratio highlighted from generation of Job plots (see below). Crystallisations were carried out in 20 ml glass vials, with varying solvent amounts, with magnetic bottom stirring. Full details will be highlighted in sections 6.3.1.3 and 6.3.2.2.

6.2.3 NMR analysis

6.2.3.1 Job plots

In order to determine the stoichiometry of the binding between the host and guest, the method of continuous variation to generate Job plots was used. [241] Instead of varying the concentration of one component at a time, the method of continuous variation holds the total concentration of host and guest constant (in this case at 4 mM) and varies the relative proportions of the host and guest (illustrated in Figure 6.4).[242]

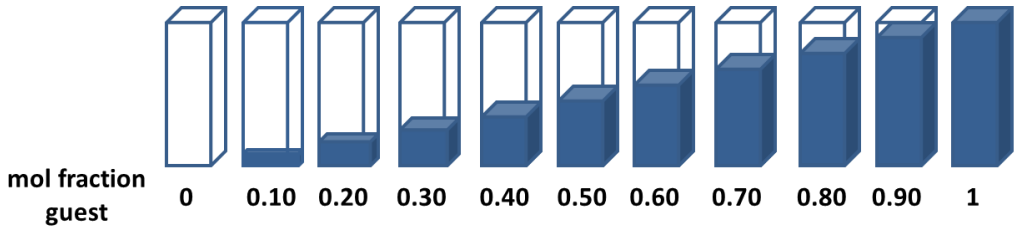

Figure 6.4: Illustration of the method of continuous variation, used to generate data for the Job's plot approach to determine host-guest stoichiometry

NMR analysis was used in order to track shifts in certain proton peaks upon changing the ratio of host to guest. Reference samples of the host and guest molecules were taken and the peaks for each of the protons identified. A combination of standard ^{1}H NMR (Figure 6.9) and correlation spectroscopy (COSY)(Figure 6.5) was required to assign all peaks for the cyclodextrin molecule.

Thiamphenicol ^{1}H NMR (D_2O, 500 MHz, 298 K) δ (ppm): 3.13 (s, 3H, CH_3), 3.60 (m, 1H, CH), 3.76 (m, 2H, CH_2), 4.12 (m, 1H, CH), 5.08 (s, 1H, $CHCl_2$), 7.57 (d, 2H, ArH), 7.83 (d, 2H, ArH)

γ-CD ^{1}H NMR (D_2O, 500 MHz, 298 K) δ (ppm): 3.47 (t, 8H, H4), 3.54 (dd, 8H, H2), 3.755 (s, 24H, H5+H6), 3.82 (t, 8H, H3), 5.00 (d, 8H, H1)

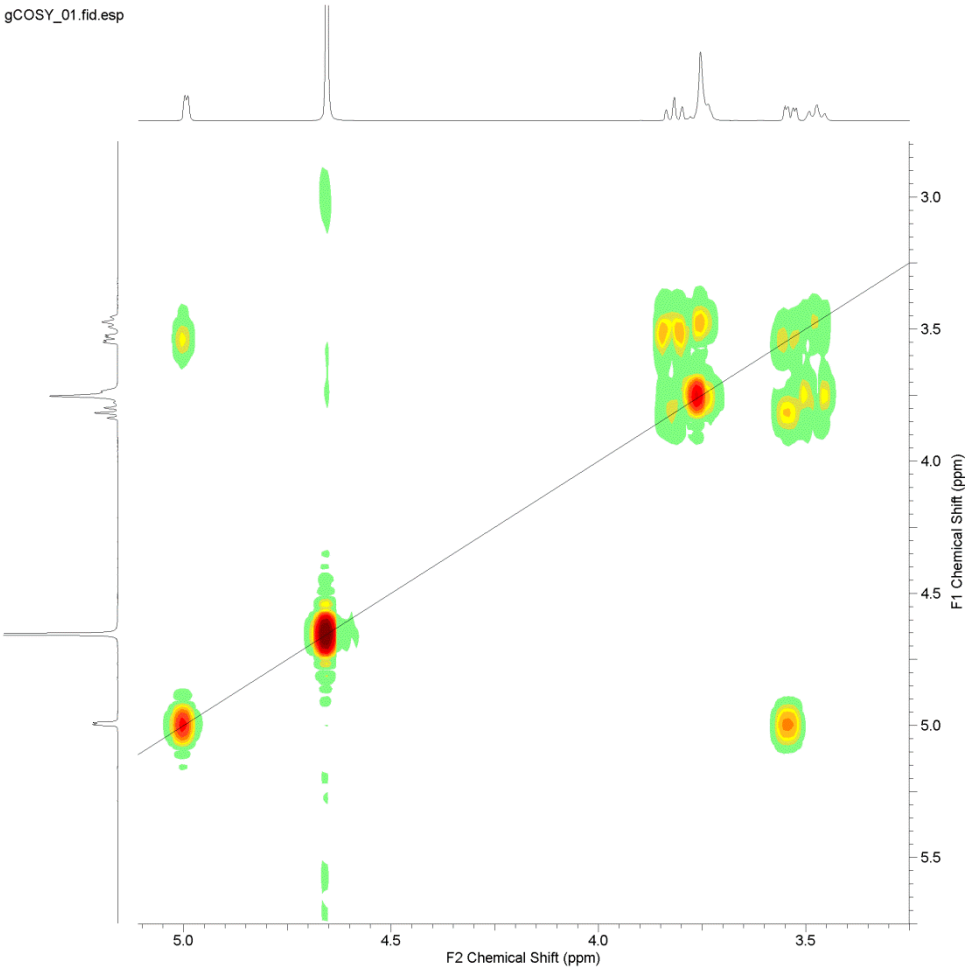

Figure 6.5: COSY NMR spectrum for γ-CD

Protons thought to be involved in interactions between the host and guest molecules upon inclusion were identified. For each of the two guests these were chosen based on those proton signals that were still easily identifiable upon inclusion into the cyclodextrin host and are labelled in Figure 6.3. For the cyclodextrin molecule, protons were chosen based on those which stereochemistry would indicate would point in towards the interior of the cavity and so would be interacting with the guest molecule upon inclusion (protons H3 and H5 in Figure 6.6).

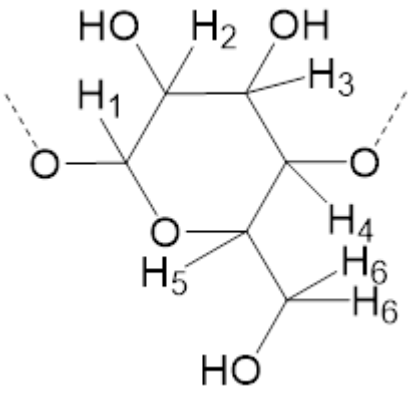

Figure 6.6: A single glucose unit showing the proton labelling scheme

A 4 mM solution of each of the molar fractions outlined in Figure 6.4 was made up in D_2O and subjected to ^1H NMR analysis using a Bruker Avance II+ 500 MHz spectrometer at 298 K. Data were processed using ACD Labs NMR processor which allowed the chemical shifts of appropriate protons to be tracked upon changing solution composition (Table 6.1- Table 6.4).

Table 6.1: Proton shifts in thiamphenicol upon inclusion into γ-CD

Thiamphenicol (THM)								
Mole fraction		[THM] (mM)	H1			H6		
THM	γ-CD		ppm	δH	δH x [THM]	ppm	δH	δH x [THM]
1	0	4.0	7.822	0.0000	0.000	6.105	0.000	0.000
0.9	0.1	3.6	7.815	0.0070	-0.0252	6.095	0.010	-0.0360
0.8	0.2	3.2	7.8105	0.0115	-0.0368	6.089	0.016	-0.0512
0.7	0.3	2.8	7.8052	0.0168	-0.0470	6.085	0.020	-0.0560
0.6	0.4	2.4	7.8057	0.0163	-0.0391	6.086	0.019	-0.0456
0.5	0.5	2.0	7.8070	0.0150	-0.0300	6.085	0.020	-0.0400
0.4	0.6	1.6	7.8040	0.0180	-0.0288	6.080	0.025	-0.0400
0.3	0.7	1.2	7.8025	0.0195	-0.0234	6.075	0.030	-0.0360
0.2	0.8	0.8	7.8025	0.0195	-0.0156	6.073	0.032	-0.0256
0.1	0.9	0.4	7.7958	0.0262	-0.0105	6.068	0.037	-0.0148
0	1	0.0	-	-	-	-	-	-

Table 6.2: Proton shifts γ-CD upon inclusion of thiamphenicol into the cavity

γ-CD								
Mole fraction		[γ-CD] (mM)	H3			H5		
γ-CD	THM		ppm	δH	δH x [γ-CD]	ppm	δH	δH x [γ-CD]
1	0	4.0	3.8170	0.0000	0.0000	3.7350	0.0000	0.0000
0.9	0.1	3.6	3.8096	0.0074	0.0266	3.7250	0.0100	0.0360
0.8	0.2	3.2	3.8081	0.0089	0.0285	3.7200	0.0150	0.0480
0.7	0.3	2.8	3.8046	0.0124	0.0347	3.7152	0.0198	0.0554
0.6	0.4	2.4	3.8036	0.0134	0.0322	3.7135	0.0215	0.0516
0.5	0.5	2.0	3.8047	0.0123	0.0246	3.7125	0.0225	0.0450
0.4	0.6	1.6	3.8015	0.0155	0.0248	3.7080	0.0270	0.0432
0.3	0.7	1.2	3.7988	0.0182	0.0218	3.7010	0.0340	0.0408
0.2	0.8	0.8	3.7950	0.0220	0.0176	3.6950	0.0400	0.0320
0.1	0.9	0.4	3.7950	0.0220	0.0088	3.6900	0.0450	0.0180
0	1	0.0	-	-	-	-	-	-

Table 6.3: Proton shifts in ALA upon inclusion into β-CD

ALA								
Mole fraction		[ALA] (mM)	H3			H6		
ALA	β-CD		ppm	δH	δH x [ALA]	ppm	δH	δH x [ALA]
1	0	4.0	1.64	0.00	0.000	3.590	0.000	0.0000
0.9	0.1	3.6	1.63	0.01	-0.036	3.580	0.010	-0.0360
0.8	0.2	3.2	1.62	0.02	-0.064	3.565	0.025	-0.8000
0.7	0.3	2.8	1.615	0.025	-0.070	3.560	0.030	-0.0840
0.6	0.4	2.4	1.61	0.03	-0.072	3.555	0.035	-0.0840
0.5	0.5	2.0	1.6	0.04	-0.080	3.545	0.045	-0.0900
0.4	0.6	1.6	1.6	0.04	-0.064	3.540	0.050	-0.0800
0.3	0.7	1.2	1.6	0.04	-0.048	3.532	0.058	-0.0696
0.2	0.8	0.8	1.59	0.05	-0.040	3.522	0.068	-0.0544
0.1	0.9	0.4	1.59	0.05	-0.020	3.519	0.071	-0.0284
0	1	0.0	-	-	-	-	-	-

Table 6.4: Proton shifts β-CD upon inclusion of ALA into the cavity

β-CD								
Mole fraction		[β-CD] (mM)	H3			H5		
β-CD	ALA		ppm	δH	δH x [β-CD]	ppm	δH	δH x [β-CD]
1	0	4.0	3.84	0.00	0.000	3.730	0.000	0.000
0.9	0.1	3.6	3.83	0.01	0.036	3.720	0.010	0.036
0.8	0.2	3.2	3.82	0.02	0.064	3.705	0.025	0.080
0.7	0.3	2.8	3.81	0.03	0.084	3.690	0.040	0.112
0.6	0.4	2.4	3.80	0.04	0.096	3.675	0.055	0.132
0.5	0.5	2.0	3.79	0.05	0.100	3.660	0.070	0.140
0.4	0.6	1.6	3.79	0.05	0.080	3.655	0.075	0.120
0.3	0.7	1.2	3.79	0.05	0.060	3.655	0.075	0.090
0.2	0.8	0.8	3.79	0.05	0.040	3.650	0.080	0.064
0.1	0.9	0.4	3.79	0.05	0.020	3.650	0.080	0.032
0	1	0.0	-	-	-	-	-	-

6.2.3.2 Diffusion ^{1}H NMR

In order to investigate whether the two components remain complexed in solution, diffusion ^{1}H NMR (DOSY) experiments were performed. Hosting complexes were dissolved in D_2O and spectra obtained at 298 K on a Bruker AV 400 spectrometer operating at 400.13 MHz.

6.2.3.3 Solid State CPMAS NMR

Solid state NMR was performed at AstraZeneca in Macclesfield. ^{13}C {^{1}H} cross-polarisation magic angle spinning (CPMAS) NMR spectra were recorded on a Bruker Avance III 500WB spectrometer. The samples were packed into 4 mm MAS rotors and spun about the magic angle at a frequency of

12 kHz. The spectra were recorded at 125 MHz for ^{13}C, i.e. a 500 MHz spectrometer. The contact time was 2 ms with a recycle delay of 5 seconds. Both spectra are externally referenced to the peak due to the carbonyl carbon of glycine at 176.03 ppm. The spectrum of the complex was recorded for a longer period of time in order to improve the signal-to-noise for the minor peaks.

6.2.4 Single crystal X-ray diffraction

Single crystal X-ray diffraction data for the molecular complex of thiamphenicol and γ-CD was collected on an Agilent Technologies Supernova diffractometer, using Cu radiation (λ = 1.5406 Å) at 150 K. The sample temperature was controlled using an Oxford Diffraction Cryojet apparatus and the data processed using CrysAlisPro version 1.171.36.21. Data were solved by direct methods using SHELXD-2013 and a full least squares refinement of the resulting structure was carried out using SHELXL-2013.

6.3 Results and discussion

6.3.1 The molecular complex of thiamphenicol and γ-cyclodextrin

6.3.1.1 Single crystal X-ray diffraction

Single crystal screening of samples produced from evaporative crystallisation experiments whereby attempts were made to host thiamphenicol inside the three native cyclodextrins confirmed the formation of a molecular inclusion complex. The molecular complex crystallises in the tetragonal space group $P42_12$ with two glucose units of three separate cyclodextrin units in the asymmetric unit (Z =6, Z'= 3/4).

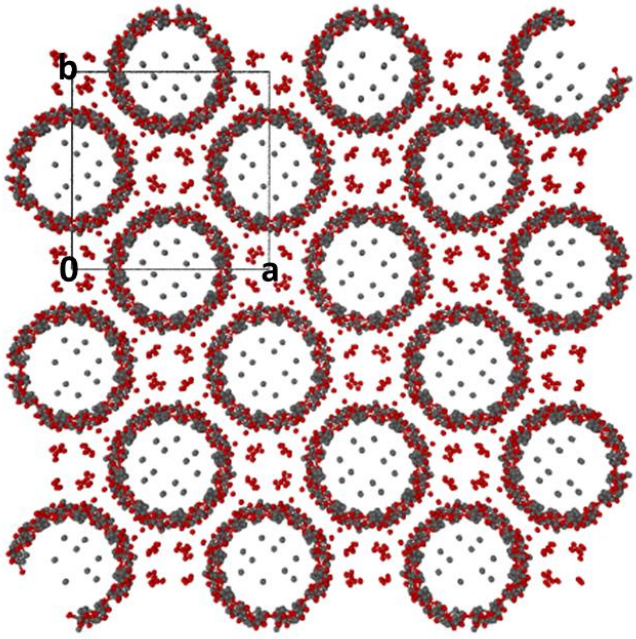

Figure 6.7: The packing in the molecular inclusion complex of thiamphenicol and γ-CD as viewed along the crystallographic *c* axis (hydrogen atoms were unable to be assigned)

The packing within the crystal structure (Figure 6.7) shows the γ-CD molecules to form distinct channels, with electron density visible inside the channels. As would be expected, the water molecules that reside inside γ-CD without a guest molecule present have been displaced to locations outside the CD molecules. However, due to the four-fold symmetry of the cyclodextrin molecules, resolution of the thiamphenicol molecule inside the channel is difficult. As such, to confirm inclusion other evidence was sought and further studies conducted. Initial confirmation of inclusion of a non-aqueous guest molecule into the cyclodextrin is obtained through crystal structure comparison. In their native form, the cyclodextrin molecules in γ-CD do not form distinct channels, rather the molecules are staggered (Figure 6.8). Upon inclusion of a non-aqueous guest this structure is changed to a channel structure, as observed in this case, suggesting molecular guest inclusion.[243]

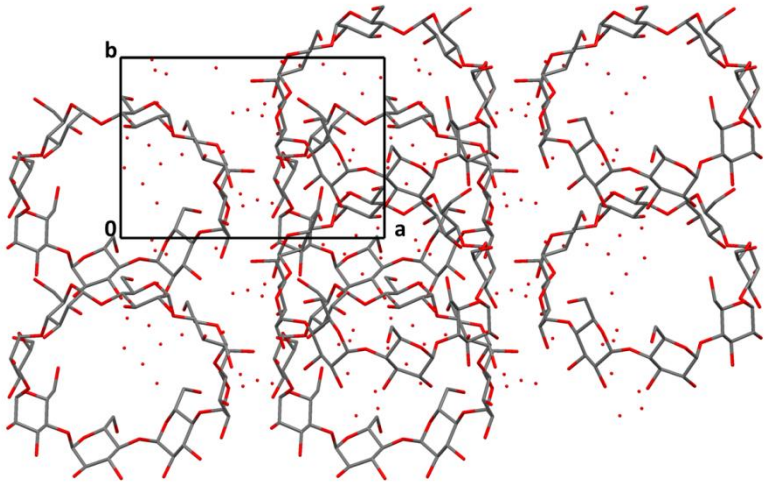

Figure 6.8: Staggered arrangement of γ–CD molecules in native γ-CD as viewed down the crystallographic *c* axis (for clarity all hydrogen atoms have been removed)

However, to confirm fully inclusion of the thiamphenicol molecule into the γ-CD pores, the molecular complex was subjected to full NMR analysis.

6.3.1.2 NMR analysis

NMR analysis was performed on single crystals screened to have the same unit cell parameters as the inclusion complex for which full single crystal data had been collected, to ensure the sample analysed by NMR was an inclusion complex and not a mixture of the two starting materials.

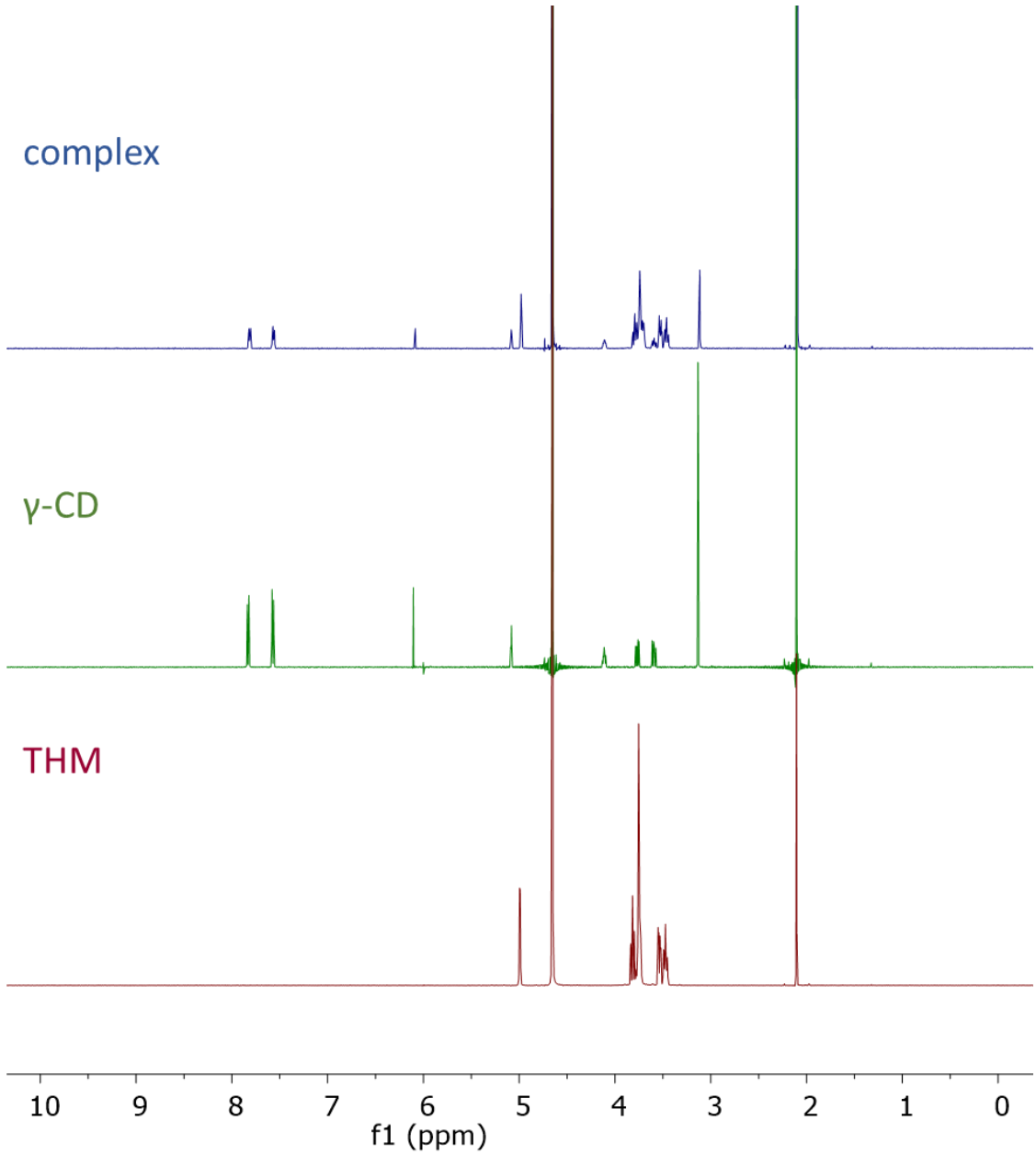

Figure 6.9: ^{1}**H** NMR spectra of each of the two starting materials and the inclusion complex

The NMR spectrum can be seen to be an amalgamation of the two individual components; the region between 3.4 and 3.9 ppm was horizontally expanded to allow resolution of overlapped peaks (Figure 6.10), thus illustrating the good agreement of the complex with the individual γ-CD and thiamphenicol spectra.

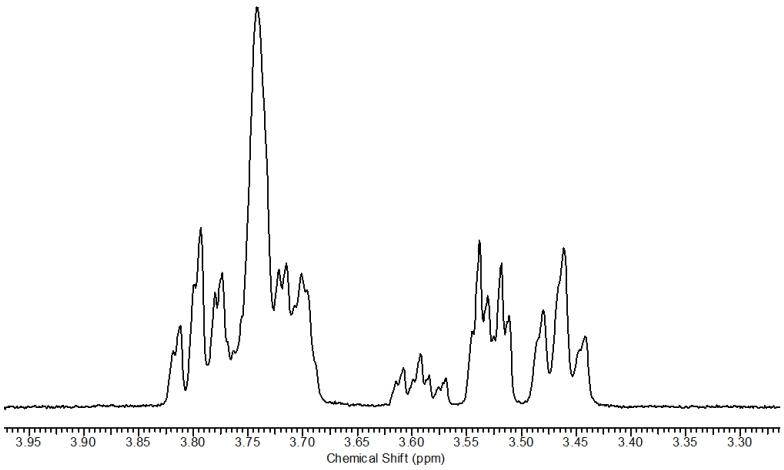

Figure 6.10: Horizontal expansion of the region between 3.4 and 3.9 ppm to allow resolution of peaks

Molecular inclusion complex of γ-CD and THM (D_2O, 500 MHz, 298 K) δ (ppm): 3.21 (s, 3H, CH_3 THM), 3.56 (t, 8H, H4 γ-CD), 3.63 (dd, 8H, H2 γ-CD), 3.69 (t, 1H, CH THM), 3.86 (m, 36H, H3, H5, H6 γ-CD), 4.21 (m, 1H, CH THM), 5.08 (s, 8H, H1 γ-CD), 5.18 (s, 1H, $CHCl_2$ THM), 7.66 (d, 2H, ArH, THM), 7.91 (d, 2H, ArH, THM)

As noted above, in order to investigate the stoichiometry of the inclusion complex, Job's method of continuous variation was employed. Plotting of the values in Table 6.1 and Table 6.2, results in the plot shown in Figure 6.11.

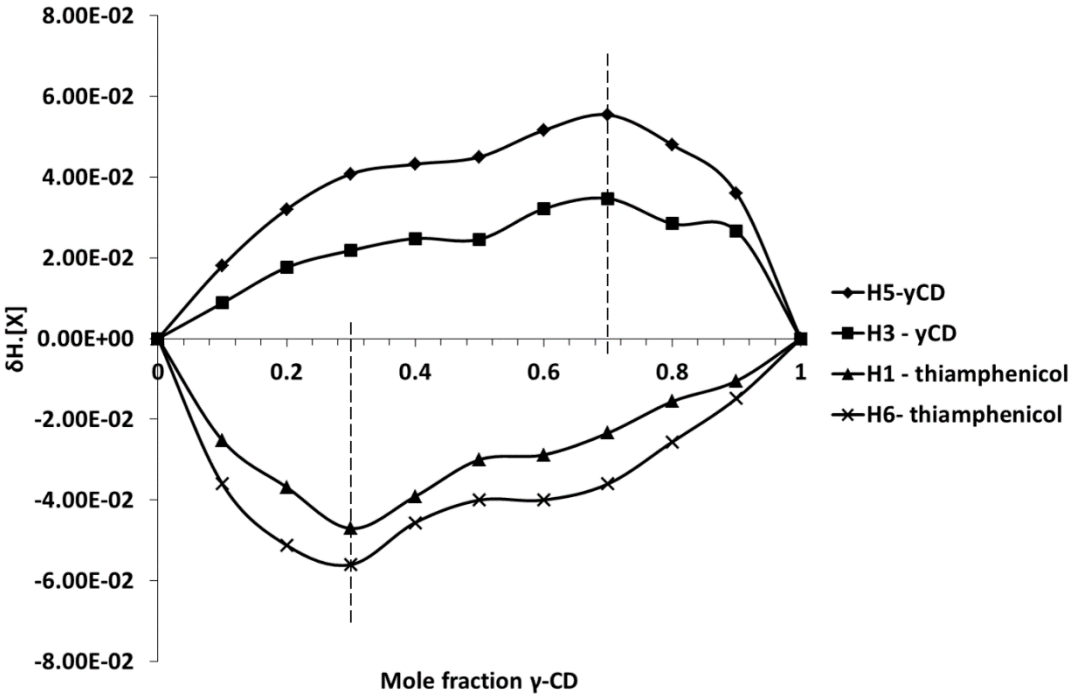

Figure 6.11: Job plot for the inclusion complex of thiamphenicol and γ-CD

The point at which the maximum in the curve is observed indicates the host: guest stoichiometry. The maxima in Figure 6.11 occur at a mole fraction of γ-CD of 0.7 for the γ-CD protons and 0.3 for the thiamphenicol protons, this indicates the two compounds bind in a 2:1 γ-CD: thiamphenicol ratio. [242] This ratio provides further indication that this system could be successful at stabilising the hydrolytically unstable thiamphenicol molecule; by incorporating inside two neighbouring CD molecules, all parts of the relatively long chain of the API will be encapsulated in a water excluded cavity. Knowledge of this binding ratio is also crucial for the transfer of this hosting system into cooling crystallisation environments (Section 6.3.1.4) by allowing solubility and stoichiometry to be controlled.

DOSY ^{1}H NMR spectroscopy (Figure 6.12) was also performed to verify if the components remain associated with one another in the solution state; this would be of relevance to the delivery of CD hosted thiamphenicol in aqueous environments such as the body. It can be seen that the thiamphenicol is diffusing at a speed of approximately 4.5 x 10^{-10} m^2s^{-1}, whereas the larger γ-CD is diffusing at a slower speed of 2.5 x 10^{-10} m^2s^{-1}. As these diffusion speeds are not comparable, it can be concluded that the thiamphenicol and γ-CD exist in equilibrium in the solution state. This is of particular interest when the stability of the complex in an aqueous environment is considered (Section 6.3.1.3) and when thinking about potential uses as a form of drug delivery.

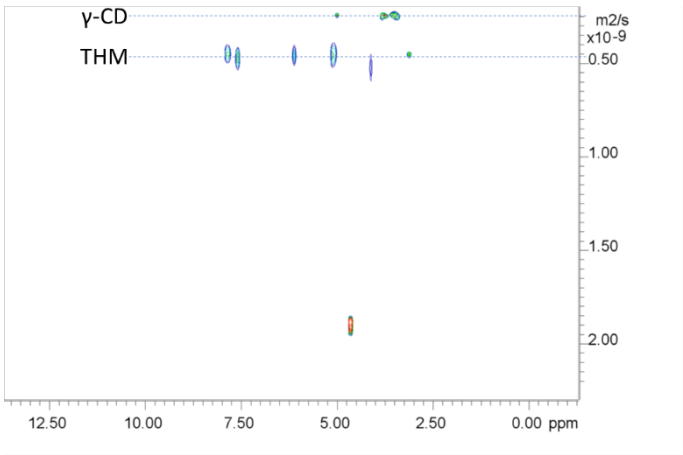

Figure 6.12: DOSY NMR spectra of the thiamphenicol: γ-CD inclusion complex

6.3.1.3 Stability analysis

A variety of different methods were considered in order to show whether by incorporating thiamphenicol inside γ-CD, the hydrolytic stability of the former is increased. In solution, the two compounds exist in equilibrium, meaning the thiamphenicol molecule is not always associated with a cyclodextrin molecule. As such, all solution based methods for both testing and analysis had to be discounted for the purposes of this work. As a method to test hydrolytic stability this eliminates slurrying techniques; owing to its higher aqueous solubility, γ-CD would preferentially dissolve in this case, leaving the thiamphenicol molecule exposed to the aqueous environment. In terms of analysis of the samples, methods such as HPLC and solution NMR also had to be eliminated from consideration.

As such, preparation and analysis using solid state methods was required. In attempts to induce hydrolysis in a solid state environment, samples were placed in a humid environment: a tub of salt with some water to add moisture was placed inside an oven set at 100 °C, with the samples placed within a small glass vial embedded into the salt. Samples of the complex and of thiamphenicol alone (to act as a control sample) were placed in these conditions for a period of one month. Analysis of the samples was undertaken using solid state ^{13}C NMR (SSNMR); PXRD was deemed inappropriate as the pattern is swamped by peaks from the cyclodextrin molecule and PXRD patterns of inclusion complexes of CDs are similar irrespective of the guest molecule included within the cavity. Thus, possible small changes in the thiamphenicol structure would not be visible through analysis with PXRD.

A SSNMR spectrum of the complex before being placed in humid conditions was taken in order to allow comparison to be made (Figure 6.13).

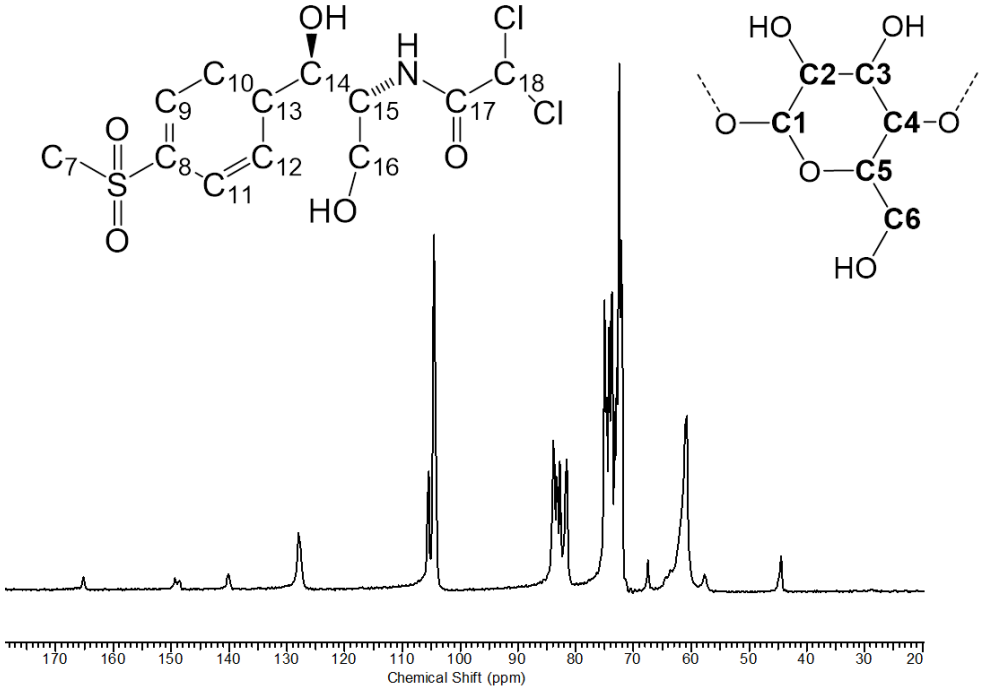

Figure 6.13: SSNMR of the inclusion complex before being placed in humid conditions

Inclusion complex of thiamphenicol and γ-cyclodextrin ^{13}C SSNMR (125 MHz, 298 K) δ (ppm):

44.4 (C16 THM), 61.0 (C6 γ-CD), 73.4 (C2, C3, C5 γ-CD C14, C15 THM), 82.5 (C4 γ-CD, C7, C8, C9, C10. C11, C12, C13 THM), 105.0 (C1 γ-CD), 127.8 (C17 THM), 140.1. 149.0, 165.3 (spinning side bands)

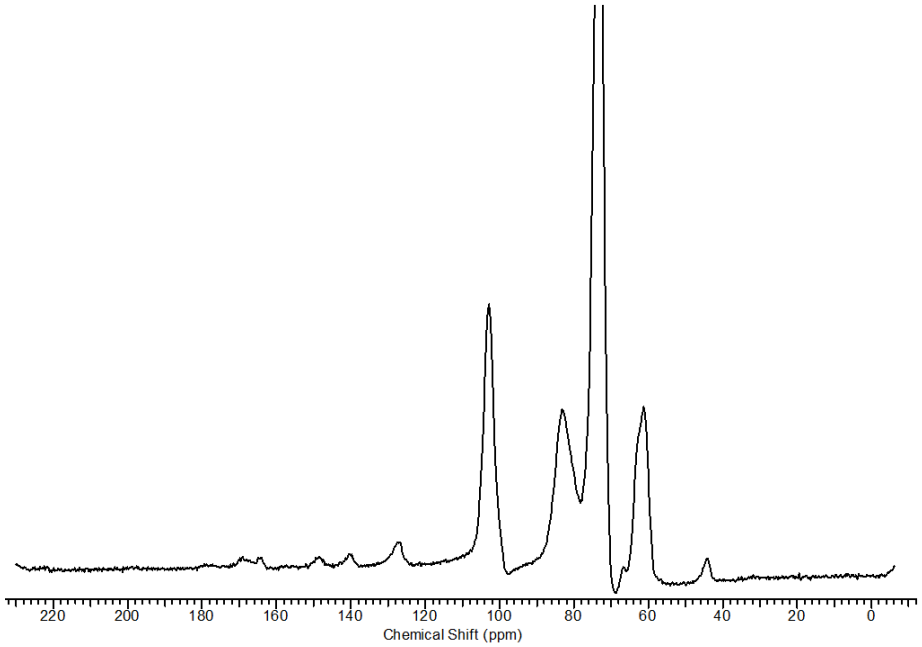

Figure 6.14: SSNMR spectrum of the complex after being subjected to stressed (humidity) conditions (the peak broadening compared with that in Figure 6.13 indicates the sample has turned amorphous)

Figure 6.14 shows the SSNMR spectrum of the molecular inclusion complex of γ-CD and thiamphenicol after being subjected to humidity conditions (90% RH, 100 °C) for a month. The broad nature of the peaks suggests the stressed conditions have resulted in the sample turning amorphous. However, all peaks positions remain the same, and despite loss of definition, it can be suggested that the complex remains intact upon exposure to humid conditions for a one month period. However, due to the peak broadening, it is not possible to track the small shifts that would be expected in the carbonyl peak at 165.3 ppm in the case where hydrolysis of the amide to a carboxylic acid group had taken place. As such, another method of monitoring potential solid-state hydrolysis in these samples is required; however, due to the time constraints of this project, this could not be performed and would be the subject of any further work on the system. Possible experiments could include using another salt such as potassium sulfate that would provide high humidity conditions at lower temperatures, aiding the sample to retain its crystallinity. The potential validity of this approach is supported by the observation that the sample of thiamphenicol placed in the same conditions melted over the exposure time.

The indication from SSNMR that the samples, while potentially retaining the integrity of the thiamphenicol within the complex, turned amorphous upon being treated under stressed conditions, prompted investigations into the relative thermal stability of the molecular inclusion complex in comparison to the two starting materials. DSC was used in order to evaluate the melting temperature of each of the three materials (Figure 6.15).

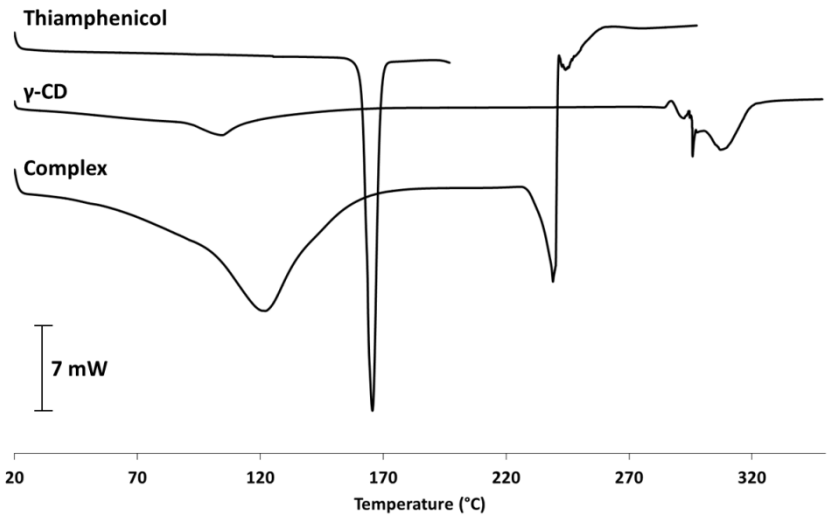

Figure 6.15: DSC analysis of thiamphenicol, γ-CD and the molecular inclusion complex of thiamphenicol and γ-CD (exothermic up)

Thiamphenicol melts at a temperature of 165.6 °C, characterised by the sharp endothermic event in Figure 6.15. There is a broad endothermic event in the region 90-120 °C in the DSC traces for

both γ-CD and the inclusion complex. Since both CD and the complex have lattice water, and since the broad nature of the peak suggests it is not a melt event, thermogravimetric analysis (TGA) (Figure 6.16) was performed in order to elucidate the origin of this event. In its native state, γ-cyclodextrin contains water molecules, bound both inside the cavity and hydrogen bonded to external hydroxyl groups. The TGA trace (Figure 6.16) shows a percentage mass loss of 7.6 % between 30 °C and 130 °C. According to the crystallographic information for γ-CD, it contains 14 water molecules in its native state, eight of which are bound within the cavity and six are bound externally, as would be seen in a conventional hydrated crystal structure. Those bound around the external perimeter of the CD molecule will be easier to release than those bound inside the cavity. As such, it is suggested that the 7.6 % mass loss observed in the TGA corresponds to those six water molecules bound around the edge of the cyclodextrin molecule (the theoretical % mass loss for these is 8.3 %). In the inclusion complex, the crystal structure confirms water to be present only around the edges of the cyclodextrin molecule, as thiamphenicol has displaced that which was in the cavity. Therefore, in the DSC of the complex, it would be expected that this water would also be lost over a similar temperature range as that in γ-CD. Although TGA was unable to be performed on the complex, it is reasonable to conclude that the endothermic event in the DSC of both γ-CD and the inclusion complex of γ-CD and thiamphenicol can be attributed to the loss of water bound around the edges of the cyclodextrin molecules.

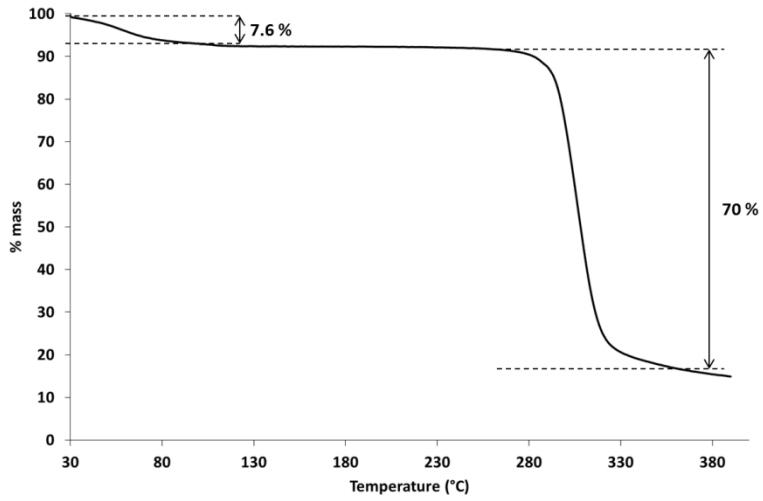

Figure 6.16: TGA analysis of γ-CD

The larger mass loss of 70 % at ~300 °C can be attributed to the thermal degradation of the glucose units in γ-CD, into carbon and water vapour. Taking into account the removal of six water molecules from the thermal event at lower temperatures, the chemical formula remaining in γ-CD is $C_{48}H_{80}O_{40}{\cdot}8H_2O$. Decomposition into carbon and water would result in the release of 48 water molecules, equivalent to a mass loss of 67 %. The DSC of γ-CD (Figure 6.15) shows an endothermic

event at the same temperature as this large mass loss in the TGA, further supporting this interpretation.

Crucially, the melt of the inclusion complex, characterised by a sharper endothermic event than the loss of water, can be seen to be at a temperature of 239.04 °C, 73.62 °C higher than the melt of pure thiamphenicol. This suggests that through complexation with γ-CD, the thermal stability of thiamphenicol has been substantially increased. This has importance when considering the high temperatures that could be encountered during processing of drug products. After the melt of the complex, there is a sharp exothermic event and upon removal of the pan from the DSC, the pan had 'jumped' off its stand. It is documented that at high temperatures glucose, which is the primary building block of γ-CD, undergoes caramelisation before decomposing into carbon and water which could provide an explanation for this exothermic event.[244]

6.3.1.4 Transfer to cooling crystallisation

Utilising the knowledge that the host-guest complex formed has a 2:1 γ-CD: thiamphenicol binding ratio, as obtained from the Job plot (Figure 6.11), it was possible to design initial cooling crystallisations at the 1.5 ml scale. As there was no prior knowledge of the solubility of system, varying concentrations of thiamphenicol (the API) ranging between 3 mg/ml and 17 mg/ml and the corresponding molar ratios of γ-cyclodextrin (24 mg/ml – 120 mg/ml) were weighed into 1.5 ml vials and 1.5 ml of water added. Water was chosen as a solvent to ensure no preferential inclusion of solvent over thiamphenicol inside the cyclodextrin cavity. The concentrations of thiamphenicol were chosen based on those utilised in the previous evaporative crystallisation experiments that were dissolved in a similar volume of solvent.

Vials were subjected to cooling from 50 °C to 5 °C at a rate of 0.1 °C min^{-1} with a magnetic bottom stirring speed of 300 rpm. Only those vials containing higher concentrations of the two components resulted in crystallisation, however not enough solid was produced to allow PXRD analysis of the solid form produced or accurate determination of crystallisation yields. This prompted experiments with higher concentrations of thiamphenicol (27 mg/ml – 40 mg/ml) and γ-CD (170 mg/ml – 270 mg/ml), still in a 1:2 (THM: γ-CD) ratio. All concentrations explored resulted in crystallisation of the molecular inclusion complex, as confirmed through PXRD and through comparison of PXRD patterns obtained from the samples generated from cooling with those from ground-up single crystals obtained from evaporative crystallisations (Figure 6.17). Some of the peaks in the PXRD display differing intensities (most obviously the peak at 35 ° 2θ), which can be attributed to preferred orientation effects; grinding of single crystals from evaporative crystallisations compared

to a fine powder as the product of a cooling crystallisation could result in preferential alignment of some lattice planes over others, giving rise to these effects.

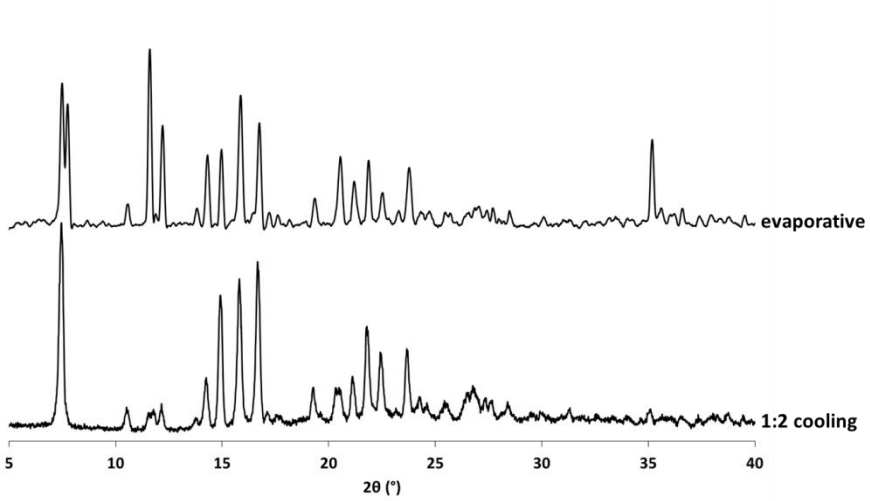

Figure 6.17: PXRD analysis confirming the formation of the molecular inclusion complex of γ-CD and thiamphenicol

As a proof of concept 2:1, 1:1 and 1:3 (THM: γ-CD) molar ratios of thiamphenicol: γ-CD were also investigated in the cooling crystallisation environment. Both the 2:1 and 1:1 molar ratios resulted in the crystallisation of thiamphenicol on its own, with the more soluble γ-CD remaining in solution. The 1:3 molar ratio resulted in the crystallisation of the molecular inclusion complex of thiamphenicol and γ-CD, however excess γ-CD was detectable by PXRD, through a small but characteristic peak at 5° 2θ (Figure 6.18).

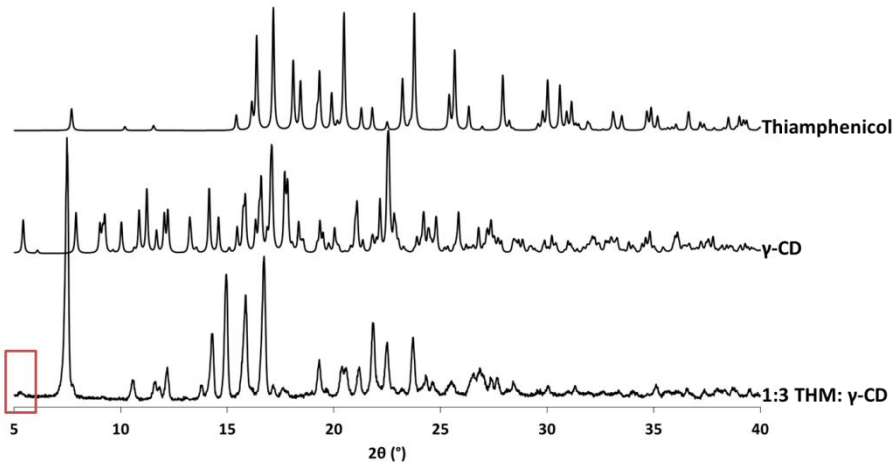

Figure 6.18: PXRD pattern of the crystallisation product using a 1:3 THM: γ-CD ratio, showing excess γ-CD boxed in red

Attempts were made to scale the system beyond the 1.5 ml scale, first utilising a working volume of 5 ml. The higher concentrations explored in the 1.5 ml scale experiments (THM between 27 mg/ml and 40 mg/ml and γ-CD between 170 mg/ml and 270 mg/ml) were used at the 5 ml scale.

Again vials were subjected to a 50-5 °C cooling regime at 0.1 °C min^{-1} with 300 rpm magnetic bottom stirring. Solids produced in the experiment were harvested through vacuum filtration and dry solid analysed by PXRD. It was observed that the solid was viscous and had 'sticky' properties. This property decreased with increasing concentration of the two components.

The PXRD patterns from the harvested solid (Figure 6.19) show a good match with the PXRD pattern obtained from single crystals of the complex. However, the peaks, particularly those at higher 2θ values, show some broadening in comparison to the evaporative pattern. This suggests some amorphous character in the solid, further supported by the observation of 'sticky' solid. It can be suggested that the grinding action of the magnetic stirrer could be contributing to this. As such, experiments utilising overhead stirring would be beneficial to see if the overall crystallinity of the product can be improved; however due to time restraints, this work was unable to be completed during this project.

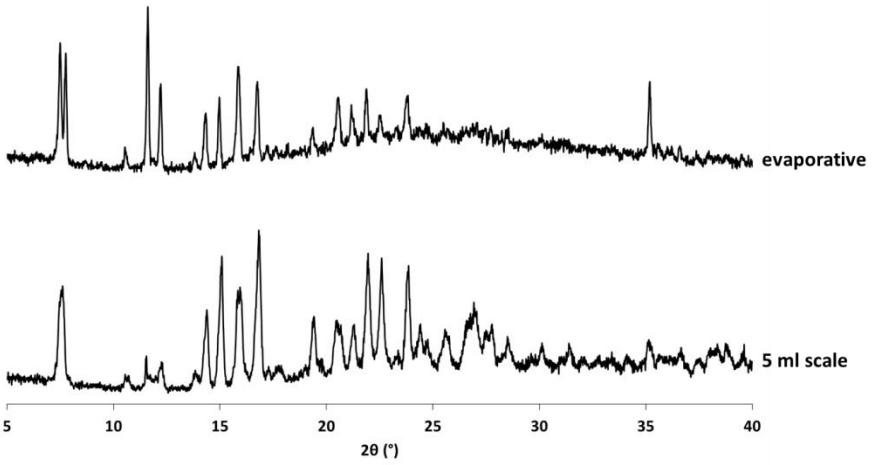

Figure 6.19: PXRD pattern showing the production of the molecular inclusion complex at the 5 ml scale

Further, only one cooling rate was explored in this work (0.1 °C min^{-1}), which would not be conducive to transfer into continuous crystallisation environments. As such, future work should look into investigating faster cooling rates that would be more amenable to transfer to continuous crystallisation platforms. However, it is important to note that initial transfer to a cooling crystallisation environment, as achieved successfully in the present work, is a crucial first step towards the continuous crystallisation of these hosting systems.

6.3.2 The molecular complex of α-lipoic acid and β-cyclodextrin

The molecular inclusion complex of α-lipoic acid (ALA) and β-cyclodextrin (β-CD) (CSD ref: HAXJIB, Figure 6.20), has been shown to improve the thermal stability of ALA, and its structure has been determined from PXRD data. This shows binding in a 1:1 molar ratio. [235]

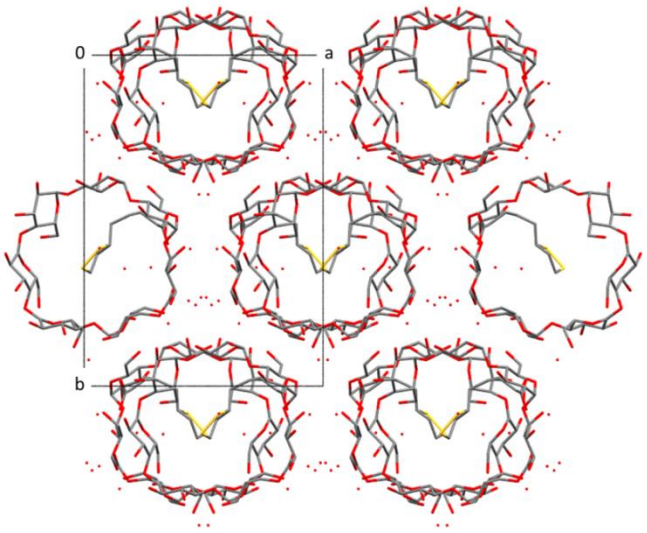

Figure 6.20: The crystal structure of the inclusion complex of ALA and β-CD, as viewed down the crystallographic *c* axis

6.3.2.1 NMR analysis

In order to confirm complexation in a 1:1 ratio, Job's method of continuous variation was used. Plotting of the data displayed in Table 6.3 and Table 6.4 resulted in the Job plot shown in Figure 6.21. The peak at a mole fraction of β-CD of 0.5 indicates binding in a 1:1 ratio.

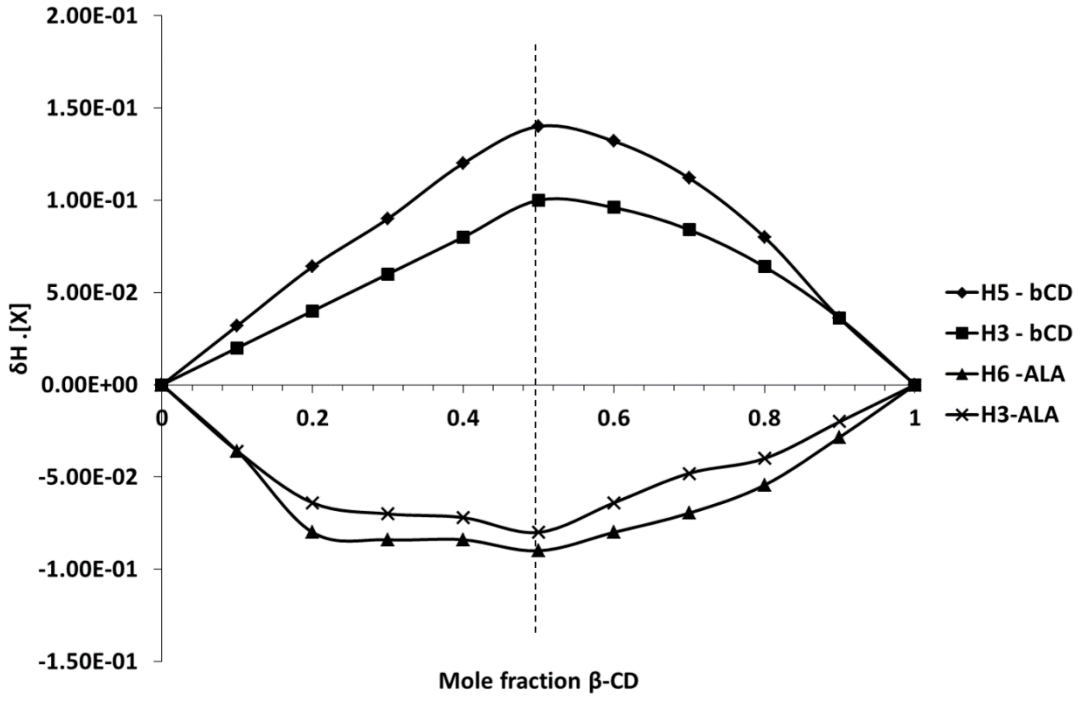

Figure 6.21: Job plots for the inclusion complex of ALA and β-CD

6.3.2.2 Transfer to cooling crystallisation

The ALA-β-CD complex reported in the literature was formed from a 60:40 MeOH: H_2O mixture. This acted as an initial starting point for the transfer of synthesis of the inclusion complex to a cooling crystallisation environment. Crude solubility measurements were performed in this solvent system, which showed 30 mg of ALA to dissolve in 1 ml of solvent. As such, varying concentrations of ALA (5, 10, 15 and 20 mg/ml) with the corresponding 1:1 molar ratio of β-CD (27.5, 55, 82.5 and 110 mg/ml) were weighed into 1.5 ml vials and 1.5 ml of 60:40 MeOH: H_2O added. To allow complete dissolution of the higher concentrations, vials had to be heated to 70 °C. Vials were then cooled from 70 °C to 5 °C at 0.1 °C min^{-1}, with a magnetic bottom stirring speed of 400 rpm. Solid was harvested *via* vacuum filtration and analysed with PXRD.

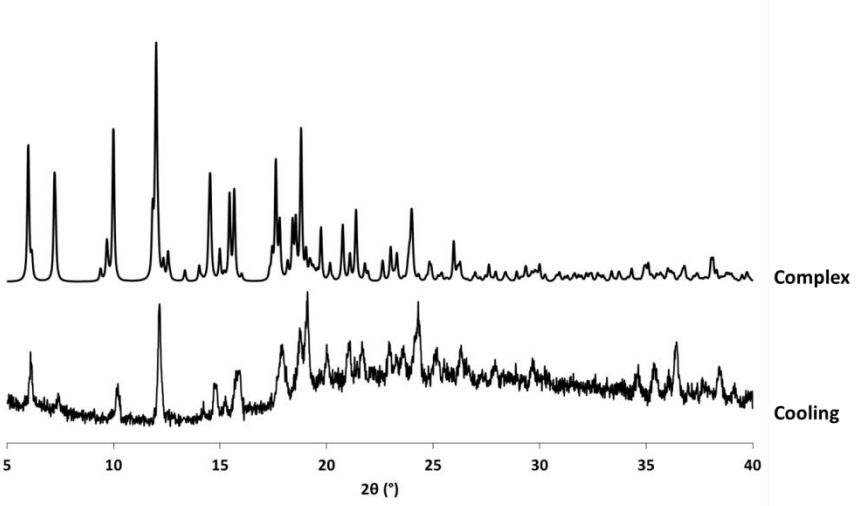

Figure 6.22: PXRD analysis from initial cooling crystallisation experiments showing comparison to the PXRD pattern predicted from single crystal data for the inclusion complex; although peaks from the complex are present the pattern displays amorphous characteristics

PXRD patterns (Figure 6.22) show peaks characteristic of the complex as predicted from single crystal data. However, the high, curved background suggests amorphous characteristics. It is possible that the need to heat the solutions to 70 °C, for dissolution of higher concentrations, caused the ALA to melt (T_m = 60 °C), could be responsible for some of the amorphous characteristics seen here. As such, for future experiments, concentrations were reduced to allow dissolution at a temperature of 55 °C. All crystallisations presented hereafter were subjected to a 55 °C to 5 °C cool, with further experimental details given in Table 6.5.

Table 6.5: Experimental information for cooling crystallisations of ALA and β-CD (throughout all experiments a concentration of ALA of 6.7 mg/ml and β-CD 36.7 mg/ml and a stirring rate of 400 rpm was used)

Experiment set	Aim	Stirring type	Volume (ml)	Cooling rate (°Cmin^{-1})
1	Varying concentrations of water and methanol	Magnetic bottom	6	0.5
2	Higher volumes of water and scale increase	Magnetic bottom	12	0.5
3	Replace MeOH with EtOH and IPA	Magnetic bottom	6	0.5
4	Change of cooling rate	Magnetic bottom	6	0.05
5	Change of cooling rate	Magnetic bottom	6	0.1
6	Increase scale	Magnetic bottom	12	0.1

Experiment Set 1

Experiment Set 1 investigated varying ratios of methanol and water on the crystallisation outcome. The percentage of methanol in a water/methanol mix was varied between 0 % (100 % water) to 100 %. Crystallisation was observed in all eight vials, with solids analysed through PXRD.

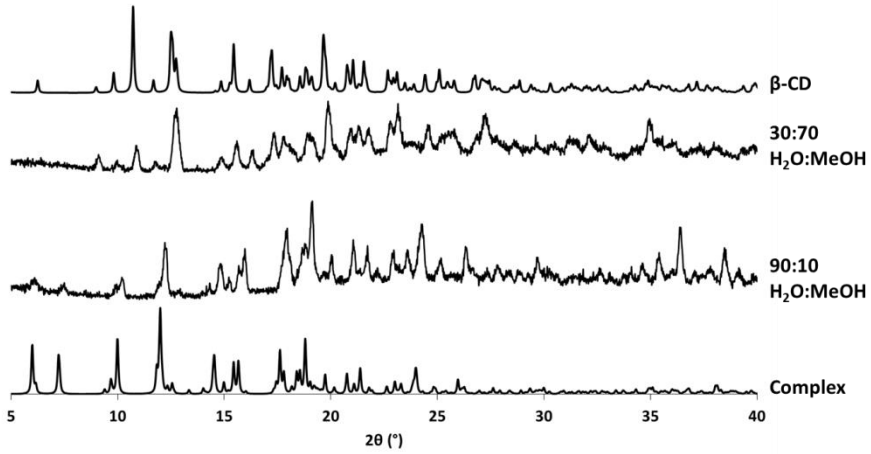

Figure 6.23: PXRD analysis showing the presence of complex in those vials containing higher percentages of water and β-CD in those vials containing higher percentages of MeOH

PXRD analysis (Figure 6.23) shows that those vials containing higher percentages of water resulted in the crystallisation of complex. However, upon increasing the concentration of methanol, the selective crystallisation of β-CD is observed. This can be explained by considering the high water solubility of β-CD; upon increasing the proportion of methanol (in which β-CD is insoluble), the β-CD becomes less soluble and starts to crystallise alongside the inclusion complex. The PXRD patterns produced still contain some broad peaks, but are more crystalline than those in previous

experiments (shown by lack of the amorphous hump that was prominent in the samples cooled from 70 °C (Figure 6.22)).

Experiment Set 2

Experiment Set 2 utilised the observations from Experiment Set 1 and only considered those crystallisations containing higher percentages of water. Two vials of each of the 100:0, 90:10 and 80:20 (H_2O: MeOH) solvent ratios were cooled from 55 °C to 5 °C. The scaling potential of the system was investigated by increasing the working volume to 12 ml. Crystallisation was observed in all vials with the solid harvested and analysed by PXRD. The PXRD patterns for the solid products of the 100:0 and 90:10 (H_2O: MeOH) were noisy and showed poor crystallinity. However, those produced from the 80:20 (H_2O: MeOH) show a higher degree of crystallinity, with peak positions matching those of the calculated pattern for the molecular inclusion complex, while still showing evidence of amorphous component (Figure 6.24).

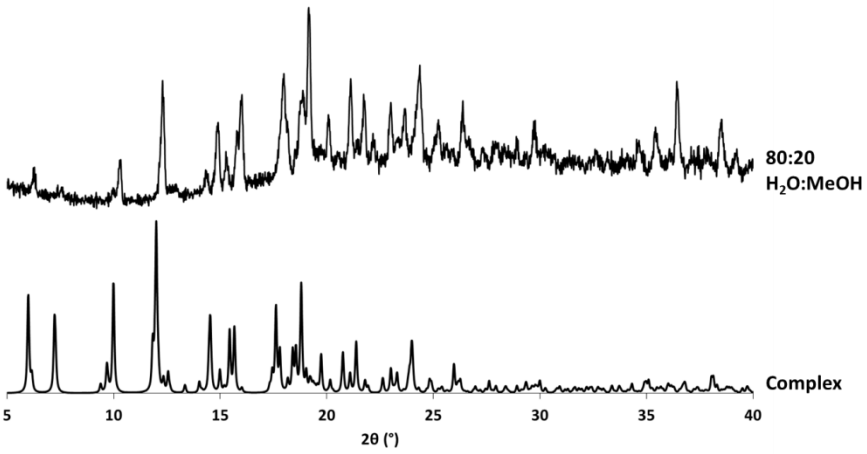

Figure 6.24: PXRD pattern confirming production of the molecular inclusion complex of ALA and β-CD at the 12 ml scale

Experiment Set 3

Experiment Set 3 investigated a change in the alcohol solvent present in the solvent mixture. Methanol is an ICH Class 2 solvent and would not be recommended for industrial large scale applications owing to its toxicity. As such ICH Class 3 alcohol solvents, namely ethanol (EtOH) and isopropanol (IPA), were investigated. Based on observations from Experiment Set 1 and Experiment Set 2, which showed that higher water: alcohol ratios resulted in the formation of the molecular inclusion complex, only 80:20, 90:10 and 100:0 (water: alcohol) ratios were investigated. The cooling profile (55 °C to 5 °C at 0.5 °C min^{-1}) remained the same as Experiment Set 2 to allow direct comparison between the results. Crystallisation of the target ALA-β-CD complex was observed in

all solvent compositions, however those containing an 80:20 water: alcohol ratio produced more crystalline PXRD patterns (Figure 6.25).

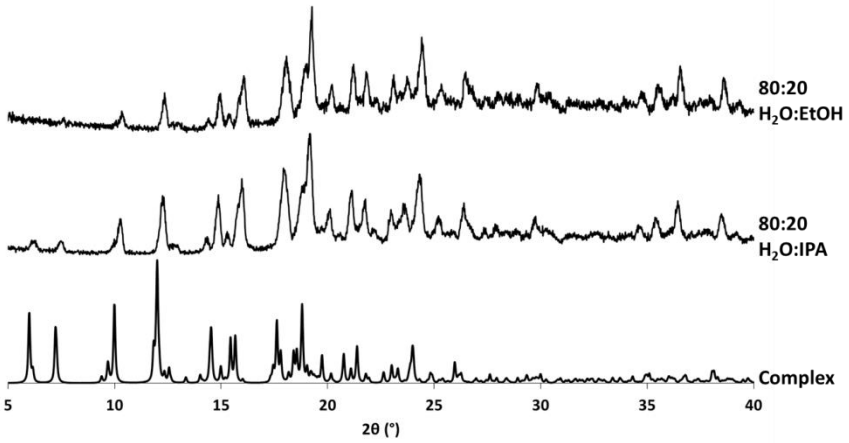

Figure 6.25: PXRD patterns for Experiment Set 3, showing the production of the molecular inclusion complex

Experiment Set 4

Although crystallinity is improved through incorporation of small amounts of alcohol in the solvent mix, some peaks are still broad. As such, Experiment Set 4 investigated the effect of a slower cooling rate on the crystallisation outcome. By employing a slower cooling rate (0.05 °C min^{-1}), the crystallisation could be under thermodynamic rather than kinetic control, giving greater control over the particle attributes; this is the same reason that slow evaporation is usually the method of choice to obtain large single crystals suitable for X-ray diffraction. All other experimental parameters remained the same as Experiment Set 3, only investigating those solvent compositions containing higher proportions of water. Harvested solid analysed *via* PXRD confirms the presence of the molecular inclusion complex, again with the samples from the 80:20 water: alcohol mixtures producing samples with the highest crystallinity (Figure 6.26).

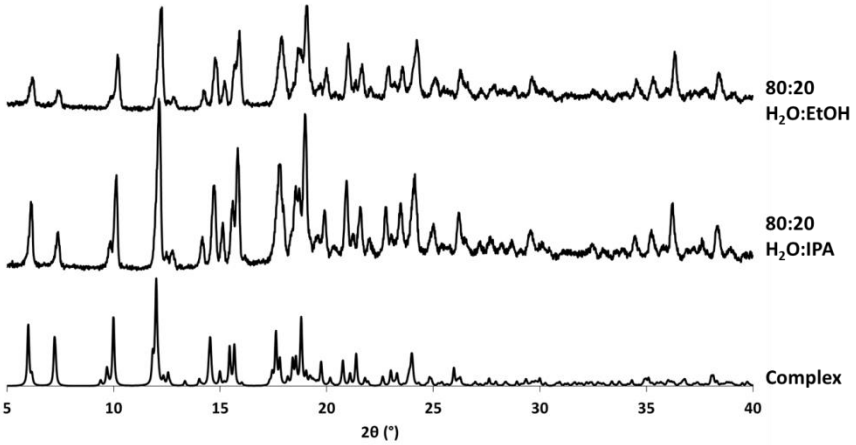

Figure 6.26: PXRD patterns for Experiment Set 4, showing the formation of the molecular inclusion complex

Interestingly, the samples produced using small quantities of EtOH and IPA display higher crystallinity than those produced in other experimental sets using methanol. It can be suggested that the complex displays a slightly lower solubility in these two solvent mixes; the lower solubility would ensure crystallisation in a more controlled manner rather than having to induce crystallisation quickly through cooling to low temperatures. The latter would give less control over the crystallisation, resulting in a less crystalline product.

Experiment Set 5 and 6

Although samples produced in Experiment Set 4 showed a good degree of crystallinity, a cooling rate of 0.05 °C min^{-1} would not be amenable to transfer to a continuous crystallisation environment, which would be the eventual aim of the work presented here. As such, a faster cooling rate was investigated. A cooling rate of 0.5 °C min^{-1} investigated in Experiment Sets 1-3 still resulted in formation of the target complex, but with PXRD showing some amorphous characteristics; as such, a cooling rate of 0.1 °C min^{-1} was investigated. Although not conducive to continuous crystallisation platforms, this cooling rate would result in a batch crystallisation of *ca* 8 hours. Although shorter experiment times are desirable in terms of maximising throughput in limited and expensive plant times, if a large scale batch crystallisation route to this hosting complex could be established, this could serve as a method for seed generation for more efficient continuous crystallisation processes.

Again, only 80:20 and 90:10 (water: alcohol) solvent mixtures were investigated. Each vial was subjected to a 55 °C to 5 °C cool at a rate of 0.1 °C min^{-1}. Experiments were performed at the 6 ml and 12 ml volume scale. Solid from each vial was harvested and analysed through PXRD (Figure 6.27).

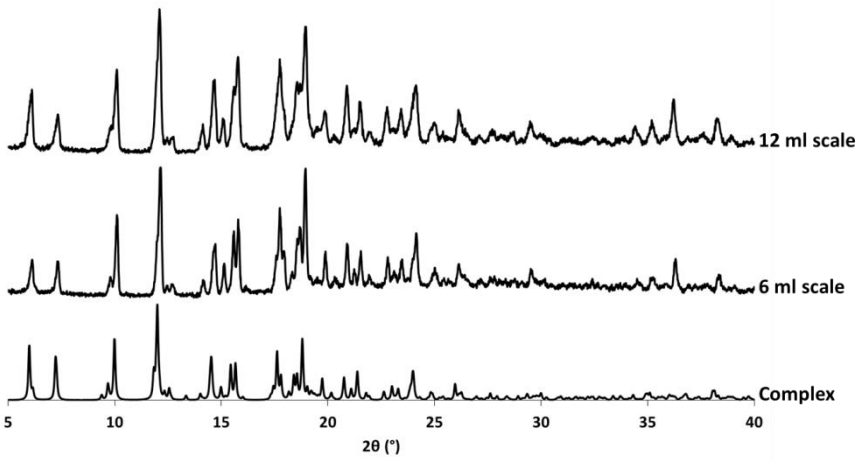

Figure 6.27: PXRD patterns showing the production of the inclusion complex at both the 6 ml and 12 ml scale

At both scales, all solvent compositions resulted in the formation of the molecular inclusion complex of ALA and β-CD, as confirmed through comparison with the calculated pattern from single crystal data. The samples produced display a good degree of crystallinity, showing sharp, well defined peaks. Scaling beyond the 12 ml scale would be desirable, in particular investigations with overhead stirring, and could be the subject of any future work on the system.

6.4 Conclusions

Two systems, in which a reactive pharmaceutical compound has been hosted within a benign molecule with a view of increasing the stability of the pharmaceutical, have been studied in the work presented in this chapter. In work presented in the literature, α-lipoic acid (ALA), which displays poor thermal stability with respect to cleavage of the S-S bond, has been shown to be hosted within β-cyclodextrin. The resulting molecular complex was shown to increase the thermal stability of the ALA.

Utilising the premise of hosting within benign cyclodextrin molecules, the second targeted molecule of the work presented in this Chapter was the antibiotic thiamphenicol, which displays poor hydrolytic stability. Initial evaporative crystallisations with thiamphenicol and the three native cyclodextrins (α-CD, β-CD and γ-CD) resulted in the formation of the molecular inclusion complex of thiamphenicol and γ-cyclodextrin (γ-CD). Initial evidence for inclusion of thiamphenicol inside the γ-CD molecule was provided by a change in the crystal structure; in its native state, γ-CD forms staggered chains, whereas once a molecule is included within its pore this changes to a channel structure. However, the thiamphenicol molecule was unable to be resolved from crystallographic data. As such, other methods for confirming inclusion were required and full NMR analysis on the system was conducted. Initial NMR analysis on single crystals screened to have the same unit cell parameters as the molecular inclusion complex showed both γ-CD and thiamphenicol to be present in the sample, providing further evidence of inclusion of the thiamphenicol into the cavity of the γ-CD molecule. The method of continuous variation, whereby shifts in peaks in an NMR spectrum upon changing the ratio of the two components whilst keeping the total concentration of the solution constant, was used in order to determine the binding ratio of the complex through formation of Job plots. The protons tracked during these titration experiments were those that would be involved in the interaction between the thiamphenicol molecule and the inner cavity of γ-CD. The mole fraction at which the peak in the Job plot is seen indicated the stoichiometry in which the two components bind; here it was determined that the two molecules bind in a 2:1 (γ-CD : thiamphenicol) ratio.

Following full NMR analysis on the molecular inclusion complex, the effect of stressed conditions on the hydrolytic stability of the thiamphenicol was investigated. Samples were placed in a humid environment for a period of a month, analysed before and after with SSNMR. The stressed conditions resulted in the samples turning amorphous, characterised by broad peaks in the SSNMR, with the thiamphenicol sample melting under these conditions. However, all key peaks were still present after being subjected to humid conditions, indicating both compounds remain within the molecular complex. However, the small shifts that would be expected upon hydrolysis of the amide carbonyl in thiamphenicol to a carboxylic acid were unable to be tracked due to the broad peaks. As such, another method is sought in order to generate conditions for the examination of potential hydrolysis in the solid state; solution state methods are deemed inappropriate as the two components do not remain associated in solution (as confirmed through DOSY NMR) which would leave the thiamphenicol molecule exposed to hydrolysis.

However, the observation that the samples turned amorphous under stressed conditions prompted analysis of the thermal stability of the inclusion complex. DSC analysis confirms an increase in the melting point of the complex in comparison to the thiamphenicol starting material (239 °C *vs* 165 °C), indicating the thermal stability of thiamphenicol has been increased. The ability to increase the thermal stability of APIs through incorporation inside benign host molecules is of great interest if the pharmaceutical displays a low thermal stability; many downstream processes can require high temperatures that would be detrimental to the solid form of these APIs.

Due to the evident improvement in physical properties achieved through complexation, the transfer to a cooling crystallisation environment for both the molecular inclusion complex of ALA: β-CD and thiamphenicol: γ-CD was targeted. Binding ratios from each of the Job plots were used to aid initial cooling crystallisation design. Both systems produced the desired formation of the inclusion complexes, but with samples that displayed poor crystallinity initially. However optimisation of crystallisation conditions such as cooling rate and solvent composition allowed the crystallinity to be improved. The cooling crystallisation of the molecular inclusion complex of ALA and β-CD was further optimised in two different solvent systems, using three cooling rates and scaled to volumes of 12 ml. The transfer of the synthesis of these hosting complexes, which increase the thermal stability of the API, to cooling crystallisation is a key first step in the transfer to continuous crystallisation platforms.

7 Conclusions and Future Work

7.1 Conclusions

The work presented in this thesis has looked at obtaining solid form control of active pharmaceutical ingredients (APIs) through multi-component techniques; here solid form encompasses different polymorphic forms of the same chemical entity as well as the chemical and physical stability of single molecular components. This work was performed with a view of transferring systems displaying solid form control into a continuous crystallisation environment.

The ability to control the polymorphic form of APIs is of great interest to both academia and industry with different polymorphic forms often displaying markedly different properties. Literature reports on large scale manufacture of metastable polymorphic forms are limited, with no reports on the continuous crystallisation of metastable APIs. In the work presented in this thesis a second molecular component is added to the crystallisation process to direct the formation of a metastable polymorphic form; this second molecular component is termed a template molecule.

Work on controlling polymorphism through this templated approach has focussed on the API paracetamol (PCM). Two of PCM's five polymorphic forms have been of interest in this work; the thermodynamically stable PCM-I and the metastable PCM-II. PCM-II displays a layered arrangement of molecules in the crystal structure, giving this form enhanced compressibility; PCM-II also displays an enhanced solubility in comparison to the stable PCM-I. As such it represents a desirable target for large scale production.

Initial studies built on previous literature work that highlighted the possibility to template PCM-II with a variety of *p*-substituted benzoic acid derivatives in an evaporative crystallisation environment. The transfer to a cooling crystallisation environment, which is the principle on which many of the currently marketed continuous crystallisers operate, was targeted. Use of 4-fluorobenzoic acid (4-FBA) as a template molecule in a 60:40 H_2O:IPA solvent system allowed for the reproducible production of PCM-II on the 1 ml solvent scale. However, attempted scale up of this templated crystallisation was largely unsuccessful; it is postulated that this is due to the low solubility of the templating molecule combined with the poorer mass transfer that is experienced upon scaling to larger volumes and vessel sizes. Seeding experiments at the 50 ml scale in both the absence and presence of 4-FBA as a template molecule were also performed to investigate the scaling potential of this system, however all these crystallisations resulted in the production of PCM-I.

The lack of success, in terms of scaling potential, with the substituted benzoic acids as additives prompted work with template molecules which display a structural similarity to PCM, which had only previously been studied in relation to their effect on the morphology of PCM-I. Small scale studies with magnetic bottom stirring were conducted with six structurally similar, size-matched template molecules: metacetamol (MCM), orthocetamol (OCM), 3'-amino-4-methoxyacetanilide (3A4MA), p-acetanisidide (PACN), 4-acetamidobenzoic acid (4ABA) and methyl paraben (MP). The use of 2.4 % OCM combined with a cooling rate of 0.02 °C min^{-1} resulted in the reproducible production of PCM-II at the 1 ml scale. However, attempts at scaling beyond this volume were unsuccessful, owing to the low solubility of the template molecule and poor mass transfer, as was observed with the substituted benzoic acids. Higher percentages of 3A4MA (35 %) were required in order to direct the formation of PCM-II; however, use of this template molecule allowed for production at the 10 ml scale with a cooling rate of 1 °C min^{-1}, a cooling rate which is more conducive to transfer to a continuous crystallisation environment. However all attempts at scaling beyond this volume have been unsuccessful and the presence of excess template molecule is detectable in the solid product through PXRD.

Use of MCM as a template molecule has provided the most success, with the reproducible production of PCM-II observed initially up to the 20 ml solvent scale in two different solvent systems (60:40 H_2O: IPA and ethanol) at three different cooling rates (0.02, 0.2 and 1 °C min^{-1}). Percentages of MCM as high as 25 % were required in order to direct the formation of PCM-II, resulting in the crystallisation of metacetamol hydrate impurity alongside PCM-II in the final solid product when the crystallisations were cooled to a temperature of 5 °C. However, truncation of the cooling profile at a temperature of 20 °C resulted in elimination of this hydrated form from the final solid product. PCM-II samples produced from these small-scale additive experiments with both the substituted benzoic acids and the structurally similar template molecules are stable for a period of 24 months at the time of writing, indicating the high polymorphic purity of these samples. Investigations carried out in this thesis whereby samples of PCM-II were doped with varying quantities of PCM-I showed that the presence of 1 % or more of PCM-I within a PCM-II sample initiates the conversion to PCM-I within one month.

Further investigations into the scaling potential of the PCM/MCM system were conducted at the 100 ml scale utilising overhead stirring. A full factorial Design of Experiments (DoE) analysis with five factors was conducted at this scale in order to determine the conditions under which PCM-II could be produced in highest yield and both polymorphically and chemically pure (i.e. in the absence of any PCM-I or MCM.H_2O). This DoE analysis highlighted the importance of stirring rate

and the temperature at which the cooling profile was truncated, for the production of PCM-II samples with a high degree of purity; a faster stirring rate and higher truncation temperature were required. Optimal concentrations of PCM and MCM were also highlighted to result in highest yields; as such for all future experiments a concentration of PCM of 300 mg/g coupled with a wt. % MCM of 25 % were used. Further batch scaling of the templated crystallisation of PCM-II with MCM as a template molecule was conducted at the 800 ml volume at the CMAC National Facility, housed within the Technology and Innovation Centre at the University of Strathclyde. The crystallisation was monitored with inline PAT: a Raman PhAT probe to monitor the polymorphic form produced and an FBRM probe to track nucleation events. This crystallisation allowed for the production of 120 g of PCM-II in a single process run, one of the only reported examples of the scaled production of a metastable polymorphic form of an API. However, solid samples did contain small quantities of the metacetamol hydrate impurity that proved challenging to eliminate from large scale batch crystallisation experiments, likely due to inefficient mixing upon scale-up.

The transfer of the templated crystallisation of PCM-II with MCM as a template molecule to three continuous crystallisation platforms was investigated. In order to mimic the stepped cooling profile utilised in a batch crystallisation platform, a two-stage MSMPR set-up at AstraZeneca in Macclesfield, operated in periodic mode, was employed. Initial crystallisations resulted in the crystallisation of PCM-II, however some PCM-I was present in the solid product. SEM images of the dry solid product show two distinct crystal morphologies: hexagonal blocks attributed to PCM-II with small needle crystals postulated to be due to the presence of PCM-I. However, this PCM-I was eliminated from future experiments through alteration of the temperature profile, allowing more controlled crystallisation at a lower supersaturation ratio. This crystallisation platform eliminates the metacetamol hydrate impurity from the final PCM-II solid product, producing samples of high polymorphic purity that show the expected good stability with respect to the PCM-II to PCM-I solid state transformation.

The continuous templated crystallisation of PCM-II was investigated in two tubular continuous flow platforms. A re-configurable continuous oscillatory baffled crystalliser (COBC), ranging from four to twelve straights, allowed for reproducible production of PCM-II; however elimination of the metacetamol hydrate impurity seen in batch crystallisations proved problematic. Varying temperature regimes and a reduction in the percentage of MCM were investigated in order to eliminate this hydrate impurity from the solid product. It was found that the system had to be set up to allow crystallisation at a sufficiently high temperature to ensure elimination of this hydrate phase, however the limited residence times experienced in the crystalliser meant lower

temperatures had to be used in order to induce any crystallisation in the system; the presence of MCM in the system has the effect of widening the MSZ, delaying the onset of nucleation. These relatively short residence times within the crystalliser resulted in incomplete desupersaturation of the system, causing detrimental filtration issues in many crystallisations. However, the superior mixing conditions seen in the COBC, owing to its baffled geometry with small volumes of fluid contained within each baffle, meant that the additive concentration of MCM could be considerably reduced from that used in batch crystallisation experiments (from 25 % to 18 %). With a need for high product purity, this reduction in template molecule concentration is highly desirable.

The second tubular continuous flow crystallisation platform employed to investigate the continuous crystallisation of PCM-II was the kinetically regulated automated input crystalliser (KRAIC), an open tubular crystalliser that operates on the principle of segmented flow. A cold tube needed to be incorporated into the set-up to induce nucleation in the crystalliser, to account for the main coils not being able to be cooled below ambient temperature. Initial adjustment of the cooling profile was needed after nucleation before the mixer piece resulted in the crystallisation of PCM-I. Upon this adjustment and confining the controlled nucleation to the cold tube, PCM-II was produced. However, in all experiments performed in this platform solid yields were poor and so further optimisation of the cooling crystallisation is needed to improve these yields. As with the COBC, the poor yields can be attributed to the relatively short residence times within the system; as the residence time within the crystalliser is determined by a fixed length of tubing and limited by experimentally achievable flow rates, it cannot be increased and modification to the current set-up would be required.

Although the crystallisation of PCM-II has been successfully observed, for the first time, in three separate continuous crystallisation platforms, only one of these platforms (the PMSMPR) yields samples of PCM-II that display both high chemical purity, indicated by the absence of any metacetamol hydrate impurity, and high polymorphic purity, indicated by both the absence of any detectable PCM-I and by good stability with respect to the PCM-II to PCM-I solid state transformation. Operation of the MSMPR in periodic mode is more suitable for systems, such as the one investigated here, that display slow nucleation kinetics, as opposed to flow crystallisers where the residence time is dictated by experimental limits on flow rates and crystalliser length.

Investigations were also conducted into the possible mechanism of action of the template molecule in the production of PCM-II. Slurrying experiments, whereby PCM-II was slurried in the chosen solvent system with varying percentages of MCM, showed inhibition of the solution mediated phase transformation from PCM-II to PCM-I at higher percentages of MCM, indicating solution

stabilisation of PCM-II in the presence of MCM. Analysis of the crystal structure of PCM-II and corresponding molecular structure of each of the template molecules allowed rationalisation as to why some template molecules were successful in the production of PCM-II, whilst others resulted in the crystallisation of PCM-I.

The second approach to multi-component solid form control explored in this thesis was hosting of APIs which display poor stability, within benign host molecules. The antibiotic thiamphenicol, which displays poor hydrolytic stability, and α-lipoic acid (ALA), which displays poor thermal stability, were the API targets of this work. Previous literature work had shown that through incorporation inside β-cyclodextrin (β-CD), the thermal stability of ALA was increased. Utilising the premise of hosting within cyclodextrins, small scale evaporative crystallisations of thiamphenicol with the three native CDs yielded a new molecular inclusion complex of thiamphenicol and γ-cyclodextrin (γ-CD) which showed an increased thermal stability of the thiamphenicol molecule. Full NMR analysis was conducted on this new molecular inclusion complex to confirm inclusion of the thiamphenicol molecule, including the generation of a Job plot to show that the two components bind in a 2:1 (γ-CD: thiamphenicol) ratio. Job plot analysis was also performed on the literature ALA: β-CD complex, confirming binding in a 1:1 ratio. The knowledge of these binding ratios was used to design successful cooling crystallisation routes to the molecular inclusion complexes, the first key step towards transfer to continuous crystallisation platforms.

7.2 Future work

7.2.1 Templating for polymorph control

Much of the future work on the templated crystallisation of PCM-II would be directed towards the optimisation of the continuous crystallisation processes described in Chapter 5. It is clear that with the two tubular continuous flow crystallisers described (the COBC and the KRAIC) the limited residence time, due to fixed experimental parameters such as crystalliser length and flow rates, combined with a widening of the MSZ in the presence of MCM, were responsible for the small crystallisation yields observed in these systems. As such, further work would look to increase the residence time within these systems. For the COBC, it is highly likely that the addition of further straights would allow for the crystallisation of PCM-II in the absence of any metacetamol hydrate impurity. Therefore, a COBC set-up of increased length with the oscillation provided by either a full bellows set-up or a piston, to improve suspension of particles in later straights, would be targeted initially. Furthermore, sampling of the solution and operation in recycle mode would reduce the filtration problems experienced in many crystallisations as well as increasing operation times; the

latter would be of particular interest to observe whether the polymorphic form outcome could be retained over time. The KRAIC platform, which operates on much lower volumes than the COBC, highlights an interesting possibility for those systems outlined in Chapter 3, where the formation of PCM-II was only seen at much smaller volumes. As such, future work with the KRAIC set-up would look towards developing the continuous crystallisation of these systems.

It would also be of interest to implement seeding approaches into the crystallisation of metastable PCM-II. The use of seeding may allow for a reduction in the concentration of MCM required to template PCM-II, a highly desirable objective with a need for product purity. However, considerations need to be taken into account regarding the suitability of conventional slurry seeding approaches as this would result in the solution mediated phase transformation from PCM-II to PCM-I. As such, investigations into dry seeding approaches in continuous crystallisation would need to be conducted.

7.2.1.1 Assessing the transferability to the CMAC workflow

A lot of work within the CMAC Hub consortium has been directed towards generating a workflow to aid in the development of a continuous crystallisation of a target compound. At the time of writing, the workflow consists of seven steps, outlined in the flow chart shown in Figure 7.1. The workflow has been applied to the development of a process for the continuous crystallisation of PCM-I, but is yet to be developed for a metastable polymorphic form. Owing to its enhanced physical properties, the development of this workflow for the metastable PCM-II would be of great interest. Some of the stages outlined have been wholly or partly covered by the work in this thesis (in particular Stage 1, Stage 5 and Stage 7). Future work should look towards developing the other stages in more detail. From the outset, owing to solubility data available at the time, a limited solvent selection was used in this work. It would be of interest to explore a variety of other solvents as this may also aid with the elimination of the hydrate impurity. The solvents could initially be screened for suitability based on solubility; if PCM is too soluble in a solvent the solution mediated phase transformation would be too rapid and stabilisation of the PCM-II would be difficult. These solubilities would have to be calculated by the use of ratios based on the solubility of PCM-I (see Chapter 3); this work is currently ongoing. This work on solubility and solvent choice encompasses

Stages 2-4 of the workflow. The PAT calibration subsection of Stage 4 has been conducted as part of the work presented in this thesis (Chapter 4).

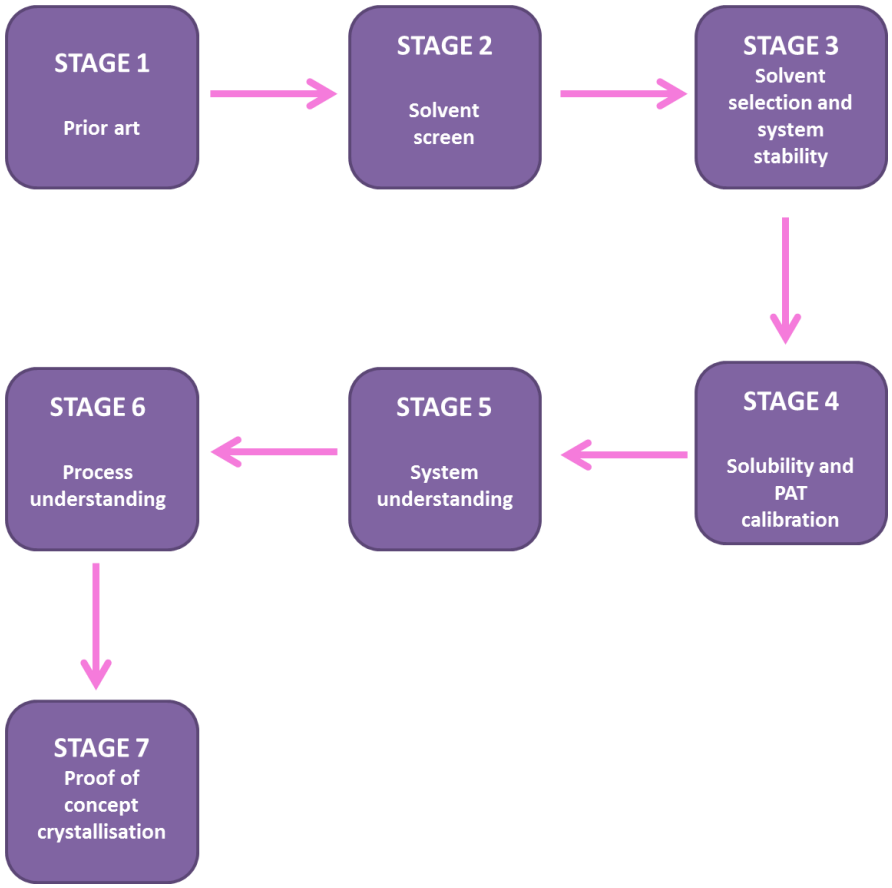

Figure 7.1: The CMAC Hub developed workflow for a continuous cooling crystallisation process

Much of the work presented in this thesis has given a strong system understanding (Stage 5), however further work in the understanding of agglomeration and fouling as well as measurement of both primary and secondary nucleation rates would be needed to complete this stage of the workflow. No work has currently been performed using model predictive control approaches, however their implementation into the crystallisation process could prove vital in obtaining optimal crystallisation conditions and would be very desirable for future work on the system. Proof of concept crystallisations, in the 60:40 H_2O: IPA solvent system explored in this work, have been performed in three different continuous platforms, indicating a PMSMPR to be most amenable to the production of polymorphically and chemically pure PCM-II. However, the large scale continuous crystallisation of this templated crystallisation has yet to be investigated and would be the subject of future work.

7.2.2 Hosting

The subject of future work for the hosting compounds presented in Chapter 6 would be the determination of hydrolytic stability of the molecular inclusion complex of thiamphenicol and γ-CD. All methods currently investigated have proved unsuccessful in confirming whether, through incorporation inside a γ-CD host, the hydrolytic stability of thiamphenicol has been increased. A method of generating a humidity environment without subjecting the samples to high temperatures would reduce the tendency for the samples to become amorphous over time, as observed in this work; an example would be use of a K_2SO_4 tub at room temperature.

The continuous crystallisation of the molecular of inclusion complex of ALA with β-CD and thiamphenicol with γ-CD will also be targeted, with the transfer of both systems to a cooling crystallisation environment demonstrated in Chapter 6 a key starting point. The continuous crystallisation of these systems is unprecedented in the current literature. Observations from cooling crystallisation experiments indicate that cooling to a temperature of 5 °C is required in order to induce significant crystallisation in the system. As such, it can be suggested that the COBC or an MSMPR crystalliser would be most suitable as initial targets for continuous crystallisation platforms for these hosted systems.

8 References

1. Beckmann, W., *Crystallization: Basic Concepts and Industrial Applications*. Wiley-VCH: Germany, 2013; p 346.

2. Davey, R. J.; Garside, J., *From Molecules to Crystallizers*. Oxford Univeristy Press Inc.: United States, 2006.

3. Davey, R. J.; Schroeder, S. L. M.; ter Horst, J. H.*Angewandte Chemie-International Edition* 2013, *52* (8), 2166-2179.

4. Volmer, M.; Webwe, A.*Z. Physikal. Chemie* 1925, *119*, 227.

5. Vekilov, P. G.*Journal of Crystal Growth* 2005, *275* (1–2), 65-76.

6. Farkas, L.*Z., Physikal. Chemie* 1927, *125*, 236-242.

7. Roger, D.; Garside, J., *From Molecules to Crystallisers: An Introduction to Crystallisation*. Oxford University Press: New York, United States, 2000; Vol. 86.

8. Turkmen, I. R.; Baumgartel, H.*Zeitschrift Fur Physikalische Chemie-International Journal of Research in Physical Chemistry & Chemical Physics* 2014, *228* (4-5), 471-491.

9. Dhanaraj, P. V.; Mathew, S. K.; Rajesh, N. P.*Journal of Crystal Growth* 2008, *310* (10), 2532-2536.

10. Chadwick, K.; Myerson, A.; Trout, B.*CrystEngComm* 2011, *13* (22), 6625-6627.

11. Caridi, A.; Kulkarni, S. A.; Di Profio, G.; Curcio, E.; ter Horst, J. H.*Cryst. Growth Des,* 2014, *14* (3), 1135-1141.

12. Hartman, P.; Perdock, W. G.*Acta Crystallographica* 1955, *8* (49), 521.

13. Mullin, J. W., *Crystallization*. Third ed.; Butterworth-Heinemann: Great Britain, 1992.

14. Myerson, A.; Rajiv, G., *Handbook of Industrial Crystallisation*. 2nd edition ed.; Butterworth-Heinemann: United States of America, 2002; p 305.

15. Ohara, M.; Reid, R. C., *Modeling crystal growth rates from solution*. Prentice-Hall: 1973.

16. Sunagawa, I.; Tsukamot.*Journal of Crystal Growth* 1972, *15* (1), 73-&.

17. Liu, X. J.; Wang, Z. Y.; Yu, G. W.; Sun, Z. H.; Zhang, G. H.; Wang, X. Q.; Zhu, L. Y.; Yu, G.; Xu, D.*Journal of Physics and Chemistry of Solids* 2007, *68* (4), 608-610.

18. Cano, H.; Gabas, N.; Canselier, J. P.*Journal of Crystal Growth* 2001, *224* (3-4), 335-341.

19. Sullivan, R. A.; Davey, R. J.*Crystengcomm* 2015, *17* (5), 1015-1023.

20. Cang, H. X.; Huang, W. D.; Zhou, Y. H., *Journal of Crystal Growth* 1998, *192* (1-2), 236-242.

21. Sudha, C.; Srinivasan, K.*Crystal Research and Technology* 2014, *49* (11), 865-872.

22. Klapwijk, A. R.; Simone, E.; Nagy, Z. K.; Wilson, C. C.*Cryst. Growth Des,* 2016.

23. Salvalaglio, M.; Vetter, T.; Mazzotti, M.; Parrinello, M.*Angewandte Chemie-International Edition* 2013, *52* (50), 13369-13372.

24. Thompson, C.; Davies, M. C.; Roberts, C. J.; Tendler, S. J. B.; Wilkinson, M. J.*International Journal of Pharmaceutics* 2004, *280* (1-2), 137-150.

25. Britain, H. G., *Polymorphism in pharmaceutical solids*. Second ed.; Taylor & Francis: New York, 2009.

26. Mullin, J. W., 8 - Industrial techniques and equipment. In *Crystallization (Fourth Edition)*, Butterworth-Heinemann: Oxford, 2001; pp 315-402.

27. Dong, Y.; Ng, W. K.; Hu, J.; Shen, S.; Tan, R. B. H.*Int. J. Pharm.* 2010, *386* (1-2), 256-261.

28. Hu, J.; Ng, W. K.; Dong, Y.; Shen, S.; Tan, R. B. H.*Int. J. Pharm.* 2011, *404* (1-2), 198-204.

29. Dalvi, S. V.; Dave, R. N.*Ind. Eng. Chem. Res.* 2009, *48* (16), 7581-7593.

30. Paulino, A. S.; Rauber, G.; Campos, C. E. M.; Mauricio, M. H. P.; de Avillez, R. R.; Capobianco, G.; Cardoso, S. G.; Cuffini, S. L.*European Journal of Pharmaceutical Sciences* 2013, *49* (2), 294-301.

31. Kaneniwa, N.; Otsuka, M.; Hayashi, T.*Chemical & Pharmaceutical Bulletin* 1985, *33* (8), 3447-3455.

32. Beckmann, W.*Journal of Crystal Growth* 1999, *198*, 1307-1314.

33. Roelands, C. P. M.; Jiang, S. F.; Kitamura, M.; ter Horst, J. H.; Kramer, H. J. M.; Jansens, P. J.*Cryst. Growth Des.* 2006, *6* (4), 955-963.

34. Brittain, H. G., *Polymorphism in Pharmaceutical Solids, Second Edition*. Taylor & Francis: 2009.

35. Zencirci, N.; Gelbrich, T.; Kahlenberg, V.; Griesser, U. J.*Cryst. Growth Des.* 2009, *9* (8), 3444-3456.

36. Al-Zoubi, N.; Malamataris, S.*Int. J. Pharm.* 2003, *260* (1), 123-135.

37. Besenhard, M. O.; Hohl, R.; Hodzic, A.; Eder, R. J. P.; Khinast, J. G.*Crystal Research and Technology* 2014, *49* (2-3), 92-108.

38. Beckmann, W.*Organic Process Research & Development* 2000, *4* (5), 372-383.

39. Abu Bakar, M. R.; Nagy, Z. K.; Rielly, C. D.*Organic Process Research & Development* 2009, *13* (6), 1343-1356.

40. Hu, Y. R.; Liang, J. K.; Myerson, A. S.; Taylor, L. S.*Ind. Eng. Chem. Res.* 2005, *44* (5), 1233-1240.

41. O'Brien, L. E.; Timmins, P.; Williams, A. C.; York, P.*Journal of Pharmaceutical and Biomedical Analysis* 2004, *36* (2), 335-340.

42. Minkov, V. S.; Goryainov, S. V.; Boldyreva, E. V.; Gorbitz, C. H.*Journal of Raman Spectroscopy* 2010, *41* (12), 1748-1758.

43. Huang, J.; Da, M.*Journal of Pharmaceutical and Biomedical Analysis* 2013, *86*, 92-99.

44. Lin, S.-Y.; Cheng, W.-T.*Journal of Raman Spectroscopy* 2012, *43* (8), 1166-1170.

45. Barthe, S. C.; Grover, M. A.; Rousseau, R. W.*Cryst. Growth Des,* 2008, *8* (9), 3316-3322.

46. Wang, I.-C.; Lee, M.-J.; Seo, D.-Y.; Lee, H.-E.; Choi, Y.; Kim, W.-S.; Kim, C.-S.; Jeong, M.-Y.; Choi, G. J.*Aaps Pharmscitech* 2011, *12* (2), 764-770.

47. Zhao, Y.; Yuan, J.; Ji, Z.; Wang, J.; Rohani, S.*Ind. Eng. Chem. Res.* 2012, *51* (38), 12530-12536.

48. O'Sullivan, B.; Barrett, P.; Hsiao, G.; Carr, A.; Glennon, B.*Organic Process Research & Development* 2003, *7* (6), 977-982.

49. Lawton, S.; Steele, G.; Sharing, P.; Ni, X.-W.; Zhao, L.; Laird, I.*Organic Process Research & Development* 2009, *13*, 1357-1363.

50. Quon, J. L.; Zhang, H.; Alvarez, A.; Evans, J.; Myerson, A. S.; Trout, B. L.*Cryst. Growth Des,* 2012, *12* (6), 3036-3044.

51. Baxendale, I. R.; Braatz, R. D.; Hodnett, B. K.; Jensen, K. F.; Johnson, M. D.; Sharratt, P.; Sherlock, J.-P.; Florence, A. J.*Journal of Pharmaceutical Sciences* 2015, *104* (3), 781-791.

52. Chen, J.; Sara, B.; Evans, J. M. B.; Myerson, A. S.*American Chemical Society* 2011, *11* (11), 887 -895.

53. Li, J.; Trout, B. L.; Myerson, A. S.*Organic Process Research & Development* 2016, *20* (2), 510-516.

54. Powell, K. A.; Saleemi, A. N.; Rielly, C. D.; Nagy, Z. K.*Chemical Engineering and Processing* 2015, *97*, 195-212.

55. Powell, K.; Saleemi, A.; Ali, N.; Rielly, C. D.; Nagy, Z. K.*Organic Process Research & Development* 2016.

56. Tahara, K.; O'Mahony, M.; Myerson, A. S.*Cryst. Growth Des,* 2015, *15* (10), 5149-5156.

57. Galan, K.; Eicke, M. J.; Elsner, M. P.; Lorenz, H.; Seidel-Morgenstern, A.*Cryst. Growth Des,* 2015, *15* (4), 1808-1818.

58. McGlone, T.; Briggs, N.; Clark, C.; Brown, C.; Sefcik, J.; Florence, A., *Organic Process Research & Development* 2015, *19* (19), 1186-1202.

59. Mazubert, A.; Fletcher, D. F.; Poux, M.; Aubin, J., *Chemical Engineering and Processing* 2016, *108*, 78-92.

60. Mazubert, A.; Fletcher, D. F.; Poux, M.; Aubin, J., *Chemical Engineering and Processing* 2016, *102*, 102-116.

61. Harvey, A. P.; Mackley, M. R.; Seliger, T., *Journal of Chemical Technology and Biotechnology* 2003, *78* (2-3), 338-341.

62. Siddique, H.; Brown, C. J.; Houson, I.; Florence, A. J., *Organic Process Research & Development* 2015, *19* (12), 1871-1881.

63. Brown, C. J.; Lee, Y. C.; Nagy, Z. K.; Ni, X.*Crystengcomm* 2014, *16* (34), 8008-8014.

64. Ejim, L. N.; Yerdelen, S.; McGlone, T.; Onyemelukwe, I.; Johnston, B.; Florence, A. J.; Reis, N. M.*Chemical Engineering Journal* 2017, *308*, 669-682.

65. Briggs, N. E. B.; Schacht, U.; Raval, V.; McGlone, T.; Sefcik, J.; Florence, A. J.*Organic Process Research & Development* 2015, *19* (12), 1903-1911.

66. Zhao, L.; Raval, V.; Briggs, N. E. B.; Bhardwaj, R. M.; McGlone, T.; Oswald, I. D. H.; Florence, A. J.2014, *16*, 5769-5780.

67. Robertson, K.; Flandrin, P. B.; Klapwijk, A. R.; Wilson, C. C.*Cryst. Growth Des,* 2016, *16* (8), 4759-4764.

68. Karpinski, P. H.*Chemical Engineering & Technology* 2006, *29* (2), 233-237.

69. Yu, L.*Accounts of Chemical Research* 2010, *43* (9), 1257-1266.

70. Shah, J. C.; Chen, J. R.; Chow, D.*Drug Development and Industrial Pharmacy* 1999, *25* (1), 63-67.

71. Liu, J.; Svaerd, M.; Hippen, P.; Rasmuson, A. C.*Journal of Pharmaceutical Sciences* 2015, *104* (7), 2183-2189.

72. Zhang, J.; Wu, Y.; Liu, A.; Li, W.; Han, Y.*Rsc Advances* 2014, *4* (41), 21599-21607.

73. Bauer, J.; Spanton, S.; Henry, R.; Quick, J.; Dziki, W.; Porter, W.; Morris, J.*Pharmaceutical Research* 2001, *18* (6), 859-866.

74. Lai, T.-T. C.; Cornevin, J.; Ferguson, S.; Li, N.; Trout, B. L.; Myerson, A. S.*Cryst. Growth Des,* 2015, *15* (7), 3374-3382.

75. Gracin, S.; Rasmuson, A. C.*Cryst. Growth Des,* 2004, *4* (5), 1013-1023.

76. Chen, C.; Cook, O.; Nicholson, C. E.; Cooper, S. J.*Cryst. Growth Des,* 2011, *11* (6), 2228-2237.

77. Lancaster, R. W.; Karamertzanis, P. G.; Hulme, A. T.; Tocher, D. A.; Lewis, T. C.; Price, S. L.*Journal of Pharmaceutical Sciences* 2007, *96* (12), 3419-3431.

78. Li, J. J.; Bourne, S. A.; Caira, M. R.*Chem. Commun* 2011, *47* (5), 1530-1532.

79. Karanam, M.; Dev, S.; Choudhury, A. R.*Cryst. Growth Des,* 2012, *12* (1), 240-252.

80. Sudha, C.; Nandhini, R.; Srinivasan, K.*Cryst. Growth Des,* 2014, *14* (2), 705-715.

81. Bolla, G.; Mittapalli, S.; Nangia, A.*Cryst. Growth Des,* 2014, *14* (10), 5260-5274.

82. Joiris, E.; Di Martino, P.; Berneron, C.; Guyot-Hermann, A. M.; Guyot, J. C.*Pharm Res* 1998, *15* (7), 1122-30.

83. de Villiers, M. M.; Terblanche, R. J.; Liebenberg, W.; Swanepoel, E.; Dekker, T. G.; Song, M.*Journal of Pharmaceutical and Biomedical Analysis* 2005, *38* (3), 435-441.

84. Lohani, S.; Grant, D. J. W., *Polymorphism in the Pharmaceutical Industry*. Wiley-VCH: 2006.

85. Burger, A.; Ramberger, R.*Mikrochim. Acta* 1979, *2*, 259-271.

86. Ostwald, W.*Z.Phys.Chem* 1897

22, 289-330.

87. O'Mahony, M. A.; Maher, A.; Croker, D. M.; Rasmuson, A. C.; Hodnett, B. K.*Cryst. Growth Des,* 2012, *12* (4), 1925-1932.

88. Thirunahari, S.; Chow, P. S.; Tan, R. B. H.*Cryst. Growth Des,* 2011, *11* (7), 3027-3038.

89. Lu, J.; Wang, X. J.; Yang, X.; Ching, C. B.*Journal of Pharmaceutical Sciences* 2008, *97* (4), 1629-1629.

90. Cardew, P. T.; Davey, R. J.; Ruddick, A. J.*Journal of the Chemical Society, Faraday Transactions 2: Molecular and Chemical Physics* 1984, *80* (6), 659-668.

91. Avrami, M.*J. Chem. Phys* 1939, *7*, 1103.

92. Davis, B. L.; Adams, L. H.*Journal of Geophysical Research* 1965, *70* (2), 433-441.

93. Agnew, L. R.; Cruickshank, D. L.; McGlone, T.; Wilson, C. C.*Chem. Commun.* 2016.

94. Matsuo, K.; Matsuoka, M.*Journal of Chemical Engineering of Japan* 2007, *40* (6), 468-472.

95. Zhang, G. G. Z.; Gu, C. H.; Zell, M. T.; Burkhardt, R. T.; Munson, E. J.; Grant, D. J. W.*Journal of Pharmaceutical Sciences* 2002, *91* (4), 1089-1100.

96. Pfeffer-Hennig, S.; Piechon, P.; Bellus, M.; Goldbronn, C.; Tedesco, E.*Journal of Thermal Analysis and Calorimetry* 2004, *77* (2), 663-679.

97. Zhang, Q.; Jiang, L. L.; Mei, X. F.*Pharmaceutical Development and Technology* 2016, *21* (2), 196-203.

98. Aakeroy, C. B.; Wijethunga, T. K.; Desper, J.*Chemistry-a European Journal* 2015, *21* (31), 11029-11037.

99. Blagden, N.; de Matas, M.; Gavan, P. T.; York, P.*Advanced Drug Delivery Reviews* 2007, *59* (7), 617-630.

100. Miroshnyk, I.; Mirza, S.; Sandlert, N.*Expert Opinion on Drug Delivery* 2009, *6* (4), 333-341.

101. Vangala, V. R.; Chow, P. S.; Tan, R. B. H.*Cryst. Growth Des,* 2012, *12* (12), 5925-5938.

102. Araya-Sibaja, A. M.; Soldi, V.; de Campos, C. E. M.; Cardoso, S. G.; Cuffini, S. L.*Crystal Research and Technology* 2016, *51* (1), 49-57.

103. Lou, B. Y.; Bostroem, D.; Velaga, S. P.*Cryst. Growth Des,* 2009, *9* (3), 1254-1257.

104. Thomas, L.; Wales, C.; Zhao, L.; Wilson, C.*Cryst. Growth Des.* 2011, *11*, 1450-1452.

105. Weissbuch, I.; Lahav, M.; Leiserowitz, L., *Crystal morphology control with tailor-made additives; A stereochemical approach*. 2001; p 381-400.

106. Simone, E.; Cenzato, M. V.; Nagy, Z. K.*Journal of Crystal Growth* 2016, *446*, 50-59.

107. Desiraju, G. R.*Journal of Chemical Sciences* 2010, *122* (5), 667-675.

108. Politzer, P.; Murray, J. S.*Chemphyschem* 2013, *14* (2), 278-294.

109. Mukherjee, A.; Tothadi, S.; Desiraju, G. R.*Accounts of Chemical Research* 2014, *47* (8), 2514-2524.

110. Yamada, H.; Tamada, T.; Kosaka, M.; Miyata, K.; Fujiki, S.; Tano, M.; Moriya, M.; Yamanishi, M.; Honjo, E.; Tada, H.; Ino, T.; Yamaguchi, H.; Futami, J.; Seno, M.; Nomoto, T.; Hirata, T.; Yoshimura, M.; Kuroki, R.*Protein Science* 2007, *16* (7), 1389-1397.

111. Lin, Z.; Jiang, X.; Kang, L.; Gong, P.; Luo, S.; Lee, M.-H.*Journal of Physics D-Applied Physics* 2014, *47* (25).

112. Park, H. J.; Cheon, Y. E.; Suh, M. P.*Chemistry-a European Journal* 2010, *16* (38), 11662-11669.

113. Allendorf, M. D.; Stavila, V.*Crystengcomm* 2015, *17* (2), 229-246.

114. Ghosh, A.; Bansal, M.*Journal of Molecular Biology* 1999, *294* (5), 1149-1158.

115. Crick, F.*The chemical basis of heredity* 1957, 532-539.

116. Martin, A. E.*Nature* 1947, *159* (4038), 403-404.

117. Navarro, E.; Subirana, J. A.; Puiggali, J.*Polymer* 1997, *38* (13), 3429-3432.

118. Franco, L.; Cooper, S. J.; Atkins, E. D. T.; Hill, M. J.; Jones, N. A., *Journal of Polymer Science Part B-Polymer Physics* 1998, *36* (7), 1153-1165.

119. Villasenor, P.; Franco, L.; Subirana, J. A.; Puiggali, J.*Journal of Polymer Science Part B-Polymer Physics* 1999, *37* (17), 2383-2395.

120. *Industrial and Engineering Chemistry* 1965, *57* (11), 14-&.

121. Jeffrey, G. A., *Introduction to Hydrogen Bonding*. Oxford University Press: New York, 1997.

122. Wood, P. A.; Olsson, T. S. G.; Cole, J. C.; Cottrell, S. J.; Feeder, N.; Galek, P. T. A.; Groom, C. R.; Pidcock, E.*Crystengcomm* 2013, *15* (1), 65-72.

123. Galek, P. T. A.; Allen, F. H.; Fabian, L.; Feeder, N.*Crystengcomm* 2009, *11* (12), 2634-2639.

124. Sivasakthi, V.; Anbarasu, A.; Ramaiah, S.*Cell Biochemistry and Biophysics* 2013, *67* (3), 853-863.

125. Hunter, C. A.; Sanders, J. K. M., *JACS,* 1990, *112* (14), 5525-5534.

126. Martinez, C. R.; Iverson, B. L.*Chemical Science* 2012, *3* (7), 2191-2201.

127. Dr., G. R. D. P., Crystal Engineering: A Holistic View. Angewandte Chemie International Edition: 2007; Vol. 46, pp 8305-8519.

128. Etter, M. C.*Journal of Physical Chemistry* 1991, *95*, 4601-4610.

129. Blagden, N.; Colesb, S. J.; Berry, D. J.*Crystengcomm* 2014, *16* (26), 5753-5761.

130. Aitipamula, S.; Banerjee, R.; Bansal, A. K.; Biradha, K.; Cheney, M. L.; Choudhury, A. R.; Desiraju, G. R.; Dikundwar, A. G.; Dubey, R.; Duggirala, N.; Ghogale, P. P.; Ghosh, S.; Goswami, P. K.; Goud, N. R.; Jetti, R. R. K. R.; Karpinski, P.; Kaushik, P.; Kumar, D.; Kumar, V.; Moulton, B.; Mukherjee, A.; Mukherjee, G.; Myerson, A. S.; Puri, V.; Ramanan, A.; Rajamannar, T.; Reddy, C. M.; Rodriguez-Hornedo, N.; Rogers, R. D.; Row, T. N. G.; Sanphui, P.; Shan, N.; Shete, G.; Singh, A.; Sun, C. C.; Swift, J. A.; Thaimattam, R.; Thakur, T. S.; Thaper, R. K.; Thomas, S. P.; Tothadi, S.; Vangala, V. R.; Variankaval, N.; Vishweshwar, P.; Weyna, D. R.; Zaworotko, M. J.*Cryst. Growth Des.* 2012, *12* (5), 2147-2152.

131. Childs, S. L.; Stahly, G. P.; Park, A.*Molecular Pharmaceutics* 2007, *4* (3), 323-338.

132. Jones, C. L.; Wilson, C. C.; Thomas, L. H.*Crystengcomm* 2014, *16* (26), 5849-5858.

133. Zhao, L.; Raval, V.; Briggs, N. E. B.; Bhardwaj, R. M.; McGlone, T.; Oswald, I. D. H.; Florence, A. J.*Crystengcomm* 2014, *16* (26), 5769-5780.

134. Bruni, G.; Maietta, M.; Maggi, L.; Mustarelli, P.; Ferrara, C.; Berbenni, V.; Freccero, M.; Scotti, F.; Milanese, C.; Girella, A.; Marini, A.*Journal of Physical Chemistry B* 2013, *117* (27), 8113-8121.

135. Sanphui, P.; Rajput, L.*Acta Crystallographica Section B-Structural Science* 2014, *70*, 81-90.

136. Martin, F. A.; Pop, M. M.; Borodi, G.; Filip, X.; Kacso, I.*Cryst. Growth Des.* 2013, *13* (10), 4295-4304.

137. Surov, A. O.; Voronin, A. P.; Manin, A. N.; Manin, N. G.; Kuzmina, L. G.; Churakov, A. V.; Perlovich, G. L.*Molecular Pharmaceutics* 2014, *11* (10), 3707-3715.

138. Sugandha, K.; Kaity, S.; Mukherjee, S.; Isaac, J.; Ghosh, A.*Cryst. Growth Des.* 2014, *14* (9), 4475-4486.

139. Song, J.-X.; Yan, Y.; Yao, J.; Chen, J.-M.; Lu, T.-B.*Cryst. Growth Des.* 2014, *14* (6), 3069-3077.

140. Chen, C.-T.; Ghosh, S.; Reddy, C. M.; Buehler, M. J.*Physical Chemistry Chemical Physics* 2014, *16* (26), 13165-13171.

141. Maeno, Y.; Fukami, T.; Kawahata, M.; Yamaguchi, K.; Tagami, T.; Ozeki, T.; Suzuki, T.; Tomono, K.*Int. J. Pharm.* 2014, *473* (1-2), 179-186.

142. Gillon, A. L.; Feeder, N.; Davey, R. J.; Storey, R.*Cryst. Growth Des,* 2003, *3* (5), 663-673.

143. Griesser, U. J., The Importance of Solvates. In *Polymorphism*, Wiley-VCH Verlag GmbH & Co. KGaA: 2006; pp 211-233.

144. Pudipeddi, M.; Serajuddin, A. T. M.*Journal of Pharmaceutical Sciences* 2005, *94* (5), 929-939.

145. Shimanovich, R.; Cooke, M.; Peterson, M. L.*Journal of Pharmaceutical Sciences* 2012, *101* (10), 4013-4017.

146. Cashell, C.; Corcoran, D.; Hodnett, B. K.*Cryst. Growth Des,* 2005, *5* (2), 593-597.

147. Rusin, M.; Ewan, B. C. R.; Ristic, R. I.*Crystengcomm* 2013, *15* (12), 2192-2196.

148. Kitamura, M.; Ishizu, T.*Journal of Crystal Growth* 1998, *192* (1–2), 225-235.

149. Kelleher, J. M.; Lawrence, S. E.; McAuliffe, M. T.; Moynihan, H. A.*Crystengcomm* 2007, *9* (1), 72-77.

150. Davey, R. J.; Blagden, N.; Potts, G. D.; Docherty, R.*Journal of the American Chemical Society* 1997, *119* (7), 1767-1772.

151. Qu, H. Y.; Louhi-Kultanen, M.; Kallas, J.*Cryst. Growth Des,* 2007, *7* (4), 724-729.

152. Skrdla, P. J.*Cryst. Growth Des,* 2008, *8* (11), 4185-4189.

153. Mukuta, T.; Lee, A. Y.; Kawakami, T.; Myerson, A. S.*Cryst. Growth Des,* 2005, *5* (4), 1429-1436.

154. Surov, A. O.; Solanko, K. A.; Bond, A. D.; Perlovich, G. L.; Bauer-Brandl, A.*Cryst. Growth Des,* 2012, *12* (8), 4022-4030.

155. Simone, E.; Steele, G.; Nagy, Z. K.*Crystengcomm* 2015, *17* (48), 9370-9379.

156. Boukerche, M.; Mangin, D.; Klein, J. P.; Monnier, O.; Hoff, C.*Chemical Engineering Research & Design* 2010, *88* (11A), 1474-1478.

157. Quon, J. L.; Chadwick, K.; Wood, G. P. F.; Sheu, I.; Brettmann, B. K.; Myerson, A. S.; Trout, B. L.*Langmuir* 2013, *29* (10), 3292-3300.

158. Diao, Y.; Myerson, A. S.; Hatton, T. A.; Trout, B. L.*Langmuir* 2011, *27* (9), 5324-5334.

159. Giacovazzo, C., *Fundamentals of Crystallography*. Oxford University Press: New York, 2002.

160. Clegg, W., *Crystal Structure Analysis Principles and Practice*. Oxford University Press: New York, 2001.

161. Stout, G. H.; Jensen, L. H., *X-ray structure determination: a practical guide*. Macmillan: 1968.

162. IUCr, Structure factor. In *Online Dictionary of Crystallography*, IUCr, Ed. 2015.

163. Agilent *CrysAlis PRO*, Oxford Diffraction Ltd: Abingdon, Oxfordshire, England, 2014.

164. Farrugia, L. J.*J. Appl. Cryst.* 2012, *45*, 849-854.

165. West, A. R., *Basic Solid State Chemistry*. John Wiley & Sons Ltd: 1991.

166. Kim, Y. S.; Rousseau, R. W.*Cryst. Growth Des,* 2004, *4* (6), 1211-1216.

167. Bag, P. P.; Ghosh, S.; Khan, H.; Devarapalli, R.; Reddy, C. M.*Crystengcomm* 2014, *16* (32), 7393-7396.

168. Planas, J. G.; Vinas, C.; Teixidor, F.; Light, M. E.; Hursthouse, M. B.*Crystengcomm* 2007, *9* (10), 888-894.

169. Atkins, P., *The Elements of Physical Chemistry*. Third Edition ed.; Oxford University Press: 2002.

170. Todedo, M. FBRM (Focused Beam Reflectance Measurement) Technology. http://us.mt.com/us/en/home/supportive_content/specials/Lasentec-FBRM-Method-of-Measurement.html (accessed 13/01/2015).

171. Harris, P. Introduction to scanning electron microscopy. iitkgp.vlab.co.in/?sub=40&brch=263&sim=1582&cnt=3311 (accessed 25/07/2017).

172. Nichols, G.; Frampton, C. S.*Journal of Pharmaceutical Sciences* 1998, *87* (6), 684-693.

173. Perrin, M.-A.; Neumann, M. A.; Elmaleh, H.; Zaske, L.*Chem. Commun* 2009, (22), 3181-3183.

174. Zhang, G. G.; Law, D.; Schmitt, E. A.; Qiu, Y.*Advanced drug delivery reviews* 2004, *56* (3), 371-390.

175. Smith, S. J.; Montgomery, J. M.; Vohra, Y. K.*Journal of Physics-Condensed Matter* 2016, *28* (3).

176. Telford, R.; Seaton, C. C.; Clout, A.; Buanz, A.; Gaisford, S.; Williams, G. R.; Prior, T. J.; Okoye, C. H.; Munshi, T.; Scowen, I. J.*Chem. Commun* 2016, *52* (81), 12028-12031.

177. DiMartino, P.; Conflant, P.; Drache, M.; Huvenne, J. P.; GuyotHermann, A. M.*Journal of Thermal Analysis* 1997, *48* (3), 447-458.

178. Prasad, K. V. R.; Ristic, R. I.; Sheen, D. B.; Sherwood, J. N.*International Journal of Pharmaceutics* 2001, *215* (1-2), 29-44.

179. Hendriksen, B. A.; Grant, D. J. W.; Meenan, P.; Green, D. A.*Journal of Crystal Growth* 1998, *183* (4), 629-640.

180. Barthe, S. C.; Grover, M. A.; Rosseau, R. W.*Cryst. Growth Des,* 2008, *8*, 3316-3322.

181. Lee, H. L.; Lin, H. Y.; Lee, T.*Organic Process Research & Development* 2014, *18* (4), 539-545.

182. Sudha, C.; Srinivasan, K.*CrystEngComm* 2013, *15* (10), 1914-1921.

183. Burley, J. C.; Duer, M. J.; Stein, R. S.; Vrcelj, R. M.*European Journal of Pharmaceutical Sciences* 2007, *31*, 271-276.

184. McGregor, L.; Rychkov, D. A.; Coster, P. L.; Day, S.; Drebushchak, V. A.; Achkasov, A. F.; Nichol, G. S.; Pulham, C. R.; Boldyreva, E. V.*Crystengcomm* 2015, *17* (32), 6183-6192.

185. Wood, W. M. L.*Powder Technology* 2001, *121* (1), 53-59.

186. Bravi, M.; Di Cave, S.; Mazzarotta, B.; Verdone, N.*Chemical Engineering Journal* 2003, *94* (3), 223-229.

187. Iggland, M.; Mazzotti, M.*Cryst. Growth Des,* 2011, *11* (10), 4611-4622.

188. Kuvadia, Z. B.; Doherty, M. F.*Cryst. Growth Des,* 2013, *13* (4), 1412-1428.

189. Sano, C.; Kashiwagi, T.; Nagashima, N.; Kawakita, T.*Journal of Crystal Growth* 1997, *178* (4), 568-574.

190. Agnew, L. R.; McGlone, T.; Wheatcroft, H. P.; Robertson, A.; Parsons, A. R.; Wilson, C. C.*Cryst. Growth Des,* 2017.

191. Lee, S. H.; Lee, G. H.; Lee, K. H.; Jazbinsek, M.; Kang, B. J.; Rotermund, F.; Kwon, O. P.*Cryst. Growth Des,* 2016, *16* (7), 3555-3561.

192. Kim, I. W.; Robertson, R. E.; Zand, R.*Cryst. Growth Des,* 2005, *5* (2), 513-522.

193. Murray, P. M.; Tyler, S. N. G.; Moseley, J. D.*Organic Process Research & Development* 2013, *17* (1), 40-46.

194. Renzi, P.; Kronig, C.; Carlone, A.; Eroksuz, S.; Berkessel, A.; Bella, M.*Chemistry-a European Journal* 2014, *20* (37), 11768-11775.

195. Eriksson, L.; Johsnsson, E.; Kettaneh-Wold, N.; Wikstrom, C.; Wold, S., *Design of Experiments Principles and Applications*. 2008.

196. Narula, U.; Tan, C. M.*Applied Sciences-Basel* 2016, *6* (7).

197. Draheim, C.; de Crecy, F.; Hansen, S.; Collnot, E. M.; Lehr, C. M.*Pharmaceutical Research* 2015, *32* (8), 2609-2624.

198. Draper, N. R.; Pukelsheim, F.*Statistical Papers* 1996, *37* (1), 1-32.

199. Umetrics *MODDE Pro*, 2017.

200. Paul, E. L.; Tung, H. H.; Midler, M.*Powder Technology* 2005, *150* (2), 133-143.

201. Singh, U. K.; Pietz, M. A.; Kopach, M. E.*Organic Process Research & Development* 2009, *13* (2), 276-279.

202. Szelagiewicz, M.; Marcolli, C.; Cianferani, S.; Hard, A. P.; Vit, A.; Burkhard, A.; von Raumer, M.; Hofmeier, U. C.; Zilian, A.; Francotte, E.; Schenker, R.*Journal of Thermal Analysis and Calorimetry* 1999, *57* (1), 23-43.

203. Hou, G. Y.; Power, G.; Barrett, M.; Glennon, B.; Morris, G.; Zhao, Y.*Cryst. Growth Des,* 2014, *14* (4), 1782-1793.

204. Ferguson, S.; Ortner, F.; Quon, J.; Peeva, L.; Livingston, A.; Trout, B. L.; Myersont, A. S.*Cryst. Growth Des,* 2014, *14* (2), 617-627.

205. Power, G.; Hou, G. Y.; Kamaraju, V. K.; Morris, G.; Zhao, Y.; Glennon, B.*Chemical Engineering Science* 2015, *133*, 125-139.

206. Lai, T. T. C.; Ferguson, S.; Palmer, L.; Trout, B. L.; Myerson, A. S.*Organic Process Research & Development* 2014, *18* (11), 1382-1390.

207. Hostomsky, J.*Collection of Czechoslovak Chemical Communications* 1987, *52* (5), 1186-1197.

208. Nebel, H.; Epple, M.*Zeitschrift Fur Anorganische Und Allgemeine Chemie* 2008, *634* (8), 1439-1443.

209. Hostomsky, J.; Jones, A. G.*Journal of Physics D-Applied Physics* 1991, *24* (2), 165-170.

210. Tai, C. Y.; Chen, P. C.*Aiche Journal* 1995, *41* (1), 68-77.

211. Powell, K.; Bartolini, G.; Wittering, K.; Saleemi, A.; Wilson, C.; Rielly, C.; Nagy, Z.*Cryst. Growth Des,* 2015, *15*, 4821-4836.

212. Newton, S.; Carter, C. F.; Pearson, C. M.; Alves, L. D.; Lange, H.; Thansandote, P.; Ley, S. V.*Angewandte Chemie-International Edition* 2014, *53* (19), 4915-4920.

213. Baxendale, I. R.*Journal of Chemical Technology and Biotechnology* 2013, *88* (4), 519-552.

214. Solutions, N. DN15 range. http://www.nitechsolutions.co.uk/products/dn15-range/ (accessed 27/07/2017).

215. Klapwijk, A. R. Disorder and additive control of solid form and morphology in continuous crystallisation. University of Bath, 2016.

216. Schwalbe, T.; Kadzimirsz, D.; Jas, G.*Qsar & Combinatorial Science* 2005, *24* (6), 758-768.

217. Carrel, F. R.; Geyer, K.; Codee, J. D. C.; Seeberger, P. H.*Organic Letters* 2007, *9* (12), 2285-2288.

218. Tanaka, Y.; Tonomura, O.; Isozaki, K.; Hasebe, S.*Chemical Engineering Journal* 2011, *167* (2-3), 483-489.

219. Phan, A. N.; Harvey, A.*Chemical Engineering Journal* 2010, *159* (1-3), 212-219.

220. Witt, P. M.; Somasi, S.; Khan, I.; Blaylock, D. W.; Newby, J. A.; Ley, S. V.*Chemical Engineering Journal* 2015, *278*, 353-362.

221. Hall, J. F.; Barigou, M.; Simmons, M. J. H.; Stitt, E. H.*Industrial & Engineering Chemistry Research* 2005, *44* (25), 9695-9704.

222. Gunther, A.; Jhunjhunwala, M.; Thalmann, M.; Schmidt, M. A.; Jensen, K. F.*Langmuir* 2005, *21* (4), 1547-1555.

223. Lu, J.; Litster, J. D.; Nagy, Z. K.*Cryst. Growth Des,* 2015, *15* (8), 3645-3651.

224. Jiang, M.; Papageorgiou, C. D.; Waetzig, J.; Hardy, A.; Langston, M.; Braatz, R. D.*Cryst. Growth Des,* 2015, *15* (5), 2486-2492.

225. Abolhasani, M.; Singh, M.; Kumacheva, E.; Gunther, A.*Lab on a Chip* 2012, *12* (22), 4787-4795.

226. Sobieszuk, P.; Aubin, J.; Pohorecki, R.*Chemical Engineering & Technology* 2012, *35* (8), 1346-1358.

227. Kurkov, S. V.; Loftsson, T.*International Journal of Pharmaceutics* 2013, *453* (1), 167-180.

228. Liu, L.; Guo, Q. X.*Journal of Inclusion Phenomena and Macrocyclic Chemistry* 2002, *42* (1-2), 1-14.

229. Vaitkus, R.; Grinciene, G.; Norkus, E.*Journal of Inclusion Phenomena and Macrocyclic Chemistry* 2011, *69* (3-4), 345-347.

230. Loftsson, T.; Brewster, M. E.*Journal of Pharmaceutical Sciences* 1996, *85* (10), 1017-1025.

231. Nair, A. B.; Attimarad, M.; Al-Dhubiab, B. E.; Wadhwa, J.; Harsha, S.; Ahmed, M.*Drug Delivery* 2014, *21* (7), 540-547.

232. Nerurkar, J.; Beach, J. W.; Park, M. O.; Jun, H. W.*Pharmaceutical Development and Technology* 2005, *10* (3), 413-421.

233. Ansari, M. T.; Batty, K. T.; Iqbal, I.; Sunderland, V. B.*Archives of Pharmacal Research* 2011, *34* (5), 757.

234. Kreaz, R. M. A.; Dombi, G.; Kata, M.*Journal of Inclusion Phenomena and Molecular Recognition in Chemistry* 1998, *31* (3), 189-196.

235. Takahashi, H.; Bungo, Y.; Mikuni, K.*Bioscience Biotechnology and Biochemistry* 2011, *75* (4), 633-637.

236. Glinka, T. W., Water-soluble prodrugs of chloramphenicol, thiamphenicol, and analogs thereof. Google Patents: 2011.

237. Mitchell, S. M.; Ullman, J. L.; Teel, A. L.; Watts, R. J.*Chemosphere* 2015, *134*, 504-511.

238. Gong, L.; Li, T.; Chen, F.; Duan, X.; Yuan, Y.; Zhang, D.; Jiang, Y.*Food Chemistry* 2016, *206*, 292.

239. Alves, O. L.; Fonseca, S. F.*Journal of Inclusion Phenomena* 1989, *7* (6), 589-597.

240. Balmas, V.; Delogu, G.; Sposito, S.; Rau, D.; Migheli, Q.*Journal of Agricultural and Food Chemistry* 2006, *54* (2), 480-484.

241. Job, P.*Anal. Chim. Appl* 1928, *9*, 113-203.

242. Renny, J. S.; Tomasevich, L. L.; Tallmadge, E. H.; Collum, D. B.*Angewandte Chemie (International ed. in English)* 2013, *52* (46), 11998-12013.

243. Steiner, T.; Saenger, W.*Acta Crystallographica Section B-Structural Science* 1998, *54*, 450-455.

244. Woo, K. S.; Kim, H. Y.; Hwang, I. G.; Lee, S. H.; Jeong, H. S.*Preventive Nutrition and Food Science* 2015, *20* (2), 102-109.

9 Appendices

9.1 A3 (Chapter 3)

Metacetamol crystallisations yields at 10 ml

0.02 °C min^{-1}

Repeat 1		
% MCM	**Solvent**	**Yield (%)**
5	EtOH	12.95
10	EtOH	35.87
25	EtOH	45.15
10	60:40 H_2O:IPA	71.98
25	60:40 H_2O:IPA	89.04

Repeat 2		
% MCM	**Solvent**	**Yield (%)**
5	EtOH	18.06
10	EtOH	23.68
25	EtOH	38.44
10	60:40 H_2O:IPA	76.66
25	60:40 H_2O:IPA	72.86

Repeat 3		
% MCM	**Solvent**	**Yield (%)**
5	EtOH	46.74
10	EtOH	35.21
25	EtOH	39.95
10	60:40 H_2O:IPA	73.79
25	60:40 H_2O:IPA	81.72

0.2 °C min^{-1}

Repeat 1		
% MCM	**Solvent**	**Yield (%)**
5	EtOH	31.83
10	EtOH	35.89
25	EtOH	16.96
5	60:40 H_2O:IPA	65.98
10	60:40 H_2O:IPA	66.95
25	60:40 H_2O:IPA	70.72

Repeat 2		
% MCM	**Solvent**	**Yield (%)**
5	EtOH	43.26
10	EtOH	42.71
15	EtOH	48.94
5	60:40 H_2O:IPA	67.98
10	60:40 H_2O:IPA	66.82
15	60:40 H_2O:IPA	97.25

Repeat 3		
% MCM	**Solvent**	**Yield (%)**
5	EtOH	43.05
10	EtOH	47.28
15	EtOH	43.12
5	60:40 H_2O:IPA	78.75
10	60:40 H_2O:IPA	74.95
15	60:40 H_2O:IPA	74.00

1 °C min^{-1} stepped

Repeat 1		
% MCM	**Solvent**	**Yield (%)**
10	EtOH	47.73
25	EtOH	32.39
10	60:40 H_2O:IPA	69.48
25	60:40 H_2O:IPA	68.49

Repeat 2		
% MCM	**Solvent**	**Yield (%)**[5]
10	EtOH	*
20	EtOH	*
25	EtOH	*
10	60:40 H_2O:IPA	65.76
20	60:40 H_2O:IPA	63.28
25	60:40 H_2O:IPA	64.52

Repeat 3		
% MCM	**Solvent**	**Yield (%)***
10	EtOH	*
15	EtOH	*
20	EtOH	*
10	60:40 H_2O:IPA	55.16
15	60:40 H_2O:IPA	61.76
20	60:40 H_2O:IPA	46.45

1 °C min^{-1} linear

Repeat 1		
% MCM	**Solvent**	**Yield (%)**
10	EtOH	36.64
20	EtOH	36.47
25	EtOH	35.77
10	60:40 H_2O:IPA	58.64
20	60:40 H_2O:IPA	69.74
25	60:40 H_2O:IPA	55.26

Repeat 2		
% MCM	**Solvent**	**Yield (%)**
10	EtOH	21.59
15	EtOH	37.24
20	EtOH	30.91
10	60:40 H_2O:IPA	55.34
15	60:40 H_2O:IPA	65.88
20	60:40 H_2O:IPA	61.54

Repeat 3		
% MCM	**Solvent**	**Yield (%)**
10	EtOH	36.87
15	EtOH	41.19
20	EtOH	45.60
10	60:40 H_2O:IPA	68.68
15	60:40 H_2O:IPA	61.17
20	60:40 H_2O:IPA	58.53

[5] Filtration problems meant the yields for the ethanol crystallisations could not be determined accurately

9.2 List of Publications

L. R. Agnew, T. McGlone, H. P. Wheatcroft, A. Robertson, A. R. Parsons and C. C. Wilson, 'Continuous Crystallization of Paracetamol (Acetaminophen) Form II: Selective Access to a Metastable Solid Form', *Cryst. Growth Des*., 2017, 17(5), 2418-2427

L. R. Agnew, D. L. Cruickshank, T. McGlone and C. C. Wilson, 'Controlled production of the elusive metastable form II of acetaminophen (paracetamol): a fully scalable templating approach in a cooling environment, *Chem. Commun*., 2016, **52**, 7368-7371

K. E. Wittering, **L. R. Agnew**, A. R. Klapwijk, K. Robertson, A. J. P. Cousen, C. C. Wilson and D. L. Cruickshank, Crystallisation and physicochemical property characterisation of conformationally-locked co-crystals of fenamic acid derivatives, *CrystEngComm*., 2015, 17 (19), 3610-3618

9.3 List of oral conference presentations

'Towards the continuous crystallisation of paracetamol form II', British Crystallographic Association (BCA) Spring Meeting, University of Nottingham, April 2016

'Towards the continuous crystallisation of paracetamol form II', British Association of Crystal Growth (BACG)/ Crystal Growth of Organic Materials (CGOM) 12, University of Leeds, June 2016